DISS. ETH NO. 30121

REDOX PROMOTED REACTIVITY OF BIMETALLIC RHODIUM AND IRIDIUM COMPLEXES WITH NON-INNOCENT LIGANDS

A thesis submitted to attain the degree of

DOCTOR OF SCIENCES

(Dr. sc. ETH Zürich)

presented by

Clara Schweinzer

Dipl.-Ing. Technische Universität Wien

born on 20.02.1993

accepted on the recommendation of

Prof. Hansjörg Grützmacher (examiner)

Prof. Karl Kirchner (co-examiner)

2024

I

"There is no 'useless' science only the time of its use is unknown."

"The most exciting phrase to hear in science, the one that heralds new discoveries, is not 'Eureka! I found it!' but 'That's funny…'"

ISAAC ASIMOV

Acknowledgement

This work would not have been possible without the continuous support of many people, who helped me scientifically and in many other ways to complete this thesis. First of all, I want to thank Prof. Hansjörg Grützmacher for giving me a lot of freedom to follow my own research interests within his group, and for many interesting discussions and the possibility to develop as a scientist. This is especially true for the opportunity I got to collaborate with the group of Prof. Shannon Stahl in the US, where I had the pleasure of working with Asmaul Hoque for several weeks. I also want to thank Prof. Karl Kirchner for accepting to be my co-examiner and for the nice atmosphere he created during his visit at ETH.

Many thanks to Christine Rüegg and Andrea Sachs for all their administrative work, making sure the group runs smoothly. Thanks Andrea for paying so many bills for me. I would also like to thank Hartmut Schönberg for supporting us with his knowledge about instruments, IT, electrochemistry and non-standard chemical reactions. We were lucky to have him around for (very early) lunches as well as fixing gloveboxes. I want to thank René Verel and Michael Wörle for always helping with any issues coming up with NMR or XRD measurements. Thanks also to Marcel, Pascal and Grégoire for teaching me a lot about NMR and performing some interesting measurements with me.

The most important people were my fellow colleagues that I had the pleasure of working with. I am grateful to have become part of the Grützi group, which was my ETH family from the beginning. Most importantly, I was so lucky to have Stefan Banz going the whole way from the beginning to the end of my PhD with me, first as a lab neighbor, then as a desk neighbor in our new lab H114 and finally also as a "real" neighbor. We shared endless amounts of laughs, great conversations and bad jokes, mostly accompanied by tea or smoothies on the balcony on the "Klappstühle". I couldn't have wished for anyone else to share so much time with, not only during working hours but also in our free time.

Jonas Bösken was not only a great "Senior PhD" to me, but also a great friend who provided multiple different ways of motivation to me when I needed it most. I am also thankful that he gathered enough patience to teach me all he knew about how to measure CV and build a wooden table in his garage.

At the beginning of my doctorate, Pascal Jurt was so kind to give me some guidelines for my research and helped me a lot with new ideas. I am very glad that I had him as a mentor

Table of contents

Abstract

The properties of organometallic compounds not only depend on the nature of the metal center(s) but are also strongly determined by ligand characteristics. As such, reactions involving coordination compounds can take place at the central atom or within the ligand sphere. Prominent examples for ligand centered reactivity are the class of non-innocent ligands, where redox reactions can take place within the organic molecule. The extension from single metal atom centers to bimetallic complexes offers a large variety of reactivities resulting from the interaction of two metal centers. This thesis describes the investigation of bimetallic Rh and Ir complexes in redox reactions and / or under basic conditions. All compounds presented in this work show reactivity within the ligand sphere. For example, C−C bond formation and cleavage was observed as well as rearrangement within the ligand.
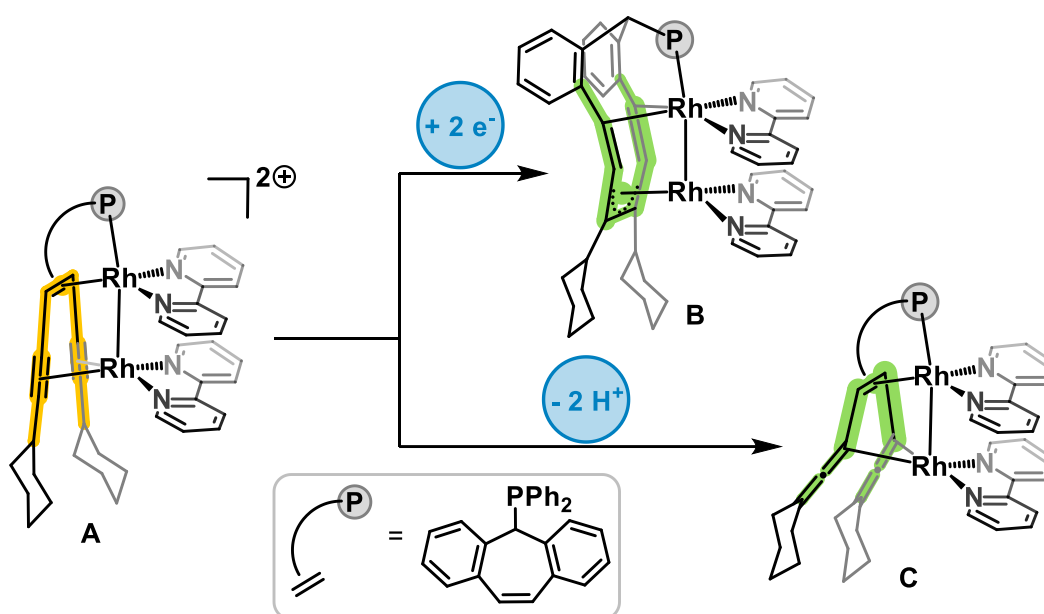
Scheme I. Reactivity of dirhodium complex **A** under reductive (**B**) or basic conditions (**C**).

The first part of this thesis describes the structural changes in the carbon sphere of a dirhodium complex (**A**) induced by redox or deprotonation reactions (Scheme I). The trop-based ligand coordinates the metal centers only with conjugated sp^2 and sp hybridized carbon centers and a phosphorus donor atom. Alkenyl and alkynyl binding sites are arranged to accommodate a binuclear metal unit with a Rh^I–Rh^I bond. The remarkably stable dicationic complex $[(CyC≡C)_2tropPPh_2Rh_2(bipy)_2](OTf)_2$ (**A**) allows for the investigation of possible responses of the carbon-framework to redox reactions as well as deprotonation reactions. It is shown that C−C bond rearrangement reactions of extraordinary diversity take place. Reduction by two electrons leads to a ring expansion reaction, which cleaves the trop double bond and extends the C_7 to a C_{11} cycle (**B**). Deprotonation of the cyclohexyl CH units in proximity to the metal centers leads to a change of the carbon hybridization and leads to a η^1 coordinating allenyl substructure emerging from the alkyne

groups (**C**). In combination with DFT studies, these results allow to gain insight into the structural changes caused by metal sites in a carbon-rich environment. This may be of relevance for the properties of metal particles on carbon support materials when they are exposed to hydrogen, electrons, or protons.
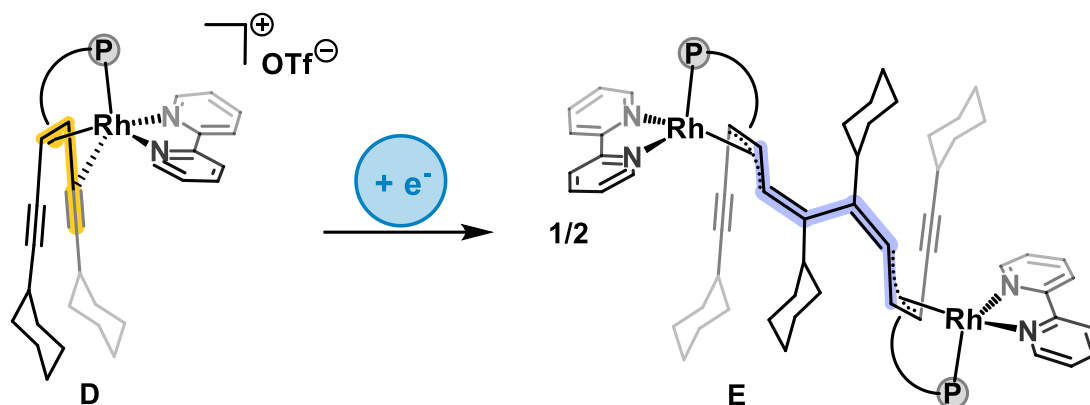
Scheme II. Reduction of mono rhodium complex leading to a dimerized complex upon C−C bond formation.

The described reactivity does not take place with the related mono rhodium complex (Scheme II, **D**). Its chemical reduction selectively leads to dimerization of the ligand upon C−C bond formation (Scheme II, **E**). While the bimetallic Rh$_2$ compound forms a stable product upon deprotonation, no such product of the mono rhodium complex can be obtained. This leads to the assumption of the need of both metals to form a stable product.

Furthermore, the same carbon-rich ligand - and similar ligands - are used to synthesize hetero bimetallic complexes involving Rh^I, Pt^{II}, Cu^I centers (an example is shown in Scheme III, **F**). They were structurally characterized and tested for N$_2$O reduction with H$_2$.
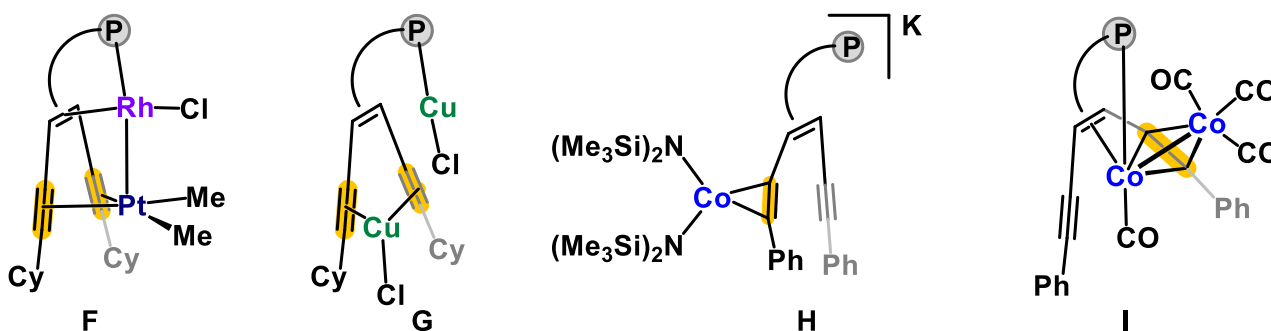
Scheme III. Selected examples of bimetallic complexes showing different coordination modes of the alkyne groups.

Homo bimetallic complexes with copper and cobalt metal centers showed new coordination modes of the two alkyne ligands (examples are shown in Scheme III). The metal center further away from the phosphorus atom can either coordinate perpendicular (**F**) to or in plane (**G**) with both alkyne groups. Furthermore, examples are shown where only one of the alkyne groups is bound to the metal

2

Abstract

center (**H**). The bimetallic Co^0–Co^0 core in complex **I** bridges one C≡C bond, spanning a tetrahedron including the metal-metal bond.
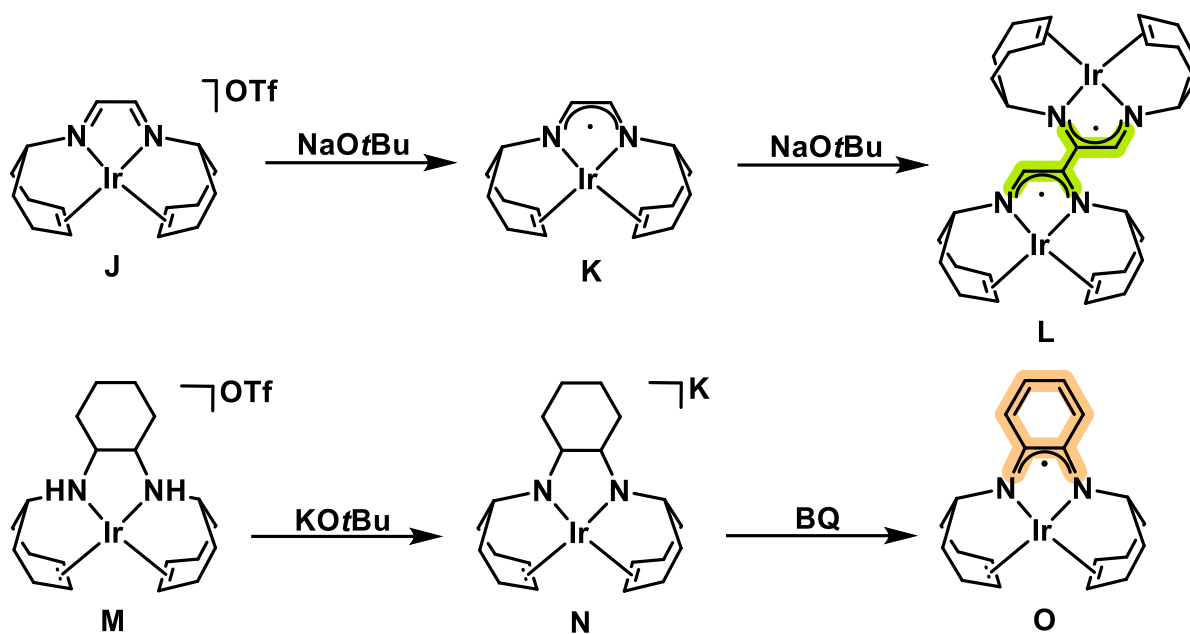
Scheme IV. Ligand reactivity of iridium complexes **J** and **M** under catalytic conditions.

The last part of this thesis aims to answer mechanistic questions concerning long-known iridium-based alcohol oxidation catalysts. The catalytic systems involve NaOtBu as base and 1,4-benzoquinone (BQ) as oxidant. Under these conditions, the fate of the iridium catalysts was unclear. This work shows that [Ir(trop$_2$dad)]OTf (**J**) reacts with NaOtBu in more than a simple deprotonation reaction: reduction to the intermediate compound (**K**) and subsequent dimerization upon C−C bond formation and deprotonation of C-H groups takes place (**L**) (Scheme IV, top). DFT calculations revealed the electronic structure to be a coupled radical with 26% diradical character. A similar iridium catalyst with a saturated cyclohexyl backbone, [Ir(trop$_2$dach)]OTf (**M**), shows dehydrogenation at its backbone under the catalytic conditions (2 eq. of KOtBu and excess BQ) (Scheme IV, bottom). It is assumed that this complex (**O**) is the true active species in the catalytic alcohol oxidation.

In summary, this work shows that the presence of a second metal can be beneficial and alters the reactivity of the ligand sphere. Several ligand reactivities of the carbon-based parts of the ligands are observed: dimerization upon C−C bond formation, ring expansion, rearrangement and dehydrogenation. Some structural changes within the ligands lead to significant changes in the observed colour of complexes: the red dirhodium complex turns green upon the described reactions, while the initially green iridium complex turns red during the reactions studied here.

Zusammenfassung

Die Eigenschaften metallorganischer Verbindungen hängen nicht nur von den Eigenschaften der Metallzentren des Komplexes ab, sondern werden auch stark von der Art der organischen Liganden bestimmt. So können die Reaktionen in Koordinationsverbindungen nicht nur am Zentralatom, sondern auch innerhalb der Liganden Moleküle stattfinden. Prominente Beispiele sind die Klasse der „non-innocent" Liganden, an denen häufig Redoxreaktionen beobachtet werden. Die Erweiterung von monometallischen zu bimetallischen Komplexen bietet eine erweiterte Vielfalt an Reaktivitäten, die sich aus der Wechselwirkung zweier Metallzentren ergeben. Diese Arbeit beschreibt die Untersuchung von bimetallischen Rhodium und Iridium Komplexen bei Redoxreaktionen und/oder unter basischen Bedingungen. Alle der hier vorgestellten Verbindungen zeigen Reaktivität am Liganden, wie die Bildung, Spaltung und Umlagerung von C−C Bindungen.
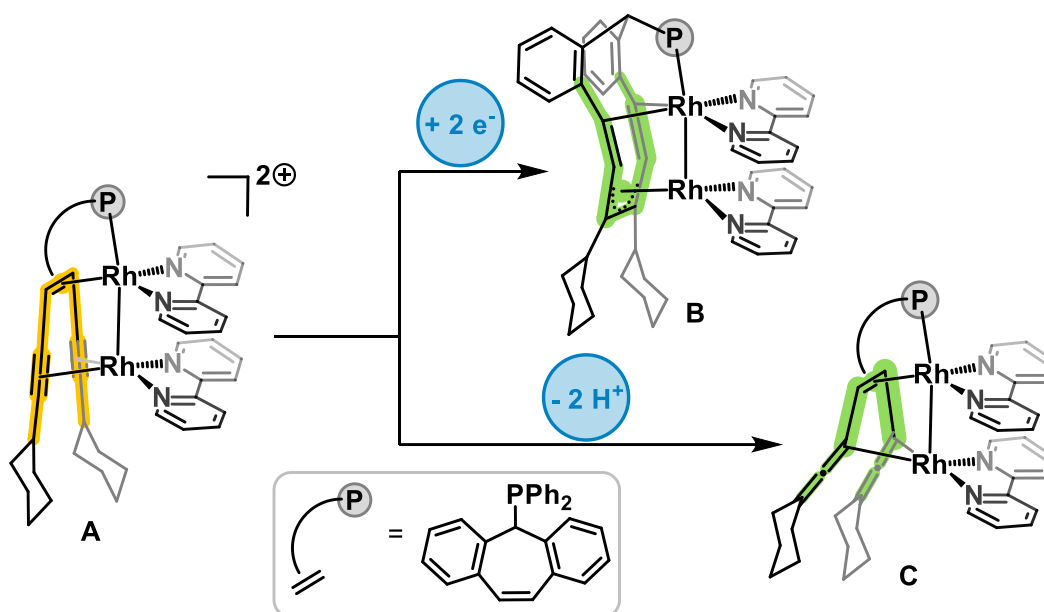
Schema I. Reaktivität des Dirhodium-Komplexes **A** unter reduktiven (**B**) oder basischen Bedingungen (**C**).

Der erste Teil dieser Arbeit beschreibt die strukturellen Veränderungen in der Kohlenstoffsphäre eines Dirhodiumkomplexes, die durch Redox- oder Deprotonierungsreaktionen ausgelöst werden (Schema I). Der trop-basierte Ligand koordiniert nur mit konjugierten sp^2- und sp-hybridisierten Kohlenstoffzentren und einem Phosphor Donoratom. Die Alkenyl- und Alkinyl-Bindungsstellen sind so angeordnet, dass sie eine zweikernige Metalleinheit mit einer Rh^I–Rh^I Bindung beherbergen können. Der bemerkenswert stabile dikationische Komplex $[(CyC{\equiv}C)_2tropPPh_2Rh_2(bipy)_2](OTf)_2$ (**A**) ermöglicht die Untersuchung möglicher Veränderungen innerhalb des Kohlenstoffgerüsts auf Redox- und Deprotonierungsreaktionen. Es wird gezeigt, dass C−C Bindungsumlagerungs-reaktionen von außerordentlicher Vielfalt stattfinden. Die Reduktion um zwei Elektronen führt zu einer Ringerweiterung, wobei die trop-Doppelbindung gespalten und der C_7- zu einem C_{11}-Ring erweitert wird (**B**). Die Deprotonierung der Cyclohexyl-CH-Einheiten in der Nähe der Metallzentren

führt zu einer Änderung der Kohlenstoff-Hybridisierung und bewirkt, dass aus dem Alkin eine η^1 koordinierende Allenyl-Substruktur entsteht (**C**). In Kombination mit DFT-Studien ermöglichen diese Ergebnisse einen Einblick in die Veränderungen der elektronischen Struktur, die durch Metallatome in einer kohlenstoffreichen Umgebung verursacht werden. Dies kann für die Untersuchung der Eigenschaften von Metallpartikeln auf Kohlenstoffträgermaterialien von Bedeutung sein, wenn diese Wasserstoff, Elektronen oder Protonen ausgesetzt sind.
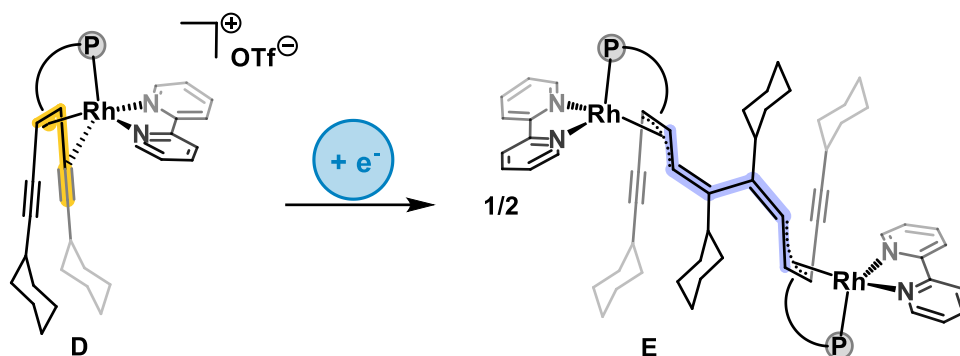
Schema II. Reduktion eines Mono-Rhodium-Komplexes unter Bildung einer neuen C−C-Bindung.

Die beschriebene Reaktivität findet bei dem verwandten Mono-Rhodium-Komplex (**D**) nicht statt. Dessen chemische Reduktion führt selektiv zur Dimerisierung des Liganden unter der Bildung einer neuen C−C Bindung (Schema II, **E**). Während die bimetallische Rh_2-Verbindung in basischem Milieu ein stabiles Produkt bildet, wird kein sauberes Produkt eines deprotonierten Mono-Rhodium-Komplexes erhalten. Daher sind beide Metalle zur Bildung eines stabilen Produkts erforderlich.

Darüber hinaus wird dieser kohlenstoffreiche Ligand - und ähnliche Liganden - zur Synthese von hetero-bimetallischen Komplexen mit Rh^I-, Pt^{II}- und Cu^I-Zentren verwendet, ein Beispiel ist in Schema III, **F**, gezeigt. Sie werden strukturell charakterisiert und werden für die Reduktion von N_2O mit H_2 untersucht.
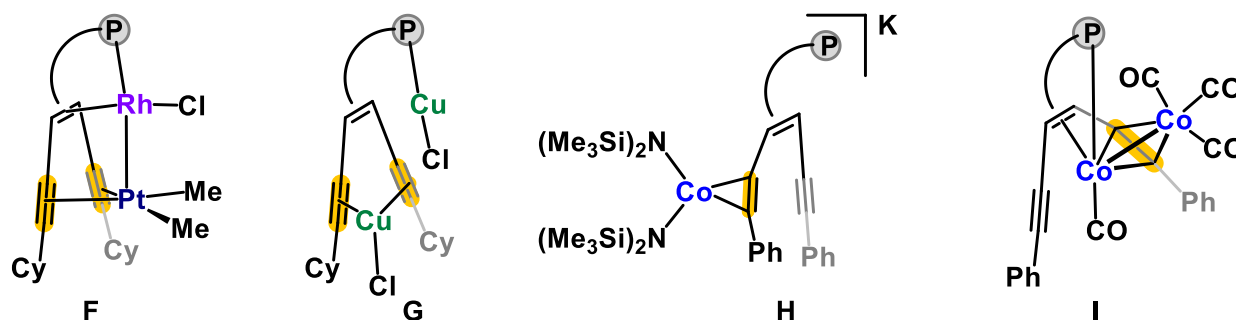
Schema III. Ausgewählte Beispiele für bimetallische Komplexe mit unterschiedlichen Koordinationsmodi der Alkine.

Homo-bimetallische Komplexe mit Kupfer- und Kobalt-Metallzentren zeigen neue Koordinationsmodi der beiden Alkin Gruppen (Beispiele sind in Schema III dargestellt). Während bei den zuvor beschriebenen Rh- und Pt-Komplexen der Koordinationsmodus unverändert bleibt, werden weitere

Zusammenfassung

Möglichkeiten für Kupfer und Kobalt Komplexe entdeckt. Das vom Phosphoratom weiter entfernte Metallzentrum kann entweder senkrecht (**F**) zu oder in der Ebene (**G**) mit den beiden Alkinen koordinieren. Außerdem werden Beispiele gezeigt, bei denen nur eine der Alkin-Gruppen an das Metallzentrum gebunden ist (**H**). Ein weiteres Beispiel enthält einen bimetallische $Co^0–Co^0$ Kern, der eine C≡C Bindung überbrückt, was einen Tetraeder mit der Metall-Metall-Bindung überspannt (**I**).
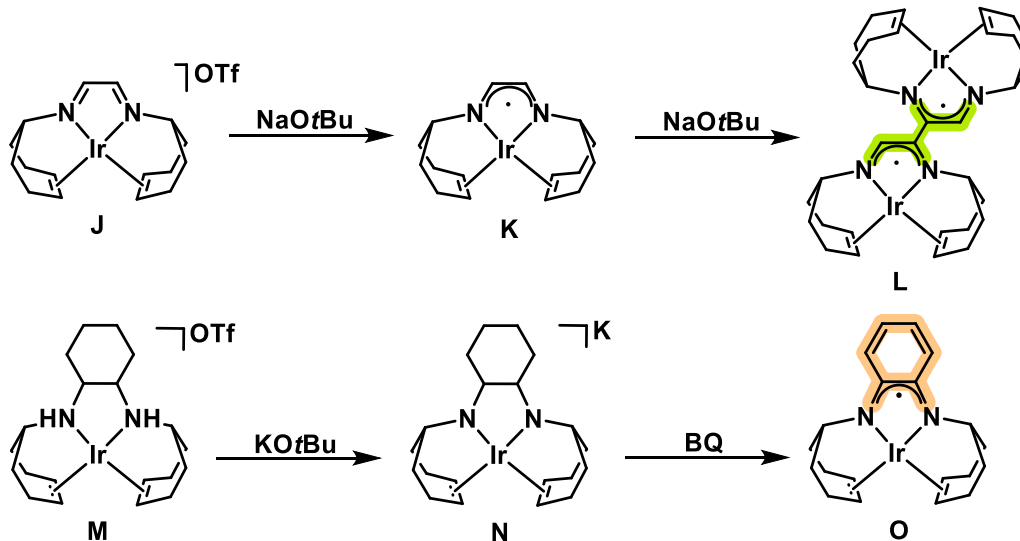
Schema IV. Ligandenreaktivität von Iridiumkomplexen **J** und **M** unter katalytischen Bedingungen.

Der letzte Teil dieser Arbeit zielt auf die Beantwortung mechanistischer Fragen in Bezug auf die seit langem bekannte selektive Alkoholoxidation zu Aldehyden mit Iridium-Komplexen als Katalysatoren ab. Die katalytischen Systeme enthalten NaOtBu als Base und 1,4-Benzochinon (BQ) als Oxidationsmittel. Unter diesen Reaktionsbedingungen war das Schicksal der Iridiumkatalysatoren bisher unklar. Diese Arbeit zeigt, dass [Ir(trop$_2$dad)]OTf (**J**) mit NaOtBu in mehr als nur einer einfachen Deprotonierungsreaktion reagiert: Die Verbindung wird reduziert (**K**), und dimerisiert schliesslich unter Bildung einer C−C Bindung und der Deprotonierung der C−H Gruppen (**L**) (Schema IV, oben). DFT-Berechnungen zeigen, dass die elektronische Struktur als gekoppeltes Radikal mit 26% Diradikalcharakter beschrieben werden kann. Bei einem ähnlichen Iridiumkatalysator mit einem gesättigten Zyklohexyl-Grundgerüst, [Ir(trop$_2$dach)]OTf (**M**), wird der gesättigte Sechsring unter den katalytischen Bedingungen (zwei Äquivalente Base und Überschuss an BQ) vollständig dehydriert (Schema IV, unten). Es wird angenommen, dass dieser Komplex (**O**) die eigentliche aktive Spezies in der Alkoholoxidation ist.

Zusammenfassend wird gezeigt, dass die Anwesenheit eines zweiten Metalls von Vorteil sein kann. Es werden mehrere Ligandenreaktivitäten der auf Kohlenstoff basierenden Liganden beobachtet: Dimerisierung unter Bildung von C−C Bindungen, Ringerweiterung, Umlagerung und Dehydrierung. Dabei findet zusätzlich oft eine signifikante Farbänderung der Komplexe statt.

CHAPTER I - Introduction

1. Cooperativity in bimetallic complexes

Bimetallic transition metal complexes have been heavily investigated in the 1970s and 1980s, and interest in them has recently seen a renaissance.[1–3] These compounds show unique features, often exhibiting superior properties to corresponding monometallic compounds. Not only nature is often relying on bimetallic centers,[4] but also chemists have well established the field of bimetallics.[5–9] The electronic coupling of metal centers can make more redox states accessible than individual metals can, which may be beneficial in catalytic applications.[9,10]

Several types of metal-metal bonds have been observed, some examples are shown in Scheme 1. Within the classical covalent bonds, distinctions can be made between polar and non-polar bonds. Furthermore, M-M single and multiple bonds are possible, with a bond order of up to five, which was first reported for a Cr-Cr complex.[2,11] At the opposite extreme are metallophilic interactions, which are non-covalent and in comparable strength to hydrogen bonds.[12] Apart from covalent bonds, also dative metal-metal bonds are possible, where one metal center acts as Lewis-basic donor site to a Lewis-acidic acceptor site.[13]
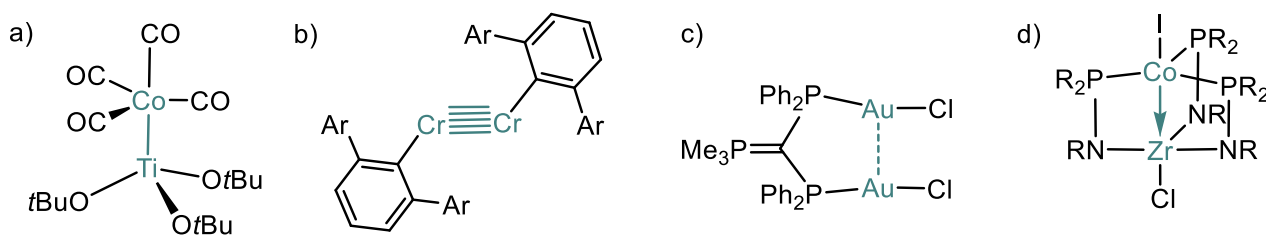
Scheme 1. Different bonding types in bimetallic complexes: a) polar, covalent single bond; b) non-polar, covalent quintuple bond (Ar = DIPP); c) non-covalent, metallophilic interaction (here: aurophilic); d) dative metal-metal bond.

The presence of two metal centers in organometallic catalysts can be of advantage since they can activate chemical bonds in substrates in multiple ways that would not be possible with monometallic counterparts. Several different modes of bond activation are shown in Scheme 2. Synergistic effects lead to several advantages such as metal-metal cooperativity and acting as an electron reservoir. As a result, they often outperform monometallic alternatives in terms of activity and selectivity, functional group tolerance and catalyst loading.[14–16] Selected catalytic applications include CO_2 activation,[17] hydrogenation[18] and C−C coupling reactions.[19] $Rh^{II}Rh^{II}$-carbenes were found powerful catalysts for selective C−H functionalization.[20] Heterobimetallic complexes with two late transition metals with a direct metal-metal bond are becoming a heavily investigated field with hundreds of compounds known already.[21,22] Especially relevant these days is the reduction of CO_2, and even more so its electrochemical reduction, which is being excessively studied with bimetallic complexes.[23]

a)
$$M_A — M_B$$
$$X — Y$$

b)
$$M_A — M_B$$
$\downarrow$ XY
$$M_A --- X — Y --- M_B$$

c)
$$X — Y ---- M_A — M_B$$
or
$$X$$
$$| ---- M_A — M_B$$
$$Y$$
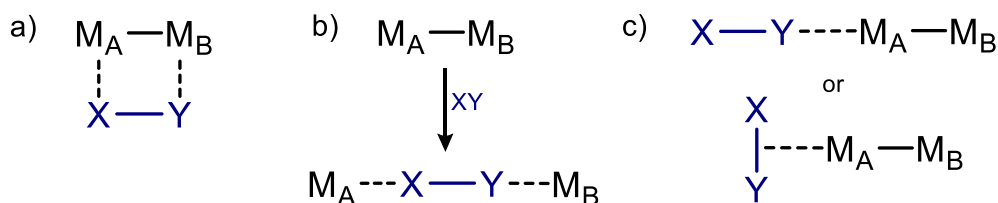
Scheme 2. Different modes of X-Y bond activation by a M_A-M_B bimetallic unit: a) multi-site; b) insertion; c) single-site.

Cooperative effects in bimetallic compounds are not only limited to transition metals, but they are also of great interest for main group elements (often Na, Mg, Zn or Al are used).[24] It was found that such heterobimetallic compounds are active in many types of catalytic transformations, which their mono-metallic counterparts were not able to perform.[25,26] Some reports show the cooperativity of transition metals with main group elements such as Rh-Al[27] or Co-Na[28] complexes.

Dirhodium(II,II) paddlewheel complexes have been known for a long time and are widely used in industrial applications and academic research.[29] Among those, dirhodium tetraacetate $[Rh_2(OAc)_4L_2]$ is the best-known compound. Ligand exchange reactions give rise to a large class of bimetallic $Rh^{II}Rh^{II}$ complexes with rich chemistry and wide application in catalysis.[8,29,30] Other prominent homobimetallic transition metal complexes are $Pd^{III}Pd^{III}$ [31] and $Ni^{I}Ni^{I}$[32,33] complexes, as depicted in Scheme 3.
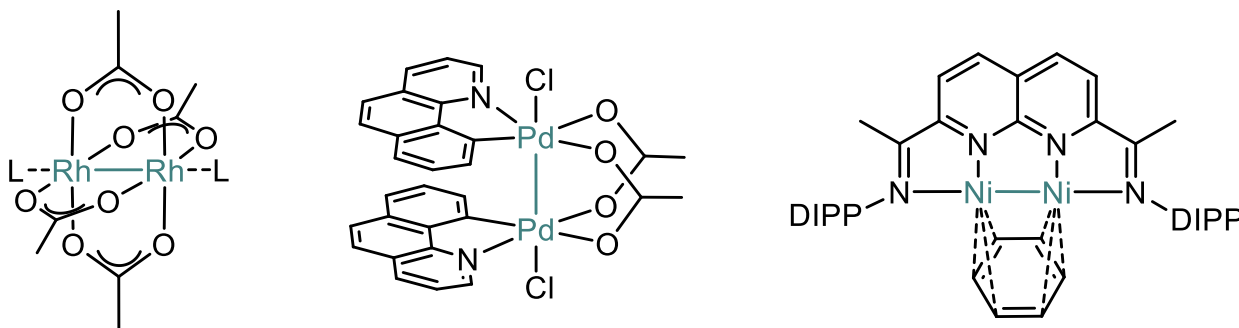
Scheme 3. Prominent examples of homobimetallic complexes with a metal-metal bond.

2. Metal-ligand cooperativity

2.1. Non-innocent and redox-active ligands

While second and third row transition metals are known to mostly undergo two consecutive single electron redox steps, first row transition metals often take one electron steps. Reaction intermediates can often be unstable radicals, which is often unfavourable in catalytic reactions. Therefore, redox-active ligands may help by providing an additional source or sink of electrons and thus allowing for multistep chemistry, even for the base metals. In general, stabilization of disfavoured oxidation states can be achieved by non-innocent ligands.[34,35]

Reactions within coordination compounds are not solely confined to the metal center, often the ligand will also participate. In some cases, the ligand undergoes reduction or oxidation reactions, while the metal retains its oxidation state. These ligands, named redox-active or non-innocent, are attracting increasing interest due to their multifunctional roles beyond metal binding.[36–38] Often, such ligands contain a conjugated diene fragment. The alterations in ligand properties bring about significant changes in the overall characteristics of the complex, which are relevant in catalytic applications.[39–41] Sometimes the distinct types of redox states in ligands can even be distinguished via X-ray structural analysis. A general reaction scheme of redox processes in non-innocent ligands is shown in Scheme 4. Specific examples of the redox behaviour of a catecholate ligand and a dithiolene complex are shown in Scheme 5 and Scheme 6, respectively.[42]

X, Y = O, S, NR
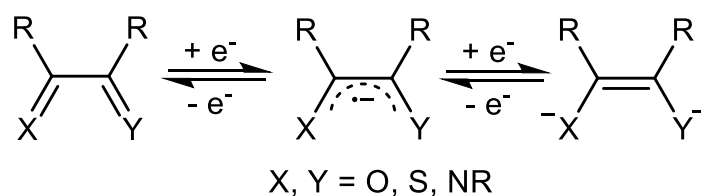
Scheme 4. General redox-active behaviour of non-innocent ligands.
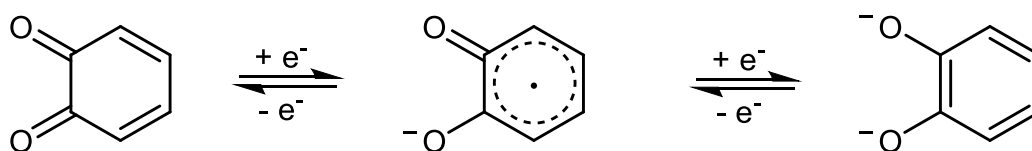
Scheme 5. Redox behaviour of redox-active catecholate ligands
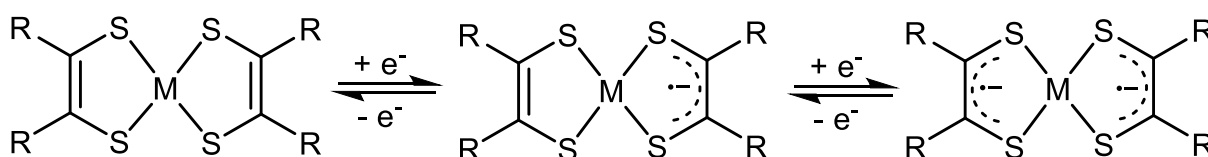
Scheme 6. Dithiolene complex and its redox-non innocent behaviour.

Redox non-innocent ligands can make the assignment of oxidation states of the metal ambiguous. One of the most prominent examples of redox non-innocent ligands are diazadienes (dad), which have found applications in many fields.[43] Electrons can be assigned to the metal center (diimine) or the nitrogen atoms (amido) or to a state in between. Resonance structures are shown in Scheme 7 and depend on the chemical environment (substituents on the dad ligand, the nature of the metal and ancillary ligands). Determination of redox states can be achieved experimentally with spectroscopic methods such as XRD, EPR and UV-Vis, and additionally be verified via theoretical DFT or CASSCF calculations.[34,35]
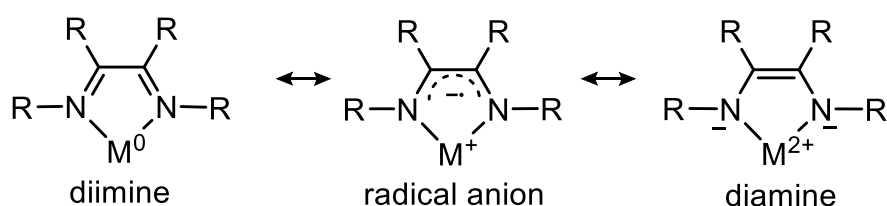
Scheme 7. Ambiguity of oxidation states in complexes with redox active diazadiene (dad) ligands.

There is a wide range of organic molecules that can behave as non-innocent ligands, selected examples are shown in Scheme 8. They all share the ability to distribute part of the electron density. Typical non-innocent ligands show extended π-conjugation, which is brought fore by aromatic or heteroaromatic moieties, especially those having low-lying unoccupied π* orbitals as electron acceptors. Hybrid ligands such as iminosemiquinone exist, where N and O coordination sites are combined within one ligand. Furthermore, small molecules such as NO, CO and O_2 can act as non-innocent ligands. Even though some molecules are classified as non-innocent, they might as well behave innocently under certain circumstances, which also depend on the nature of the metal. Other compounds clearly lack the ability of non-innocence and are classified as spectator ligands.[34,35]
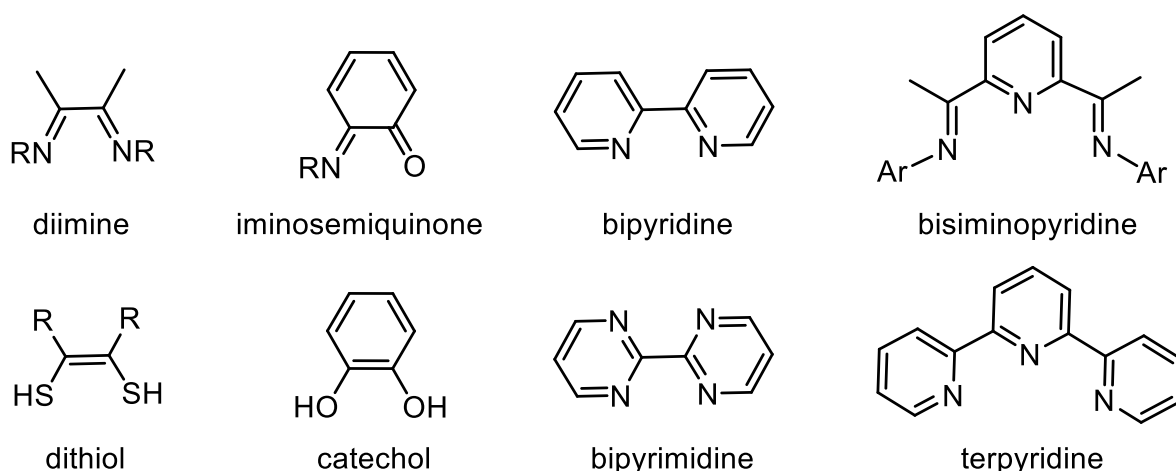
Scheme 8. Selected examples of redox non-innocent ligands containing N, O and S heteroatoms.

Besides electronic non-innocence, also chemically non-innocent ligands exist, where the ligand is involved in substrate bond breaking and making, rather than electron transfer.[35,39,41] If both, ligand and metal, are involved in a reaction, ligands are classified as being cooperative.[36] Cooperative effects have been observed with certain ligand types, where the organic framework effectively participates in catalysis by adding a part of the substrate onto the ligand. Within this category fall deprotonation or protonation reactions on the ligand scaffold. For instance, incorporation of NH groups can transform a neutral amine donor into a negatively charged amido species upon deprotonation. An example is a [(trop$_2$N)Rh(PPh$_3$)] complex, which is obtained upon deprotonation of the amine species and can undergo reversible addition of dihydrogen gas.[44,45] Thereby, H$_2$ is cleaved heterolytically on the Rh-N bond as depicted in Scheme 9. This reactivity finds wide application in different types of catalysis. [44,45]
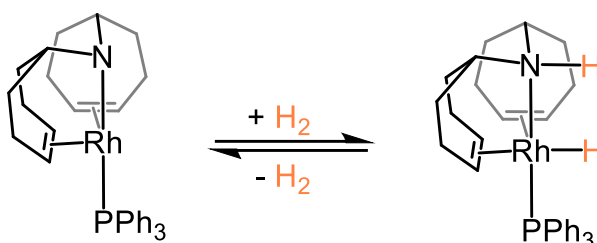
Scheme 9. Reversible heterolytic cleavage of H$_2$ on a rhodium amido complex.[44]

2.2. Alkenes, alkynes and allenes as ligands

A well-known class of organometallic compounds are π-complexes, where the metal interacts with the π-bonds of the ligand.[46] Thereby, donation of the carbon-carbon multiple bond π-electrons to an empty metal d-orbital occurs together with backbonding from the metal to the ligand. This involves donation from a metal d-orbital into the anti-bonding C=C π*-orbital. Only d^2–d^{10} metals are capable of back donation, which is required to bind alkenes. There are two extreme descriptions of such complexes: the Dewar-Chatt-Duncanson model or a metalacyclopropane structure (most experimental structures fall somewhere in between).[46] The C=C bond length increases upon coordination because of donation of electron density from C=C π-bond into a metal centered orbital and filling of π* orbital through back-donation. Therefore, elongation of the C=C bond is a measure of the M−(C=C) bond strength and helps to find out which model applies. The elongation can even approach single bond length for the coordinating alkene.

The coordination chemistry of π-bound alkynes can be described in the same way, although binding to metals may sometimes be stronger due to increased back donation to the more electronegative sp-hybridized carbons.[46] Upon coordination, the C≡C bond is elongated and the R-C≡C-R angle bends away from 180°. The complexation can also be followed via IR spectroscopy, as the characteristic C≡C vibration of alkynes shifts to lower wavenumbers, indicating weakening of the C≡C bond.[46] In alkynes, the same bonding concepts apply as for alkenes. In extreme cases, alkynes

can be considered 4e donors by involving their second π-bonding electron pair (dicarbene in Scheme 10a).[47] σ-Alkynyl complexes are able to undergo isomerization to vinylidene complexes under certain conditions (Scheme 10b).[48] If available, a terminal σ-alkynyl can coordinate a second metal center in a η^2 fashion, as depicted in Scheme 10c. Furthermore, alkynes readily bridge metal-metal bonds, where they serve as 2e donor to each metal center (Scheme 10d).
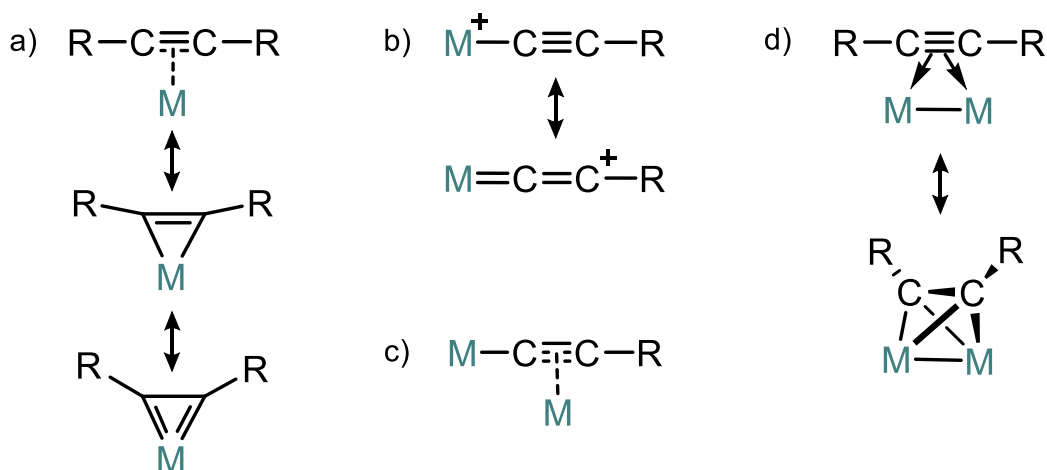
Scheme 10. Bonding modes of alkynes with different resonance forms: a) η^2 / π-alkynyl, b) η^1 / σ-alkynyl, c) bridging η^1-η^2-alkynyl, d) metal-metal bridging η^2-η^2-alkynyl.

If 1-alkynes are coordinated side-on to a metal center, structural rearrangement to a vinylidene motif often occurs via an intramolecular proton transfer process, as depicted in Scheme 11. This vinylidene (also depicted in Scheme 12) is structurally related to coordinating allenes – which, again can have different modes of coordination. Allenes can either form a terminal σ-bond to a metal center or a side-on π-bond (Scheme 12). All structures in Scheme 12 can also be bridging multiple metal atoms, forming a mixture between σ and π M−C bonds, which can lead to large multi-metallic cluster compounds (see also Scheme 10c and d). Carbenes, carbynes and σ-alkynes can additionally be bridging several metal atoms via the terminal carbon atom (Scheme 12).
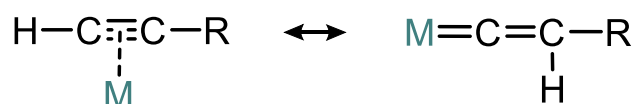
Scheme 11. Rearrangement of 1-alkynes to vinylidenes in an intramolecular proton transfer process.
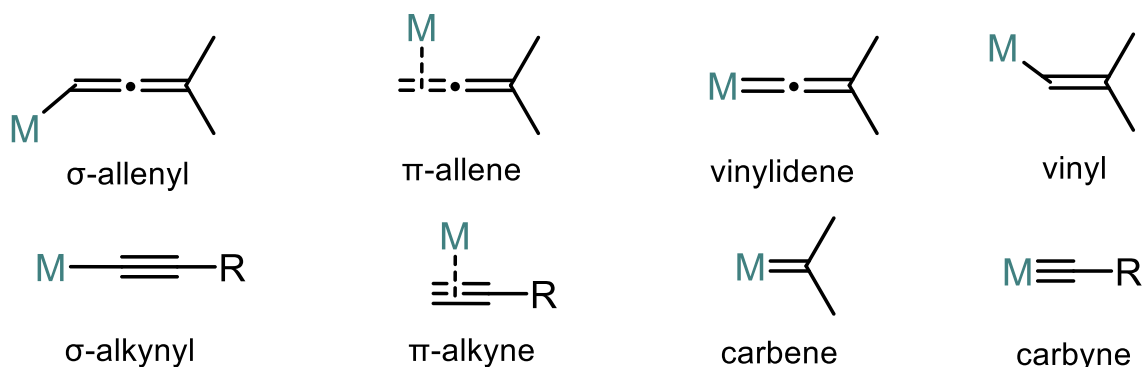
Scheme 12. Overview of several M−C bond types where C−C multiple bonds are involved.

Alkynyl complexes have many applications, examples range from liquid crystals to nonlinear optics as well as luminescence.[49] The related vinylidene complexes are an important class of compounds for catalysis, most notably the well-known olefin metathesis with ruthenium.[50] Allenyl complexes of rhodium were, for example, found to be active in C−C coupling reactions.[51]

Open shell organometallics can show reactivity on the carbon atoms within the ligand, such as alkene, alkyne, vinyl, allyl and propargyl groups.[52] Part of the unpaired electron density can be shifted to the organic ligand framework, as depicted in Scheme 13. Thereby, the formal oxidation state of the metal can be increased by +1. These carbon-centered radicals often undergo C−C coupling or H-atom abstraction as follow-up reactions, depending on the reaction conditions.
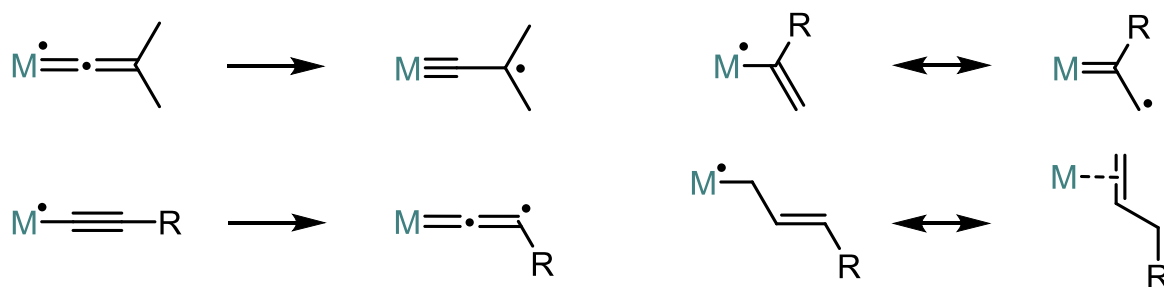
Scheme 13. Examples of ligand centred radicals in vinyl, alkynyl, vinyl and allyl complexes.

3. Electrochemical investigations of organometallic compounds

3.1. Cyclic voltammetry (CV)

Cyclic voltammetry is often used for the determination of redox properties of organometallic analytes, which can be helpful to find appropriate chemical redox agents.[53,54] In this technique, the current response is measured while applying a potential. This potential is scanned in both directions ("cyclic"). For comparative reasons, it is especially important to always reference redox potentials versus the ferrocene / ferrocenium (Fc / Fc$^+$) redox couple in organic solvents.

A chemical redox reaction and an electrochemical reaction have in common that the driving force is the energy difference of electrons: in a chemical redox reaction the driving force is the energy difference of molecular orbitals (which are at a fixed potential), while in electrochemical reactions it is between the orbitals and the potential at the electrode (which is tunable by a potentiostat).[53,54] Usually, a three-electrode setup is used for CV experiments (Figure 1a) consisting of working electrode (WE), reference electrode (RE) and counter electrode (CE).

During the course of a CV experiment, a diffusion layer builds up at the electrode surface, leading to characteristic "duck-shaped" curves, as depicted in Figure 1b. From the shape and the position of the peaks (forward and backward scan), the redox potential of the species, $E^{1/2}$, and the reversibility of the redox process can be determined. If the electron transfer step is followed by a relatively fast chemical reaction, irreversibility is observed in CV. In organometallic compounds, this could be for example ligand dissociation or exchange, solvent coordination, ligand rearrangement, dimerization, fragmentation or decomposition. Irreversibility manifests in a disappearance of the peak in the reverse scan or decrease in current and shift to more extreme potentials. A measure for the reversibility is the peak-to-peak separation, ΔE_p, which is 57 mV for perfectly reversible processes.[55]
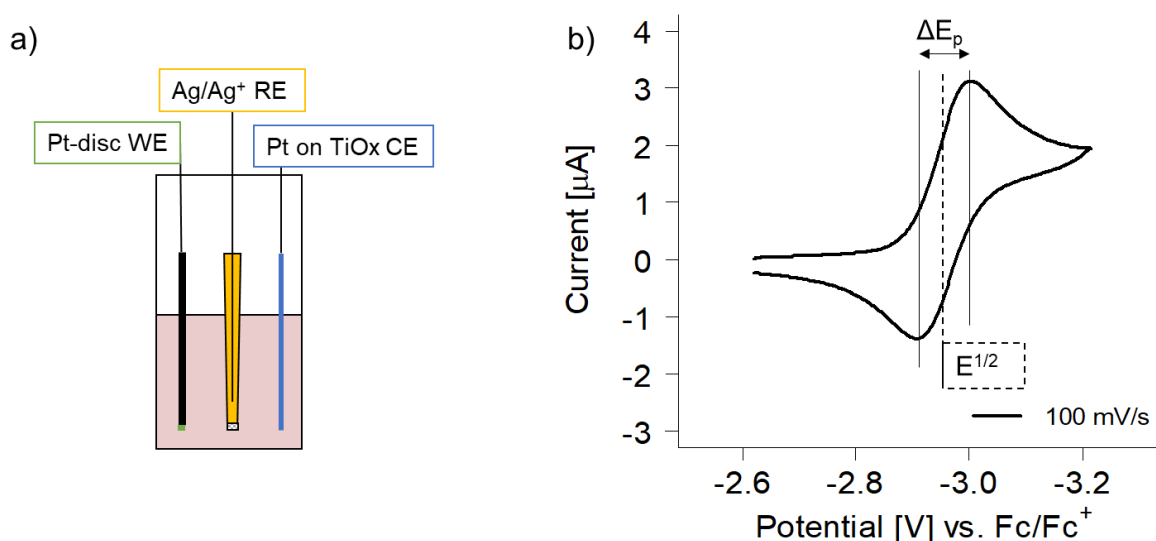
Figure 1. a) Schematic representation of a CV setup with 3-electrode setup: working electrode (WE), reference electrode (RE) and counter electrode (CE); b) cyclic voltammogram of a reversible redox event.

3.2. Electrocatalysis

An advantage of electrochemistry is that catalytic experiments can be performed with formally naked electrons as reactants. If catalysis takes place, a significant current increase is observed in a CV of the solution containing substrate and catalyst. Usually, this takes place at the redox potential of the active catalyst, where it is continuously regenerated due to the high concentration of substrate. Ideally, the working potential is also shifted to less extreme potentials, leading to a lower overpotential.[56,57] This is favourable because less side reactions occur at milder potentials. An example of the increase of peak current and shift in onset potential are shown in Figure 2.
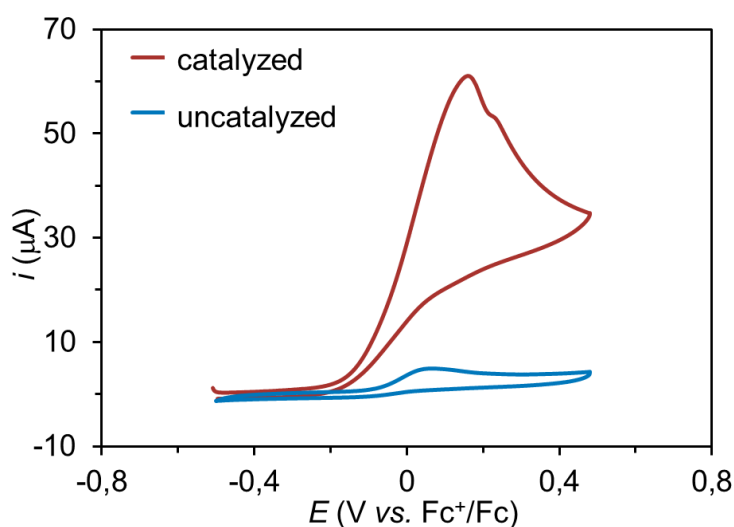
Figure 2. CV of an uncatalyzed peak (blue) and peak where catalysis is taking place (red).

3.3. Electrosynthesis (preparative, lab-scale, bulk electrolysis)

The voltametric experiments discussed so far are of pure analytical nature, only taking place in very small amounts at the electrode surface. If preparative electrochemistry is performed, electrodes with very large surface area are needed, for example platinum mesh or grid, RVC (reticulated vitreous carbon), graphite foam or nickel foam. Note that the counter electrode should be of similar surface area to not be limiting the reaction of interest at the working electrode. In reduction reactions, a sacrificial anode such as zinc wire can be used as CE. For oxidations, the formation of hydrogen gas as side-product at the CE is desirable. Furthermore, the electrochemical cell can either be an undivided or divided cell, the latter containing a porous frit to separate anodic and cathodic side to avoid cross-contamination.

In electrosynthesis, a constant potential or current is applied for an extended period of time (usually several hours), rather than relatively fast scanning as in CV. The standard methods are called chronoamperometry (CA) or chronopotentiometry (CP), where the fixed potential or current are determined by a previously run CV.[58]

This seemingly simple method has the drawbacks of a relatively complicated setup (shown in Figure 3) and the isolation of products can be tedious as still a large excess of electrolyte needs to be used. Still, it is often preferred over chemical reactions, as the applied potential can be very precise and the amount of hazardous waste products is strongly reduced.

Figure 3. Pictures of preparative electrolysis setups in a divided (left) and undivided (right) cell with RVC electrodes.

3.4. (Electro)catalytic alcohol oxidation

The oxidation of primary alcohols to aldehydes is an essential functional group transformation in organic synthesis[59] and finds application in energy storage and direct alcohol fuel cells.[60,61] Traditional oxidants, such as chromium compounds, are often toxic and produce large amounts of side products. In contrast, countless catalytic systems have been developed to proceed under mild conditions and reduce the amount of toxic waste produced. Further advantages are the use of mild oxidants, selectivity towards primary or secondary alcohols, selectivity of aldehyde over carboxylic acid formation and functional group tolerance.

An attractive oxidant is molecular oxygen because of its availability and benign stoichiometric by-products (water and / or hydrogen peroxide).[62] Such aerobic alcohol oxidation is currently heavily investigated, but often, the used catalysts do not tolerate such conditions, or the oxygen uptake of the reaction mixture is too slow. Quinones are a well studied class of oxidants among which *para*-benzoquinone (BQ) is the most established.[63] This approach has been applied by our group before, where an iridium complex [Ir(trop$_2$DACH)]OTf was successfully employed as an alcohol oxidation catalyst with only 0.01 mol% catalyst loading.[64,65] The very low catalyst loading contrasts with many other iridium[59] or palladium-based catalysts, where up to 10 mol% of catalyst are used. This amount of precious metal waste is not to be neglected. With the iridium complex [Ir(trop$_2$DACH)]OTf, high turnover numbers (TON) and exclusive oxidation of primary alcohols was observed. The catalytic

system is shown in Figure 4 (top pathway). The described system still has the drawback of forming hydroquinone (HQ) as stoichiometric side product. It was shown that HQ can later be reoxidized to BQ with a second catalytic cycle, which often contains a cobalt salophene catalyst and uses molecular oxygen as oxidant.[66]

Another approach to avoiding side-products is the use of electric potential instead of molecular oxidants. Therefore, many molecular electro-oxidation catalysts have been investigated.[57,67] What must be taken into account for finding a suitable electrocatalyst is that keeping the applied overpotential low is favourable.[67] Often, platinum counter electrodes are employed to facilitate and enhance hydrogen evolution reaction, which would ideally be the only side-product of this electrochemical reaction. The previously described iridium catalyst was shown to be also active in electrochemical oxidation of alcohols at low potentials (see Figure 4).[68]
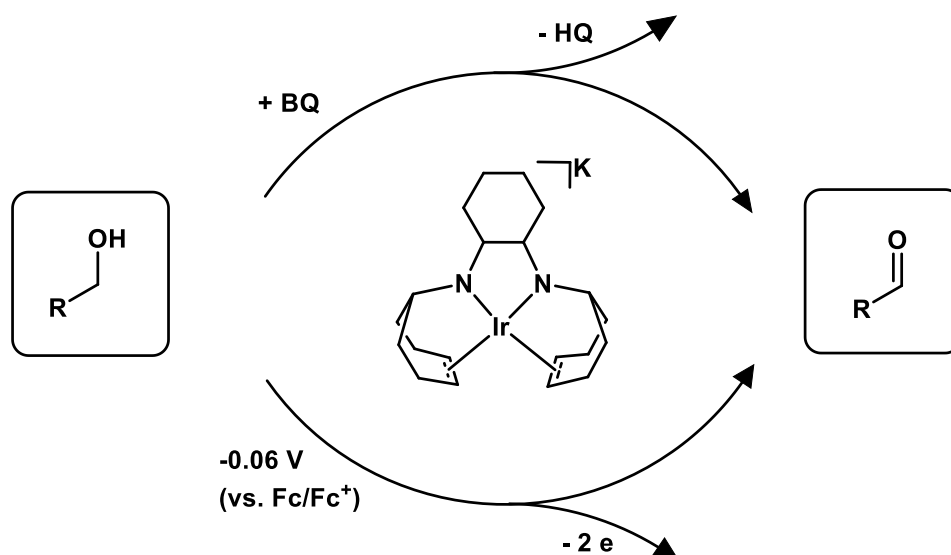
Figure 4. Oxidative alcohol dehydrogenation with an iridium complex via a chemical oxidation pathway with *p*-benzoquinone (BQ) (top) or electrochemical oxidation at -0.06 V (bottom).

4. Thesis objective and outline

For the past 20 years the Grützmacher group has been designing chelating ligands featuring a "trop" (trop = 5-dibenzosuberene) unit, i.e. a seven-membered ring bearing a double bond and an easily modifiable benzylic carbon atom (C_{benz}). This rigid and very stable unit allows for the design of chelating ligands, in which the double bond and a σ-donating anchoring group (e.g. P, N) attached to C_{benz} can chelate low-valent late transition metals.

For the synthesis of a new kind of bimetallic complexes, the well-established trop ligand was modified by attaching alkyne substituents.[69,70] This carbon rich ligand, (RC≡C)$_2$tropPPh$_2$ (R = TMS, Ph) can coordinate to two electron rich group 9 and 10 d^8-metals in close proximity, while leaving coordination

sites trans to the trop-ligand open. One metal can be bound to the trop moiety via interaction with the phosphine and alkene as in earlier examples of tropPPh$_2$ complexes,[71,72] while a second metal atom can coordinate via the two alkyne groups. While the TMS substituents render the alkynes rather electron rich, the phenyl groups lead to rather electron poor alkynes. Due to the previously described bonding model, the electron richness of the C=C and C≡C bonds is relevant for metal coordination properties. Furthermore, the electron configuration of the metal center is important and it is evident that the trop ligand - and especially the alkyne substituted ligands - can stabilize low-valent metal centers.
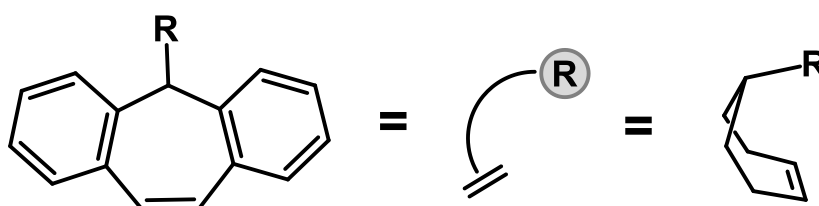
Scheme 14. Trop fragment and its schematic representations used in this thesis.

The first part of this thesis focuses on the synthesis and characterization of bimetallic dirhodium complexes with a cyclohexyl-alkyne substituted trop ligand. Their reactivity towards reductants and bases was investigated. Due to the ligands non-innocent properties, it was found that the reaction takes place within the ligand framework in different ways. Remarkable rearrangements and ligand effects were found. Parts of this Chapter were published as a research paper.[73]

After the discovery that similar but hetero-bimetallic complexes were active in N$_2$O reduction, the previously investigated Rh−Pt catalyst was modified in several ways to improve catalytic activity. Thereby, not only the substituents at the alkynes were exchanged, but also the type of second metal added to mono-rhodium complexes. In addition to that, the presence of the easy to oxidize phosphorus atom within the ligand was avoided by synthesising a new amine-based ligand, which was assumed to be more resistant to oxidative conditions.

Since the supply of expensive precious metals is limited and will likely decrease, the next Chapter deals with the synthesis of first row bimetallic complexes. Cobalt and copper have shown interesting coordination modes, where again the nature of the ligand plays a key role.

In the last Chapter, some well-known iridium complexes with redox non-innocent ligands were further investigated, which have previously been found to be highly active in alcohol oxidation reactions. Detailed mechanistic studies were performed with redox agents and / or under basic conditions and the resulting compounds isolated and structurally characterized. Additional electrochemical investigations helped in further understanding the catalytic reactions.

"Creativity comes from an empty mind."
HANSJÖRG GRÜTZMACHER

CHAPTER II – Synthesis and Reactivity of Dirhodium Complexes

1. Introduction

Carbon allotropes vary significantly in their chemical and physical properties and have a wide range of applications, not only the commonly known diamond and graphene, but also non-graphitizing carbons such as carbon black, activated carbon and glassy carbon. While for the first two types, the structures are well understood and show only sp^3 or sp^2 hybridization of the carbon atoms, the nature of the carbon bonds in the latter examples is more complex. A mixture of different bond types occurs including different ring sizes, not only hexagonal but also five-membered and seven-membered rings were found to be stable.[74–79] For models of various carbon allotropes see Figure 5.[80] Besides carbon atoms, these materials also have active functional groups on the surface (e.g. CO, COOH, CN) and can be doped with heteroatoms (e.g. nitrogen, sulfur, boron),[74,75,81] a schematic illustration is shown in Figure 6a. In fact, these defects in carbon support materials are often crucial for catalysis as they enhance electron transfer and (electro)catalytic activity.[82,83]
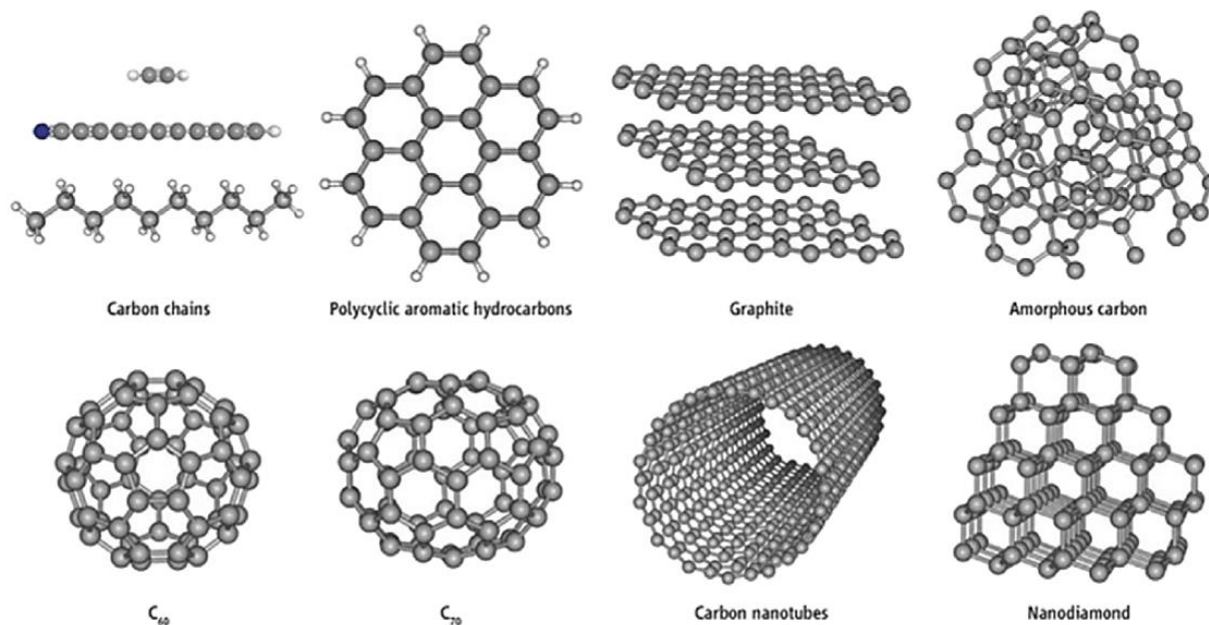
Figure 5. Various carbon allotropes reproduced from reference [80].

The investigation of redox induced changes of the properties and reactivity of transition metal complexes belongs to one of the core disciplines of organometallic chemistry.[84–89] Redox reactions find applications ranging from synthetic chemistry to the development of molecular machines.[90] "Ring-slippage" rearrangements can occur when arene complexes are subjected to redox reactions which often leads to a change from η^6 to η^4 or η^2 bonding mode.[86,91–94] Mainly mononuclear complexes were investigated in that regard but these ligand rearrangements were also observed with polynuclear complexes.[95–97] Another type of such phenomena are redox promoted C−C coupling reactions of metal vinylidene or alkynyl complexes.[88,89,98] The fundamental organometallic reaction steps may also be of relevance for the chemistry of metal atoms or small particles deposited

22

onto carbon support materials such as carbon black, activated carbon, and glassy carbon.[76,79,99] The exact structure in these materials is not well defined and a mixture of C−C bond types and C_n rings can consist of different sizes with n = 5, 6, and 7.[75,77,78] The deposition of metal atoms onto carbon support (shown in Figure 6b), often leads to dramatic changes in its physical and chemical properties, such as catalytic activity, selectivity and stability.[75,100–102] Platinum on carbon is a well-established system for electrochemical applications such as fuel cells.[75,83,103,104] Thereby the question arises of how a metal affects the carbon support that it is grafted on. The importance of the structure of carbon support on catalytic activity was shown with Ru on different types of carbon.[100]
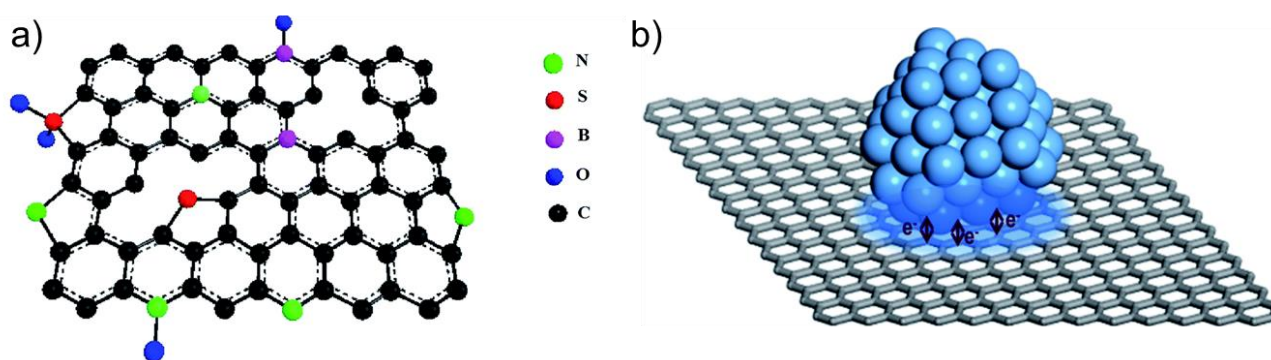
Figure 6. a) Illustration of heteroatom doped graphene, reproduced from [105]; b) metal particle on graphene from [106].

Because of the difficulty in structural analysis, this challenge has been addressed by DFT calculations of interactions between activated carbon and small rhodium clusters.[107] It was found that the presence of the metal particles modifies the carbon hybridization leading to an elongation of the C−C bonds. Furthermore, according to those calculations, the carbon ring size indeed plays a crucial role in H_2 activation. Although there have been some theoretical studies, experimental data is still underrepresented.

Previously, our group investigated the ligand transformations of a carbon-based ligand bound to two rhodium centers upon treatment with H_2.[69] When this complex was exposed to hydrogen gas, reversible addition of H_2 to the Rh_2 unit was observed and remarkably a compound could be identified, which closely resembles the ones proposed by DFT for small Rh clusters units deposited on carbon (Figure 7, bottom left). When the ligand sphere in the dinuclear, molecular Rh_2 complex was modified, hydrogen was cleaved and up to two equivalents of H_2 were transferred to carbon centers within the ligand skeleton (shown in Figure 7, bottom right). It was found that the alkyne of the carbon framework is hydrogenated to a carbene, which is bound to a rhodium atom.

Mondal 2018
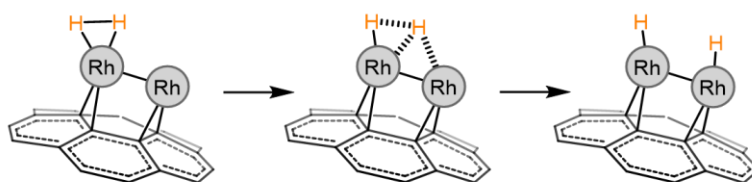
Grützmacher 2019
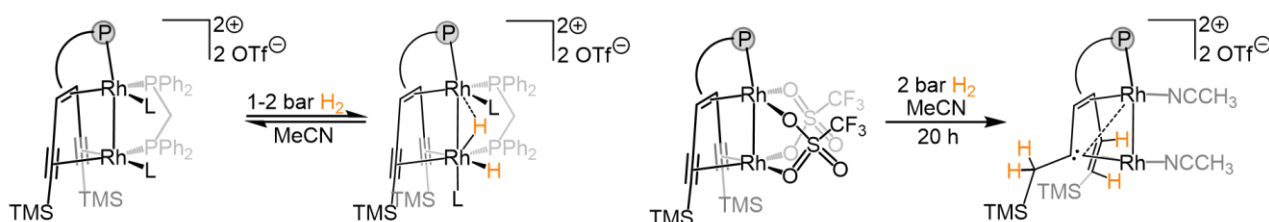
Figure 7. DFT calculated H_2 splitting on a heterogenous small rhodium cluster and carbon support (top), H_2 activation by a dirhodium complex as homogeneous model system with an additional phosphine ligand (bottom left) and a different activation mode in the presence of triflate ligands (bottom right). TMS = $SiMe_3$, L = MeCN.

We were therefore encouraged to investigate in more detail the structural modifications within the carbon sphere of a bis(alkynyl)-substituted trop ligand bound to a low-valent dinuclear Rh_2 unit when it is either involved in redox or acid-base reactions (Scheme 15). Both transformations reduce the charge of the complex from dicationic to neutral. The conjugated carbon framework undergoes C−C bond rearrangement under reduction or the deprotonation of a C-H bond. A diphenylphosphanyl group, PPh_2, is used as additional anchoring group in the ligand, which enhances the stability and serves as an NMR handle. The studies are further complimented by [103]Rh NMR spectroscopy and detailed electrochemical studies for further characterization.
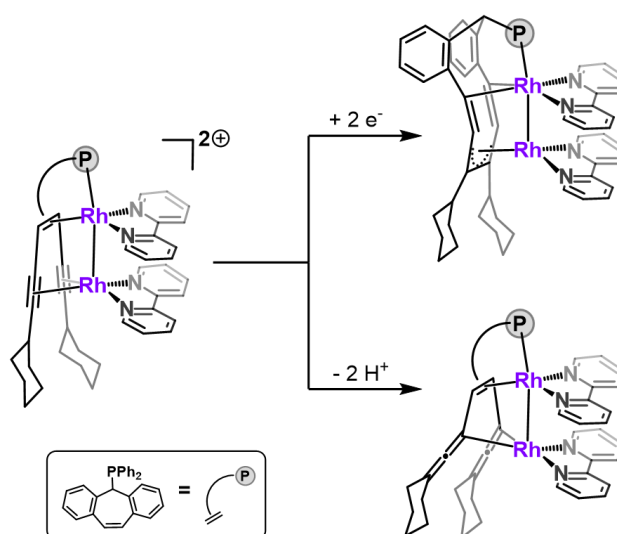
Scheme 15. Overview of the reactivity of dirhodium complexes described in this Chapter.

2. Reactivity of a dirhodium complex under reductive and basic conditions

2.1. Synthesis and characterization

2.1.1. *Synthesis of ligand 1 ((CyC≡C)₂tropPPh₂)*

A possible irregular carbon support material was modelled using a modification of the well-studied trop moiety (trop = 5H-dibenzo[a,d]cyclohepten-5-yl). The synthesis of ligand **1** is depicted in Scheme 16, which was adapted from previous reports from our group.[69,70] Here, we used a slightly modified procedure to synthesize the cyclohexyl (Cy) substituted ligand (CyC≡C)₂tropPPh₂) (**1**) with two electron-rich alkyne groups. The ligand is based on a trop unit to which on one side of the central seven-membered ring a diphenylphosphanyl group and to the other two alkynyl units are attached. Due to its overall concave shape and its electron accepting properties provided by the conjugated Cy−C≡C−C$_{trop}$=C$_{trop}$−C≡C−Cy unit, this molecule offers an ideal binding pocket for the coordination of two low-valent metal centers in close proximity.
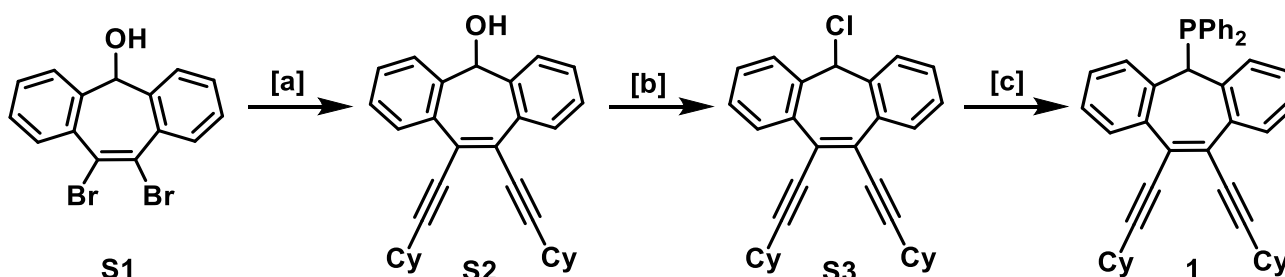
Scheme 16. Synthesis of ligand **1**. Conditions: [a] CyC≡CH, 5 mol% [Pd(PPH₃)₄], CuI, toluene, Et₃N, 60°C; [b] SOCl₂, DCM, 0°C; [c] 1. HPPh₂, toluene/hexane, 50°C 3 days, 2. Na₂CO₃, water.

2.1.2. *Synthesis and characterization of dirhodium complexes ([2], [3] and, [4](OTf)₂)*

The dinuclear Rh(I) bis(2,2'-bipyridine) (bipy) complex [((CyC≡C)₂tropPPh₂)Rh₂bipy₂](OTf)₂, [**4**](OTf)₂, is synthesized either by combining [Rh₂(μ₂-Cl)₂(COE)₄] (COE = cyclooctene) with **1** to form the chloride-bridged tetranuclear complex [**2**], which upon reaction with bipy and potassium triflate (KOTf) forms the desired dinuclear complex [**4**](OTf)₂. Alternatively, [Rh₂(COE)₄(μ₂-κO,κO'-OTf)₂] can be used to form complex [**3**], which reacts to complex [**4**](OTf)₂ by simply adding bipy. The synthetic routes are shown in Scheme 17. With these two methods, the use of a silver salt to convert [**2**] to [**3**], can be avoided. This reaction often leads to unwanted redox reactions or polymerization of THF if used as solvent. Furthermore, complex [**4**]²⁺ can be prepared with different counter anions, e.g. the BArF anion by replacing KOTf with NaBArF in the second step. Since the nature of the counter ion has not shown any significant influence on the reactivity, only the triflate anion is reported here. The molecular structures of all compounds were confirmed by X-ray diffraction (XRD) methods

using single crystals. The solid state structures of [**2**] and [**3**] are shown in Figure 8 and a plot of the structure of [**4**](OTf)$_2$ is depicted in Figure 9.
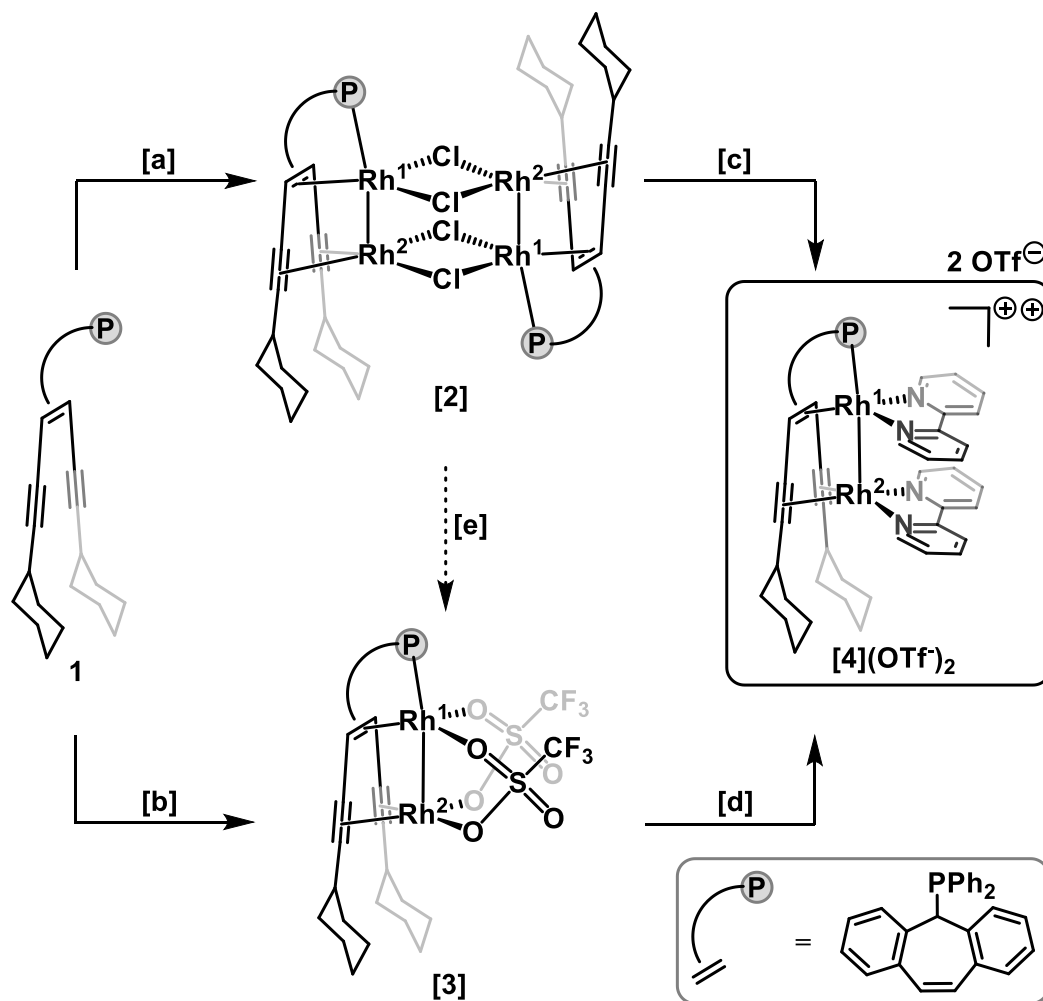
Scheme 17. Synthetic route for the synthesis of dicationic complex [**4**](OTf)$_2$ via chloride bridged [**2**] or monomeric [**3**]. Conditions: [a] [Rh$_2$(µ$_2$-Cl)$_2$(COE)$_4$], benzene, 18 h; [b] [Rh$_2$ (COE)$_4$(µ$_2$-OTf)$_2$], THF, 2 h; [c] KOTf, bipy, THF, 4 h; [d] bipy, THF, 1 h; [e] AgOTf, DCM, 4 h.

The molecular structures of all compounds were confirmed by X-ray diffraction (XRD) methods using single crystals. Plots of [**2**] and [**3**] are shown in Figure 8 and a plot of the structure of [**4**](OTf)$_2$ is depicted in Figure 9. Bimetallic complexes [**2**] - [**4**]$^{2+}$ show close Rh−Rh distances of 2.63 - 2.80 Å (see Table 1) that are in the same range of previously described metal-metal interactions attributed to Rh−Rh single bonds.[29,108–110] All complexes possess a distorted trigonal pyramidal structure around Rh^1 and a distorted square pyramidal structure around Rh^2. The Rh^1-Rh^2 unit in the dinuclear complexes [**2**], [**3**], and [**4**]$^{2+}$ is securely integrated into the ligand framework. Notably, Rh^1 exhibits a strong interaction with the olefinic C1=C2 unit of the ligand **1**, resulting in short distances between Rh^1 and the centroid ct1 of the C1=C2 bond (around 1.923 Å). Meanwhile, the C1=C2 bond undergoes elongation from 1.366 Å in **1** to approximately 1.503 Å (averaged) in the Rh$_2$ complexes.

The coordination of the alkynyl units C3≡C4 and C6≡C7 (average 1.203 Å) to Rh^2 similarly causes an elongation of the C≡C bond lengths (average 1.243 Å), although to a much lesser degree.
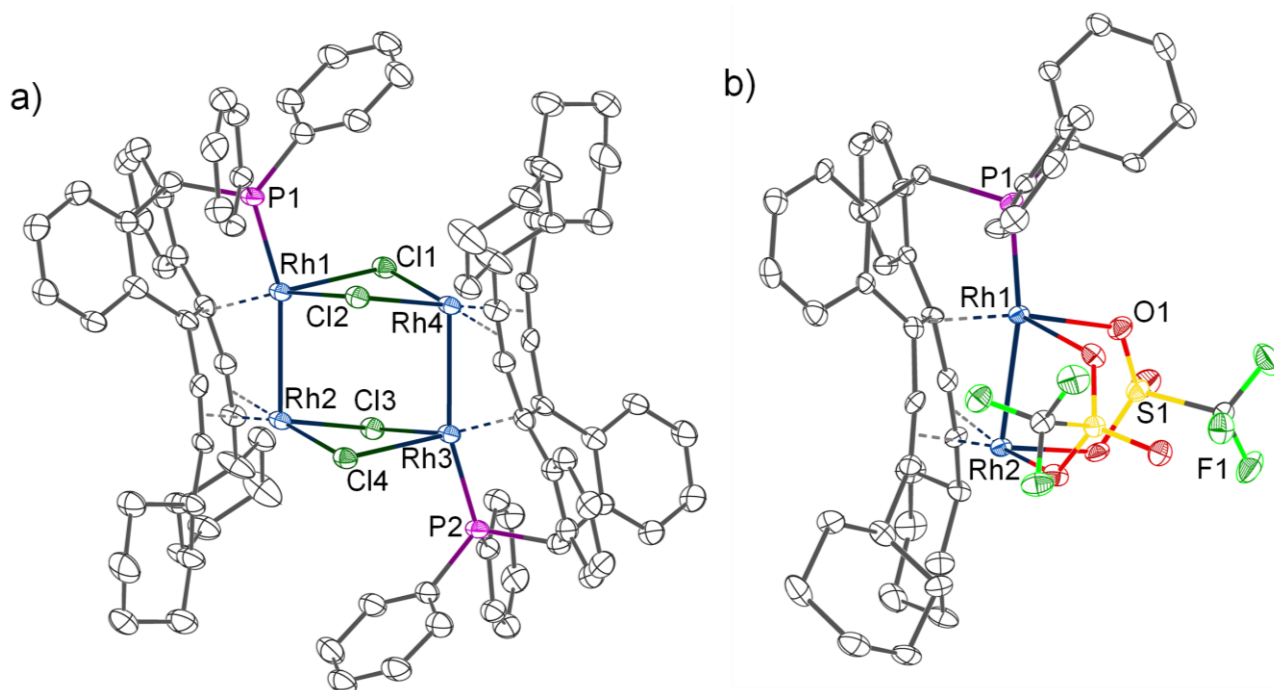
Figure 8. Solid state structures of a) [2] and b) [3]. Hydrogen atoms and solvent molecules omitted for clarity.
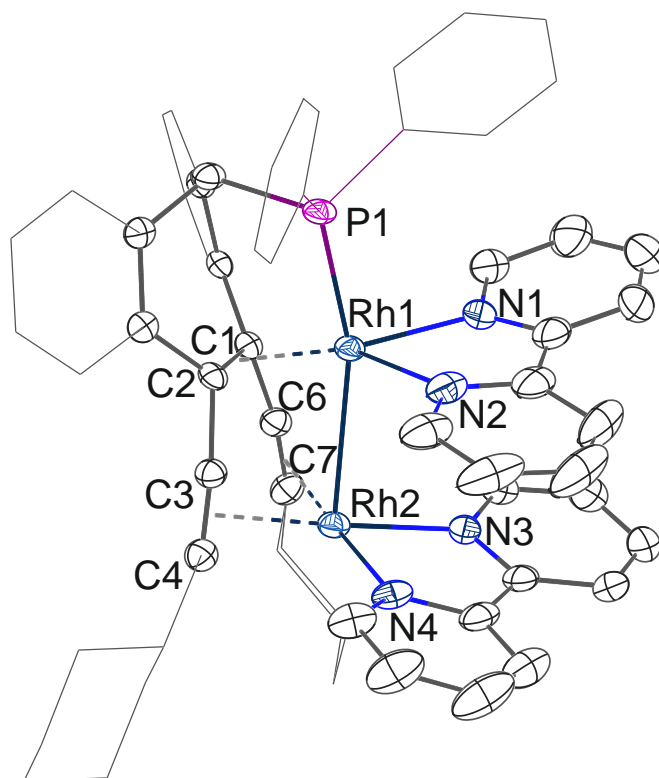
Figure 9. Solid state structure of [4]$^{2+}$. Hydrogen atoms, counter ions and solvent molecules omitted for clarity.

The nature of the metal-metal interaction can be explained in a simplified way as a trigonal pyramidal coordination sphere around Rh^1 (not taking the Rh−Rh interaction into account), which is an unusual and rare coordination sphere for a 16 valence electron metal complex, which makes the metal center Lewis-acidic.[111] On the other hand, Rh^2 is situated in a 16 valence electron square-planar coordination environment, which makes the metal center with its filled dz^2 orbital Lewis-basic. This holds true for all complexes [2] – [4]$^{2+}$ and as a result, the Rh−Rh bonds in all complexes can be interpreted as a dative Rh→Rh donor-acceptor interaction. This assumption is fully supported by DFT calculations, where a molecular orbital was found representing this donor-acceptor interaction (see Figure 10a). Quantum theory of atoms in molecules (QTAIM) was used to locate a bond critical point (BCP) between Rh^1 and Rh^2 (for a contour map of the Laplacian of the electron density of complex [4]$^{2+}$ see Figure 10b). The electron localization function shows a value of 0.208, which indicates a weak Rh−Rh bond. Overall, the Rh−Rh bond is best viewed as a very weak Rh^2-donor→Rh^1-acceptor bond, which is significantly longer than a typical Rh−Rh single bond as observed in rhodium(II) acetate, $[Rh_2(O_2CMe)_4]$: 2.29 Å.[52]
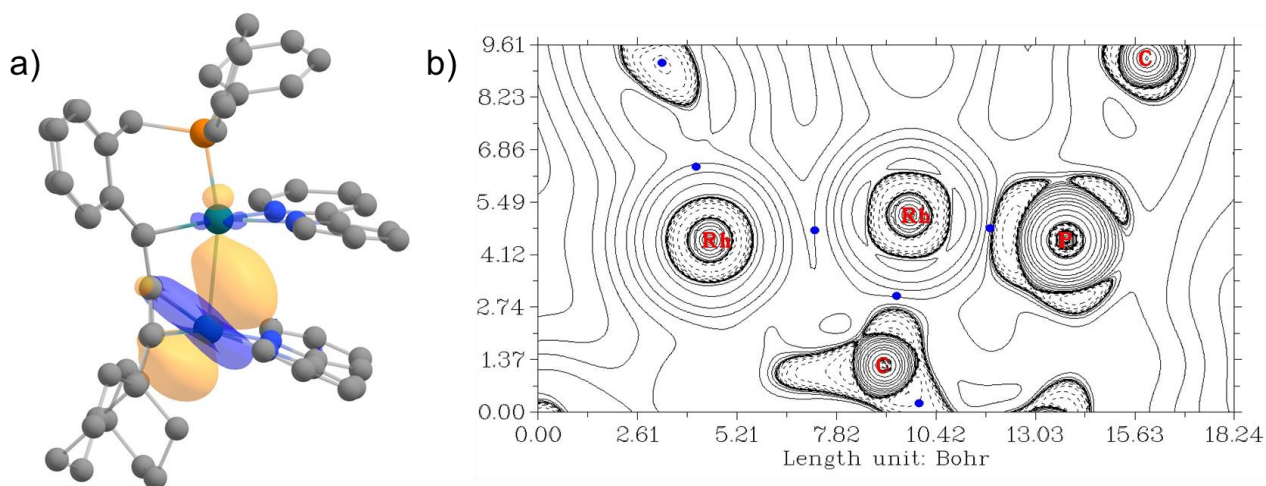
Figure 10. a) Relevant IBO (intrinsic bond orbital) of [4](OTf)$_2$ for the description of the Rh−Rh bond; b) contour map of the Laplacian of the electron density of dicationic complex [4](OTf)$_2$.

Table 1. Selected bond lengths [Å], NMR chemical shifts [ppm] and coupling constants [Hz] of **1** and complexes [**3**] - [**7**].

	1	**[6]**[+]	**[3]**	**[4]**[2+]	**[4]**[•+]	**[7]**
Rh[1]−Rh[2]	-	-	2.6310(4)	2.7923(4)	2.7096(6)	2.7109(6)
C1−C2	1.366(2)	1.502(3)	1.494(5)	1.512(6)	1.508(7)	-
Rh[1]−ct(C1-C2)	-	1.93624(14)	1.9044(3)	1.9292(3)	1.9398(4)	2.076(6) [b]
C3−C4	1.202(2)	1.213(4)	1.245(6)	1.232(6)	1.211(8)	1.450(9)
C6−C7	1.202(2)	1.210(4)	1.250(6)	1.239(6)	1.185(9)	1.418(8)
Rh[2]−ct(C3-C4)	-	-	2.0285(3)	2.0925(3)	2.1660(5)	1.9937(4)
Rh[2]−ct(C6-C7)	-	-	2.0285(3)	2.0835(3)	2.1505(4)	1.9990(4)
[31]P	-14.0	111.6	106.0	96.4	-[e]	17.8
[103]Rh[1]	-	-7086	-6973	-7043	-[e]	-7168
[103]Rh[2]	-	-	-688	-743	-[e]	-[f]
[1]J_{P-Rh1}	-	225.4	191.7	192.8	-[e]	180.7
[2]J_{P-Rh2}	-	-	5.7	9.3	-[e]	20.9
C1/C2	130.4	47.3	37.5	37.6	-[e]	143.0
C6/C3	102.0	107.9	83.5	87.2	-[e]	72.2
C7/C4	84.4	78.7	68.6	78.4	-[e]	118.1

[a] Calculated bond lengths. [b] Rh[2]−C1 bond length. [c] Rh[2]−C3 bond length. [d] Rh[2]−C6 bond length. [e] Paramagnetic radical. [f] Not detected.

2.1.3. *Synthesis and characterization of mono-rhodium complexes ([5] and [6](OTf))*

In order to further verify the nature of the Rh−Rh bond, the mononuclear rhodium complex [((CyC≡C)₂tropPPh₂)Rhbipy](OTf), [**6**](OTf), was synthesized through a sequential reaction starting with the labile precursor complex [Rh₂(µ₂-Cl)₂(H₂C=CH₂)₄] and ligand **1**. This synthetic route first yielded the dinuclear complex [**5**]. Subsequent addition of KOTf and bipy effectively cleaved [**5**], resulting in the formation of the desired mononuclear complex [**6**](OTf) (Scheme 18). Single crystals of [**6**][+] were grown and subjected to XRD analysis, revealing the structural characteristics depicted in Figure 11. Indeed, the coordination environment around the Rh center in [**6**][+] is most accurately described as a slightly distorted trigonal pyramid, evidenced by a deviation of 0.252(2) Å from the Rh center to the best plane through C1, C2, N1, N2. In comparison to the dinuclear dication [**4**][2+], the Rh[1]−C distances in [**6**][+] exhibit notable similarity (Rh−ct(C1−C2) 1.936 Å, C1=C2 1.504 Å). A noteworthy observation is the interaction (2.435(3) Å) between Rh[1] and one of the carbon centers, C3, within one of the alkynyl units, highlighting the Lewis acidity of the 16 e⁻ Rh[I] center in a trigonal pyramidal environment, as previously discussed.
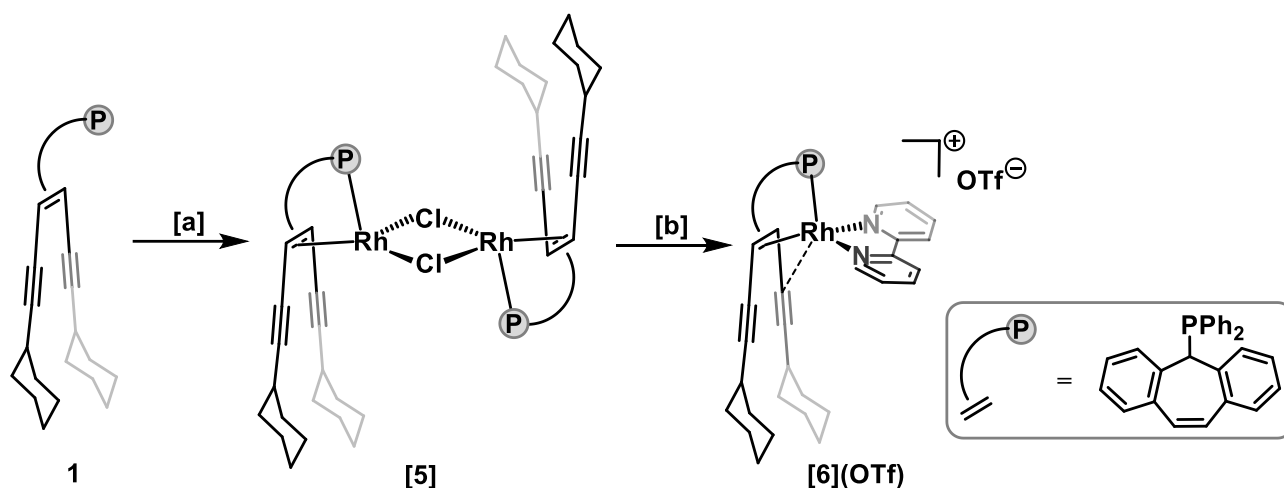
Scheme 18. Synthetic route for the synthesis of complex [6]+ via chloride bridged [5].
Conditions: [a] [Rh2(μ2-Cl)2(H2C=CH2)4], benzene, 18 h; [b] KOTf, bipy, THF, 4 h.
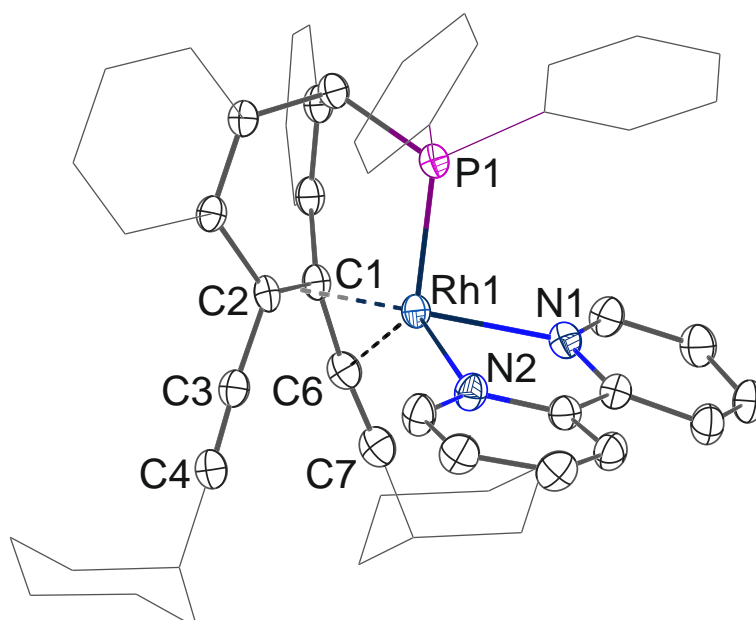
Figure 11. Solid state structure of [6]+, hydrogen atoms, counter ions and solvent molecules omitted for clarity.

2.1.4. NMR spectroscopic characterization of complexes [2] – [6](OTf)

All compounds [2] – [6]+ were fully characterized by NMR spectroscopy in solution and selected data are listed in Table 1. The attached phosphorus atom serves as an NMR probe, since the ^{31}P chemical shifts change significantly from the uncoordinated molecule 1 (δ^{31}P = -14.0 ppm) to complexes [2] – [4]$^{2+}$ (101.2, 106.0, 96.4 ppm, respectively). Monometallic complexes [5] and [6]+ show an even larger shift to δ^{31}P = 113.5 and 111.6 ppm. Since ^{103}Rh, just like ^{31}P, is a spin ½ nucleus with 100% natural abundance, the rhodium atoms couple with the phosphorus atom. Coupling of the ^{31}P nucleus with both ^{103}Rh nuclei in the dinuclear complexes leads to doublets of doublets with $^1J_{RhP}$ = 180 – 195 Hz and $^2J_{RhP}$ = 9 – 52 Hz, as depicted in Figure 12a. This presence of a $^2J_{PRh2}$ coupling supports the assumption of a direct metal-metal bond. ^{103}Rh NMR is usually measured indirectly as ^{1}H-^{103}Rh

HMBC, because of its low gyromagnetic value. Thereby the rhodium signal is detected via a proton in proximity to the metal nucleus. For these compounds, the correlation could be found via the benzylic proton of the trop-moiety (C9), which is three and four bonds away from Rh^1 and Rh^2 respectively, the spectra are depicted in Figure 12b and c. The chemical shifts for Rh^1 in complexes [**2**] – [**4**]$^{2+}$ range from $\delta^{103}Rh$ = -6724 to -7043 ppm (referenced to Rh(acac)$_3$) and correlate well with literature values.[69,112,113] The chemical shift for Rh^2 was found to be around $\delta^{103}Rh$ = -700 ppm for complexes [**3**] and [**4**]$^{2+}$, but significantly more low-frequency shifted for the dimeric compound [**2**] at $\delta^{103}Rh$ = -4736 ppm. This difference could arise from the dimeric nature of chloride bridged [**2**]. Even though ^{103}Rh NMR is widely employed, there have not been any chemical shifts reported for Rh^I alkyne complexes so far. To the best of our knowledge, this work represents the first such data.
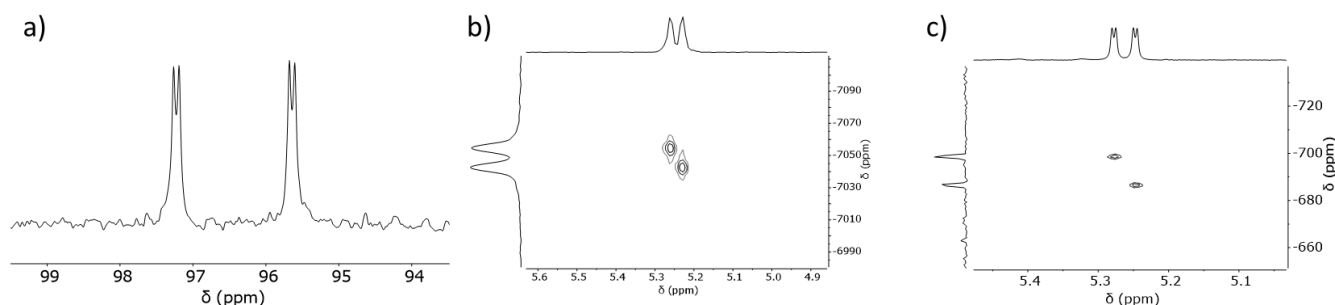
Figure 12. NMR spectra of complex [**4**](OTf)$_2$: a) ^{31}P, b) ^1H-^{103}Rh HMBC (Rh^1), c) ^1H-^{103}Rh HMBC (Rh^2).

The ^{13}C nuclei of the coordinated C=C$_{trop}$ and C≡C−Cy units of all dinuclear complexes [**2**], [**3**], and [**4**]$^{2+}$ show resonances within a narrow window of 37.5 – 38.9 ppm (C=C$_{trop}$), and 83.5 – 87.2 (_C_≡C−Cy) or 68.6 – 78.4 ppm (C≡_C_−Cy) indicating coordination shifts $\Delta\delta_{av}$ = $\delta_{(ligand)}$ − $\delta_{(complex)}$ to lower frequencies, which, with 92 ppm, is especially large for the C=C$_{trop}$ unit [ligand **1**: $\delta^{13}C$ = 130.4 ppm (C=C$_{trop}$), 102.0 ppm (_C_≡C−Cy), 84.4 ppm (C≡_C_−Cy)]. The $\Delta\delta_{av}$ is much smaller for the alkyne units [$\Delta\delta_{av}$(_C_≡C−Cy) = 17.3 ppm; $\Delta\delta_{av}$(C≡_C_−Cy) = 14.2 ppm]. These findings are fully in accordance with the structural parameters discussed above, which show a strong Rh^1 C=C$_{trop}$ interaction while the Rh^2 alkynyl interactions are weaker. For the complexes [**5**] and [**6**]$^+$ with only one Rh^I center coordinated to **1**, the $\Delta\delta_{av}$(C=C$_{trop}$) = 77.4 ppm is less pronounced, which underscores the assumption that in the dinuclear complexes Rh^2 donates electron density to Rh^1, which in turn donates more electron density back into the π^*-orbital of the C=C$_{trop}$ unit. In the mononuclear complex [**6**]$^+$, only one set of ^{13}C NMR resonances at $\delta^{13}C$(_C_≡C−Cy) = 118.8 ppm and $\delta^{13}C$(C≡_C_−Cy) = 78.7 ppm is observed indicating that coordination of the alkyne unit is fluxional on the NMR time scale in solution, or only appears in solid state.

2.2. Electron Transfer Processes – Redox chemistry of [6](OTf) and [4](OTf)$_2$

2.2.1. Redox chemistry of mono-rhodium complex [6](OTf)

The cyclic voltammograms of the mononuclear rhodium complex [((CyC≡C)$_2$tropPPh$_2$)Rhbipy](OTf), [6](OTf), reveal a reversible reduction at E$^{\frac{1}{2}}$ = -1.63 V (vs Fc$^+$/Fc) (ferrocene/ferrocenium) (Figure 13 and Figure 14), displaying a more negative potential than related trop phosphane rhodium(I) complexes (E$^{\frac{1}{2}}$ = -1.00 V and -1.19 V)[114] and trop amine complexes (E$^{\frac{1}{2}}$ = -1.27 V to -1.46 V).[115] An additional, irreversible reduction wave occurs at E^p = -2.06 V (shown in Figure 14) characterized by a triangular peak shape indicative of an adsorption phenomenon of the generated species.
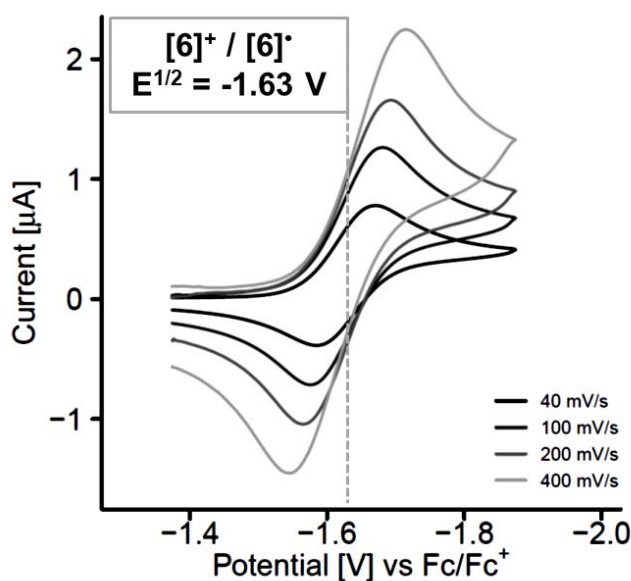
Figure 13. CV of complex [6]$^+$, isolated reversible reduction event at different scan rates. Conditions: 1 mM analyte, 100 mM [nBu$_4$N]PF$_6$ electrolyte, DME (1,2-Dimethoxyethane), Pt WE, Pt on TiO$_x$ CE, Ag/Ag$^+$ RE.
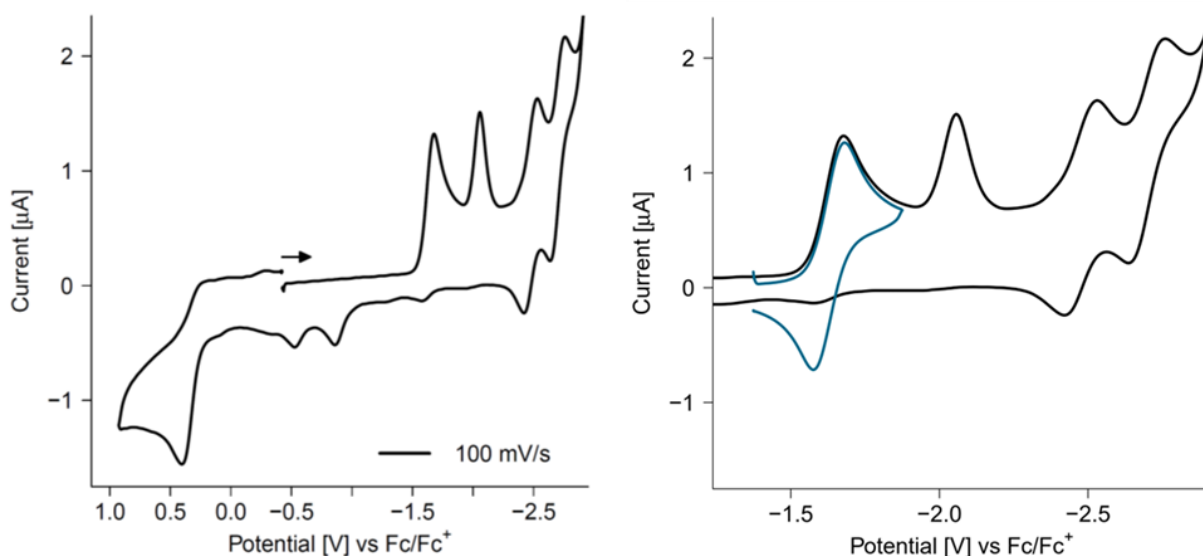
Figure 14. Cyclic voltammogram of complex [**6**]+ (left) and with overlay of isolated peak (right). Conditions: 1 mM analyte, 100 mM [nBu4N]PF6 electrolyte, DME solvent, Pt WE, Pt on TiOx CE, Ag/Ag+ RE, scan rate 100 mV/s.

Utilizing CoCp*2 as a chemical reductant, the mono reduced neutral radical [((CyC≡C)2tropPPh2)Rhbipy]•, [**6**]•, with a formally d^9-Rh^0 center was generated *in-situ* (Scheme 19) and detected via EPR spectroscopy (Figure 15a). DFT calculations indicate a slight structural change in [**6**]• in comparison to [**6**]+, which now adopts a nearly perfect trigonal pyramidal structure (deviation of Rh from the trigonal plane: 0.32 Å). The spin density is predominantly localized on the bipy ligand, with only 22% attributed to the rhodium center, a plot of the SOMO of the [**6**]•, radical is depicted in Figure 15b. This aligns with previous data on formally d^9-Rh^0 complexes featuring trop-type ligands and distorted tetrahedral structures, exhibiting relatively low spin densities in the range of 24% – 36% on the metal center, best described as delocalized organometallic radicals[116] (though it is noteworthy that slight structural changes may result in electromeric structures where >80% of the spin density resides on the metal center).[117,118]
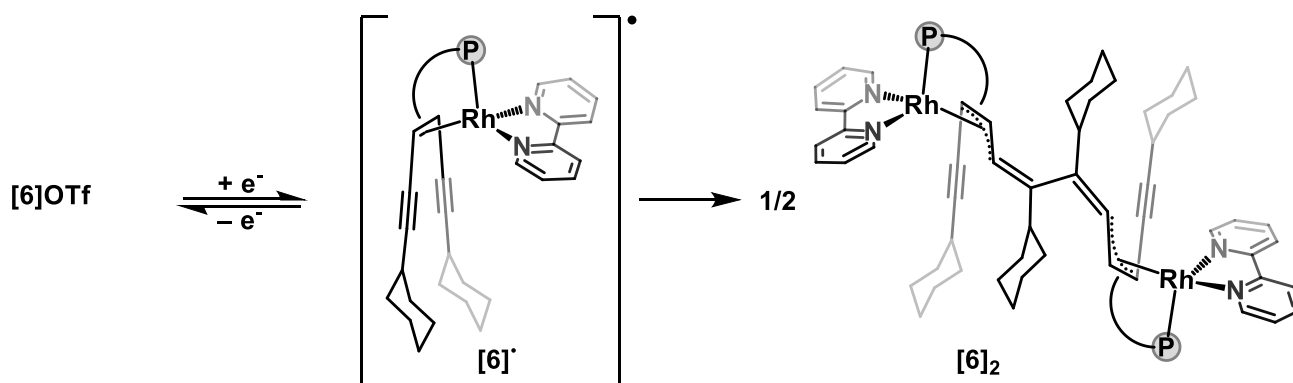
Scheme 19. Reduction reaction of [**6**]+ via intermediate monomer [**6**]• to dimerized [**6**]2.
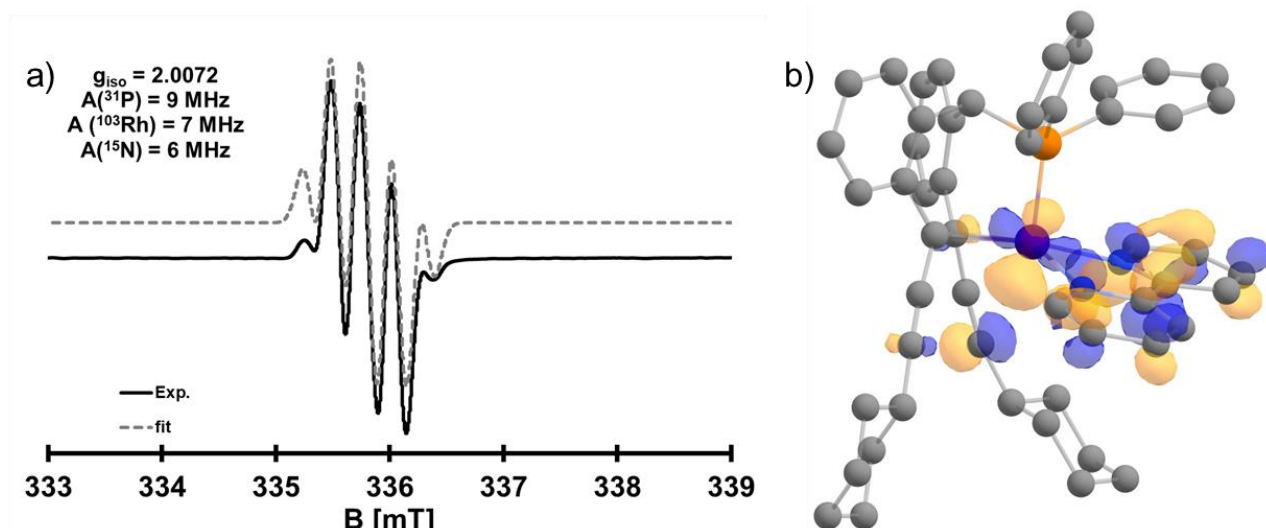
Figure 15. a) EPR spectrum of [**6**]˙ generated in situ with one equivalent of CoCp*$_2$ at room temperature in Toluene/MeCN, overlay of experimental and simulated spectra; b) calculated orbital plot of SOMO of [**6**]˙.

Interestingly, when the reduction is conducted on a larger scale with the intent to isolate [**6**]˙, a reaction between two such radicals is observed. This process involves C−C bond formation between two β-alkyne-C7 atoms, yielding the dimer [**6**]$_2$ from which single crystals could be obtained (see Scheme 19 and the solid state structure in Figure 16). ^{31}P NMR spectra indicate that this dimeric species [**6**]$_2$ is formed as the predominant species.
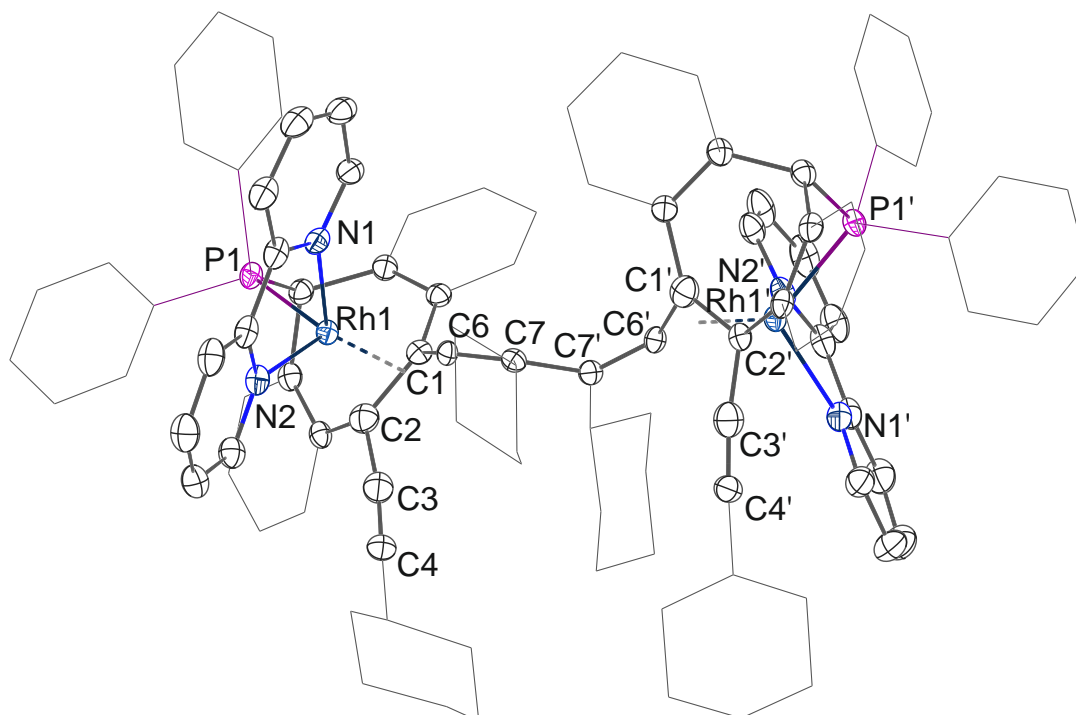
Figure 16. Solid state structure of [**6**]$_2$, hydrogen atoms and solvent molecules omitted for clarity.

2.2.2. Redox chemistry of dirhodium complex [4](OTf)$_2$

Cyclic voltammograms (CV) of dinuclear complex [4](OTf)$_2$ in THF show two reversible redox events at E$^{\frac{1}{2}}$ = -1.35 V and E$^{\frac{1}{2}}$ = -1.61 V vs. Fc/Fc$^+$ (Figure 17), which are attributed to the processes [4]$^{2+}$ + e$^-$ ⇆ [4]$^{•+}$ and [4]$^{•+}$ + e$^-$ ⇆ [4]. The equilibrium constant was calculated from the separation of the redox waves (ΔΔE = 0.26 V) to be K_{disp} = 4.0 × 10^{-5} at room temperature for the disproportionation 2 × [4]$^{•+}$ ⇆ [4]$^{2+}$ + [4], therefore the observation and eventually even isolation of the radical species [4]$^{•+}$ was expected to be possible.
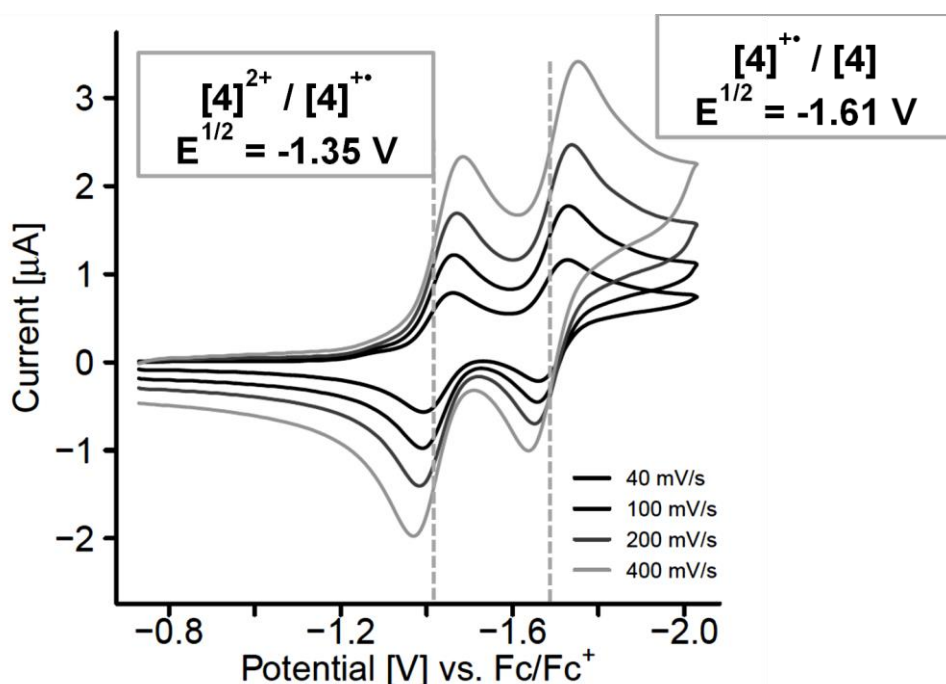
Figure 17. CV of isolated reduction waves of [4]$^{2+}$ at different scan rates. CV conditions: 1 mM analyte, 100 mM [nBu$_4$N]PF$_6$ electrolyte, THF, Pt WE, Pt on TiO$_x$ CE, Ag/Ag$^+$ RE.

Indeed, if complex [4]$^{2+}$ is treated with one equivalent of reductant (sodium naphthalenide in THF or CoCp$^*_2$ in DFB), the dark red paramagnetic complex [4](OTf) is obtained (see Scheme 20). Single crystals were subjected to an X-ray diffraction experiment, which allowed the determination the structure of [4]$^{•+}$. Little structural change is observed in comparison to [4]$^{2+}$ and only slight variations in bond lengths occurred. Compared to [4]$^{2+}$, the Rh−Rh bond is shortened (from 2.7923(4) to 2.7096(6) Å) while no significant differences in bond lengths were observed for the C=C$_{trop}$ and C≡C bonds within the accuracy of the measurement (see also Table 1).
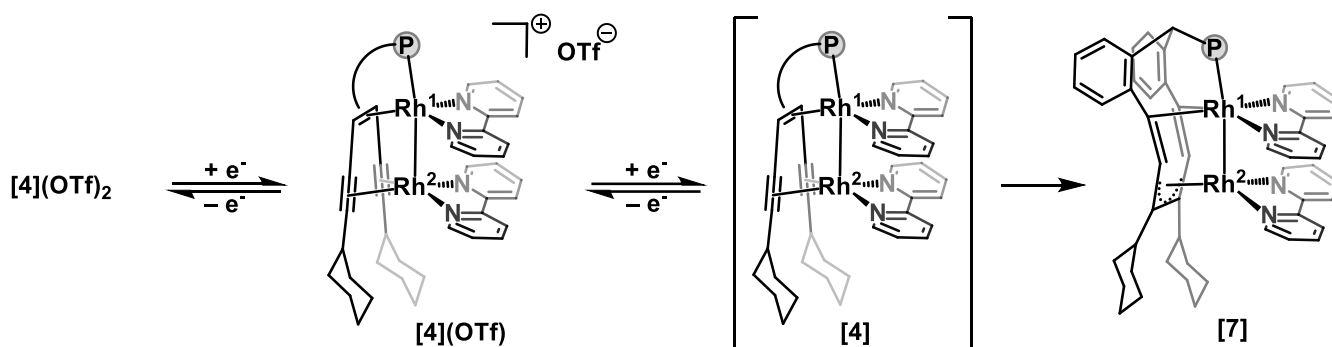
Scheme 20. Reduction reaction of [4]$^{2+}$ via [4]$^{•+}$ and unstable [4] to isolated [7].

The radical cation [4]$^{•+}$ was further characterized by electron paramagnetic resonance (EPR) spectroscopy. A rhombic g-tensor with a small anisotropy and an isotropic g-value (2.0170 vs. 2.0023 of the free electron) indicate that the unpaired electron is mainly localized on the ligand scaffold with little spin density on the dinuclear Rh−Rh unit (Figure 18a). Therefore, it can be assumed that the radical is mostly ligand centered and the Rh^I-Rh^I core remains. Supporting this assumption, DFT calculations show a strong delocalization of spin density that is mostly situated on the bipy ligand coordinated to Rh^2. See Figure 18b for an orbital plot of the SOMO in complex [4]$^{•+}$. We can therefore conclude that this one electron reduction occurs mainly on a non-innocent bipy ligand and no significant change in the carbon sphere is observed.
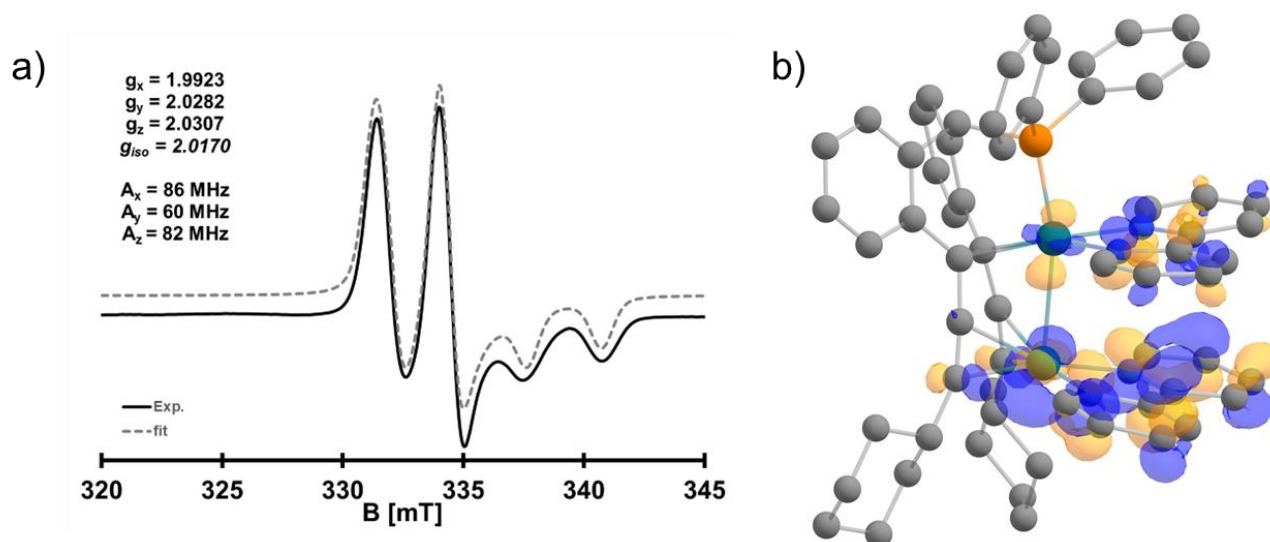
Figure 18. a) EPR spectrum of [4]$^{•+}$ in frozen solution in Toluene/MeCN, b) orbital plot of calculated SOMO of [4]$^{•+}$.

The use of two equivalents of strong reductant leads to the formation of poorly soluble green complex [7] (λ_{max} = 696 nm). Single crystals were grown and XRD methods used to determine the solid state structure, depicted in Figure 21 and Scheme 20, which surprisingly is not the one of the expected neutral complex [4]. Instead, the obtained complex, [7], shows a unique rearrangement of the carbon ligand framework. Cleavage of the C=C$_{trop}$ double bond of the central seven membered ring occurred (increase of the C1-C2 distance from 1.51 to 2.58 Å). This is accompanied by the formation of a new

C−C bond of 1.468(8) Å between the carbon atoms of the former alkynes (C4−C7), which were 3.224(6) Å apart in [**4**]$^{2+}$. This new C−C bond is in the range between a single and a double bond. With this we report the first example of opening the trop-molecule at the alkene unit ("troppelbond") and thereby expanding the C_7 ring to a C_{11} cycle.
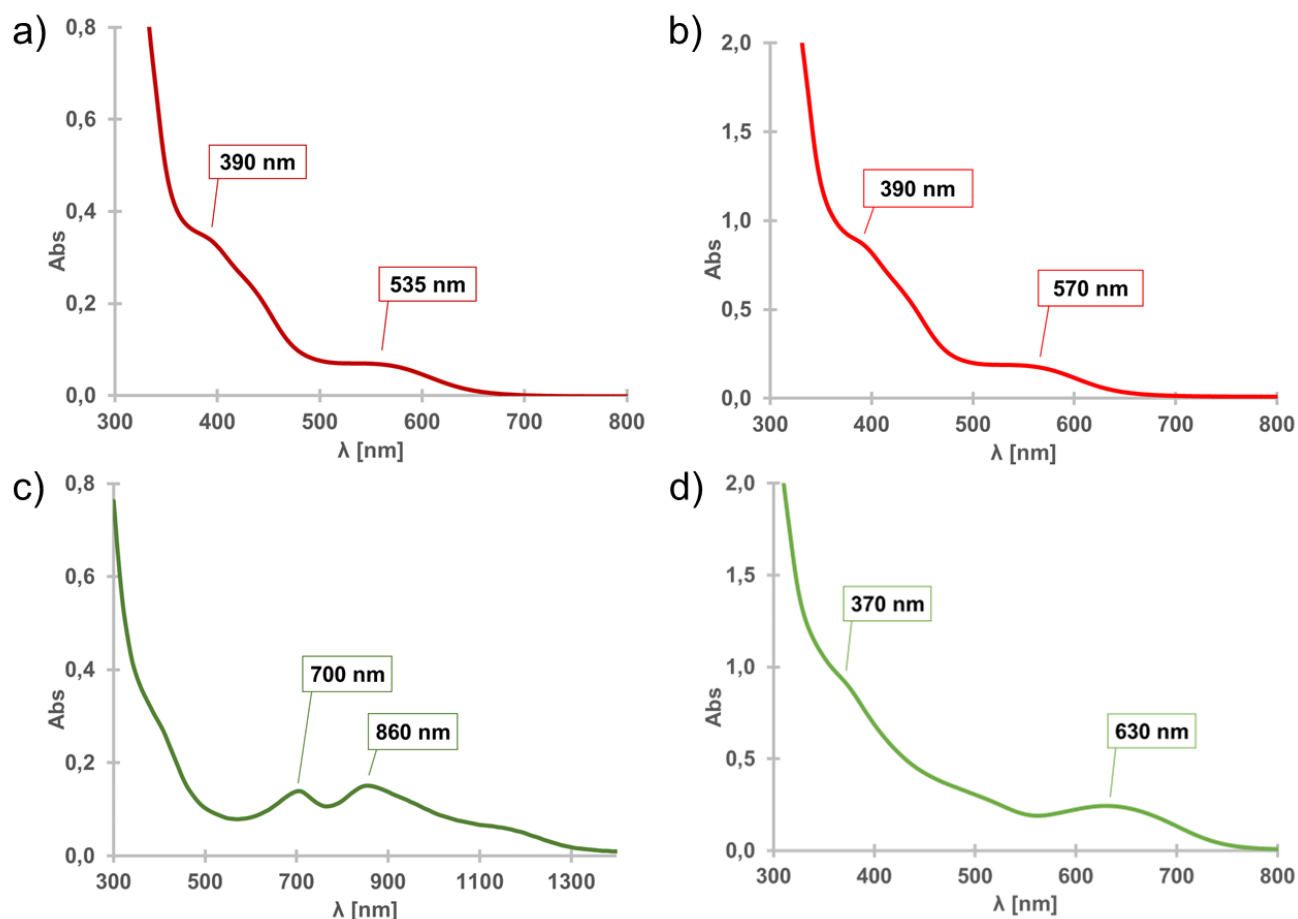
Figure 19. UV/VIS-spectra of solutions of [**4**]$^{2+}$ (a), [**4**]$^{•+}$ (b), [**7**] (c) and [**8**]$^+$ (d) in THF. Layer thickness: 2 mm.

Apart from the sp^3-hybridized carbon center C11, which carries the PPh$_2$ group on the benzylic site of the eleven-membered ring, all other carbon centers are sp/sp^2-hybridized and form a conjugated delocalized π-electron system in which the C−C distances lay between 1.315 Å (average of C2−C3/C1−C6) and 1.470 Å (average of C1−C9/C2−C13). The Rh^1 center is bound to the phosphorus donor (2.2017(15) Å), the second rhodium metal (Rh^1−Rh^2 = 2.7109(6) Å), and the two carbon atoms C1 (2.073(7) Å) and C2 (2.076(6) Å) in addition to the bipy ligand. The former alkene atoms C1 and C2 are now negatively charged η^1-alkenyl ligands, with C−Rh σ-bonds of around 2.07 Å in length. The other Rh^2 center is coordinated to the second bipy ligand, the Rh^1 metal atom, and to the C6−C7−C4−C3 unit of the C_{11} ring with a bond length of Rh^2−ct1 1.7332(4) Å (ct1 = centroid of C6−C7−C4−C3). Formally, the −C1=C6=C7(Cy)−C4(Cy)=C3=C2− part of the ring is therefore best described as a dianionic bisallenyl with Rh^1 bound via two σ-bonds to two carbon atoms while Rh^2 coordinates in a η^4-fashion to the delocalized system of the ring. This makes the

C$_{11}$ ring an eight-electron donor ligand in total: 2 × 2 e$^-$ (η^1-C$^-$) and 1 × 4 e$^-$ (η^4-C6−C7−C4−C3). Presuming a formal oxidation state of +1 for each Rh center, an additional 6 donor electrons from supplementary ligands are necessary to attain a formal valence electron count of 18 for the Rh^1 center. These additional electrons are provided by the bipy ligand (4 e$^-$) and the phosphorus center (2 e$^-$). Attaining a formal valence electron count of 16, the Rh^2 center incorporates an additional four electrons from the bipy ligand, resulting in a square pyramidal coordination geometry. This description is further supported by DFT, where calculation of intrinsic bond orbitals (IBO) shows that two negative charges are carried by the rearranged ligand framework, while both rhodium atoms remain in the formal oxidation state of +I. Furthermore, an IBO was found with an overlap between Rh^1 and Rh^2 (Figure 20a). QTAIM calculation also shows a bond critical point located between Rh^1 and Rh^2, indicating a metal-metal single bond. The contour map of the Laplacian of the electron density of complex [**7**] is shown in Figure 20b. The electron density at the BCP in the dication [**4**]$^{2+}$ exhibits a slightly lower value (0.042) in comparison to [**7**] (0.048), suggesting a closer interaction between the rhodium centers in the reduced, rearranged species. This aligns with the observed shorter Rh−Rh distance in complex [**7**]. Additionally, the analysis of energy parameters at the BCP indicates that the Rh−Rh interaction in both species is best described as a weak dative metal-metal interaction. To summarize, upon two-electron reduction, the carbon sphere changed from a conjugated bis-alkyne system to a bis-alkenyl-allenyl system that included ring-expansion.
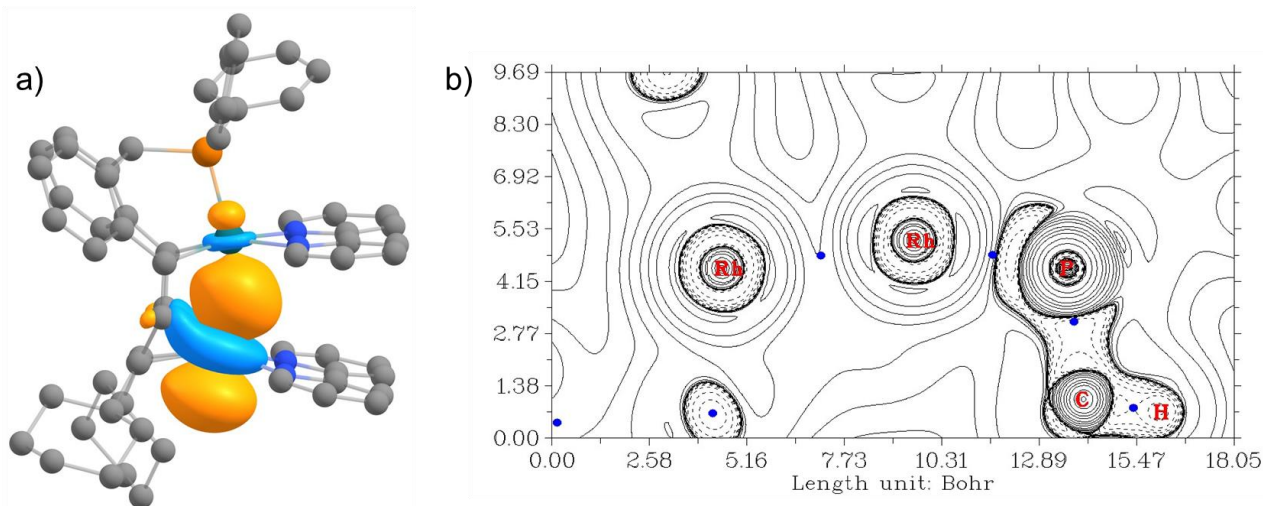
Figure 20. a) Relevant IBO for the description of the Rh−Rh bond in neutral complex [**7**]; b) contour map of the Laplacian of the electron density of rearranged [**7**].
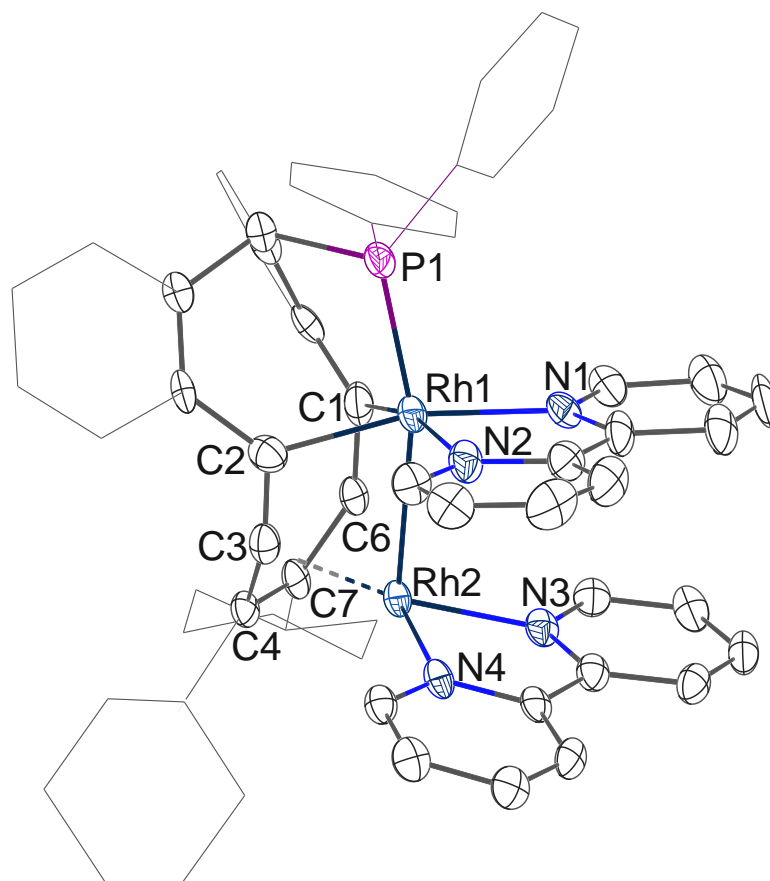
Figure 21. Solid state structure of [**7**], hydrogen atoms and solvent molecules omitted for clarity.

DFT calculations show that the singlet state is around 15 kcal mol^{-1} more stable than the triplet state, while the rearranged structure [**7**] is only slightly (-3.2 kcal mol^{-1}) more stable than the calculated reduced native form [**4**] bearing the two alkynes. The rearrangement proceeds smoothly in one step via opening of the C1=C2 bond and simultaneous formation of the C4−C7 bond via one activated complex **TS** at the transition state, which is 29.2 kcal mol^{-1} higher in energy than [**4**], see Figure 22. Due to the high activation barrier, we assume that the equilibrium state between the two forms is reached only very slowly at room temperature, so that only [**7**] is observed. Acquiring the equilibrium state is further hindered by the very low solubility of [**7**]. These results are in agreement with the reversibility of the redox events in the CV of [**4**]$^{2+}$ indicating that [**4**] is sufficiently long lived on the time scale of the CV experiment, while upon chemical reduction it rearranges to [**7**] upon isolation. The ^{31}P NMR chemical shifts of both species were calculated as δ^{31}P = 54 ppm [**4**] and 7 ppm [**7**], the latter being closer to the experimental value of δ^{31}P = 18.9 ppm. Consequently, [**7**] most likely retains its structure upon dissolution.

Although, when a solution of [**7**] in THF is heated to 50 °C for 10 min, ^{31}P NMR shows two new species that appear as doublets of doublets (confirming the presence of both Rh atoms coordinated) at 74.3 and 78.3 ppm, while the initial signal disappears. Unfortunately, these species could not be isolated and no hints about their structural motifs can be given.
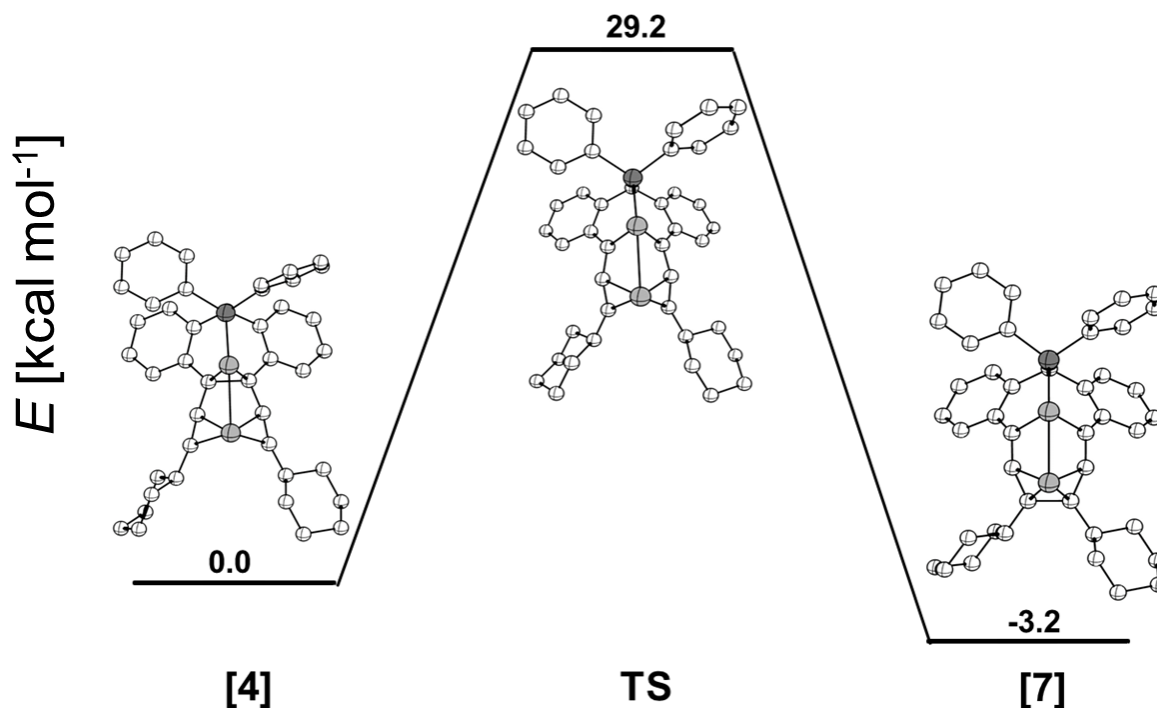
Figure 22. Minimum energy path for the interconversion between the native form of double reduced complex [**4**] to the rearranged complex [**7**] via transition state (**TS**). Bipy ligands and H atoms omitted in the calculated structures.

2.2.3. *Further electrochemical investigations*

After isolation and characterization of reduced complexes [**4**]⁺ and [**7**] more detailed electrochemical studies were performed. An overview of redox potentials of complexes [**6**]⁺, [**4**]²⁺ and [**7**] is listed in Table 2. When a CV of [**4**]²⁺ is measured with MeCN as solvent and a Pt working electrode (WE), the same two reversible reduction waves are obtained as in THF solvent. This leads to the assumption that on the CV timescale, no C−C bond rearrangement takes place under these conditions. Surprisingly, when the same solution is measured with a glassy carbon (GC) working electrode, the redox waves are irreversible by exhibiting a surface adsorption phenomenon. This is reflected by the strong triangular oxidation peak at around -1.2 V, which is scran-rate independent. An overlay of the CVs with Pt and GC WE is depicted in Figure 23a, for a comparison of scan rates see Figure 23b. It is assumed that under these conditions (MeCN and GC WE) a rearrangement in the carbon structure can take place on the CV timescale. The formed species seems to have a strong affinity to adsorb onto glassy carbon surfaces.
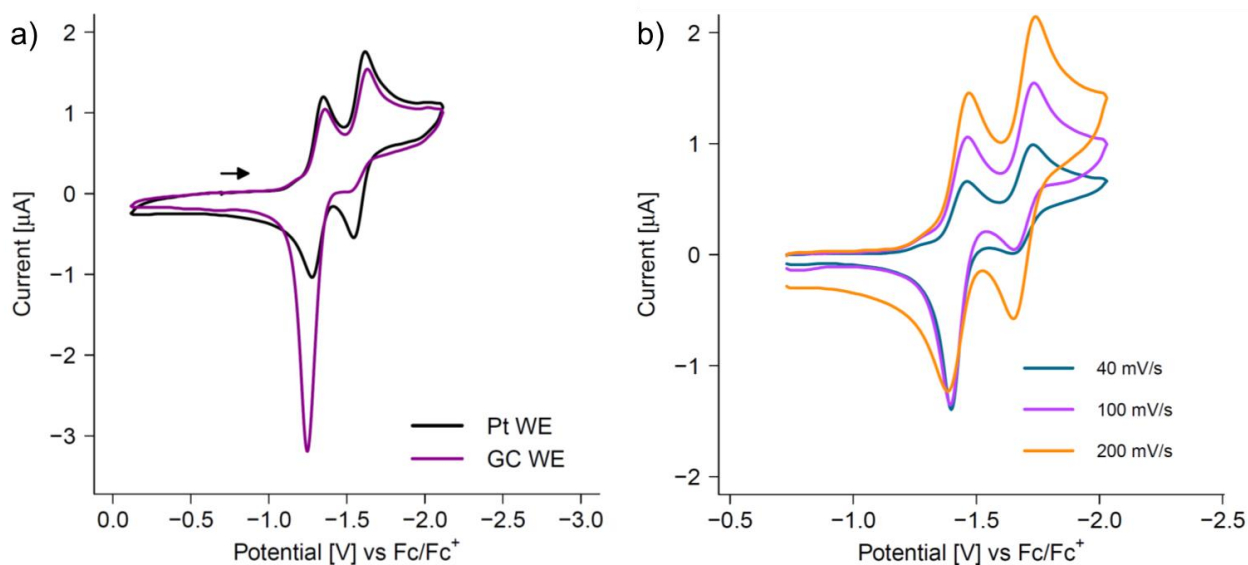
Figure 23. a) CV of [**4**](OTf)$_2$ in MeCN at 100 mV/s scan rate, overlay of GC and Pt WE measurements; b) scan rate depended CV of [**4**](OTf)$_2$ in MeCN with GC WE. CV conditions: 1 mM analyte, 100 mM [nBu$_4$N]PF$_6$ electrolyte, Pt or GC WE, Pt on TiO$_x$ CE, Ag/Ag$^+$ RE.

To confirm the ligand rearrangement during electrochemical reduction, bulk electrolysis was performed. The electrosynthesis was set up in a divided cell with a Pt mesh working electrode and Zn-wire counter electrode as sacrificial anode, depicted in Figure 24. During electrolysis, a dark green solid formed on the cathode. The solid product was separated from the reaction mixture and dissolved in pyridine-d$_5$. Indeed, NMR spectroscopic characterization revealed formation of complex [**7**] by means of electrochemical reduction, which is thus an alternative and simple way of its preparation.
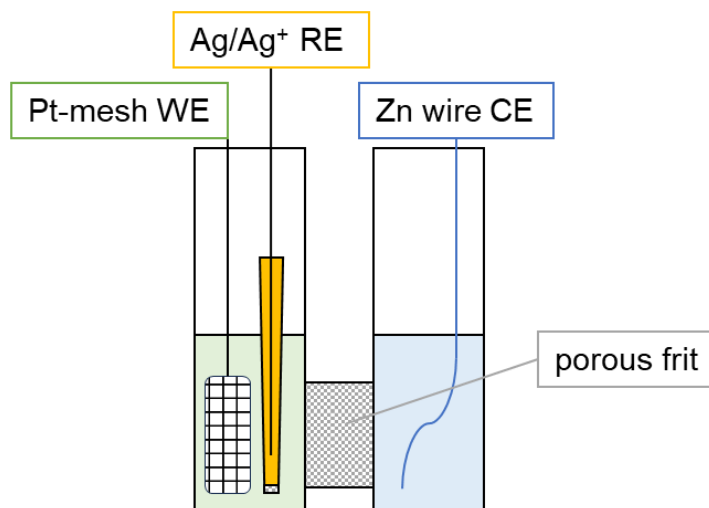
Figure 24. Schematic setup used for the electrochemical generation of [**7**].

Table 2. Redox potentials [V] of complexes [6]+, [4]2+, [7] and [8]+.

	[6]+	[4]2+	[7]	[8]+
$E^{1/2}_{(red)}$	-1.63 -2.06 [a]	-1.35 -1.61	-	-1.89 -2.28
$E^{1/2}_{(ox)}$	0.53 [a]	0.57 [a]	-1.01 -1.37	-0.50

[a] Peak potential at 100 mV/s.

A CV of the rearranged complex [7] was recorded and shows the expected two redox events (Figure 25): Starting from the open-circuit-potential (OCP) at -1.59 V, the complex can be oxidized at $E^{1/2}$ = -1.37 V and -1.01 V. Both oxidations are considered quasi-reversible but show a rather low current (around 0.2 µA) due to low solubility in THF. The rather negative value of the OCP already gives a hint to the presence of a strongly reducing species. Note that the oxidation potentials of [7] are shifted to less negative potentials in comparison to the reductions of [4]2+ ($E^{1/2}$ = -1.35 and -1.61 V, shown in Figure 17) indicating that [7]•+ and [7]2+ likely retain the overall structure of [7] on this timescale. These changes prove that with the direct measurement of complex [7], a different carbon-based ligand environment than in [4]2+ was obtained. 31P NMR spectroscopy showed that [4]2+ is partly regenerated upon chemical oxidation of [7] together with two unidentified products. Therefore, it is assumed that follow-up reactions also occur after the second oxidation on the time scale of the CV experiment.
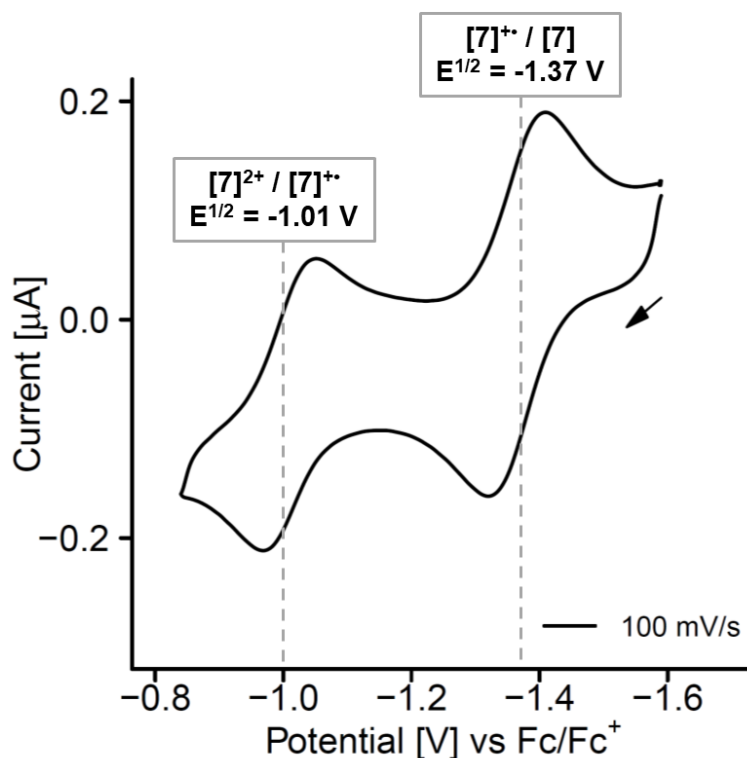
Figure 25. CV of [7] in THF. The open circuit potential (OCP) and scan direction are shown by an arrow. CV conditions: 1 mM analyte, 100 mM [nBu4N]PF6 electrolyte, Pt WE, Pt on TiOx CE, Ag/Ag+ RE, 100 mV/s scan rate.

2.3. Proton Transfer Processes of complex [4](OTf)$_2$

Next, the potential for deprotonating dicationic [4]$^{2+}$, which contains a propargylic proton at each of the cyclohexyl groups, was explored. This offers an alternative method for gradually converting the dicationic complex into a neutral form and thereby alter the interaction between the metal and the carbon-based coordination environment. Furthermore, base-assisted alkynyl/allene isomerization was considered, a phenomenon related to the rearrangement observed during the reduction of [4]$^{2+}$. Although such isomerization reactions are well-established subjects of research, they frequently require harsh reaction conditions or the addition of Lewis acids.[119–123] When [4]$^{2+}$ is reacted with one equivalent of KOtBu, an immediate color change from red to deep green (λ_{max} = 630 nm, Figure 19d) is observed and cleanly leads to the formation of a new product [8]$^{+}$ (see Scheme 21).
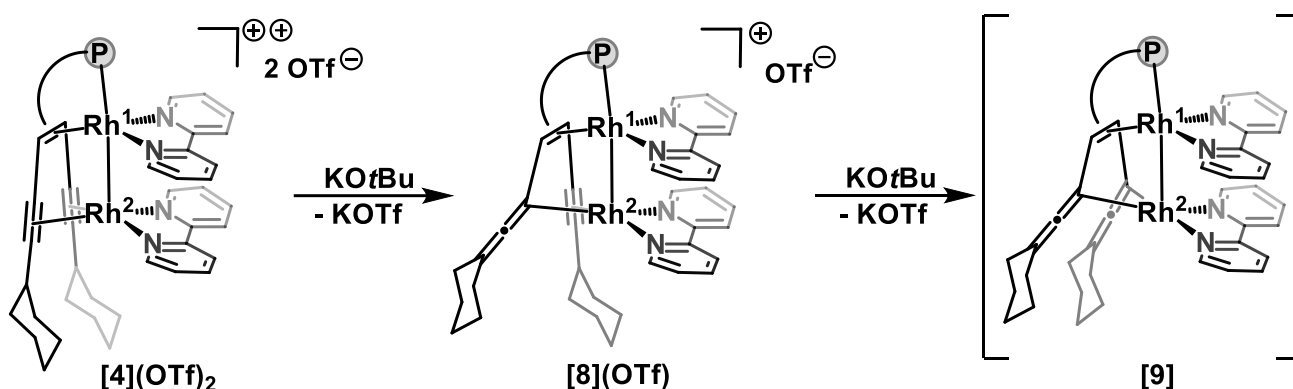
Scheme 21. Deprotonation of [4](OTf)$_2$ with KOtBu base to cationic [8](OTf) and subsequently to neutral [9].

This compound was crystallized, and its structure analyzed by XRD methods (Figure 26a). The CH unit of the cyclohexyl substituent in α-position to the alkynyl group was deprotonated and an allenyl unit, $R_2C=C=C^-(R)$, is formed (C3=C4 1.300 Å and C4=C5 1.340 Å). This allenyl-rhodium substructure coordinates with its anionic terminus to Rh^2 (C3−Rh^2 2.035(11) Å). The carbon center C4 of the former alkynyl unit, previously coordinated to Rh^2, is now at a distance of 2.86 Å from the metal center, which no longer corresponds to a chemical bond. Related structural motifs are observed in mono- and dinuclear rhodium complexes,[124–127] or in Ru and Os clusters, where usually the allenyl moiety additionally coordinates side-on to a second metal center.[51,128]

Table 3. Selected bond lengths [Å], chemical shifts [ppm] and coupling constants [Hz] complexes [4]$^{2+}$, [8]$^{+}$ and [9].

	[4]$^{2+}$	[8]$^{+}$	[9] [a]
Rh^1−Rh^2	2.7923(4)	2.6930(9)	2.693
C1−C2	1.512(6)	1.509(7)	1.461
Rh^1−ct$_{(C1-C2)}$	1.9292(3)	1.9454(2)	2.003
C3−C4	1.232(6)	1.298(15)	1.296
C6−C7	1.239(6)	1.278(9)	1.325
Rh^2−ct$_{(C3-C4)}$	2.0925(3)	2.035(9) [c]	2.056 [c]
Rh^2−ct$_{(C6-C7)}$	2.0835(3)	2.0084(9)	2.013 [d]
^{31}P	96.4	78.2	61.3
^{103}Rh^1	-7043	-7343	-7606
^{103}Rh^2	-743	-5373	-6183
$^1J_{P-Rh1}$	192.8	194.8	191.7
$^2J_{P-Rh2}$	9.3	29.5	52.3
C1/C2	37.6	37.9	37.9
C6/C3	87.2	87.1 / 109.6	114.6
C7/C4	78.4	85.3 / 184.0	184.4

[a] Calculated bond lengths. [b] Rh^1−C1 bond length. [c] Rh^2−C3 bond length. [d] Rh^2−C6 bond length. [e] Not detected.
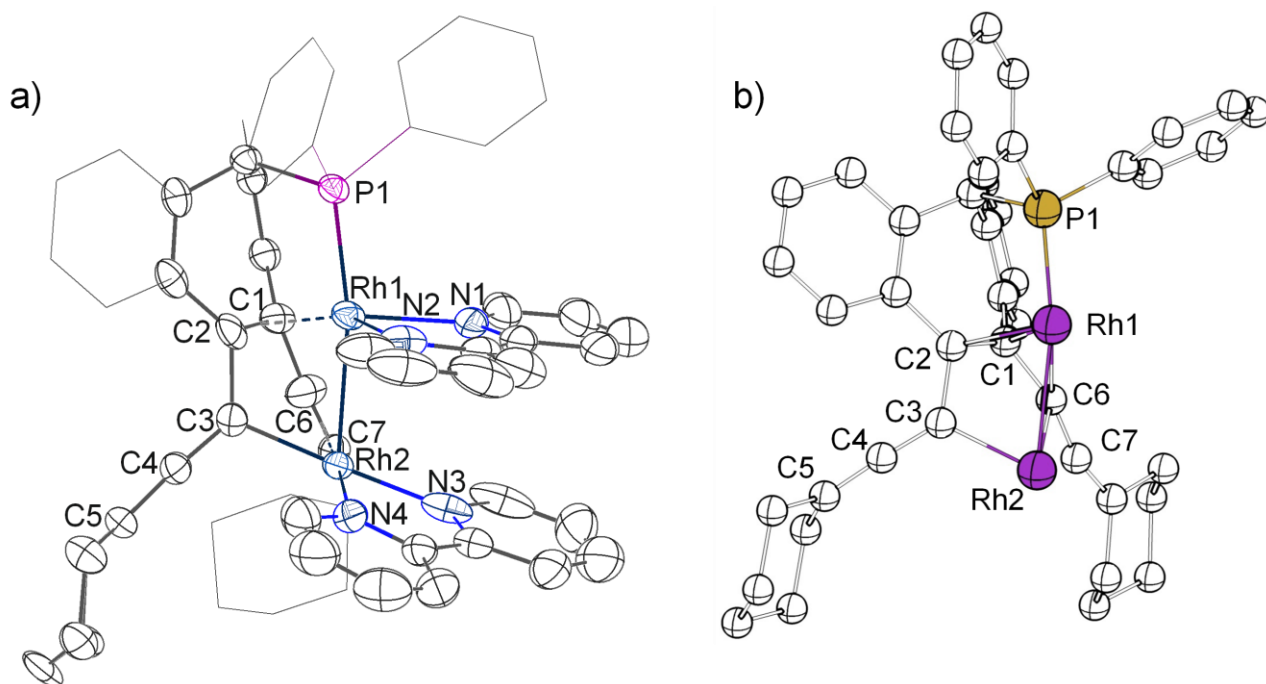
Figure 26. a) Solid state structure of [8]$^{+}$, hydrogen atoms, counter ion and solvent molecules omitted for clarity; b) optimized geometry of [9] calculated with DFT, hydrogen atoms and both bipy ligands omitted for clarity.

The structural change in the carbon framework leads to a significant shortening of the Rh−Rh distance from 2.792 Å in dicationic [4](OTf)$_2$ to 2.693 Å in cationic complex [8](OTf). The decrease in Rh−Rh distance is accompanied by an elongation of P−Rh1 bonds (2.203 vs 2.222 Å for [4]$^{2+}$ and [8]$^{+}$, respectively). While $^1J_{P-Rh1}$ remains roughly the same ($^1J_{PRh1}$ = 193 Hz), the ^{31}P NMR spectrum shows a doublet of doublets at δ^{31}P = 78 ppm with a significant shift to lower frequencies (δ^{31}P = 96 ppm for [4]$^{2+}$) shown in Figure 27. A remarkable increase in the coupling constant from P to Rh^2 of $^2J_{PRh2}$ = 30 Hz, compared to around 10 Hz for [4]$^{2+}$. This finding, together with the reduced Rh−Rh bond distance, leads to the assumption of an increased metal-metal interaction upon deprotonation and formation of the allenyl unit. For a list of bond lengths and NMR data, see Table 3. Large differences between the bis(alkynyl) complex [4]$^{2+}$ and allenyl-rhodium complex [8]$^{+}$ are observed in the ^{103}Rh and ^{13}C NMR spectra. While δ^{103}Rh^1 is similar in [4]$^{2+}$ and [8]$^{+}$ (δ^{103}Rh = -7043 ppm and -7343 ppm, respectively), the resonance of Rh^2 is shifted over 4500 ppm to lower frequencies ([4]$^{2+}$: δ^{103}Rh^2 = -743 ppm; [8]$^{+}$: δ^{103}Rh^2 = -5373 ppm), which is explained by the transformation of the coordination environment from a bis-alkyne ligand to an anionic alkyne-allenyl ligand. The ^{13}C NMR spectrum of [8]$^{+}$ shows signals at δ^{13}C = 109.6 ($\underline{C}$=C=C$_{cy}$), 184.0 (C=$\underline{C}$=C$_{cy}$) and 94.6 (C=C=$\underline{C}_{cy}$) ppm, which correspond to the κ^1-C coordinated allenyl fragment. Signals at 87.1 and 85.3 ppm are assigned to the remaining alkynyl unit which remains η^2-bound to Rh^2.
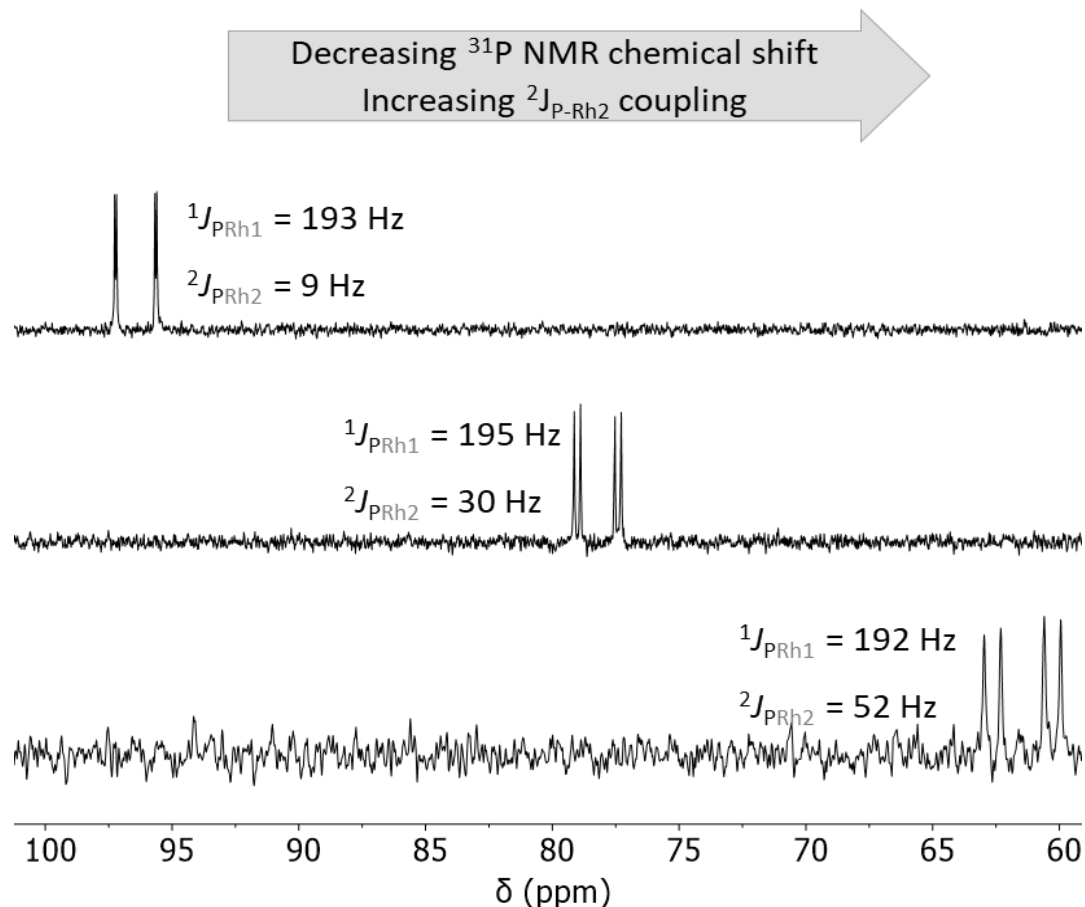
Figure 27. ^{31}P NMR spectra of [4](OTf)$_2$, [8](OTf) and [9] (top to bottom) with insets of coupling constants.

The redox properties of [**8**]+ were investigated by cyclic voltammetry. Remarkably, again, two reversible redox waves were observed at E½ = -1.89 V and -2.28 V as shown in Figure 28. The substantial shift to more negative potentials is attributed to the chemical modification of the coordination sphere from bis-alkyne dication [**4**]2+ to alkyne-allenyl mono-cation [**8**]+ with a reduction of charge and conversion of a π-electron withdrawing alkynyl unit into a σ-electron donating allenyl unit. DFT calculations indicate that the reductions mainly take place at the bipy ligands. Additionally, a reversible oxidation event was observed at -0.50 V, which is shifted around 1 V to more negative potentials when compared to the oxidation of [**6**]+ or [**4**]2+ (see also Table 2), which means oxidation is facilitated upon deprotonation of the complex. None of these electrochemically generated species were found to be stable enough to allow for isolation.
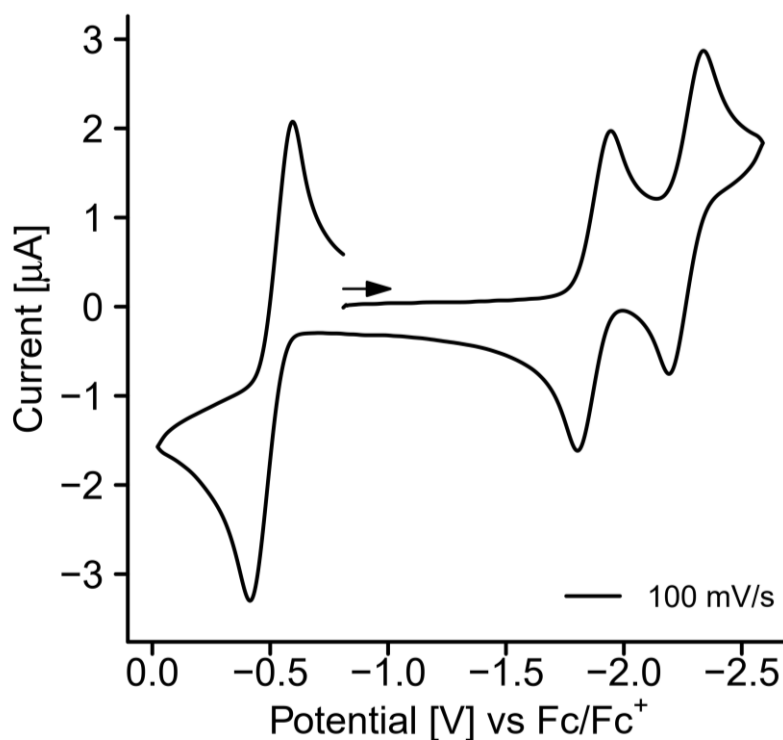
Figure 28. CV of [**8**](OTf). The open circuit potential (OCP) and scan direction are indicated by an arrow. Conditions: 1 mM analyte, 100 mM [nBu4N]PF6 electrolyte, THF solvent, Pt WE, Pt on TiOx CE, Ag/Ag+ RE, scan rate 100 mV/s.

A second equivalent of KOtBu was added to [**8**]+ in an attempt to obtain neutral [**9**], in which both propargylic CH units in the cyclohexyl substituents are deprotonated. Time dependent NMR studies (shown in Figure 29 (^{1}H NMR) and Figure 30 (^{31}P NMR)) show formation of [**9**], although the compound starts to decompose or rearrange into some unidentified species after 1-2 h. The presence of [**9**] could be confirmed by _in situ_ NMR spectroscopy and accompanying DFT calculations of ^{31}P NMR chemical shifts. A plot of the optimized geometry of [**9**] is depicted in Figure 26b. The experimental value of 61.3 ppm only slightly differs from the calculated 49 ppm (theoretical values were referenced to complex [**4**]2+). When compared to complexes [**4**]2+ and [**8**]+, the ^{31}P chemical shift is significantly decreased and the $^2J_{\text{P-Rh2}}$ coupling is increased even more to over 50 Hz (see

Figure 27 and Table 3). ^{1}H NMR data show the same trend for the benzylic proton (5.1 to 4.88 to 4.57 ppm from [**4**]$^{2+}$ to [**8**]$^+$ to [**9**]). The indicative protons on the cyclohexyl group show a symmetric compound in [**4**]$^{2+}$, which suggest an unsymmetric compound [**8**]$^+$ (determined via the integrals). In neutral complex [**9**], the ^{1}H NMR spectrum again shows a symmetric species which also suggests the disappearance of both propargylic CH groups (see Figure 29). The recorded ^{13}C NMR spectra showed the absence of the alkyne groups, and presence of a symmetric compound with signals at δ^{13}C = 114.6 ($\underline{C}$=C=C$_{cy}$), 184.4 (C=$\underline{C}$=C$_{cy}$) and 89.6 ppm (C=C=$\underline{C}_{cy}$), are attributed to the κ^1-C coordinated allenyl fragments. These values only slightly differ from related compound [**8**]$^+$ (see Table 3). The chemical shift for Rh^1 is shifted 263 and 438 ppm to lower frequencies compared to complexes [**4**]$^{2+}$ and [**8**]$^+$ respectively (δ^{103}Rh^1 = -7606 ppm for [**9**]). The resonance of the Rh^2 nucleus follows the same trend from δ^{103}Rh^2 = -743 for [**4**]$^{2+}$ to -5373 in [**8**]$^+$ to -6183 ppm in complex [**9**].
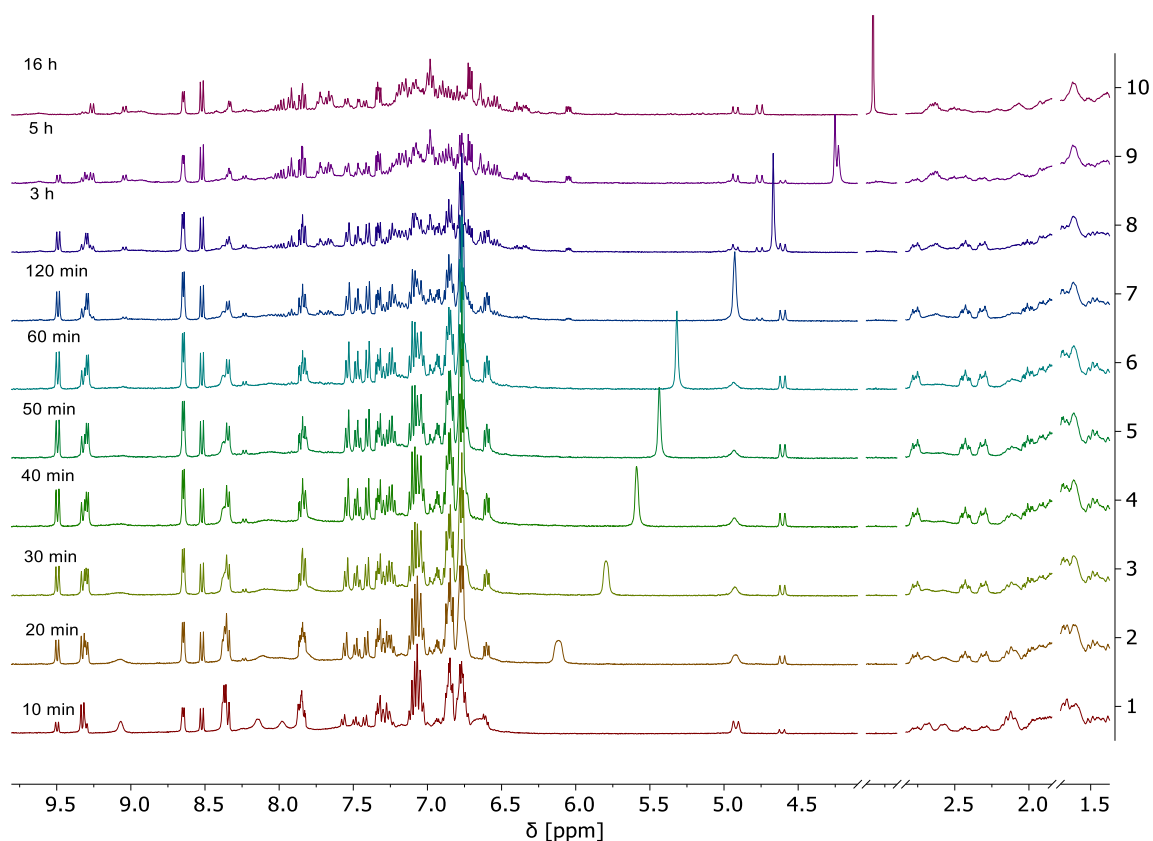
Figure 29. Time dependent ^{1}H NMR spectra of the reaction of [**4**]$^{2+}$ with 2 eq. of KOtBu to obtain [**9**] in THF-d$_8$. Notable is the prominent signal of the benzylic proton of [**9**] appearing at around 4.6 ppm.
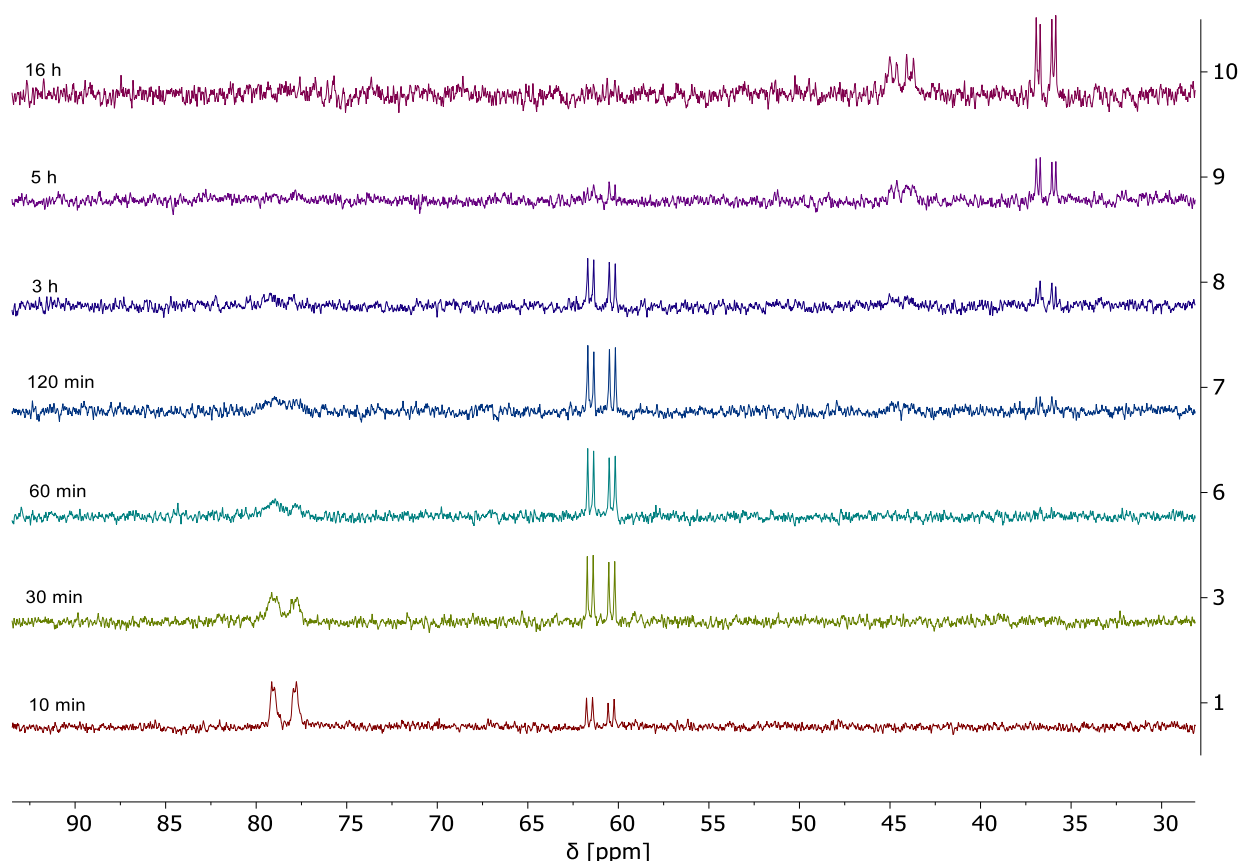
Figure 30. Time dependent ^{31}P NMR spectra of the reaction of [**4**]$^{2+}$ with 2 eq. of KO*t*Bu to obtain [**9**] in THF-d$_8$. The signal associated to [**9**] appears and disappears at around 62 ppm. Unidentified species appear at 37 and 45 ppm.

All NMR data are in accordance with a more electron rich species, as all significant values become lower frequency shifted. Since this doubly deprotonated, neutral species [**9**] is only stable for a few hours, it could not be isolated and no solid state structure could be obtained. DFT calculations give some insight into a possible structure of complex [**9**]. Geometry optimization after removal of both propargylic protons yielded the expected structure of a dianionic pentaene, consisting of two allenyl fragments which are conjugated via the double bond of the trop-moiety (for optimized geometry of [**9**] see Figure 26b). The experimental evidence from NMR spectroscopy, together with DFT calculations, mean that the presence of [**9**] can be safely suggested.

3. Ph$_2$^{F}dad as ligand in dirhodium complexes

3.1. Introduction

Diazadiene (dad) ligands are a very popular class of molecules for coordination chemistry, a detailed description is given in Chapter I and Chapter V. So far, substituent effects in Ar$_2$dad ligands have mostly been studied at the aryl groups.[129] Substituents directly attached to the dad backbone are expected to have an even larger effect on reduction potentials than those attached to the aryl groups. Functionalization of the dad backbone is mostly limited to the incorporation of methyl groups. Recently, the Grützmacher group developed a fluorinated dad ligand: Ph$_2$^{F}dad (**10**).[130] The electron withdrawing fluorine substituents show almost no steric bulk and should therefore not sterically interfere upon coordination. The recently developed strategy for the synthesis of **10** is straightforward and robust, as depicted in Scheme 22, and was described in the PhD thesis of Jonas Bösken.[130] Product **10** was purified by sublimation with an overall yield of 25% over three steps. Note that all molecules are present in their trans conformation and do not show conformational change in solution at room temperature.
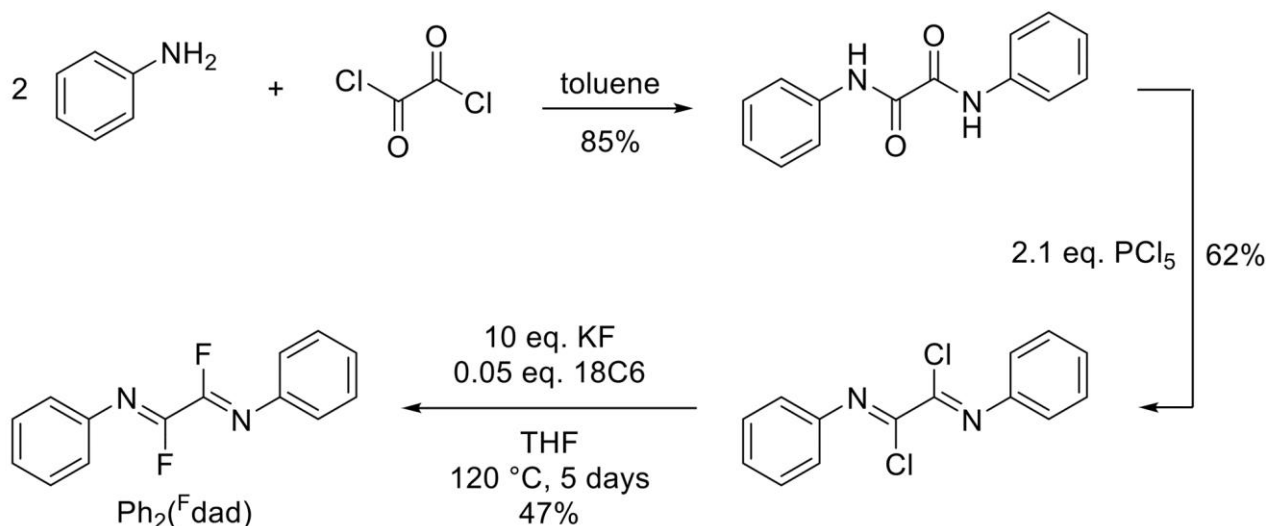
Scheme 22. Synthesis of fluorinated diazadiene molecule Ph$_2$^{F}dad, **10**, adapted from the work of Jonas Bösken.[130]

Ligand **10** was reacted with various transition metal precursors, including Ir^I and Rh^I compounds.[130] Despite significant efforts to coordinate **10** to a metal center, no reaction was observed. It was assumed that the ligand does not bind strongly enough to replace ligands from the precursor complexes due to the electron withdrawing effect of the fluorine groups. Those make the nitrogen donor atoms less electron rich and therefore weaker σ-donors. A second possible explanation is the trans conformation of **10**. It was calculated that **10** is most stable in its trans conformation,[130] which means that for coordination, a conformational change is needed. An activation energy barrier needs to be overcome to change to the cis conformation to bind both nitrogen atoms to a metal center.

3.2. Synthesis and characterization

In order to further investigate the properties of Ph_2^Fdad (**10**) as a ligand, it was reacted with dirhodium complex [**3**] in THF. Coordination of the dad ligand and formation of complex [**11**](OTf) was followed by ^{31}P and ^{19}F NMR spectroscopy. Single crystals were grown and submitted to X-ray analysis, which showed that ligand **10** exclusively coordinates to Rh^2, while one triflate ligand remains bound to Rh^1 in a η^1 fashion via an oxygen atom. The synthesis of complex [**11**](OTf) is shown in Figure 31a and its solid state structure in Figure 31c. Since the triflate ligands are rather labile – they are most likely reversibly replaced by acetonitrile when dissolved in that solvent – it is possible that only one nitrogen atom of trans **10** coordinates to Rh^2 and only then undergoes isomerization to the final cis conformation. Interestingly, reaction of [**3**] with Ph_2^Hdad (without fluorine substituents) did not lead to the formation of the expected complex [**12**](OTf) (see Figure Figure 31b).

Interestingly, only one molecule of **10** can be coordinated to the dirhodium complex. Even if a large excess of **10** is used, only complex [**11**](OTf) is obtained. On the other hand, the mono-bipy complex is not formed, even when a sub-stoichiometric amount of bipy is reacted with [**3**]. From ^{31}P NMR spectra it is obvious that there is a mixture between complex [**3**] and [**4**](OTf)$_2$ is present in solution. This difference in complexation reactivity cannot be explained yet.
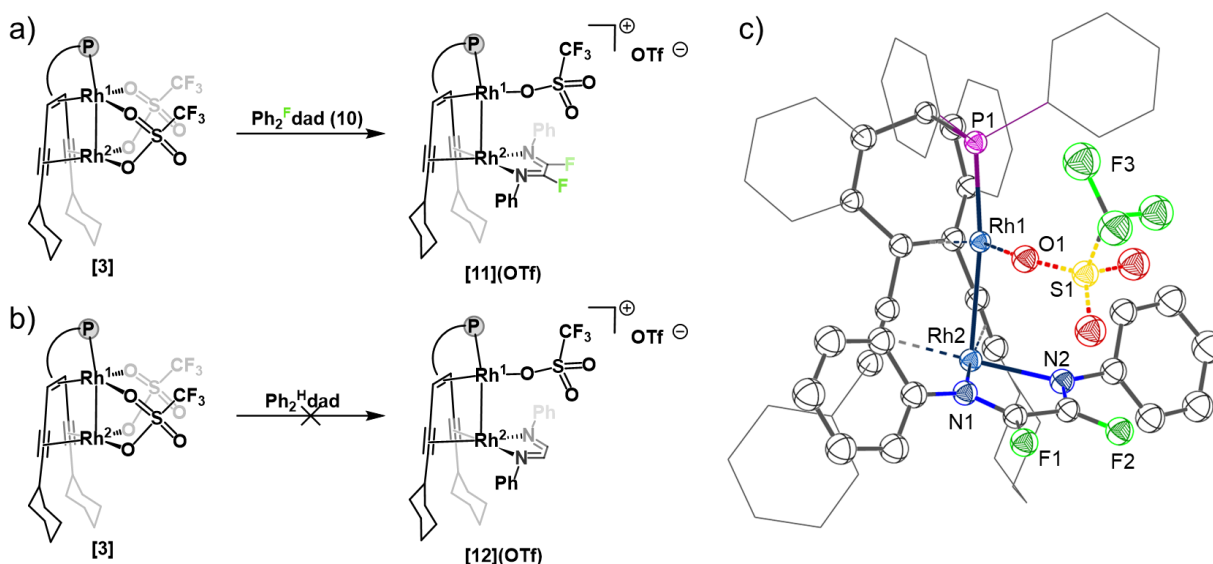
Figure 31. a) Synthesis of [**11**](OTf); b) attempted synthesis of [**12**](OTf); c) solid state structure of complex [**11**](OTf). Hydrogen atoms, counter ion and solvent molecules omitted for clarity.

Comparing the uncoordinated Ph_2^Fdad **10** with complex [**11**](OTf), where **10** is bound to a rhodium center, the bond lengths within the dad backbone change slightly: while C43−C44 is shortened (0.02 Å), the C43−N1/C44−N2 bonds are elongated (0.04 Å). Structural data is given in Table 4. It has to be taken into account, that the free ligand **10** is in its trans conformation, while upon coordination in [**11**]$^+$ it has to be in the cis form in order to coordinate with both nitrogen atoms to the metal. However,

this change in bond lengths suggests a slight shift more to a coordinating diamide. This does not affect the N1−C42/N2−C45 bond lengths within the accuracy of the measurement. The Rh^2 resides in a square planar coordination environment between the centroids of the alkyne carbon atoms and the nitrogen donor atoms from **10**. This plane is extended over the −C(F)−C(F)− part of the ligand. Interestingly, here the phenyl rings are out of this plane with a torsion angle of 54.4° which does not occur in uncoordinated **10**, where the entire molecule is planar. The tilt of the phenyl rings could be explained by simple steric hindrance of the trop based ligand.

As expected, the carbon fluorine bonds are also influenced upon coordination, seen in the significant shortening of the C_{dad}−F bond (1.352 to 1.317 Å) and the change in ^{19}F NMR chemical shifts from -48.1 ppm in **10** to -41.4 ppm in [**11**]$^+$. Selected NMR data are listed in Table 4. The high-frequency shift indicates that the, otherwise electron withdrawing, fluorine substituents donate electron density via the dad into the rhodium center. This is also reflected by the decrease in bond length which shows strengthening of the C−F bonds. Another indicative value is the ^{13}C NMR chemical shift of the C_{dad}−F, which shifts 13.4 ppm to higher values, reflecting the electron donation into the rhodium center. The signal in ^{13}C NMR for C43/C44 appears as a doublet of doublets for [**11**]$^+$ from coupling to both fluorine atoms with $^{1}J_{CF}$ = 333.8 Hz and $^{2}J_{CF}$ = 49.5 Hz. Both coupling constants decrease slightly upon coordination (11 and 7 Hz).

Table 4. Bond lengths [Å] and NMR chemical shifts [ppm] of free Ph$_2$^{F}dad **10**[130] and in complex [**11**](OTf).

	10	[**11**](OTf)
C43−F1	1.352(5)	1.317(7)
C43−C44	1.472(5)	1.451(15)
C43−N1	1.247(4)	1.283(8)
N1−C42	1.422(5)	1.417(9)
^{19}F (*F1*)	-48.1 (s)	-41.4 (s)
^{13}C (*C43*)	138.2 (dd, *J* = 344.5, 56.9 Hz)	151.8 (dd, *J* = 333.8, 49.5 Hz)

The structures of complexes [**3**], [**4**]$^{2+}$ and [**11**]$^+$ are compared in the following paragraph. An overview of bond lengths and NMR chemical shifts of [**3**], [**4**]$^{2+}$ and [**11**]$^+$ is given in Table 5. The Rh−Rh bond distance of 2.706 Å in [**11**]$^+$ lays in between the ones for [**3**] and [**4**]$^{2+}$. At the same time, all Rh−C bonds are significantly elongated: Rh^1−ct$_{(C1-C2)}$ is 0.025 to 0.05 Å longer in [**11**]$^+$ and Rh^2−ct$_{(C3-C4)}$ is even 0.01 to 0.07 Å longer compared to [**3**] and [**4**]$^{2+}$. All C−C distances do not change significantly within the accuracy of the measurement. A downfield trend appears in ^{31}P NMR data from [**3**] to [**4**]$^{2+}$ and [**11**]$^+$: chemical shifts are 106.0, 96.4 and 83.6 ppm respectively. Furthermore, ^{103}Rh^1 shows a slight low-frequency shift (-7055 ppm for [**11**]$^+$). For the coupling constants, the trend is different: $^{1}J_{P-Rh1}$ increases to 217.4 Hz while $^{2}J_{P-Rh2}$ decreases to 4.0 Hz.

Table 5. Bond lengths [Å] and NMR chemical shifts [ppm] of [3], [4]$^{2+}$ and [11]$^{+}$.

	[3]	[4]$^{2+}$	[11]$^{+}$
Rh^1−Rh^2	2.6310(4)	2.7923(4)	2.7064(7)
C1−C2	1.494(5)	1.512(6)	1.447(13)
Rh^1−ct$_{(C1-C2)}$	1.9044(3)	1.9292(3)	1.9535(5)
C3−C4	1.245(6)	1.232(6)	1.249(9)
C6−C7	1.250(6)	1.239(6)	1.249(9)
Rh^2−ct$_{(C3-C4)}$	2.0305(3)	2.0925(3)	2.1009(4)
Rh^2−ct$_{(C6-C7)}$	2.0285(3)	2.0835(3)	2.1009(4)
^{31}P	106.0	96.4	83.6
^{103}Rh^1	-6973	-7043	-7055
^{103}Rh^2	-688	-743	-
$^1J_{P-Rh1}$	191.7	192.8	217.4
$^2J_{P-Rh2}$	5.7	9.3	4.0
^{19}F	-79.3	-79.3	-41.5 (sharp, F1) -78.8 (broad, OTf) -79.2 (broad, OTf)
C1/C2	37.5	37.6	47.3
C6/C3	83.5	87.2	87.8
C7/C4	68.6	78.4	69.0

3.3. Redox properties of complex [11](OTf)

The redox properties of [11](OTf) were investigated by CV measurements, where two irreversible reduction events at -1.17 and -2.04 V were observed, together with two smaller shoulders at -0.95 and -1.61 V. All reduction events are irreversible and depicted in Figure 32a. Compared to complexes [3] and [4]$^{2+}$, the reductions take place at less negative potentials – the first reduction is shifted 0.3 and 0.2 V, respectively (see Table 6). A CV of the free ligand 10 shows three irreversible reduction waves at -2.08, -2.25 and -2.53 V in MeCN.[130] The first reduction event was assumed to be accompanied by a conformational change from trans to cis. Usually, coordination of dad type ligands to metal atoms (such as bipy as seen earlier in this Chapter) lowers their reduction potentials. Thus, it is hard to say from the CV of complex [11](OTf) where in the molecule the reduction takes place. As mentioned above, DFT calculations suggest the first reduction to take place on the dad ligand coordinated to Rh^2.

Table 6. Redox potentials [V] of [**3**], [**4**]²⁺, [**11**]⁺ and **10**.

	[3]	[4]²⁺	[11]⁺	10
$E^{1/2}_{(red)}$	-1.48 [a]	-1.35 -1.61	-0.95 [a] -1.17 [a] -1.61 [a] -2.04 [a]	-2.08 [a] -2.25 [a] -2.53 [a]
$E^{1/2}_{(ox)}$	-	0.57 [a]	-	-

[a] Peak potential at 100 mV/s.

The irreversibility of the redox processes contrasts the previously described dirhodium complex [**4**](OTf)₂, bearing two bipyridine ligands, which showed two fully reversible reduction events in CV. We assume that the bipy ligands stabilize the complex, especially under reductive conditions, by taking up the additional electrons and possibly by π-stacking (the bipy-bipy distance was found at 3.33 Å). The stabilizing properties of the redox non-innocent bipy ligands are further reinforced by comparison with dirhodium complex [**3**], which coordinates two labile triflate molecules. These co-ligands lack the ability of acting as an electron reservoir. From its CV in Figure 32b it is apparent, that there is only one irreversible reduction taking place at -1.48 V. Reduction experiments with chemical reagents only lead to decomposition of starting material. Therefore, we can conclude that the nature of the co-ligands is crucial for stabilization of such dirhodium complexes under reductive conditions.
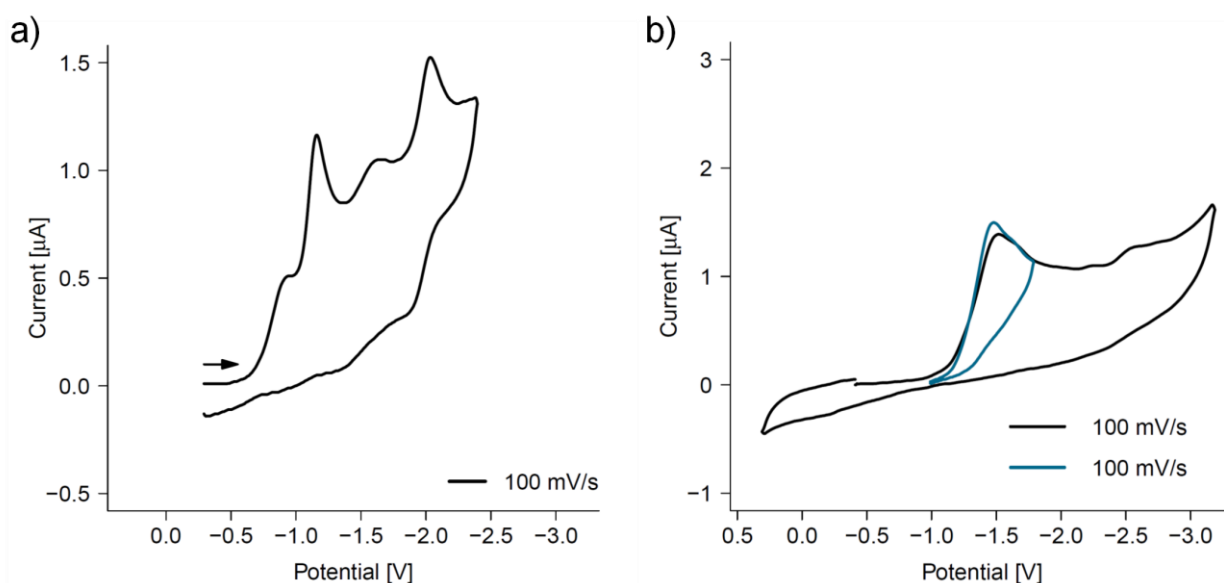
Figure 32. a) CV of [**11**](OTf); b) CV of [**3**]. Conditions: 1 mM analyte, 100 mM [nBu₄N]PF₆ electrolyte, THF solvent, Pt WE, Pt on TiOx CE, Ag/Ag⁺ RE, scan rate 100 mV/s.

DFT calculations were performed on complex [**11**]⁺, where the calculated optimized geometry agrees with the solid state structure measured with XRD methods. Furthermore, an IBO was found which shows an overlap of orbitals from both rhodium atoms (depicted in Figure 33a) like previously described metal-metal interactions in this Chapter. From this IBO analysis it was concluded that

there is again a dative interaction present between Rh[1] and Rh[2]. In addition to that, the HOMO and LUMO are depicted in Figure 33b and Figure 33c. The HOMO is mostly located on the Rh[1] metal center, while the LUMO is mostly delocalized over the Ph_2^Fdad ligand and partially on the Rh[2] center. This shows that upon reduction of complex [**11**]⁺, the spin density is expected to be mainly located at Ph_2^Fdad. However, upon chemical reduction experiments, only decomposition was observed, suggesting that a reduced species of complex [**11**](OTf) is not stable enough to allow for isolation.
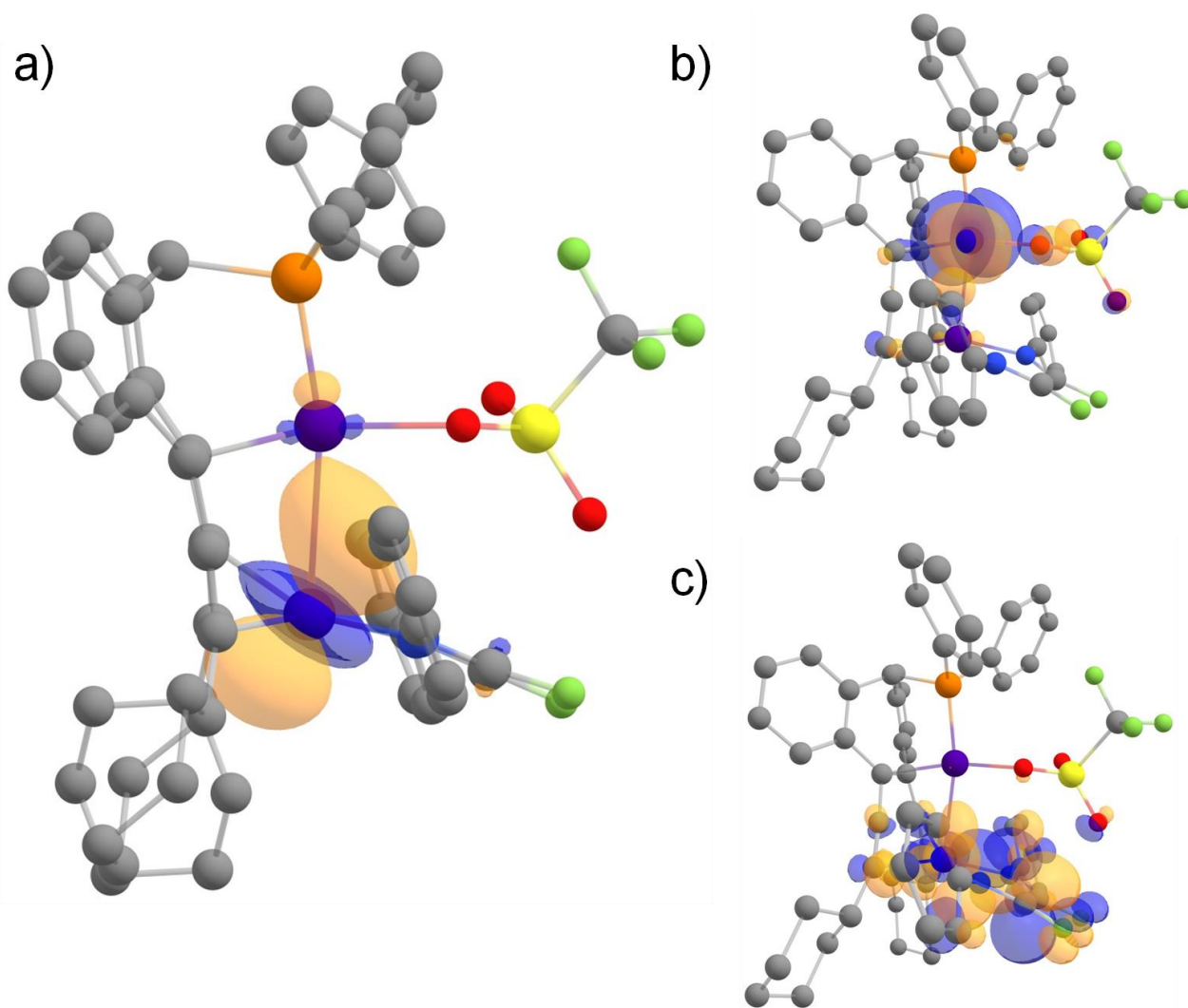
Figure 33. a) Relevant IBO for the description of the Rh−Rh bond of [**11**]⁺; b) HOMO of [**11**]⁺ and c) LUMO of [**11**]⁺.

4. Reactivity studies of dirhodium complexes

4.1. Reaction with hydrogen gas

As described in the introduction to this Chapter, a TMS substituted dirhodium complex, similar to the ones presented here, showed addition of H_2 to the ligand.[69] When cyclohexyl substituted complex [**3**] was placed under H_2 atmosphere (1 bar), fast conversion to complex [**13**] was observed, as depicted in Scheme 23a. Thereby, addition of two hydrogen atoms to C4 takes place, while C3 was transformed into a coordinating carbene. This step proceeded much faster than in the related TMS substituted complex. Furthermore, a second hydrogenation step was observed under the same conditions rendering the isolation of complex [**13**] impossible. After 3 hours at 1 bar, only hydrogenated [**13-H2**] was observed by ^1H and ^{31}P NMR spectroscopy, as seen in Figure 34 and Figure 35. Dihydrogen is split at the complex and added to the second alkyne of the ligand, forming an alkene coordinated to the Rh^2 center. This step proceeds under much milder conditions compared to previous reports, where 2 bar of H_2 and 20 hours were needed to affect both hydrogenation steps. Unfortunately, no single crystals could be obtained to analyze the solid state structure of complexes [**13**] or [**13-H2**], but NMR data together with previous reports support the assignments and our assumption.[69]
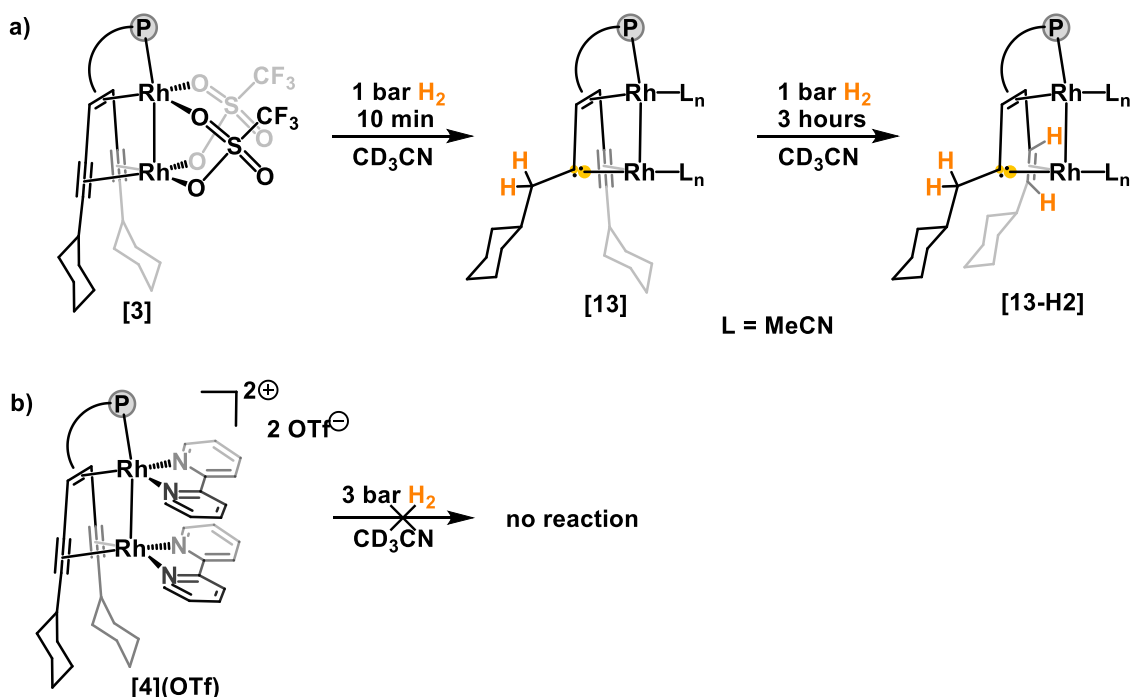
Scheme 23. a) Hydrogenation of [**3**] with H_2 in MeCN to [**13**] and [**13-H2**]; b) attempted hydrogenation of [**4**]$^{2+}$.
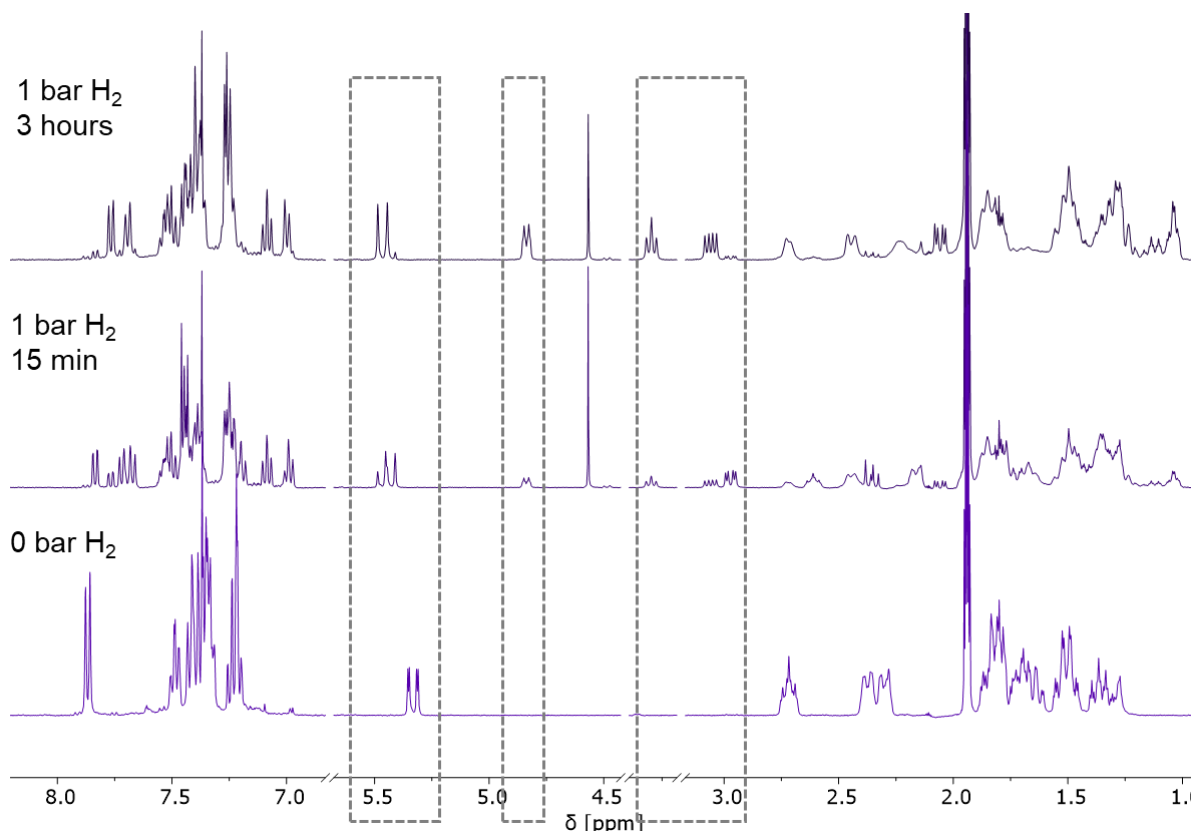
Figure 34. ^{1}H NMR spectrum overlay of complex [**3**] (bottom), 15 min after addition of 1 bar of H$_2$ gas, with mostly complex [**13**] present (middle) and after 3 hours, showing complex [**13-H2**] (top).

In contrast to complex [**3**] and previously reported complexes with similar structure,[69,70] no reaction of complex [**4**](OTf)$_2$ with dihydrogen gas could be observed, even at 3 bar and after two weeks (Scheme 23b). While the alkynes in complex [**3**] readily react with H$_2$ to form a carbene and an alkene, complex [**4**]$^{2+}$ is coordinatively saturated and stabilized by the bipyridine co-ligands. Note that the bipy ligands are strongly bound to the rhodium centers, while the labile triflate ligands are easily replaced by solvent molecules, such as MeCN and partially by THF. Furthermore, complex [**4**]$^{2+}$ is remarkably stable towards moisture and air, as it did not show any decomposition upon addition of water under aerobic conditions after 24 h. After one week, only 5% of oxidized ligand appeared in the ^{31}P NMR spectrum. This means that coordination of the P(III) to the rhodium centers prevent the phosphorus from oxidation to P(V), but very slowly, rhodium decoordination occurs upon P=O bond formation. This again reflects the robustness of complex [**4**](OTf)$_2$.
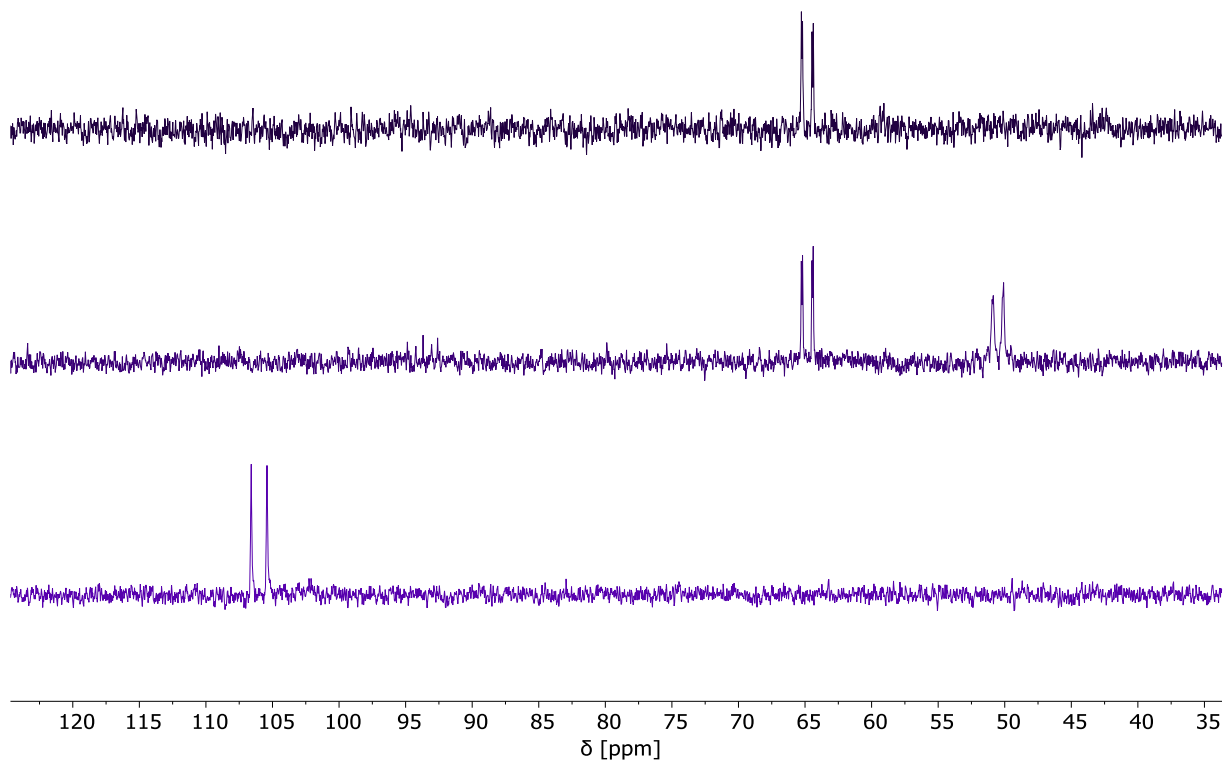
Figure 35. ^{31}P NMR spectrum overlay of complex [**3**] (bottom), 15 min after addition of 1 bar of H$_2$ gas, with mostly complex [**13**] present (middle) and after 3 hours, showing complex [**13-H2**] (top).

4.2. Catalytic semihydrogenation of alkynes

Previous reports by our group suggest the activity of dirhodium complexes in the semihydrogenation of alkynes.[131] Although, after detailed investigation, it was found that in fact rhodium nanoparticles had formed during catalysis. Preliminary data showed that molecular Rh$_2$ complexes on carbon support might be effective catalysts. Therefore, complex [**3**] was grafted onto activated carbon, by dissolving [**3**] in THF and dropwise addition to a suspension of activated carbon in THF. The mixture was stirred for one hour, then the solvent was removed in vacuo and the residue washed with hexane. After drying for 24 hours at high vacuum, [**3**]@C was obtained. Characterization was done via solid state ^{31}P NMR with magic angle spinning at 20 kHz. A broad signal around 100 ppm was obtained, proving the presence of [**3**] within the material. The spectrum is depicted in Figure 36.
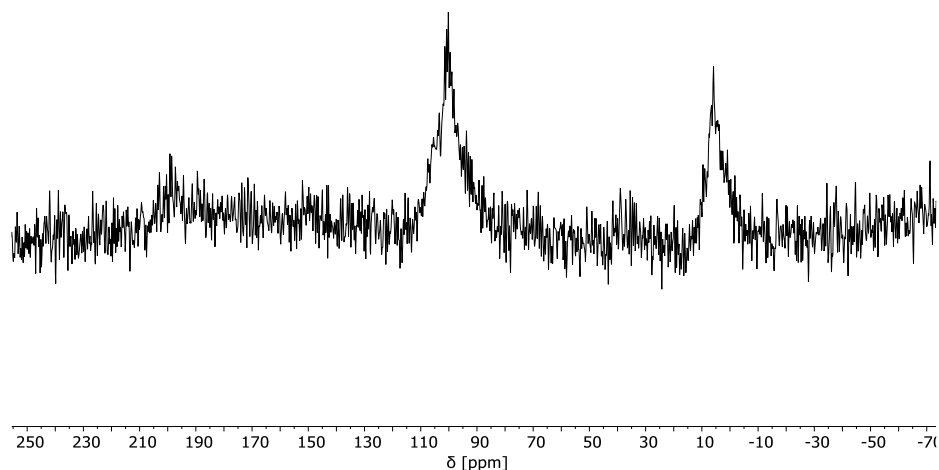
Figure 36. Solid state ^{31}P NMR of [**3**]@C.

For the semihydrogenation of alkynes, a high throughput screening machine was used, containing eight reaction vessels and automatic gas pressurizing. In each vessel, the solid catalyst was added, together with phenylacetylene (PA), dodecane as internal standard, ligand additives and toluene as solvent. The total reaction volume was 5 mL. A full factorial experiment was performed using the following levels for the input variables: catalyst loading 0.1 or 1 mol%, H_2 pressure 1 or 5 bar, dppm additive or no additive, temperature 30°C or 70°C. The conditions and results are shown in Table 7 (T = 30°C) and Table 8 (T = 70°C).

Table 7. Semihydrogenation of phenylacetylene (PA) with [**3**]@C at 30°C

Pressure [bar]	Cat loading [mol%]	Additive	PA conversion [%]	Selectivity [%]	TON (PA conv)	Carbon balance [%]
1	0.1	none	0	-	-	100
	1		1	-	-	100
5	0.1		1	-	-	100
	1		10	39	10	93
1	0.1	dppm	0	-	-	101
	1		1	-	-	101
5	0.1		0	-	-	102
	1		13	>99	13	102

Table 8. Semihydrogenation of phenylacetylene (PA) with [**3**]@C at 70°C

Pressure [bar]	Cat loading [mol%]	Additive	PA conversion [%]	Selectivity [%]	TON (PA conv)	Carbon balance [%]
1	0.1	none	9	11,7	90	92
	1		19	27,3	19	85
5	0.1		19	15,4	191	83
	1		35	44,1	34	79
1	0.1	dppm	24	13,1	236	79
	1		34	35,8	34	77
5	0.1		21	65,2	211	91
	1		95	>99	95	92

From these results, the following conclusions can be drawn: dppm as additive enhances catalytic activity and increased pressure and temperature clearly leads to a significant activity in hydrogenation. With that, almost full conversion and selectivity was reached for 70 °C, 5 bar, 1 mol% and with dppm. Although, some leaching of complex [**3**] was observed at 5 bar H_2 pressure, 1 mol% with dppm at both temperatures investigated. This was reflected by a change of color of the solution from colorless to light yellow. Therefore, the heterogeneity of the catalyst cannot be guaranteed. Furthermore, the carbon balance is often significantly below 100%, which was attributed to oligomerization of styrene. Taking all findings into account, this catalysis was not deemed promising enough to warrant further investigation.

5. Conclusion

In this Chapter, the response of a carbon framework upon treatment with base or reductants was described. The dinuclear dirhodium complex [**4**]$^{2+}$ can be seen as a homogeneous model to gain insight into possible structural changes in carbon support materials. For comparison, the corresponding mononuclear complex [**6**](OTf) was synthesized. The metal-metal bond in the presented dirhodium complexes is best described as a donor-acceptor bond, where one d^8-metal center in a trigonal pyramidal environment serves as Lewis-acidic acceptor (Rh^1) and the other in a square planar environment as Lewis-basic donor site (Rh^2).

Two distinct types of modifications of the alkyne substituents were observed upon electron transfer and deprotonation reactions. The conjugated C≡C bonds are in both cases transformed into allene-type structures, that carry one or two negative charges on a carbon atom.

The dinuclear complex [**4**]$^{2+}$ can be reduced in two consecutive electron transfer steps to neutral [**4**] (as indicated by reversible redox waves in the cyclic voltammogram) but subsequently rearranges in an into complex [**7**], which contains dibenzocyclo(undecatriene) as central part of the ligand. According to DFT calculations, this curved eleven-membered carbon cycle carries a two-fold negative charge. This indicates that in the reduction process not the metal centers – which remain Rh^I – but the carbon framework of the ligand was reduced. Oxidation of [**7**] partly re-established the central dibenzocycloheptenyl unit to which two alkynyl substituents are bound indicating that this rearrangement process is at least partially reversible. The redox non-innocent bipy ligand takes up one electron at first to form stable [**4**]$^{•+}$, and only upon addition of a second electron, both are transferred via the rhodium atoms to the trop-based ligand leading to the observed rearrangement. On the other hand, the reduction of neutral mononuclear complex [**6**] leads to dimeric [**6**]$_2$, which is obtained by C−C bond formation between two former alkynyl carbon centers and contains a conjugated octatetraene bridge between the Rh^I centers.

Stepwise deprotonation of the CH units in the cyclohexyl substituent in proximity to the Rh$^I_2$(bipy)$_2$ core of [**4**]$^{2+}$ again affect the alkynyl units, which rearrange sequentially into allenyl units to give complexes [**8**]$^+$ and [**9**].

In depth electrochemical studies were performed to gain better insight into the differences in redox properties between the presented organometallic compounds presented in this Chapter. We have found that structural changes in the carbon-based ligand have a significant influence on the redox potentials.

With dirhodium complex [**3**], bearing ligand **1** and two labile triflate ligands, it was possible to coordinate **10** to a metal center for the first time. The resulting complex [**11**]OTf shows quite distinct

properties in comparison to structurally similar complexes presented in this Chapter. However, reduction or deprotonation of [**11**]OTf did not lead to stable products.

Additionally, reactivity studies with dirhodium complexes [**3**] and [**4**](OTf)$_2$ towards dihydrogen gas were performed, where an alkynyl unit may be converted into a carbene donor unit to Rh^2. Although, none of the presented compounds from this Chapter were very active in the tested catalysis.

Further research could investigate the influence of different co-ligands on the Rh$_2$ core – for example different diamines could be tested. Non-innocent ligands, which allow for coordination in a bridging mode, could show interesting properties and might be active in the semihydrogenation of alkynes or nitrous oxide reduction.

"Hässige Chemikalien machen mehr Chemie."

STEFAN BANZ

CHAPTER III - Heterobimetallic Complexes for N$_2$O Reduction

1. Introduction - N$_2$O Reduction

The increasing concentration of greenhouse gases in the atmosphere have induced an unprecedented anthropogenic climate change. Among these, nitrogen oxides have a large impact. The widespread use of nitrogenous chemicals in agriculture, the formation of nitrogen oxide during fuel combustion and industrial processes release large quantities of nitrogen oxides into the atmosphere.[132] Nitrous oxide (N$_2$O) is a significant contributor to global warming and additionally destroys the ozone layer.[133] Its warming potential is 300-times higher than of CO$_2$ and is the main ozone depleting agent in the 21st century.[134] The formation of smog and acid rain is highly impacted by the emission of nitric oxide (NO) and nitrogen dioxide (NO$_2$) referred to as NO$_x$.[135,136] Even though the emission of greenhouse gases has to be reduced in the first place, the research on advanced technologies to degrade nitrous oxides remains of great importance due to these highly destructive environmental effects.

N$_2$O is thermodynamically unstable (ΔH_f = + 82 kJ mol^{-1}) but kinetically inert,[137] which is the main challenge for its degradation. Even though it is a weak ligand,[138] nature has developed several pathways of enzymatically converting nitrogen oxides into N$_2$ or even NH$_4^+$ (Scheme 24).[139,140] Exemplary, in an enzyme featuring a di-iron active center, NO is reduced to N$_2$O (a), which can then be converted to N$_2$ with a catalytic copper-sulfur cluster (b).
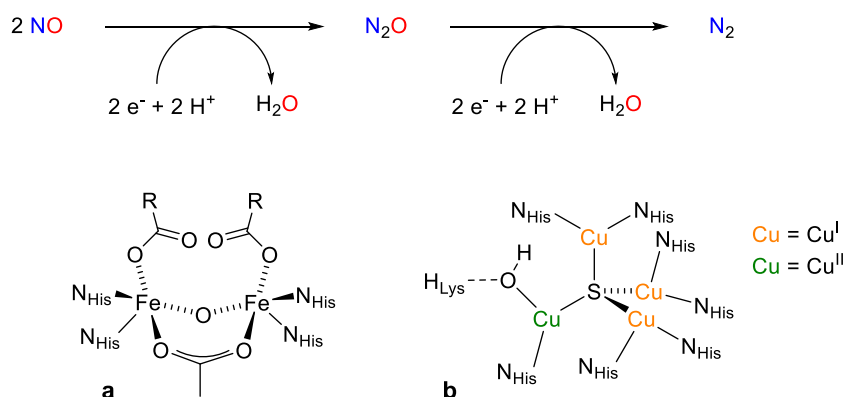
Scheme 24. Enzymatically catalyzed pathway for the reduction from NO via N$_2$O to N$_2$ with enzymes a and b.

Heterogeneous catalysts (metal surfaces, MOFs and zeolites) can decompose N$_2$O to nitrogen and oxygen under harsh conditions.[141,142] However, homogeneous catalysts have not been studied extensively although being desirable for selective structural modifications and mild reaction conditions. Additionally, such systems can also provide fundamental mechanistic information regarding N$_2$O and NO$_x$ activation and conversion.

Few homogeneous catalysts are known which reduce N$_2$O to N$_2$.[143–147] The PNP-Ru pincer complex (Scheme 25a) was reported to reduce N$_2$O into N$_2$ with H$_2$ under relatively mild conditions (65 °C, 3.5 bar each).[145] While stable NO complexes with metals from the fourth period (Sc - Cu)

are well established,[148–151] they are less common with the heavier late transitions metals. This is especially true for low valent Ru, Rh and Pt complexes which have rarely been reported.[5,152–154] A copper complex (Scheme 25b) showed to be able to reduce NO to N_2O stoichiometrically,[147] although yet no homogeneous catalyst is known to directly reduce NO to N_2.

a) N_2O + H_2 $\xrightarrow[\text{THF, 65°C, 48 h}]{\text{[cat] (0.23 mol\%)}}$ H_2O + N_2

3.5 bar   3.5 bar

[cat] = ...   P = P(^{i}Pr)$_2$

b)
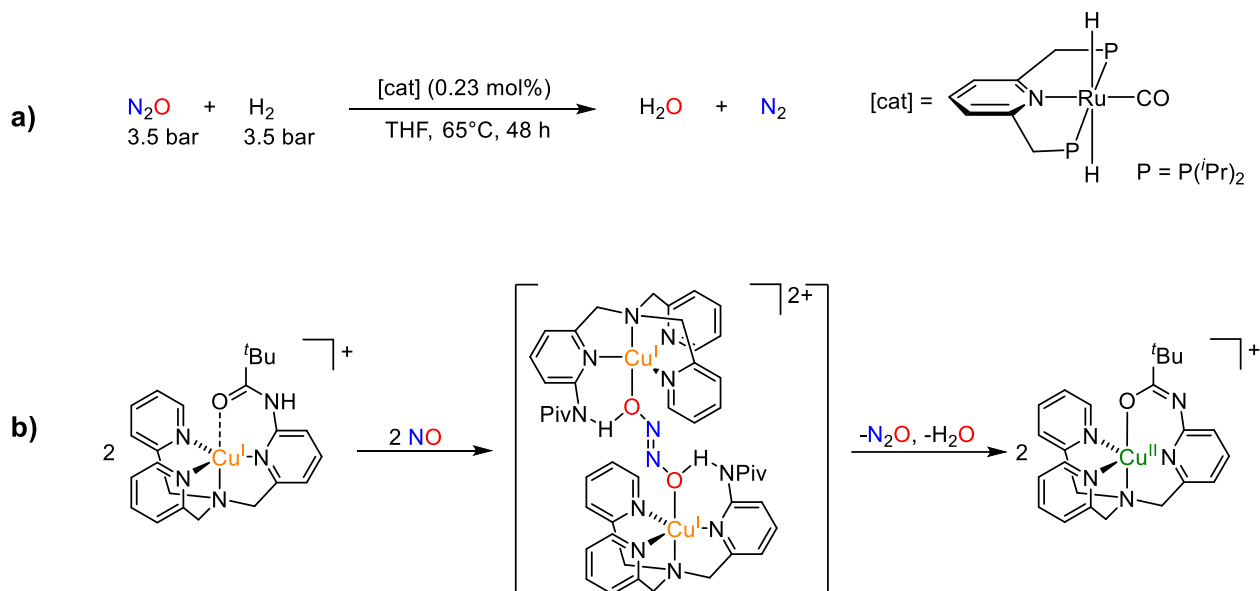
Scheme 25. a) Reduction of N₂O to N₂ catalyzed by a PNP-Ru complex; b) stoichiometric conversion of NO to N₂O promoted by a Cu complex with a dimeric transition state.

Apart from hydrogen, other reducing agents can be advantageous to obtain valuable products using N_2O as oxidizing agent while reducing N_2O to nitrogen. This was accomplished by the use of alcohols[143] (R-OH → esters, carboxylates), phosphorus-based substrates[144] (PR₃ → O=PR₃) and organosilanes[145] (R₃Si-H → R₃Si-OH and/or R₃Si-O-SiR₃) (see Scheme 26a). Furthermore, carbon monoxide has been used as reducing agent (CO → CO₂) to deplete a toxic and an environmentally harmful gas in one reaction.[146]
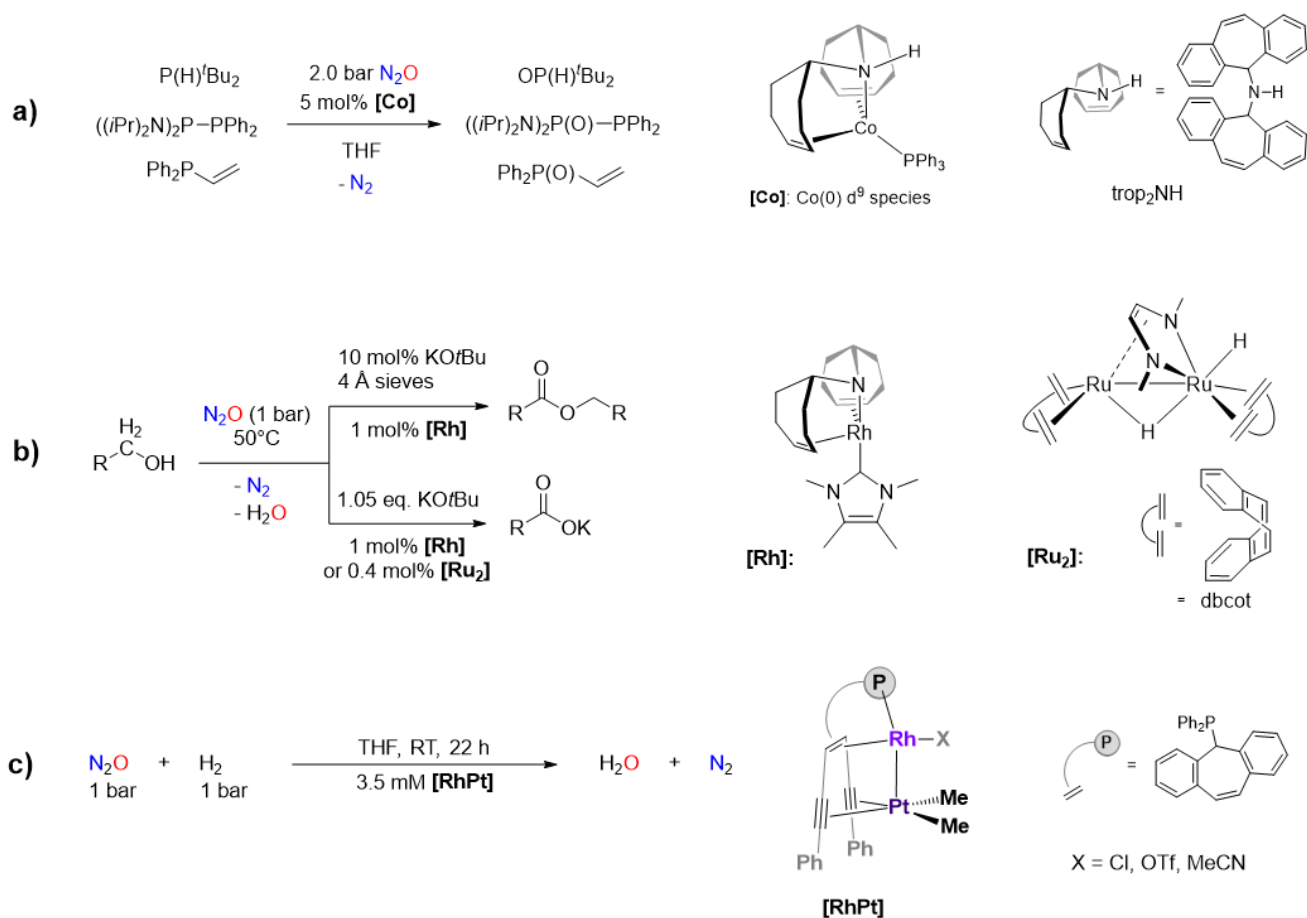
Scheme 26. Reduction of N_2O with trop-based complexes and different approaches: a) oxidation of phosphines with a trop$_2$NH-Co complex, b) oxidation of alcohols with trop$_2$N-Rh and dbcot-Ru$_2$ complexes and c) N_2O reduction by H_2 to form N_2 and H_2O with a Rh-Pt catalyst.

The Grützmacher group has recently developed bimetallic complexes for such catalytic tasks: a homobimetallic dinuclear Ru$_2$-dbcot complex (Scheme 26b) that can perform oxidation of alcohols with N_2O, and a heterobimetallic Rh-Pt complex which is very active in the homogeneous reaction of N_2O and H_2 to water and dinitrogen (Scheme 26c). This complex is able to turn N_2O into N_2 under mild conditions using dihydrogen gas as reducing agent.[70] It was shown to be more efficient than the similar mononuclear rhodium or ruthenium PNP complexes with over four-times higher conversion rate, operating under very mild conditions even at room temperature and 1 bar of gas pressure.[145] Further studies showed that this bimetallic complex [Rh-Pt] also catalyzes the hydrogenation of NO to nitrogen and water, which represents the first example of a well defined homogeneous catalyst reported for this transformation.[70] This compound contains a rather inert PtMe$_2$ fragment which likely is not involved directly as active site in the catalytic cycle, but modulates electronically the active Rh center.

The main issue with this catalytic reduction process is that NO is a strong oxidant, hence the catalyst must be robust towards oxidative degradation. The process is also pressure dependent - high pressures of N_2O or NO can increase the oxidation rate of complexes. Another requirement

is that the catalyst needs to be stable enough to withstand the formation of water as side product during the reduction of N_2O and NO_x. Often, water needs to be removed effectively from the reaction mixture to keep the reaction going, increase turn over numbers and keep the catalyst active. Since N_2O is generally a weak ligand, coordination to transition metals is a further challenging task. Note that our motivation for choosing dinuclear complexes was that nature is likewise using polynuclear complexes for the conversion of N_2O and NO_x to N_2. A naïve assumption is that at some stage of the reaction a N≡N is formed at the expense of two NO bonds and this process may be facilitated by the cooperativity of two (or more) metals in close proximity. During the preliminary mechanistic studies with the [Rh-Pt] catalyst, it was possible to isolate a hyponitrite complex from the reductive coupling of two NO molecules.[70]

Unlike in the reduction of N_2O, when converting NO to N_2, a new N−N bond needs to be formed. Therefore, we aim to create a metal-metal bond in the bimetallic complex that is short enough to facilitate formation of the new N−N bond (roughly around 2.6 Å). This means that the metals must be rather tightly connected. In our established complex, the Rh−Pt bond length is in the range of 2.64 - 2.79 Å, which presumably can be decreased by using smaller first-row transition metals.

Furthermore, it is crucial to find out whether the oxygen or the nitrogen atom of N_2O coordinates to the metal. For binding of N_2O to a transition metal center, various different coordination modes have been proposed as shown in Scheme 27.[138] Most proposed mechanisms formulate an O-terminal coordination. But very recently, a stable PNP-Rh pincer complex was reported to bind N_2O, where interestingly the terminal nitrogen atom coordinates to the metal center.[155]
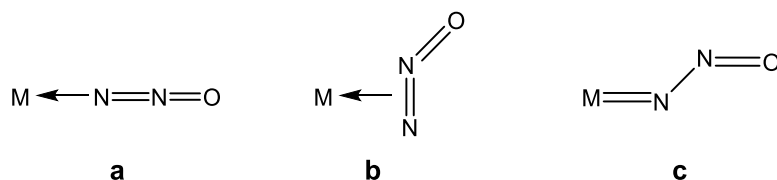
Scheme 27. N-terminal coordination modes of N_2O: a) linear, b) side-on bent and c) double bent.

2. Rhodium(I)-Platinum(II) Complexes for N₂O Reduction

2.1. Synthesis and characterization

With the aim of improving the catalytic performance of Rh−Pt complexes in the N₂O reduction, the previously employed trop-based ligand was modified: the electron-deficient phenyl groups at the alkyne substituents were replaced with electron-rich cyclohexyl groups. The synthesis of this (CyC≡C)₂tropPPh₂ ligand **1** was described in Chapter II. Apart from the electronic properties, the hybridization was changed from sp² in the phenyl substituent to a substituent with a sp³ hybridized C̲−C≡C atom in the fully saturated cyclohexyl group. At this stage we assume that there is no influence of this residue in the presented chemical reactions of this Chapter. With this ligand **1**, a series of Rh−Pt complexes could be synthesized, starting from the chloride bridged rhodium precursor [**5**], which was already described in Chapter II. The preparation of the new complexes [**14**], [**15**] and [**16**]BArF was adapted from published straightforward procedures.[70]
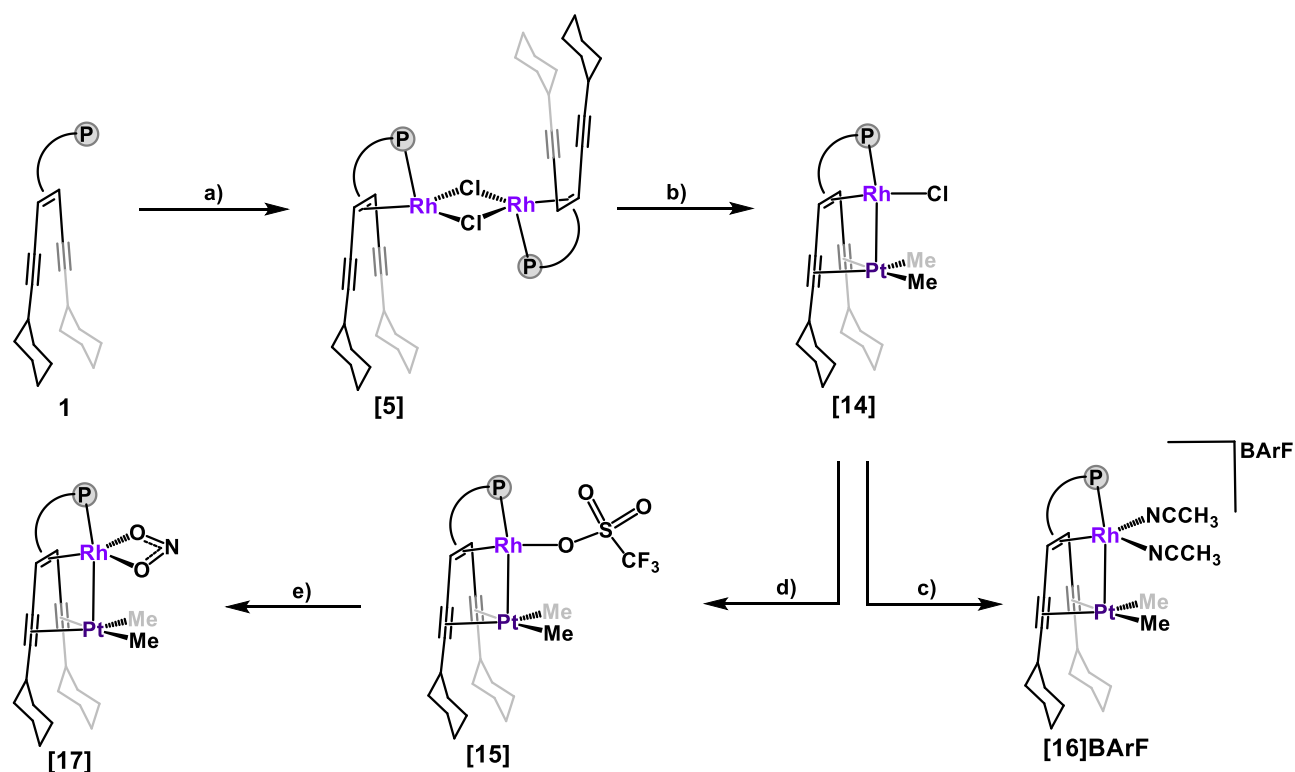
Scheme 28. Synthesis of Rh−Pt complexes [**14**] - [**17**]. Conditions: a) 0.5 eq. Rh₂(μ-Cl)₂(C₂H₄)₄, benzene; b) 0.95 eq. [PtMe₂(SMe₂)]₂, DCM; c) 1 eq. NaBArF, DCM / MeCN; d) 1 eq. AgOTf, THF; e) 1 eq. NaNO₂, THF/MeOH.

Complexes [**14**], [**15**], [**16**]⁺ and [**17**] were synthesized according to Scheme 28. The platinum center was introduced by reacting complex [**5**] with [PtMe₂(SMe₂)]₂ to first form heterobimetallic complex [**14**]. Hereby the coordination of a platinum center to the C≡C triple bonds was accomplished and a metal-metal bond was formed. The chloride ligand in complex [**14**] could be abstracted using silver(I) triflate to form complex [**15**] that contains a triflate ligand at the rhodium center. Furthermore, the chloride could also be replaced by acetonitrile to form complex [**16**]BArF,

where a cationic compound could be obtained with the weakly coordinating BArF anion and solvent molecules coordinating to Rh. When [**15**] is treated with $NaNO_2$ in MeOH/THF, the triflate ligand is replaced by NO_2^- which coordinates as κ^2-O ligand with both oxygen atoms symmetrically bound to the rhodium center, leading to the nitrite complex [**17**].

The complexes were characterized by multinuclear NMR spectroscopic studies, in particular [103]Rh and [195]Pt NMR spectroscopy. Since [103]Rh has a natural abundance of 100% and is an NMR active spin ½ nucleus, the coupling to the ^{31}P shows a doublet. Platinum-195 has a spin ½ nucleus with a natural abundance of 33.8% leading to characteristic coupling patterns: the interaction between ^{31}P and [195]Pt is visible as satellite peaks with characteristic intensity around each peak of the doublet, corresponding to the natural abundances of nuclei. Overall, the ^{31}P NMR spectra appear as an overlay of a doublet with satellites of a doublet of doublets. For representative coupling patterns of NMR spectra of complex [**15**] see Figure 37.
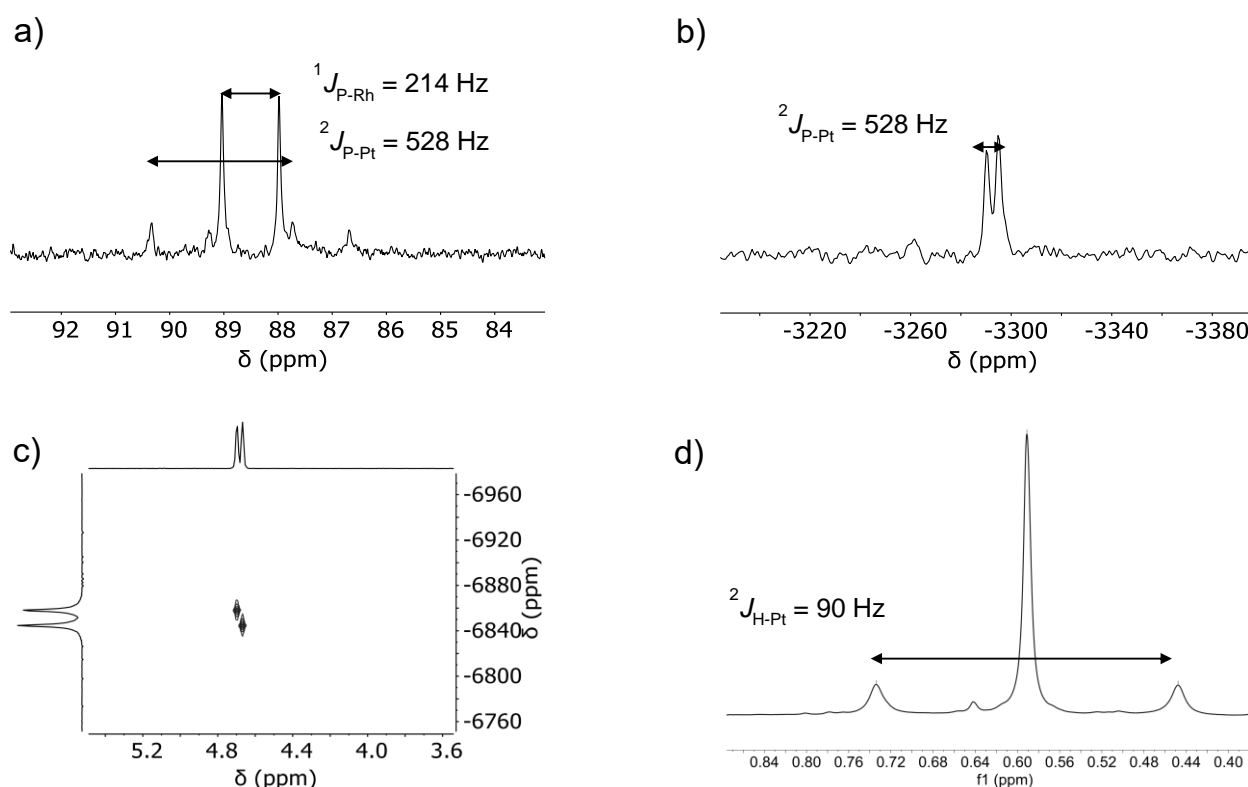
Figure 37. a) ^{31}P NMR spectrum of [**15**] with coupling pattern of rhodium and platinum to phosphorus ($^1J_{PRh}$ and $^2J_{PPt}$); b) [195]Pt NMR spectrum of [**15**]; c) ^{1}H-[103]Rh HMBC of [**15**]; d) part of the ^{1}H NMR spectrum showing the Me groups with Pt satellites.

Heterobimetallic complexes [**14**] - [**16**]⁺, were fully characterized by NMR spectroscopy in solution and selected data are listed in Table 9, where some trends can be observed which mostly result from the type of substituent at the rhodium center. As already described in Chapter II, the ^{31}P NMR chemical shifts show significantly high-frequency shifted resonances in the metal complexes compared to the free ligand **1** ($\delta^{31}P$ = -14.0 ppm) which range from 112.9 ppm for mononuclear

[**5**] to 88.4 – 89.9 ppm for bimetallic [**14**] - [**16**]⁺. Coupling of the phosphorus nucleus to [103]Rh leads to a doublet, and coupling to [195]Pt leads to a doublet of doublets (around 1/3 intensity) which is overlayed with the simple doublet resulting from NMR inactive Pt isotopes (depicted in Figure 37a). $^1J_{\text{P-Rh}}$ decreases from [**14**] to [**16**]⁺ (267.8 to 198.1 Hz) indicating a decrease in P-Rh interaction upon coordination of a Pt metal center and going from strong electron donors (chloride) to weaker donors (triflate and acetonitrile). The $^2J_{\text{P-Pt}}$ was found to increase from 527.5 to 528.0 to 529.3 ppm for [**14**], [**15**], [**16**]⁺, respectively. $^2J_{\text{H-P}}$ increases in the order [**5**] < [**14**] < [**15**] < [**16**]⁺ while $^3J_{\text{H-Rh}}$ decreases, again indicating a decrease in P-Rh interaction and an increase of electron donation by the ligand at the rhodium center.

The [103]Rh NMR shifts were determined indirectly by ^{1}H-[103]Rh HMBC NMR experiment and the spectra of [**15**] are shown in Figure 37c together with a [195]Pt NMR (Figure 37b) which was measured as a 1D experiment. No regular trends could be observed within this series. The chemical shifts of Rh in complexes [**14**] - [**16**]⁺ range from -7406 to -6851 ppm [vs. Rh(acac)₃] and correspond well to literature values.[69,112,113] For [195]Pt NMR, shifts of -3292 and -3234 ppm were observed, which are rather similar as expected as no change in directly bound ligands was conducted. The methyl ligands coordinated to the platinum center show distinct resonances between 1.46 - 1.16 ppm with satellites at one third intensity due to the [195]Pt nucleus at $^2J_{\text{H-Pt}}$ ~90 Hz. This is not to be confused with a "real" triplet which would have different intensities and arise from a very distinct chemical environment.

Table 9. Selected chemical shifts [ppm] and coupling constants [Hz] of complexes [**5**], [**14**] - [**16**]⁺.

	[**5**]	[**14**]	[**15**]	[**16**]⁺
[31]P	112.87	88.35	88.47	89.91
[103]Rh	-7406	-7087	-6851	-7329
[195]Pt	-	-	-3292	-3234
^{1}H(Me)	-	1.46	1.42	1.16
$^1J_{\text{P-Rh}}$	267.8	217.9	213.7	198.1
$^2J_{\text{P-Pt}}$	-	517.5	528.0	529.3
$^2J_{\text{H-Pt}}$	-	91.7	89.8	-
$^2J_{\text{H-P}}$	13.6	14.4	14.6	15.2
$^3J_{\text{H-Rh}}$	3.2	2.6	2.8	2.4

Single crystals of complexes [**14**] - [**17**] were obtained and analyzed by means of single crystal X-ray measurements, selected bond lengths are listed in Table 10. Images of the obtained solid state structures are shown in Figure 38. Distances for the Rh−Pt bond range from 2.76 to 2.71 Å, which is similar to previously reported bond lengths for related complexes. DFT calculations

suggest a dative metal-metal bond where the (otherwise square planar) platinum center donates electron density into the rhodium center. The Rh metal resides in a T-shaped coordination sphere in the mono rhodium complex and upon formation of the Rh−Pt bond, a square planar environment is observed for Rh. It is assumed that the same bonding situation is present in the complex series described in this Chapter. Although, when ligand **1** is used (bearing cyclohexyl groups), coordination to two acetonitrile molecules is observed in complex [**16**]BArF, which is in contrast to only one coordinated solvent molecule for the reported complex bearing phenyl groups.[70]

Table 10. Selected bond lengths [Å] of complexes [**5**], [**14**] - [**17**].

	[**5**]	[**14**]	[**15**]	[**16**]BArF	[**17**]
P−Rh	2.1716(4)	2.1865(14)	2.1975(14)	2.245(2)	2.1852(13)
Rh−Pt	-	2.7575(5)	2.7086(4)	2.7618(6)	2.7500(4)
C1−C2	1.466(3)	1.471(7)	1.477(7)	1.51(1)	1.494(6)
Rh−ct$_{(C1-C2)}$	2.01939(15)	1.9650(4)	1.9536(3)	1.9493(5)	1.9262(4)
Rh−L	2.3617(5)	2.3232(14)	2.111(3)	2.137(7) 2.168(7)	2.227(4) 2.233(4)
C3−C4	1.196(3)	1.211(8)	1.207(8)	1.217(11)	1.212(7)
Pt−ct$_{(C3-C4)}$	-	2.2430(2)	2.26132(18)	2.2147(3)	2.24444(16)
Pt−ct$_{(C6-C7)}$	-	2.2184(3)	2.2284(3)	2.2747(2)	2.21487(19)

Rh−Pt bond lengths are in the range of 2.750 - 2.762 Å for complexes [**14**], [**16**]BArF and [**17**], but are significantly shorter in [**15**] (2.709 Å). This might be explained by the electron withdrawing properties of the triflate coordinated to Rh in [**15**] which renders the Rh center less electron rich and thus more electron density can be donated from Pt into Rh. In comparison to monometallic [**5**], the Rh−ct distances are shortened in [**14**] - [**17**] (from 2.019 Å to Rh−ct$_{(C1-C2)}$ 1.926 – 1.965 Å), while the olefinic C1=C2 bond is elongated from 1.466 Å in [**5**] to 1.471 - 1.51 Å in bimetallic complexes. This demonstrates a stronger rhodium olefin bond, which results from electron donation of Pt to Rh, rendering the Rh center more electron rich, thus enhancing π-backdonation. Noteworthy is also the change in C3−C4 bond distance, which corresponds to the alkyne carbon atoms: the bond length in [**5**] (where no coordination of alkynes has taken place) elongates from 1.196 Å to 1.207 - 2.17 Å in bimetallic [**14**] - [**17**].
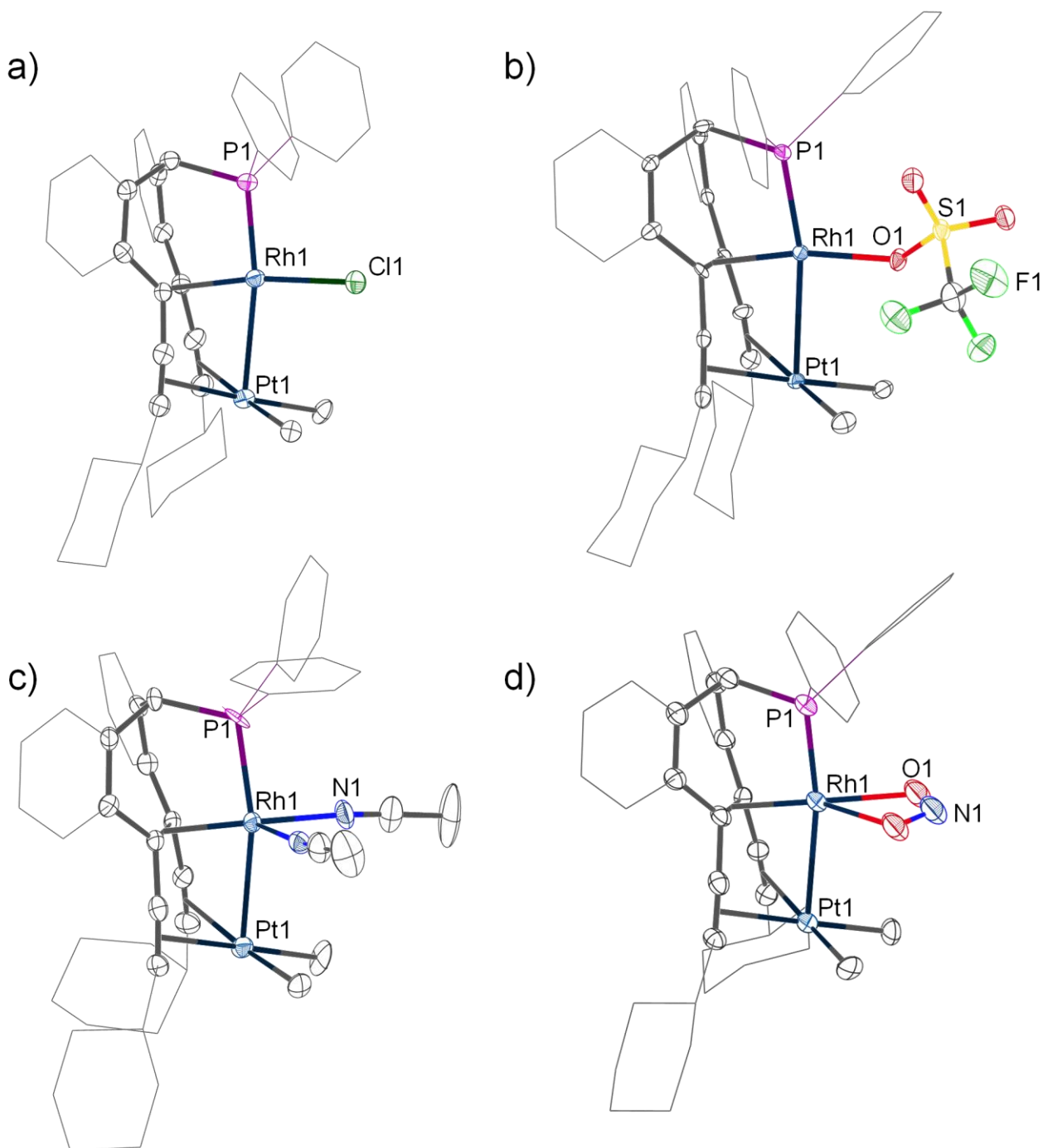
Figure 38. Solid state structures of Rh−Pt complexes [**14**] (a), [**15**] (b), [**16**]BArF (c) and [**17**] (d). Counter ions, solvent molecules and hydrogen atoms omitted for clarity.

2.2. Catalytic experiments for N₂O decomposition

Since some Rh−Pt complexes already showed very high activity in the catalytic reaction of N₂O with H₂, catalytic experiments were performed with the new complexes described in this Chapter. Therefore, the same catalytic conditions were employed: 3.5 mM catalyst was dissolved in 2 mL THF and treated with 1 bar of N₂O and 1 bar of H₂ and stirred for 22 h at room temperature. All catalyses were performed in a 100 mL J-Young Schlenk flask, the solution was subjected to three freeze-pump-thaw cycles before adding N₂O, which was dried over a column of P₂O₅. Then, the

gas was liquified by dipping the flask into liquid nitrogen before adding H$_2$ gas. Turn over numbers (TON) were determined via ^{1}H NMR spectroscopy from the integral of formed water which was referenced with an internal standard (mesitylene).

$$N_2O \quad + \quad H_2 \xrightarrow[\text{3.5 mM catalyst}]{\text{THF, RT, 22 h}} H_2O \quad + \quad N_2$$
$$\text{1 bar} \qquad \text{1 bar}$$
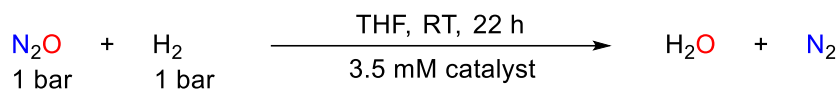
Scheme 29. General reaction scheme of nitrous oxide decomposition with dihydrogen to water and dinitrogen.

Analysis of the reaction mixtures catalyzed by complexes [**14**] - [**17**] indicated the absence of water or only show traces. ^{31}P NMR spectroscopic analysis of the catalyst revealed the complexes decomposed under the catalytic conditions. To get some insight on the reason for the unsuccessful catalysis, complexes [**14**] or [**15**] were treated with 2 bar of H$_2$ in MeCN or DCM and stirred for 24 h at room temperature. It was found that the complex decomposed under hydrogen atmosphere, as seen by the metallic mirror formed and disappearance of the ^{31}P signal in recorded NMR spectra. The dihydrogen presumably reacted with the triple bond creating a carbene and possibly an alkene, which would coincide with previous reports (see Scheme 30). We suspect de-coordination of the platinum center after the hydrogenation of the alkynes, leading to the decomposition of the complex. Note that the dirhodium complex described in Chapter II shows the same reactivity but forms a stable compound bearing a bridging carbene and an alkene (Scheme 30a). This reaction proceeds at lower gas pressure and much faster rates than previously described dirhodium complexes bearing TMS groups (Scheme 30b). This means that the new ligand **1** is hydrogenated more rapidly in comparison to complexes with other (RC≡C)$_2$tropPPh$_2$ ligands (R = Ph, TMS). Indeed, the phenyl substituted Rh−Pt complexes were stable under H$_2$ atmosphere (no reaction takes place in coordinating solvents such as MeCN or THF) and only showed hydrogenation of the organic ligand scaffold under harsh conditions (only in non-coordinating DCM) (Scheme 30d). In contrast, the complexes [**14**] - [**17**] described in this work might react too readily with H$_2$ and give unstable species. Therefore, no further experiments were performed involving dihydrogen gas.
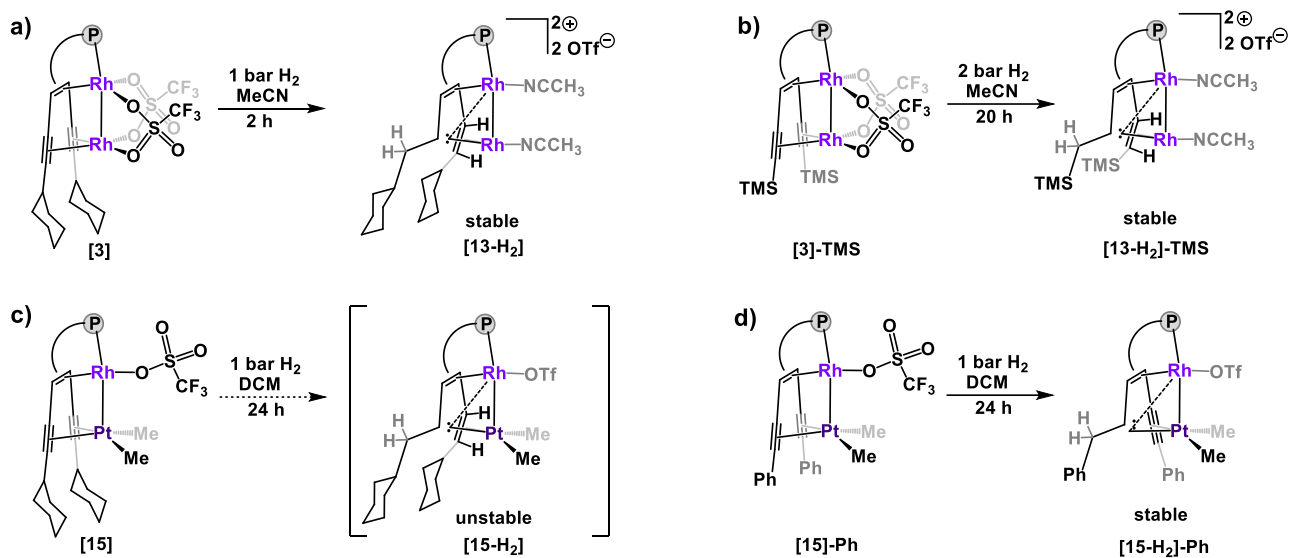
Scheme 30. Reaction of bimetallic Rh-Pt complexes with H$_2$ gas. a) Complex [**3**] forming a stable product [**13-H2**] ; b) complex [**3**]-TMS forming a stable product [**13-H2**]-TMS; c) complex [**15**] showing decomposition with possible intermediate [**15**]; d) complex [**15**]-Ph forming a stable product [**15**]-Ph under harsh conditions.

3. Rhodium(I)-Copper(I) Complexes

3.1. Synthesis and characterization

After the exploration of d^8-d^8 transition metal complexes, the investigation of to d^8-d^{10} bimetallic complexes is described in this section, an overview of the synthesis of rhodium-copper complexes is given in Scheme 31.
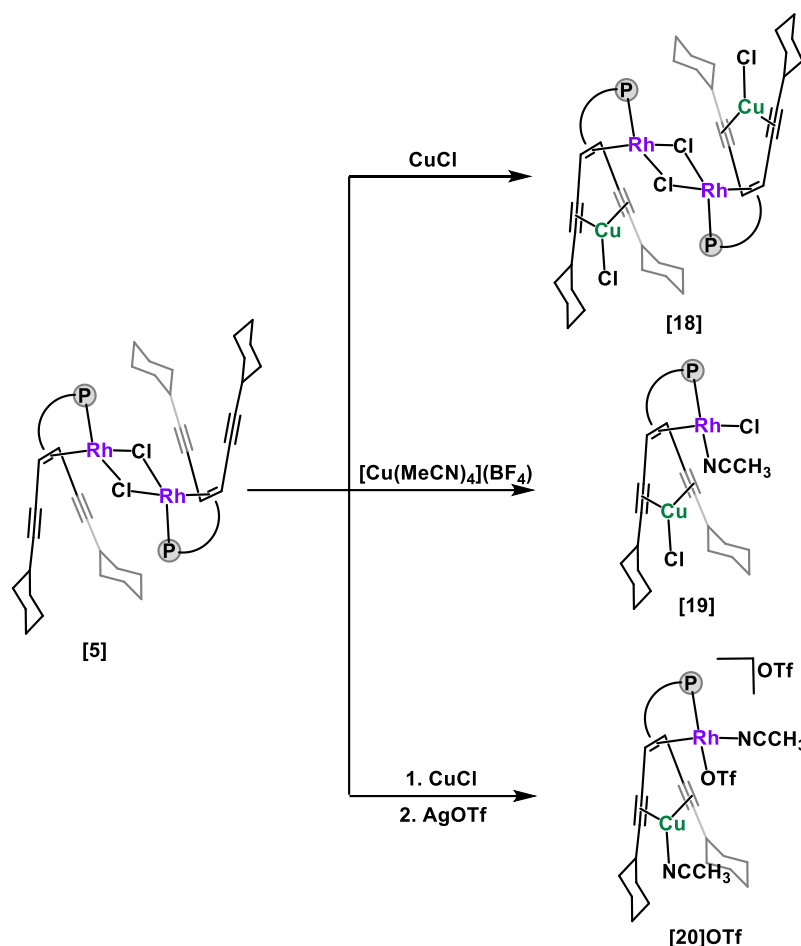
Scheme 31. Synthesis of Rh-Cu complexes [18] - [20]OTf starting from mono rhodium complex [5].

The simplest reaction is the combination of mono rhodium complex [5] with solid CuCl, which was heated to 70°C in THF to enhance solubility of the copper precursor. Red-orange single crystals of [18] were obtained upon slowly cooling to room temperature and the structure determination by XRD methods showed the retention of the central dinuclear $Rh_2(\mu_2\text{-}Cl_2)$ core as seen in [5]. Interestingly, the copper ions coordinate in a different fashion than the described Rh or Pt metals, which is also illustrated in Figure 39. Here, the Cu atom coordinates in a plane with the alkynes, similar to long known copper alkyne complexes. This leads to a trigonal planar environment around the metal center with the chloride ligand (Figure 39a). The "out-of-plane" coordination of Rh-Pt and Rh_2 complexes is depicted in Figure 39b. Due to the large metal-metal distance of around 3.8 Å resulting from this coordination mode, no direct interaction between Rh and Cu centers is possible.

In a second experiment, [Cu(MeCN)$_4$](BF$_4$) was used as a precursor to introduce a copper ion. In this case, complex [**19**] was obtained. XRD analysis with a single crystal showed that the Cu atom is again bound in a "pincer" fashion to the two alkynyl units of the ligand. The coordination sphere around the Cu$^+$ ion is completed by a chlorido ligand, which results again in a trigonal planar coordination sphere. NMR spectroscopy indicates that [**19**] is the only product, which can be detected. This leads to the assumption that the excess chloride must either come from another molecule of complex [**5**], which subsequently decomposes, or that larger amounts of CuCl are present as contamination in the commercially obtained copper precursor. A distorted square planar coordination sphere is observed for rhodium, which thereby achieves a formal electron count of 16 e$^-$ due to bound MeCN.

Chloride abstraction of [**18**] leads to MeCN and OTf substituted complex [**20**]. In this compound, the copper atom is again coordinated in plane with the alkyne moieties and binds an additional MeCN ligand. The rhodium center still shows the same coordination sphere as previously described Rh-Cu complexes, with a triflate and a MeCN bound to the metal. Although, [**20**] is a cationic species with another triflate as counter anion.
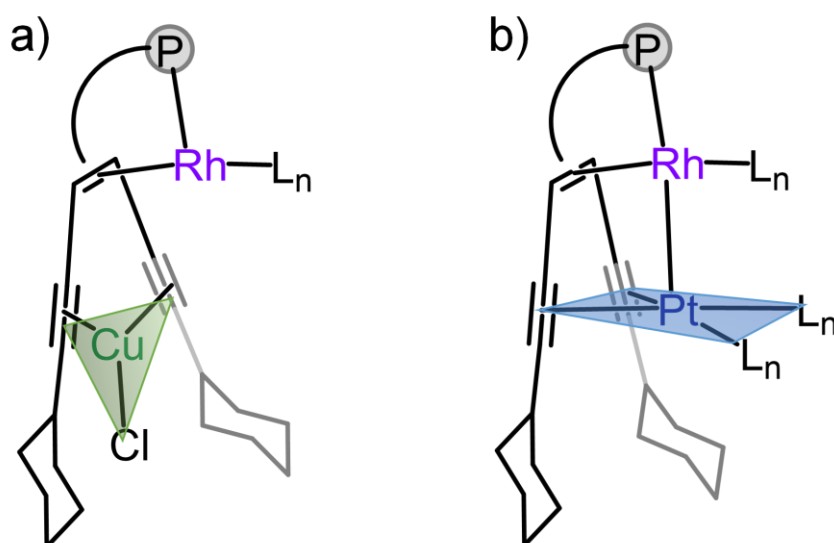
Figure 39. Coordination modes of the alkyne groups on two examples. a) Metal and alkynes in plane (for Cu), M−M bond not possible; b) metal-alkyne bonds perpendicular to alkyne-alkyne plane (for Rh, Pt) with M−M bond formation.

Single crystals of [**18**] - [**20**]OTf were subjected to XRD analysis which allowed for structural analysis. Selected bond lengths are listed in Table 11. Within the hetero bimetallic complexes, the alkyne C≡C distances, as well as alkene C=C and Cu−ct distances all lay in the same range along the series. Upon coordination of copper metal, the C≡C bonds of the alkyne units are elongated due to π-backdonation when compared to mono rhodium complex [**5**] or the free ligand **1**. The elongation of C3−C4 and C6−C7 triple bonds spans from 1.195 Å (uncoordinated) to 1.218 – 1.231 Å for Cu coordinated alkynes. Furthermore, Rh−N$_{MeCN}$ bond lengths differ significantly

between [**19**] and [**20**]: In [**19**] MeCN is bound axially leading to a rather long bond (2.148 Å), while being in equatorial position in [**20**] leading to a bond shortening to 2.071 Å. In summary, the three Rh^{I}Cu^I complexes presented here show rather distinct coordination spheres, but still show similar key bond distances.

Table 11. Selected bond lengths [Å] of complexes [**5**] and [**18**] - [**20**]OTf.

	[**5**]	[**18**]	[**19**]	[**20**]OTf
P–Rh	2.1716(4)	2.1762(6)	2.1892(8)	2.1787(7)
C1–C2	1.466(3)	1.467(4)	1.466(4)	1.467(3)
Rh–ct$_{(C1–C2)}$	2.01939(15)	2.01107(13)	2.02980(8)	2.01096(16)
Rh–L	2.3617(5)[a]	2.3734(6)[a] 2.5031(6)[a]	2.3368(8)[a] 2.148(3)[b]	2.3194(19)[c] 2.071(2)[b]
C3–C4	1.196(3)	1.221(4)	1.225(4)	1.228(4)
C6–C7	1.195(3)	1.221(4)	1.218(4)	1.231(4)
Cu–ct$_{(C3–C4)}$	-	2.0047(4)	1.99285(4)	1.9959(3)
Cu–ct$_{(C6–C7)}$	-	1.9842(4)	2.01219(4)	1.9843(3)
Cu–L	-	2.1931(7)[a]	2.1849(9)[a]	1.907(2)[b]

[a] L = Cl, [b] L = MeCN, [c] L = OTf
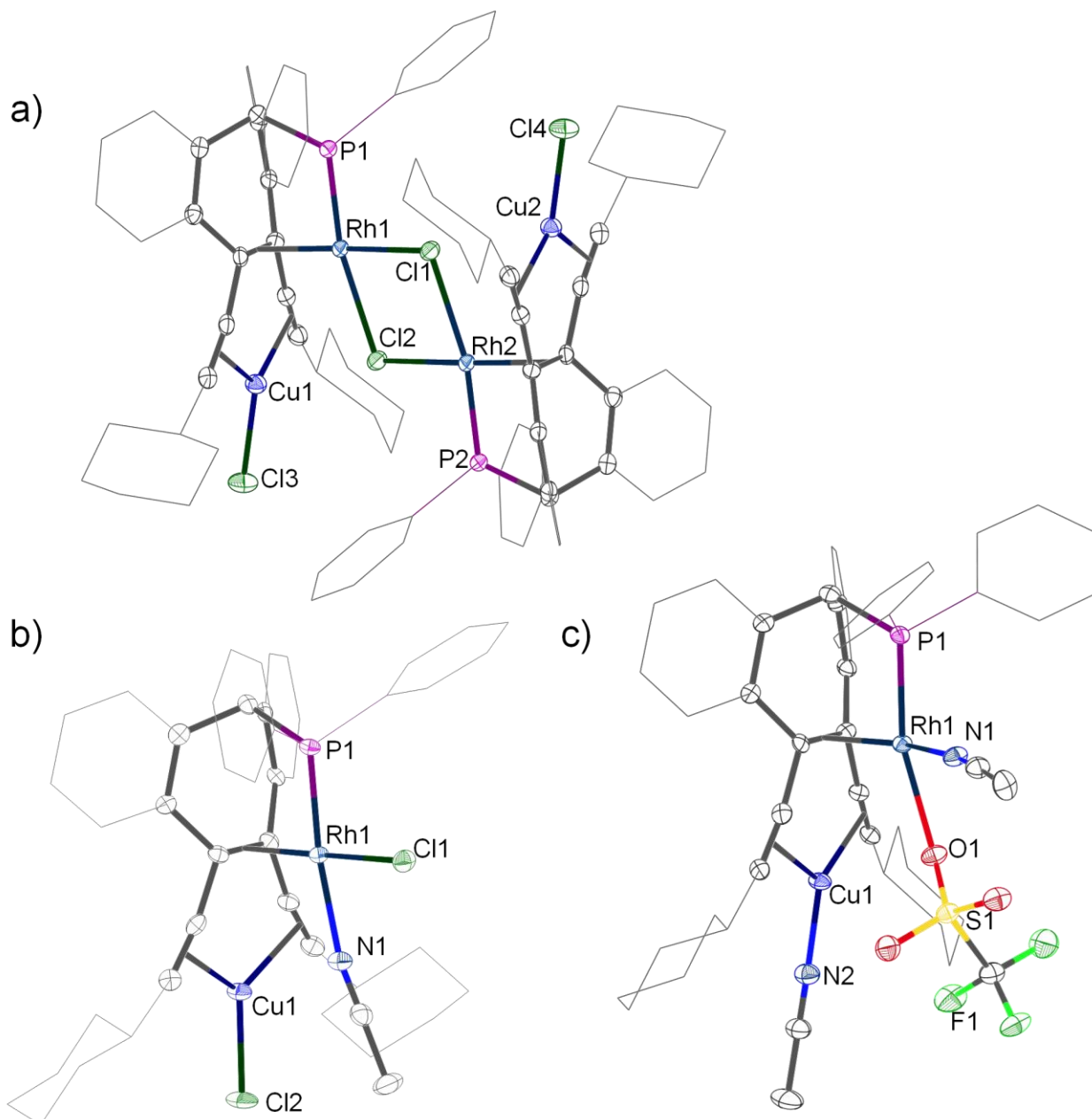
Figure 40. Solid state structures of Rh-Cu complexes [**18**] (a), [**19**] (b), and [**20**]OTf (c). Counter ions, solvent molecules and hydrogen atoms omitted for clarity.

Due to the large metal-metal distance of around 3.8 Å resulting from the described coordination mode, no direct interaction between Rh and Cu centers is possible. Although, ^{31}P NMR spectroscopy shows significant influence on the chemical shifts: the coordination of a copper atom lowers the ^{31}P shift around 12 ppm as well as the $^1J_{\text{P-Rh}}$ coupling which is lowered around 52 Hz.

Deshielding of the ^{31}P upon coordination of a second metal to the alkynes was already observed with other metals (see Chapters II and III.2). Here, the ^{31}P resonance shifts 7 - 14 ppm compared to [**5**], while the coupling constants decrease significantly from [**5**] to [**18**] - [**20**]⁺ (see Table 12). The shift is most pronounced for complex [**20**] with $^1J_{\text{P-Rh}}$ = 182.5 Hz in comparison to $^1J_{\text{P-Rh}}$ =

267.8 Hz in [**5**]. Note that direct comparison between [**5**] and [**19**] or [**20**]⁺ is difficult because of the different ancillary ligands at the Rh center.

Table 12. Selected chemical shifts [ppm] and coupling constants [Hz] of complexes [**5**] and [**18**] - [**20**]OTf.

	[**5**]	[**18**]	[**19**]	[**20**]OTf
^{31}P	112.87	100.48	98.46	105.61
$^{1}J_{\text{P-Rh}}$	267.8	215.0	201.2	182.5
$^{2}J_{\text{H-P}}$	13.6	13.4	14.6	-

3.2. Further Rh-Cu complexes

In an attempt to avoid the chlorides and MeCN ligands in heterobimetallic Rh-Cu complexes, the chloride of [**5**] was first abstracted with AgOTf and was then reacted with a (CuOTf)₂·toluene complex as precursor. The reaction mixture turned red and an ^{31}P NMR shift of 105.6 ppm was observed as a doublet with a coupling constant of 183 Hz. Orange single crystals of [**21**] suitable for XRD measurements showed an unexpected dimerization of Rh-Cu containing fragments (shown in Figure 41): to one Rh-Cu-trop complex a Rh-trop fragment is added, where the alkynes are coordinated to the Rh center of the first fragment. While in the earlier described compounds, the Cu atom is coordinated to both alkyne groups in a plane, here it is out of the plane and only coordinated to one alkyne moiety. The three metals present are in a triangular plane, where all are coordinated to a central oxygen atom. Furthermore, a triflate is bridging the Cu atom with the Rh atom of the added Trop-Rh fragment. Although this complex is interesting by itself, its formation remains unclear.
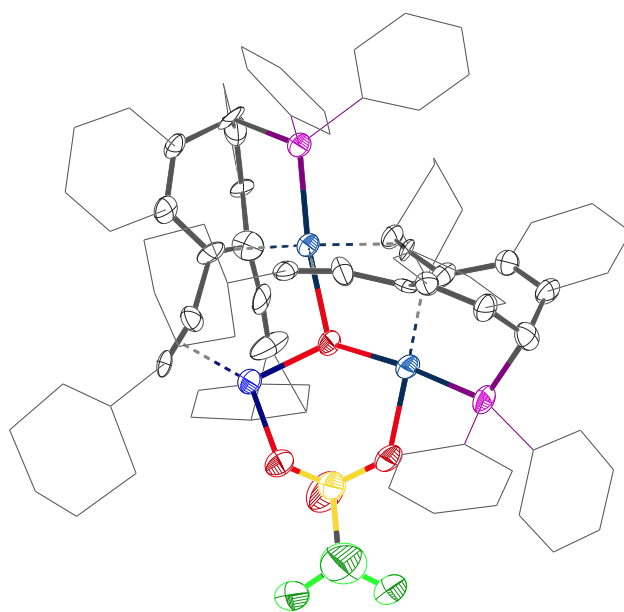
Figure 41. Solid state structure of [**21**]. Counter ions, solvent molecules and hydrogen atoms are omitted for clarity.

4. Replacing phosphorus by nitrogen in alkyne complexes

4.1. Motivation for N-donor atoms in trop ligands

All bimetallic complexes described until now featured a phosphorus donor atom covalently bonded at the benzylic position of the trop moiety. Here, variation of the donor atom will be described by the incorporation of amines instead of phosphines. Many trop-amine ligands have already been prepared by our group[156,157] and have been successfully applied for the reduction of N₂O.[143,144] The most successful catalysts were trop₂NH rhodium and cobalt complexes – see Chapter III.1 and Scheme 32a. Therefore, we sought to combine the advantages of this very stable and active bistropamine based catalyst with the possibility to coordinate a second metal atom, similar to previously described Rh−Pt complexes. Since phosphorus in its oxidation state +III can be oxidized by nitrous gases (even when coordinated to a metal) we wanted to create a ligand less prone to oxidation at the donor group in benzylic position. Therefore, an alkyne substituted bistropamine ligand and its bimetallic complexes were envisioned, a general structure is depicted in Scheme 32b.

L = PPh₃, OTf, MeCN, Cl

trop₂NH

R = Ph, cy

M = Rh, Co, Ir, Pt, Ni...
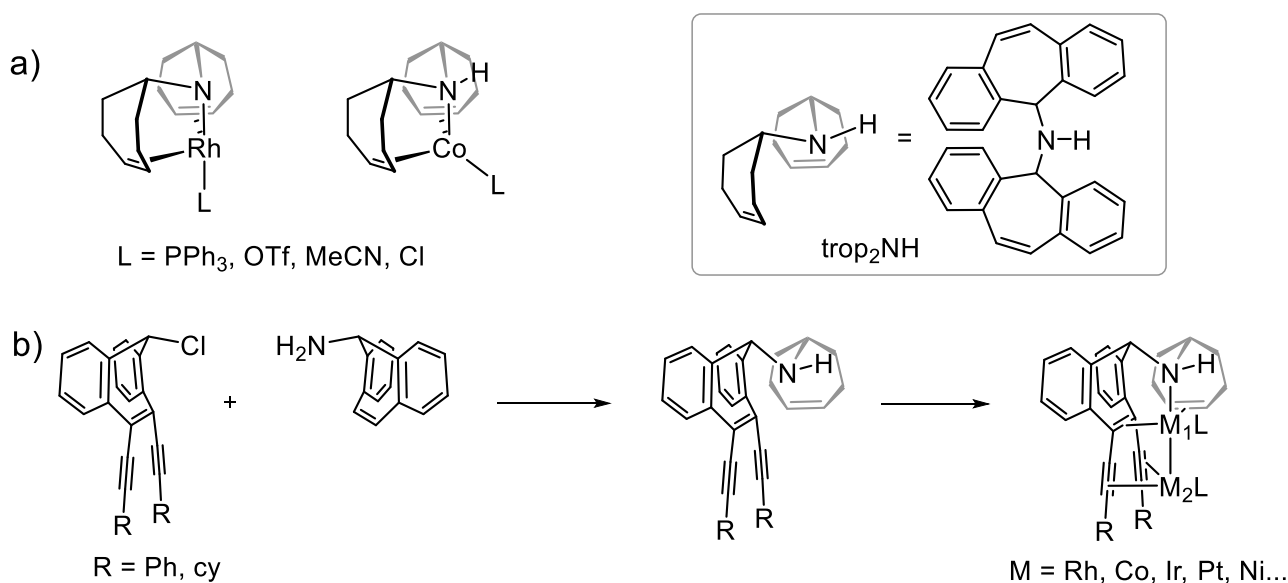
Scheme 32. a) Established trop₂NH complexes from our group;[156,157] b) synthesis of extended bimetallic framework.

4.2. Synthesis and characterization of alkyne-substituted bistropamine ligands

The synthetic route from the well-known trop₂NH was modified, since asymmetric substitution was required. Two ligands were prepared, **22a** (R = Ph) and **22b** (R = Cy), where **a** means phenyl substituted and **b** stands for the cyclohexyl substituted compounds. In order to synthesize ligands **22a** and **22b**, (RC≡C)₂tropCl and tropNH₂ were heated in toluene in the presence of CuI as a catalyst and Et₃N as a base (Scheme 33). The synthesis of (CyC≡C)₂tropCl has already been described earlier in this thesis. After aqueous Na₂CO₃ solution was added, the copper catalyst and inorganic salts were removed by extraction and phase-separation. Drying the organic phase and recrystallization from a DCM hexane mixture led to the desired ligands **22a** and **22b**.

a)

b)
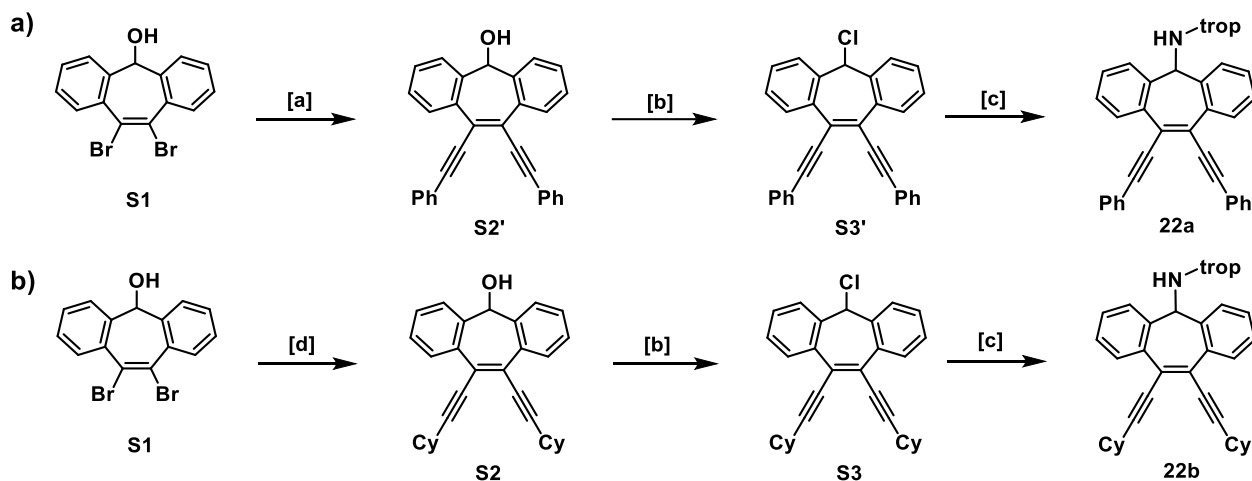
Scheme 33. Synthesis of alkyne-substituted bistropamine ligands: a) **22a** (R = Ph) and b) **22b** (R = Cy). Conditions: [a] PhC≡CH, 5 mol% [Pd(PPh₃)₄], 5 mol% CuI, Et₃N/toluene, 70°C; [b] SOCl₂, DCM, 0°C; [c] 1.) TropNH₂, 5 mol% CuI, Et₃N/toluene, 80°C, 2.) Na₂CO₃(aq); [d] CyC≡CH, 5 mol% [Pd(PPh₃)₄], 5 mol% CuI, Et₃N/toluene, 70°C.

NMR spectroscopic analysis of the ligands **22a** and **22b** in solution reveal the presence of three conformers. While four conformers would be theoretically possible (endo/endo, endo/exo, exo/endo and exo/exo), one is likely not observed due to steric hindrance. In the ¹H NMR spectrum three sets of peaks are visible, the most indicative resonances result from the benzylic protons and the NH group. The assignments were further supported by 2D NMR spectra. From the *J*-coupling - which strongly depends on the dihedral angle between the protons - information can be obtained about the angles between the vicinal protons[158] which allowed assignments of conformers.
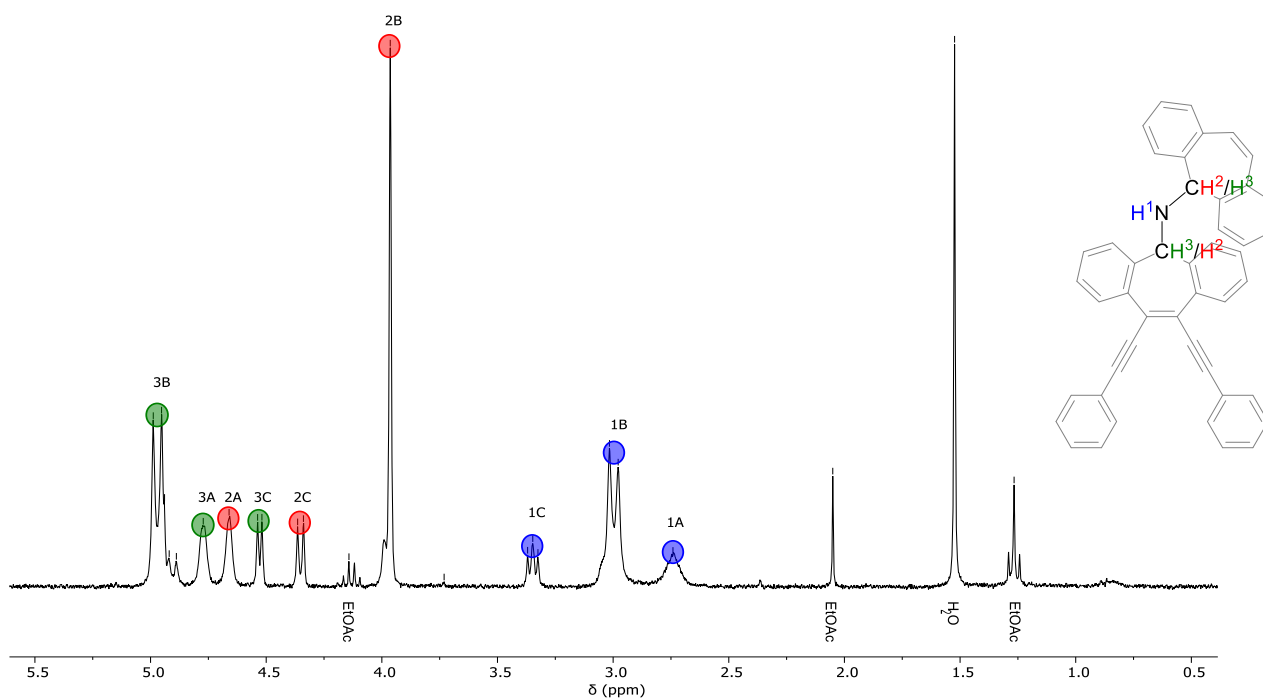
Figure 6. Selected region of ¹H NMR spectrum of ligand **22a** in CDCl₃. Insert: Proton assignment at the ligand.

The spatial orientation of the protons is the main reason for the difference in chemical shift and splitting patterns. In conformer A, the amine proton does not show strong coupling with any other protons, as all three peaks are (broad) singlets. In conformer B, the amine proton couples with one of the neighboring CH protons, resulting in two doublets and one singlet. And in conformer C the amine proton couples with both neighboring CH protons, which is reflected in a pattern of a triplet, doublet and doublet. Conformer B is the predominant species (62 %), followed by conformer A (23 %) and finally conformer C (15 %). Even though only one conformer is able to coordinate a metal center with both trop moieties, it has been established that reorientation proceeds upon coordination to a metal atom due to the possibility of the seven membered trop ring to flip over. With that, the presented ligands should show a collapse of the three sets of protons to only one single set of protons upon coordination. This endo-endo conformation might be the energetically favored one, leading to tridentate metal complexation.

4.3. Synthesis and characterization of monorhodium bistropamine complexes

To study the coordination chemistry to rhodium of the compounds **22a** and **22b**, the ligands were reacted with [Rh(COD)$_2$]X precursors (where X = BF$_4$, OTf or BArF). The reaction mixtures were stirred at 60°C for 24 h in either MeCN or toluene, as depicted in Scheme 34. If the reaction is performed in coordinating solvents such as acetonitrile, the trop-ligands coordinate in a tridentate fashion with two additional solvent molecules bound to the Rh center. In order to prevent the coordination of acetonitrile, toluene was used as solvent during the complexation reaction. Under these conditions, only one COD ligand from the precursor is replaced by the olefin moiety of a trop-ligand. The obtained complexes show coordination to the N-donor atom and the unsubstituted trop olefin double bond, while the alkyne substituted trop moiety faces away from the metal center.
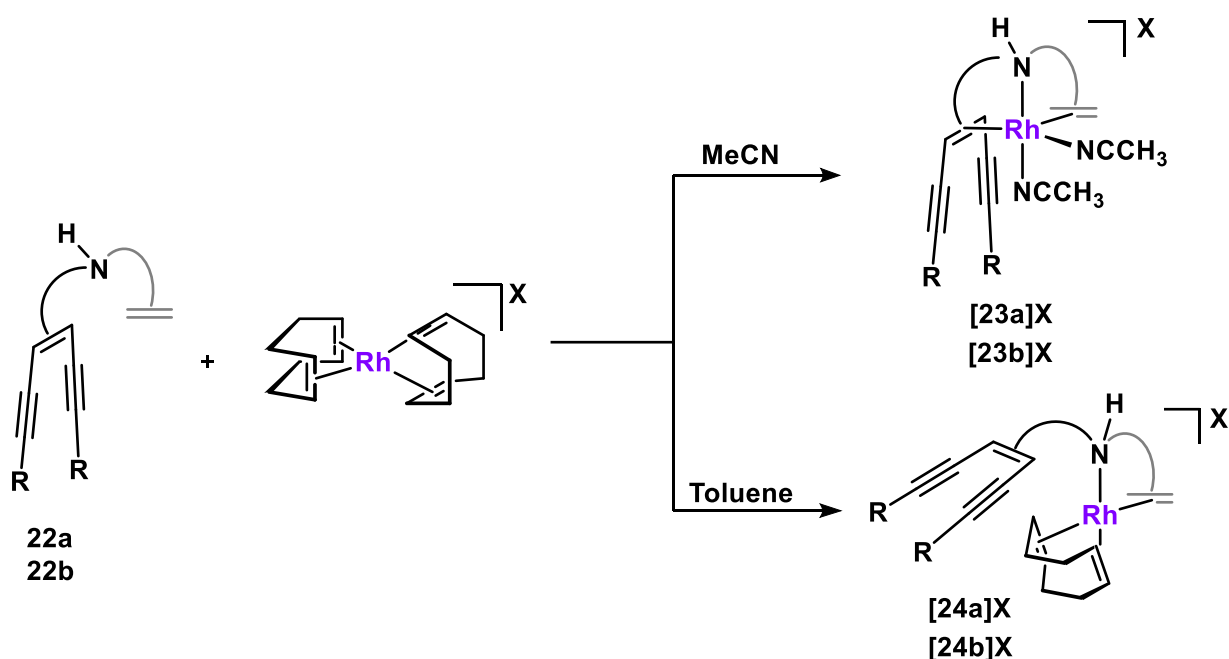
Scheme 34. Synthesis of rhodium complexes [**23a**]⁺X⁻, [**23b**]⁺X⁻ and [**24a**]⁺X⁻, [**24b**]⁺X⁻ with ligands **22a** and **22b** under different reaction conditions. R = Ph (in compounds a), R = Cy (in compounds b), X = BF₄, OTf, BArF.

Single crystals of complex [**23a**]BF₄ were obtained by slow diffusion of hexane into a solution of DCM and subjected to XRD measurements. The solid state structure reveals a distorted trigonal bipyramidal coordination sphere around the rhodium center. The distortion in the plane angles is a result of the steric rigidity of the bistropamine ligand. The solid state structure of [**23a**]BF₄ is illustrated in Figure 42a. Two molecules of MeCN are bound to rhodium, the equatorial Rh1−N2 (2.204 Å) bond is much longer than the axial Rh1−N3 bond (2.021 Å). This difference can be explained by the "trans influence" of the coordinated olefins or nitrogen donor atom. The extent of trans influence grows with π-acceptor and σ-donor ability. Since olefines are strong π-acceptors, they have a large trans influence, which weakens the Rh1−N2 bond trans to it. The π-back bonding or accepting effect is also manifested in the elongation of the C3−C4 and C5−C6 alkene bonds. Here, the rhodium atom donates some of its electron density into the π* orbital of the alkenes, which leads to an elongation of the C=C bonds and Rh1−ct$_{(C3−C4)}$ / Rh1−ct$_{(C5−C6)}$ bonds in the range of 2.06 Å, which is rather short for a rhodium carbon bond.
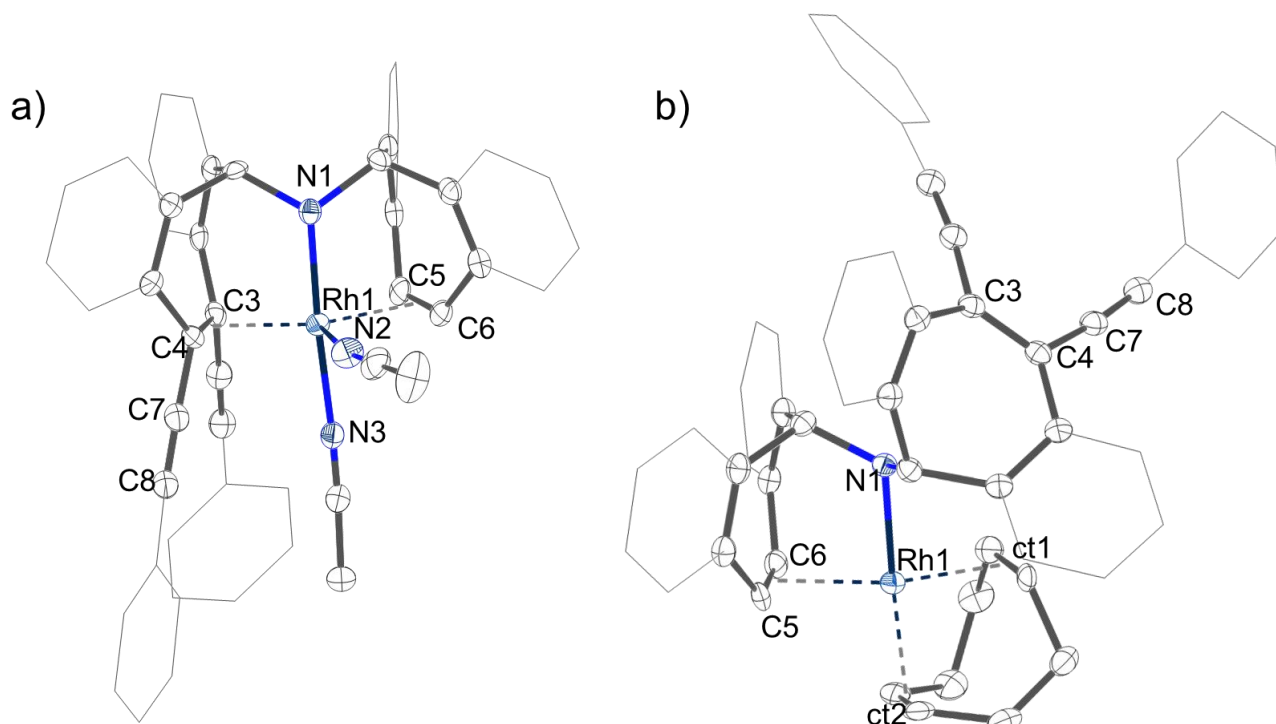
Figure 42. Solid state structures of a) cationic complex [**23a**]BF₄ and b) complex [**24a**]BArF, with 50 % probability ellipsoids. Counterions, solvent molecules and hydrogen atoms are omitted for clarity.

When the solvent in the reaction of ligand and precursor is changed from MeCN to non-coordinating toluene, complex [**24a**]⁺ is obtained. The solid state structure of [**24a**]BArF is illustrated in Figure 42b. This compound shows large structural differences: the substituted trop fragment is not coordinated and is rotated outward, while one COD ligand stays coordinated to Rh. Due to steric hinderance of the ligands in complex [**24a**]⁺, the rhodium center resides in a square planar coordination environment, which is in contrast to the trigonal bipyramid in complex [**23a**]⁺. Selected bond lengths of complexes **[23a]BF4** and **[24a]BArF** are listed in Table 13.

Table 13. Selected bond lengths [Å] of complexes **[23a]BF4** and **[24a]BArF**.

	[**23a**]BF₄	[**24a**]BArF
Rh1−N1	2.064	2.170
Rh1−L1	2.204 [a]	2.099 [b]
Rh1−L2	2.021 [a]	2.070 [b]
Rh1−ct(C3−C4)	2.061	-
Rh1−ct(C5−C6)	2.059	2.084
C3−C4	1.468	1.380
C5−C6	1.412	1.403
C7−C8	1.237	1.208
C9−C10	1.194	1.203

[a] L = NCCH₃, [b] L = COD (Rh1−ct distance).

NMR spectroscopic analysis of the complexes in solution showed the expected simplification of resonances from different conformers upon coordination of the metal, which comes from merging to one single conformer. An exemplary ^{1}H NMR spectrum of complex [**23a**]BF$_4$ is depicted in Figure 43. Resonances appear as doublets for the olefinic CH (orange, 4), singlets for the benzylic trop protons (green, 3) and a singlet for NH (red, 2) in addition to the aromatic region. Furthermore, the peaks at 1.74 ppm and 1.95 ppm can be assigned to the methyl groups of the two acetonitrile ligands (blue, 1). The two methyl groups are not identical, which is due to the different position within the complex – while one MeCN ligand is bound axially, the other one is bound in the equatorial plane of the trigonal bipyramid. This results in a difference of the electronic distribution throughout the acetonitrile ligand and therefore a difference in the chemical shift.
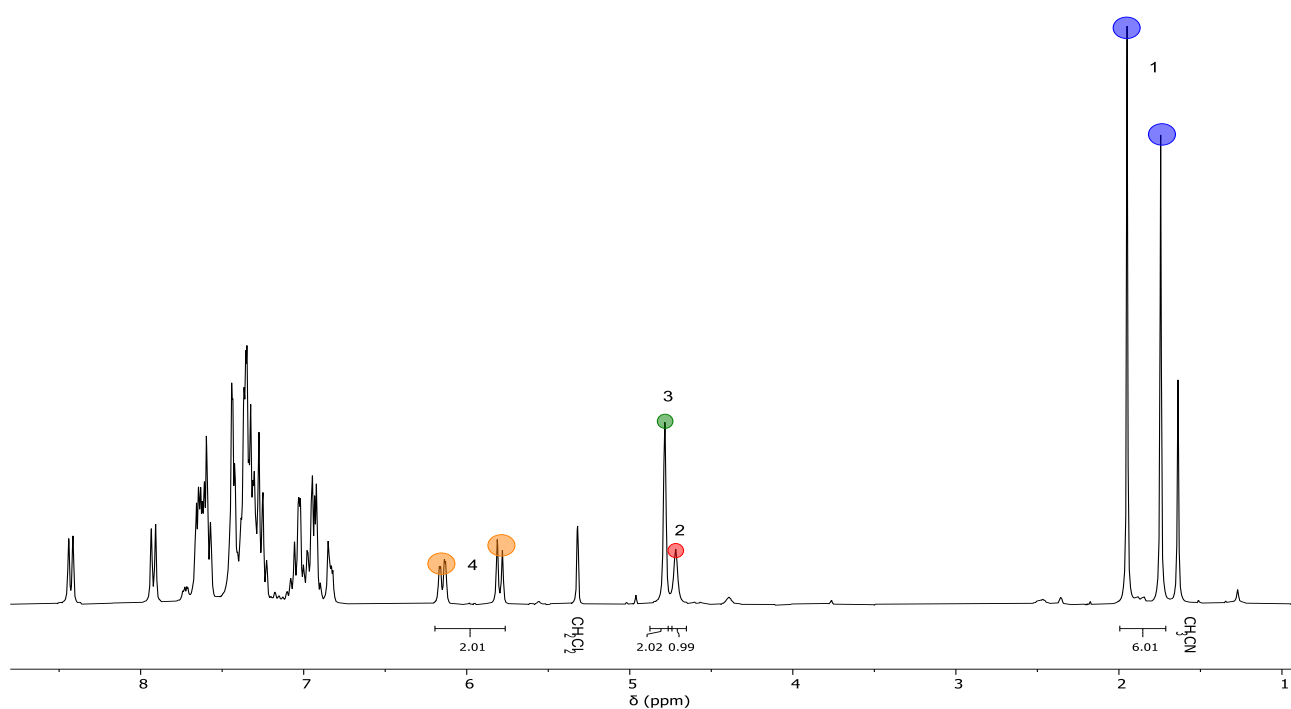
Figure 43. ^{1}H NMR spectrum of complex [**23a**]BF$_4$ in CD$_2$Cl$_2$ with assignments as described in the main text.

4.4. Attempts to synthesize bimetallic Rh−M complexes

Complexes [**23a**]⁺, [**23b**]⁺, [**24a**]⁺ and [**24b**]⁺ were subjected to different metal precursors in an attempt to create a hetero-bimetallic complex by coordinating the alkyne groups. None of the employed Pt^{II}, Co^{I}, Co^{0} or Ni^{0} precursors lead to coordination of a second metal center, and in most cases to decomposition of the reactants occurred. The main reason for this inability to coordinate another metal center was assumed to lay in the nature of the co-ligands in the rhodium complexes described above. While the MeCN ligands appear to be too strongly bound to the Rh to be cleaved off easily, if a COD co-ligand is present, the substituted trop based ligand is not aligned in the right conformation yet. This probably leads to a high activation barrier, because the conformation has to be changed at the same time as de-coordinating the COD ligand and formation of metal to alkyne bonds. Although many attempts were made to avoid this

inaccessibility of the second coordination site, the employed [Rh(COD)$_2$]X complexes were found to be the only type of Rh precursor which does not show decomposition of ligands **22a** and **22b** upon reaction.

Complex [**24a**]BArF was pressurized with CO gas to substitute the COD ligand by two CO ligands, hoping that this would enable coordination of a second metal center. When CO pressure of 1 bar was applied, the solution changed its colour from red orange to yellow, indicating that some reaction had taken place, see Scheme 35. An ATIR spectrum of the residue strongly suggests that a terminal carbonyl ligand is present (2061.62 cm^{-1}). Unfortunately, no single crystals could be obtained that would have allowed for structure determination.
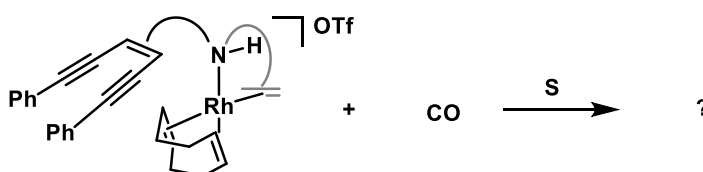
Scheme 35. Reaction of complex [**24a**]BArF with 1 bar CO with S = THF-d$_8$ or toluene-d$_8$.

4.5. Synthesis and characterization of copper(I) bistropamine complexes

The reaction of the commercially available [Cu(MeCN)$_4$](BF$_4$) with ligand **22a** in THF led to the formation of an unexpected structural motif: The N−C$_{trop}$ bond was cleaved, while the (PhC≡C)$_2$tropNH$^-$ fragment coordinated a copper atom at the N-donor. Additionally, the copper atom coordinates to the alkyne groups of a second ligand. This leads to the dimeric structure [**25**](BF$_4$)$_2$, as depicted in Scheme 36. The solid state structure obtained by XRD methods with single crystals is shown in Figure 44a. If the same reaction is conducted in DCM as solvent, complex [**26**]BF$_4$ was obtained, where ligand **22a** remains intact. Again, the alkyne substituted trop olefin does not coordinate to the metal center, as observed in rhodium complexes [**24a**]$^+$. The solid state structure of [**26**]BF$_4$ is shown in Figure 44b. The copper resides in a tetrahedral coordination sphere consisting of the N-donor, one olefin and two MeCN ligands. The bond cleavage observed with THF is likely attributed to some hydrolysis caused by traces of water in the solvent. Since the ligand itself is water stable, the hydrolysis is probably catalyzed by the copper ions present.
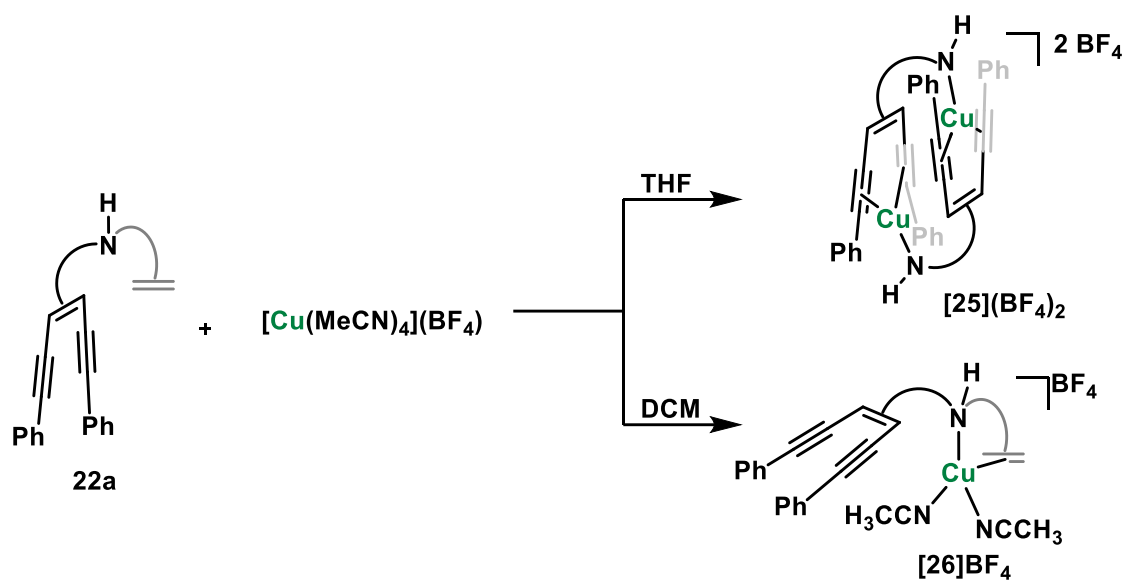
Scheme 36. Reaction of [Cu(ACN)₄](BF₄) with **22a** in THF to form dimeric [**25**](BF₄)₂ and in DCM to form [**26**]BF₄.
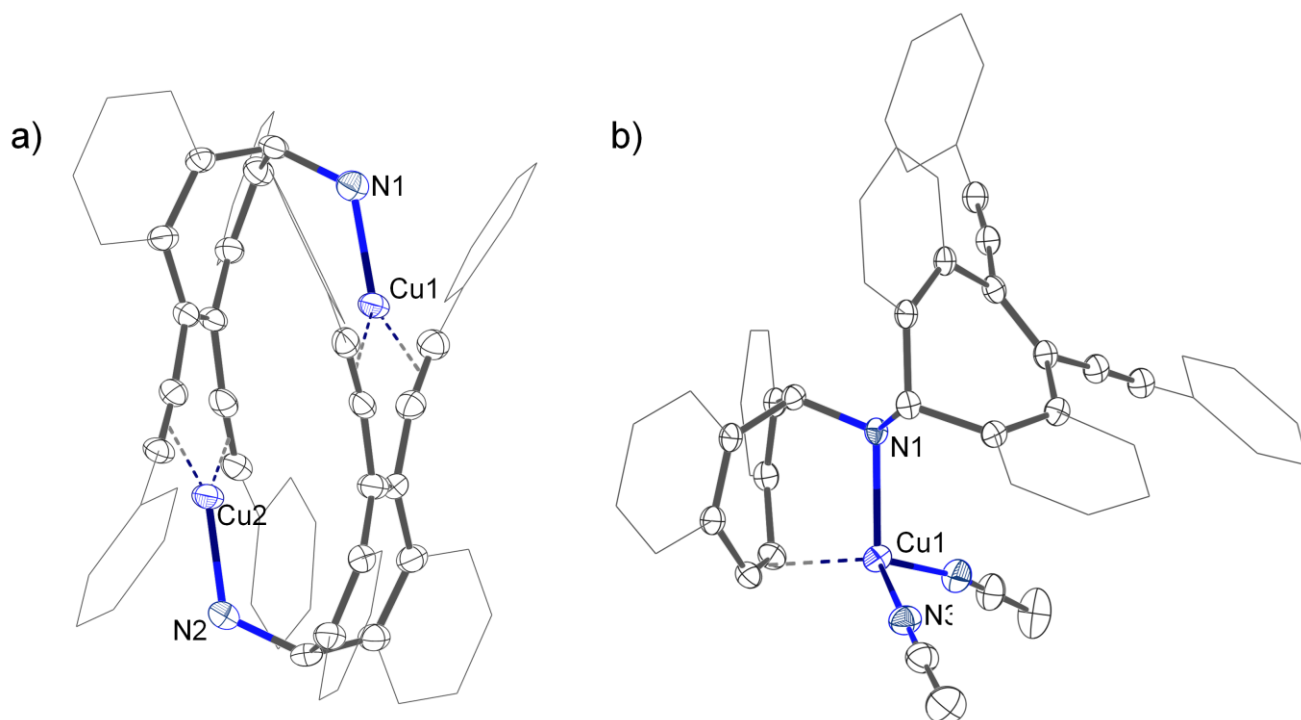
Figure 44. Solid state structure of [**25**](BF₄)₂ (a) and [**26**]BF₄ (b). Counterions and hydrogen atoms omitted for clarity.

5. Conclusion and outlook

5.1. Rhodium-Platinum complexes

Four new heterobimetallic Rh^I-Pt^{II} complexes bearing ligand **1** were synthesized and investigated that showed structural similarity to a complex that proved to be an active NO$_x$ hydrogenation catalyst. The new complexes ([**14**] - [**17**]) were characterized by NMR and XRD methods. The NMR spectra were used to identify characteristic coupling patterns as well as the effect of the different ligands at the rhodium center on the coupling constants, where some trends could be observed. N$_2$O and/or H$_2$ reactions with complexes [**14**] and [**15**] were performed, where the decomposition of complexes with dihydrogen prevented further catalytic exploration. The new complexes show slightly different electronic properties due to the exchange of phenyl substituents for cyclohexyl groups, rendering the coordinating alkynes more electron rich. This property is assumed to be the reason for the higher reactivity towards H$_2$, which is so pronounced that the new Rh-Pt complexes are unstable under a hydrogen atmosphere at the catalytic conditions. Therefore, the planned catalytic experiments for the reduction of N$_2$O could not be performed successfully.

To circumvent this problem, different modifications in the ligand sphere were envisioned to improve catalytic activity, either by changing the substituents at the alkynes or modifying the additional ligands on the platinum center. The latter might be achievable by the use of a different precursor in the synthesis (e.g. [Pt$_2$(μ-SMe$_2$)$_2$Ph$_4$]). The stability of the complex could be improved by using for example isopropyl as a substituent at the alkyne ligands. Cyclohexyl is a σ-donor, which can be deduced from the Hammett parameter $\sigma_{m, cyclohexyl}$ = -0.05[159] and therefore the complex has a more electron rich triple bond. We propose that the carbene formed after the hydrogenation may be too reactive, leading to the decomposition of the complex. A substituent with a slightly higher Hammett value could be used to reduce the reactivity of the carbene. Isopropyl has a sp^3 hybridized carbon with a Hammett parameter of $\sigma_{m, isopropyl}$ = -0.04 and triphenylmethane has a sp^3 hybridized quaternary carbon with a Hammett parameter of $\sigma_{m, triphenylmethane}$ = -0.01 and could be explored as substituents for future research. [159]

Other reactions, such as esterification, or carboxylation reactions from primary alcohols under basic conditions by dehydrogenative coupling reactions with N$_2$O as the hydrogen acceptor could be explored, as done by Thomas L. Gianetti.[143] Furthermore, complex [**17**] with its nitrite ligand is oxidatively stable and could give insights into catalytic mechanisms involving nitrous oxides.

5.2. Rhodium-Copper complexes

Another way to improve catalytic activity in N$_2$O reduction could be the exchange of the Pt^{II} center for another metal, which was shown in the second part of this Chapter, where Rh^I-Cu^I complexes were investigated. The change from a d^8 (Pt^{II} or Rh^I) to a d^{10} metal center (Cu^I) lead to a new coordination mode of the alkynes, where no metal-metal bond was observed. All presented complexes show the copper atom coordinated in a trigonal planar environment between both alkynes and an additional co-ligand such as chloride, OTf or MeCN.

The reaction of these heterobimetallic complexes with sources of N$_2$O or NO$_2^-$ was envisioned to lead to structures depicted in Scheme 37. A possible coordination mode of those small molecules could be in a bridging fashion between Rh and Cu, which has already been seen for other bimetallic complexes. This promising coordination still needs further investigation which could lead to catalytic NO$_x$ decomposition and further understanding of reactivity.

[RhCu]-NO$_2$ **[RhCu]-N$_2$O**
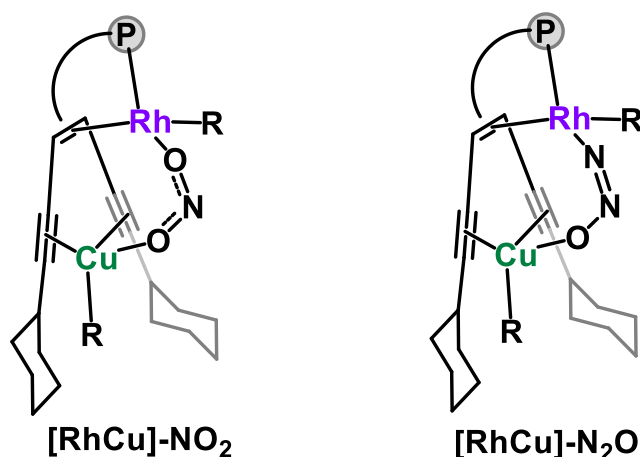
Scheme 37. Possible Rh-Cu complexes containing a NO$_2^-$ or N$_2$O ligand. R = Cl, OTf, MeCN.

5.3. Nitrogen donor containing bimetallic complexes

In order to change from a phosphorus donor atom to a nitrogen donor, being less prone to oxidation, two alkyne substituted bistropamine ligands were synthesised, **22a** and **22b**. The rhodium complexes [**23a**]$^+$, [**23b**]$^+$ and [**24a**]$^+$, [**24b**]$^+$ bearing the tridentate amine ligands could be synthesized. In [**23a**]$^+$ it was found that acetonitrile ligands could not easily be replaced from the rhodium complex and probably prevent a second metal from binding. Therefore, a rhodium cyclooctadiene complex [**24a**]$^+$ was prepared, where the bistropamine is only coordinated to the rhodium atom with the unsubstituted trop alkene and the nitrogen atom. As a second metal to incorporate in the complexes, copper looks quite promising, as it shows high affinity to the triple bonds, although it tends to cleave the carbon-nitrogen bond of the bistropamine as observed in [**25**](BF$_4$)$_2$.

To avoid decomposition of the ligand, strictly non coordinating solvents have to be used or basic reaction conditions could be a solution, as the deprotonation of the amine would make the cleavage less favorable. To conclude, the rhodium bistropamine complexes could build a solid base for more advanced structures to be synthesized and tested in catalysis, but more efforts have to be made in order to find suitable metal precursors and reaction conditions to obtain the desired homo or hetero bimetallic complexes. These could entail catalysts stable towards oxidation in NO$_x$ reduction.

91

CHAPTER IV – Cobalt and Copper Complexes on Alkyne Substituted Trop Ligands

1. Introduction to first row transition metal complexes

The importance of first row transition metals to catalytic applications is well known, as they can often replace precious metals.[160] The earth abundant elements are not only cheaper, but also more sustainable due to their higher natural abundance.[161] Several first row transition metal complexes have been prepared with trop-based ligands, which have been found to be successful in different catalytic applications.[162–166]

Cobalt complexes are known to catalyze the Pauson-Khand reaction, where the commercially available $Co_2(CO)_8$ serves as catalyst for the [2+2+1] cycloaddition of an alkyne, an alkene and CO as depicted in Scheme 38a.[167–169] This reaction can proceed in an intermolecular or intramolecular fashion. In order to study this reaction in more detail, the synthesis of a cobalt complex with the tropPPh$_2$ ligand was reported and its catalytic properties investigated, as depicted Scheme 38b.[170] Inspired by this publication, we wanted to develop similar complexes with the alkyne directly bound to the trop ligand (ligands **1** and **27**). This opens up the possibility of an intramolecular cyclization reaction within the ligand.
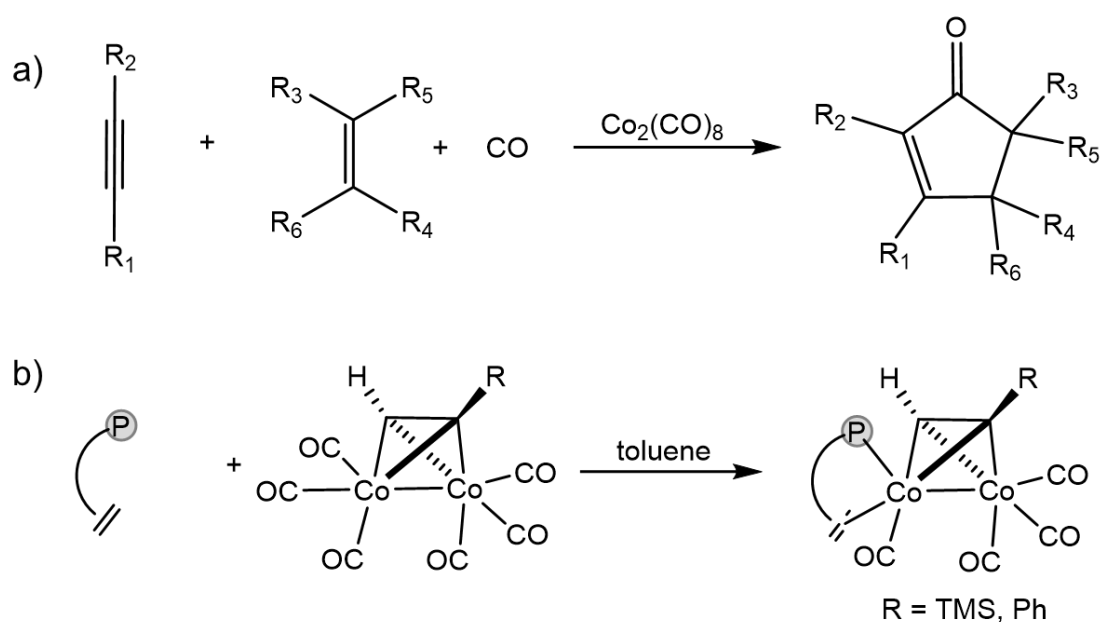
Scheme 38. a) Pauson-Khand reaction, general reaction pathway; b) synthesis of a dicobalt complex bearing the tropPPh$_2$ ligand and an alkyne.[170]

Furthermore, coinage metal complexes with the same tropPPh$_2$ ligand have been prepared and fully characterized, showing remarkably different structures for Cu, Ag and Au.[171] The synthetical routes for the corresponding metal complexes are depicted in Scheme 39. The interaction between the metal centers and the olefin moiety of the trop ligand is generally weak, although strongest for Cu complexes in this series and almost nonexistent for Au complexes.
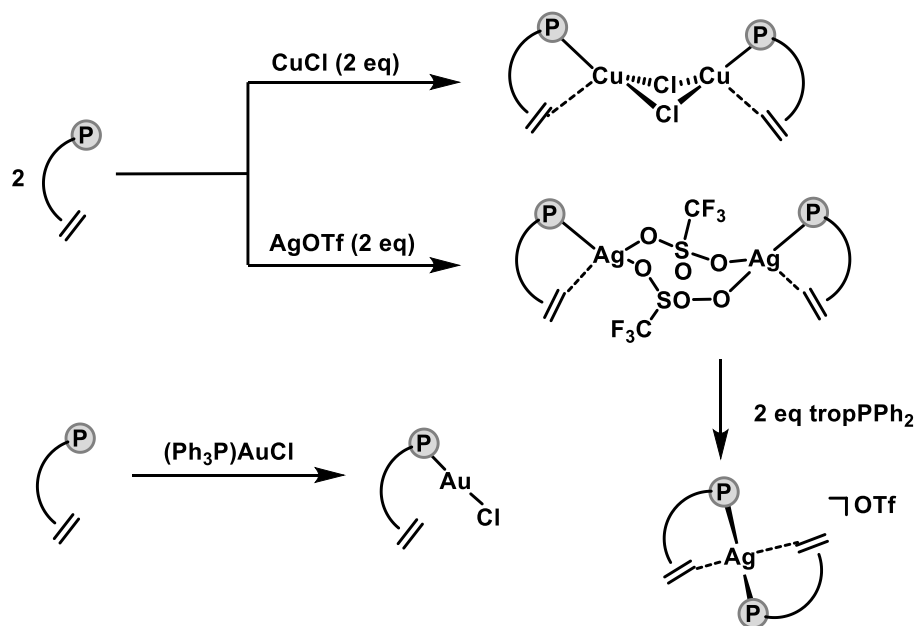
Scheme 39. Synthesis of different Cu, Ag and Au complexes with the tropPPh$_2$ ligand.[171]

In this Chapter, the coordination of specially designed bidentate ligand **27** with cobalt in its oxidation states 0 and +I and bidentate ligands **1** and **27** with copper(I) precursors will be discussed. Low valent metals were needed to coordinate the olefin to the metal center, as high valent, thus electron-poor, metals lack the ability of π-back bonding.

2. Cobalt complexes with alkyne substituted trop ligand 27

2.1. Synthesis and characterization of monometallic cobalt complexes

2.1.1.   [(PhC≡C)$_2$tropPPh$_2$CoCp] [28]

In order to synthesize a cobalt(I) complex containing ligand **27**, it was reacted with commercially available Co(CO)$_2$Cp in THF and irradiated with UV light, in order to cleave off the carbonyl ligands and open up coordination sites for the trop ligand. The reaction was monitored via ^{31}P NMR spectroscopy, a time resolved spectrum is shown in Figure 45. After 10 min of irradiation time the reaction started, visible by the appearance of an intermediate product at 74.3 ppm, which is converted to the desired product over the time course of 4 hours. The intermediate is expected to be a [**27**-Co(CO)Cp] complex that has one CO still bound to the cobalt center. The second cleavage step of CO and coordination of the olefin bond requires longer reaction times. The desired compound [**28**] was obtained in orange crystalline needles which were filtered off and did not require further purification. The synthetic pathway of [**28**] is shown in Scheme 40. Single crystal analysis revealed the solid state structure of [**28**], where the Co^I center resides in a trigonal planar coordination environment, shown in Figure 45. Bond lengths can not be discussed due to low quality of data.
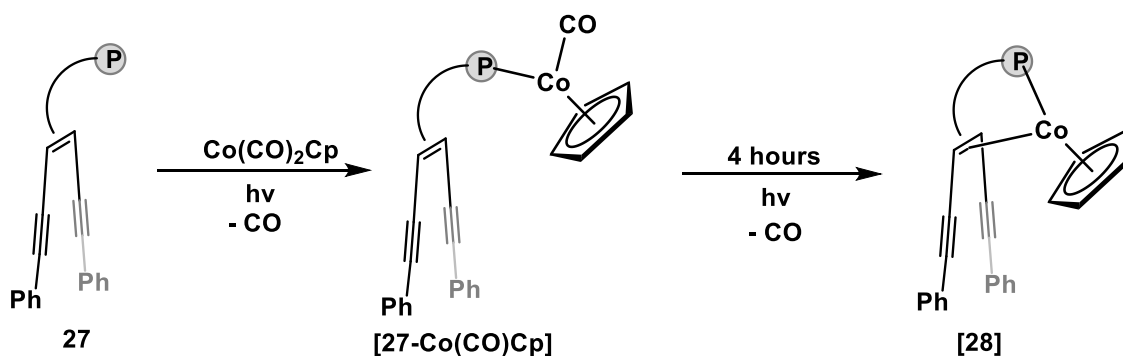
Scheme 40. Synthesis of complex [**28**] via the assumed intermediate [**27**-Co(CO)Cp].

The ^{31}P NMR spectrum of [**28**] shows a singlet at 103.4 ppm, which is in the same range as similar mono-rhodium complexes (around 110 ppm, see Chapter 2). ^{1}H NMR spectra showed resonances in the aromatic region corresponding to the coordinated ligand **27** and only one single peak for the Cp ligand. Since some symmetry is present in complex [**28**] (one mirror plane), an attempt was made to measure ^{59}Co NMR. ^{59}Co is a spin 7/2 nucleus and thus a quadrupole, which yields the detection of this nuclei by NMR difficult. In an experiment set up by Marcel Aebli, it was possible to directly detect a very broad signal from -3000 to -2200 ppm with a maximum around -2636 ppm.
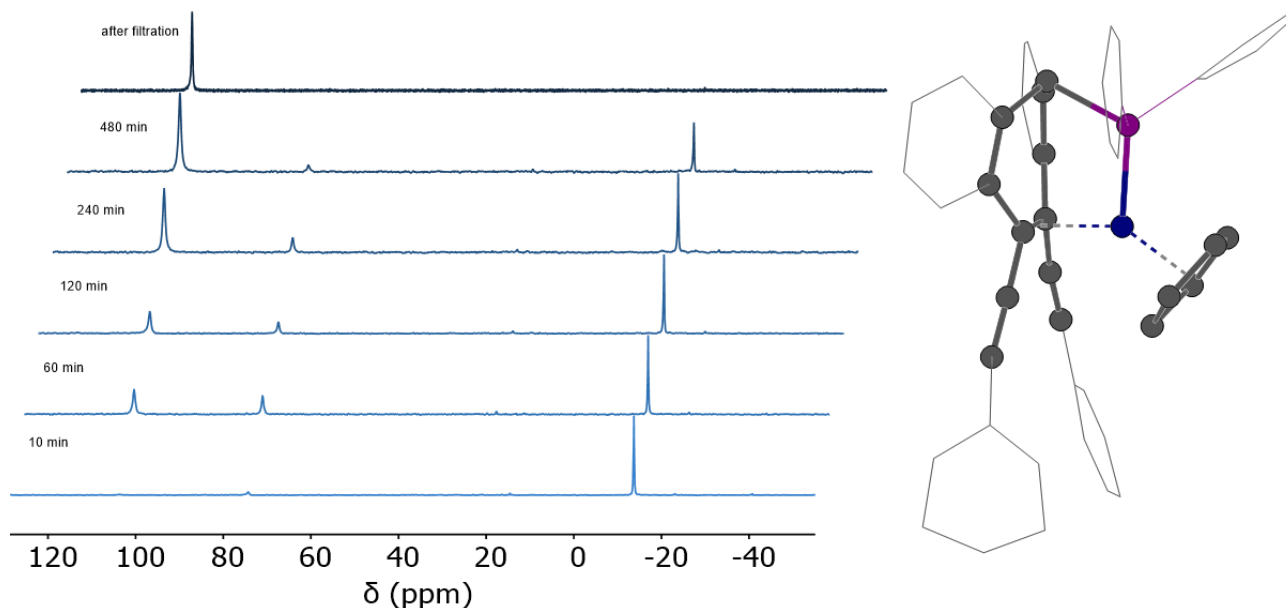
Figure 45. Time resolved ^{31}P NMR spectra showing the formation of complex [**28**] upon irradiation with UV light and solid state structure of [**28**] (hydrogen atoms, solvent molecules and counter ions omitted for clarity).

This monometallic Co[I] complex [**28**] was subjected to various metal precursors to coordinate a second metal atom to the alkynes, but unfortunately neither homo- nor hetero-bimetallic complexes were obtained. The reason for this could be steric hindrance due to the Cp ligand coordinated to the cobalt center additionally to the electronically saturated 18 e[-] complex. Furthermore, the phenyl substituted alkynes were shown to be too electron poor for the coordination of several metals (see other Chapters of this thesis).

2.1.2. K[Co(HMDS)((PhC≡C)$_2$tropPPh$_2$)] K[29]

Due to the inability to generate bimetallic compounds from Co(CO)$_2$Cp, another Co(I) source, K[Co(HMDS)$_2$], was used as a precursor, which is an anionic complex with a potassium counter ion masked with 18-crown-6. The synthesis of complex K[**29**] was performed by mixing ligand **27** with a solution of K[Co(HMDS)$_2$] in THF, as depicted in Figure 46a. ^{31}P NMR spectroscopy revealed a singlet at -22.4 ppm, which is only slightly different to the resonance of the free ligand at -14.0 ppm. The reason for this small change in chemical shift is the lack of coordination of the phosphorus atom.
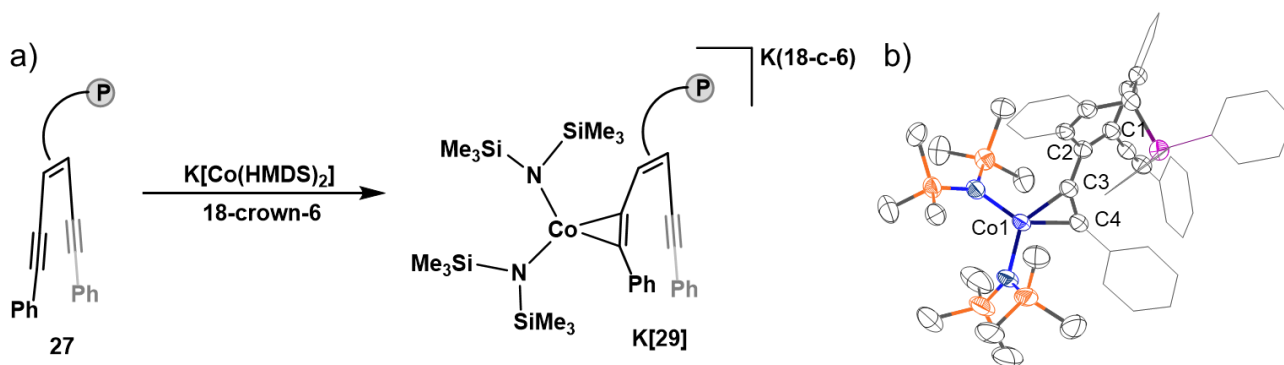
Figure 46. a) Synthetic route to obtain cobalt complex K[**29**] in THF; b) solid state structure of K[**29**]. Hydrogen atoms, solvent molecules and counter ions omitted for clarity.

Single crystals of complex K[**29**] were grown and XRD methods revealed a new bonding mode of the alkyne substituents: The Co^I atom is coordinated to only one alkyne, facing away from the other alkyne group. Surprisingly, coordination of the alkyne group is favoured over coordination of the phosphorus donor atom, which remains non-coordinated. The d^8 cobalt atom resides in a trigonal planar coordination sphere, complemented by two HMDS groups, which is the same geometry as in complex [**28**] described earlier and typical for cobalt in the oxidation state of +I. Note that this complex is anionic (two negatively charged N(TMS)$_2$ groups and one cobalt cation) and therefore forms a salt with a potassium cation (that is masked by a crown ether). Chosen bond lengths of complex K[**29**] are given in Table 14. The Co−C bond distances are in the range of single bonds (1.98 and 1.92 Å). Significant elongation of 0.075 Å of the coordinating alkyne C≡C bond is observed when compared to the non-coordinating ones in the same compound (1.278 for C2−C3 vs 1.203 Å for C5−C6), which is due to π-backdonation from the corresponding metal orbitals to the alkyne molecular orbitals.

Table 14. Selected bond lengths [Å] of complex K[**29**].

	Bond length [Å]		Bond length [Å]
Co−N1	1.975(3)	C1−C2	1.378(4)
Co−N2	1.970(3)	C2−C3	1.447(4)
Co−C3	1.976(3)	C3–C4	1.278(5)
Co−C4	1.922(4)	C5–C6	1.203(5)

2.2. Bimetallic cobalt complexes

2.2.1. [((PhC≡C)₂tropPPh₂)Co₂(CO)₄] [30]

Inspired by a previous report on a bimetallic cobalt(0) complex,[170] a related complex with alkyne substituted ligand **27** was prepared. Therefore, ligand **27** was stirred in toluene with the commercially available $Co_2(CO)_8$ complex for one hour. This cobalt carbonyl precursor is generally known for coordination to alkyne groups. The synthetic route is shown in Scheme 41. Complex [**30**] was obtained as dark blue-green crystals from a toluene solution at -20°C.
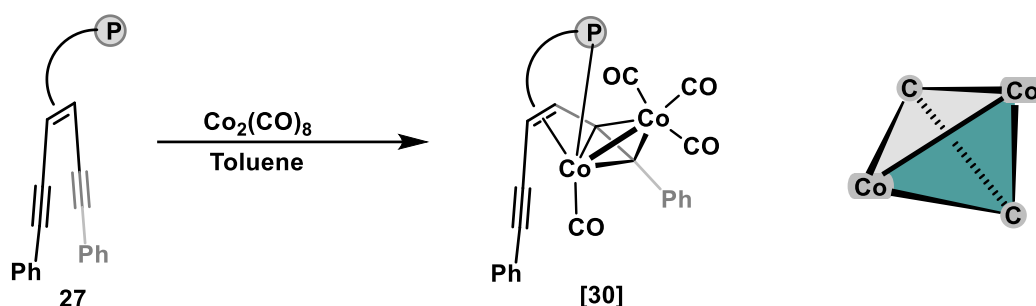
Scheme 41. Synthesis of dicobalt complex [**30**] and coordination polyhedral showing the tetrahedral structure.

Single crystal X-ray diffraction analysis revealed the structure of [**30**] (shown in Figure 47) to be a homo bimetallic Co^0–Co^0 complex with a coordination mode very well known from literature: the Co_2 core spans a tetrahedron with two carbon atoms from one alkyne group. Additionally, the phosphorus donor atom from the trop ligand is coordinating to Co1, further stabilizing this compound and enabling further coordination of a cobalt atom to the trop olefins.
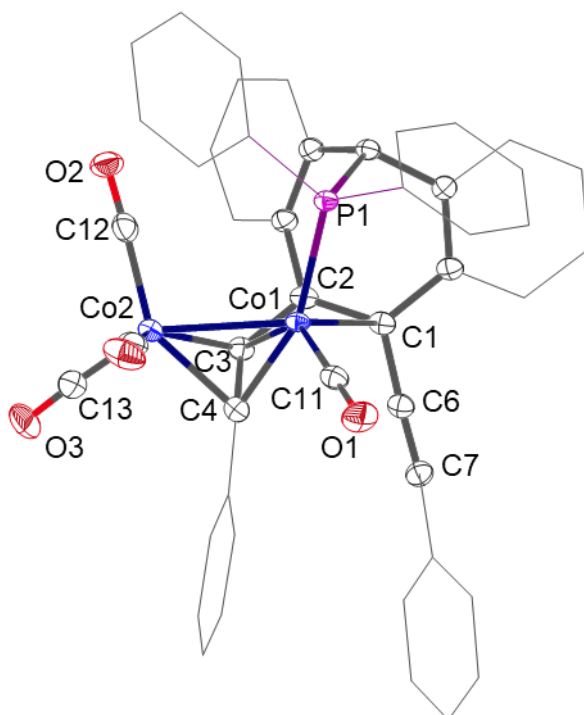
Figure 47. Solid state structure of complex [**30**] (hydrogen atoms and solvent molecules omitted for clarity).

Both cobalt centers reside in a highly distorted trigonal bipyramidal coordination sphere. The P1−Co1−ct$_{(C6-C7)}$ angle was found to be 141.5° and Co1−Co2−C13 at 147.5°, which is a large deviation from the ideal 180°. Selected bond lengths and angles are listed in Table 15. The Co1−Co2 distance was found to be 2.5768 Å which corresponds to a metal-metal single bond but is elongated in comparison to the precursor $Co_2(CO)_8$. The C≡C bond distance of the coordinated alkyne moiety is dramatically elongated to 1.356 Å, which is in the range of a C=C double bond. For comparison, the non-coordinating alkyne bond was found to be 1.202 Å within the same molecule, which is more than 0.15 Å shorter. This underlines the strong interaction between the triple bond and the two cobalt centers. Due to the strong backdonation of the electron rich metal centers, the coordination mode is best described as σ-bonds between the cobalt and the carbon atoms. Co−C distances for that interaction range from 1.935 to 2.010 Å. Notably, the Co1 bond length to the trop olefin carbon atoms (C1 and C2) is significantly longer (2.038 and 2.142 Å) than to the alkynes.

The binuclear complex [**30**] contains two Co^0 d^9 centers, where each metal atom accommodates an unpaired electron. Due to spin-spin coupling enabled by the Co−Co bond, compound [**30**] is diamagnetic which is reflected by the sharp singlet at 69.7 ppm in recorded ^{31}P NMR spectra. CO resonances were detected in ^{13}C NMR spectra at 212.4 and 200.7 ppm, which shows that the three CO ligands at Co2 show dynamic behaviour in solution and thus become magnetically equivalent.

Table 15. Selected bond lengths [Å] and angles [°] of complex [**30**].

	Bond length / angle		Bond length / angle
Co1−Co2	2.5768(4)	Co1−P1	2.2039(5)
Co1−C1	2.0382(17)	C1−C2	1.457(3)
Co1−C2	2.1424(17)	C2−C3	1.422(3)
Co1−C6	1.9888(17)	C3−C4	1.356(3)
Co1−C7	1.9875(18)	C1−C6	1.450(2)
Co2−C6	1.9335(19)	C6−C7	1.202(3)
Co2−C7	2.0096(19)	C7−C8	1.454(3)
Co1−C11 [a]	1.767(2)	O1−C11 [a]	1.144(2)
Co2−C12 [a]	1.790(2)	O2−C12 [a]	1.145(3)
Co2−C13 [a]	1.805(2)	O3−C13 [a]	1.138(3)
Co2−C14 [a]	1.829(2)	O4−C14 [a]	1.134(2)
P1−Co1−ct$_{(C6-C7)}$	141.46(5)	Co1−Co2−C13	147.53(7)

[a] Carbonyl bond distances.

2.2.2. Co$_2$ on a rearranged dimerized ligand [31]

Reacting ligand **27** with Co(HMDS)$_2$ in DME with 10 eq. of zinc powder and 1 eq. of PPh$_3$ gave complex [**31**] in black crystals. Single crystal analysis by XRD methods revealed an unexpected

structural motif shown in Figure 48: two ligands were fused together via their alkyne substituents forming a series of five connected rings. Those are, starting from left to right in Scheme 42: a seven membered ring (trop), a four membered ring (delocalized), a hexagon and a pentagon with an allenyl substructure followed by another seven membered trop-ring. This carbon framework embeds a Co^I−Co^I core, which is coordinated to the (delocalized) double bonds of the ligand framework and to the two phosphorus atoms. In addition to that, there is a carbene (originating from C≡$\underline{C}$−Ph) bridging both metal centers. With this, the bimetallic core is tightly embedded in the mostly carbon based framework that was built up around it.

Scheme 42. Synthetic route for dicobalt complex [**31**].
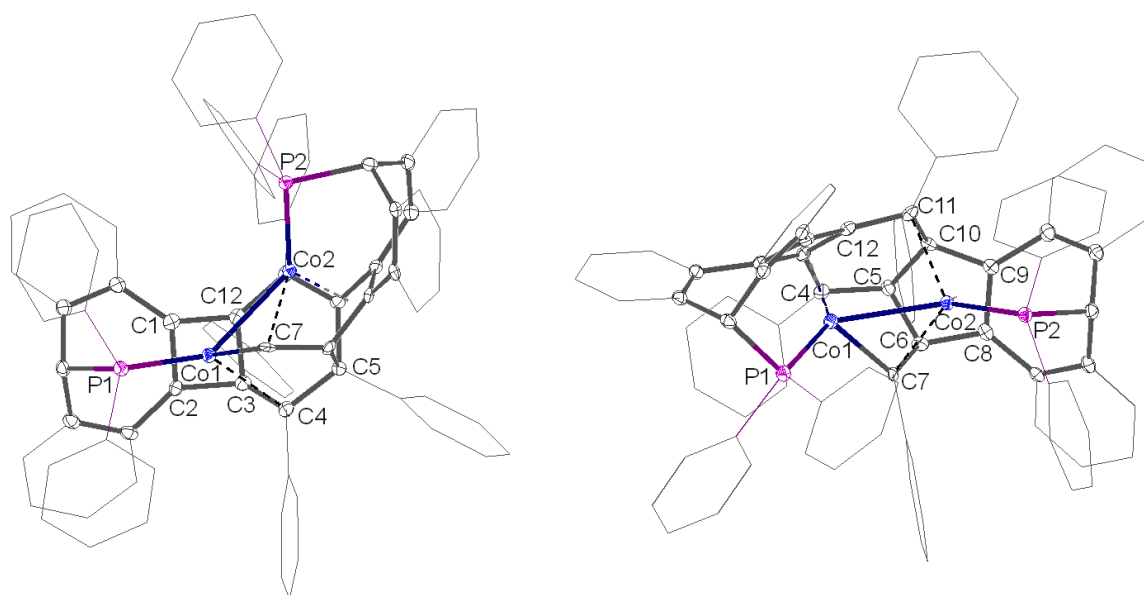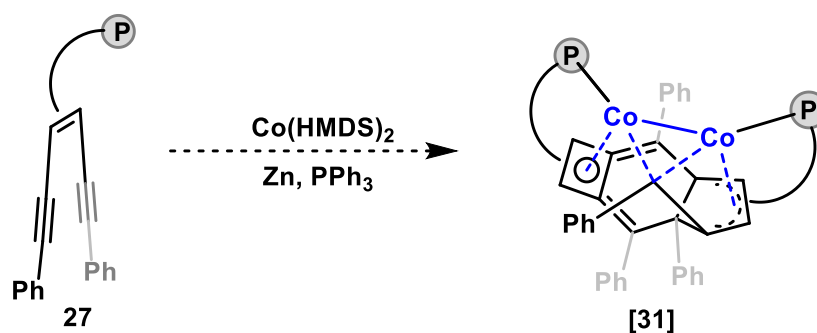
Figure 48. Solid state structure of dicobalt complex [**31**], viewed from different perspectives (hydrogen atoms and solvent molecules omitted for clarity).

Selected bond distances are listed in Table 16. The Co−Co bond length of 2.63 Å is in the range of a single bond. Co−P distances are 2.16 Å (Co1−P1) and 2.18 Å (Co2−P2), where the latter is slightly longer due to a different chemical environment. On the other hand, the Co-centroid distances show the opposite trend: Co1−ct1 1.77 Å and Co2−ct2 1.59 Å, which means that the allylic part of the five-membered ring stays in closer contact to the cobalt center than the four-membered ring does. The bridging carbene shows bond lengths of 1.97 and 2.04 Å to Co1 and Co2, respectively.

All C−C distances belonging to the four-membered and the five membered ring, and including the connecting C11, are between 1.45 and 1.49 Å, which is in between a single and a double bond, reflecting the delocalization of electrons along the C−C bonds. An exception from the delocalization is atom C5, which is sp^3 hybridized and therefore shows single bonds to C4, C6, C10 and the Ph ring. Furthermore, C3−C4 shows a C=C double bond with 1.38 Å in length.

Even though this reaction was unexpected, cobalt carbonyls are known to undergo cyclization of alkynes (see Pauson-Khand reaction, described in the introduction to in this Chapter). In this reaction, complex [**31**] was obtained as clean product, but unfortunately the complex could not be synthesized in larger quantities and therefore no further investigations on this dicobalt complex were made.

Table 16. Selected bond lengths [Å] of complex [**31**].

	Bond length [Å]		Bond length [Å]
Co1−Co2	**2.6288(6)**		
Co1−P1	2.1600(8)	Co2−P2	2.1790(9)
Co1−ct1$_{(C1,2,3,12)}$	1.7692(4)	Co2−ct2$_{(C6,8,9,10)}$	1.5948(4)
Co1−C7	1.972(3)	Co2−C7	2.042(3)
C1−C2[a]	1.472(4)	*C6−C8*[b]	*1.478(4)*
C2−C3[a]	1.489(4)	*C8−C9*[b]	*1.461(4)*
C3−C12[a]	1.485(4)	*C9−C10*[b]	*1.477(4)*
C12−C1[a]	1.458(4)	C5−C6	1.550(4)
C3−C4	1.379(4)	C6−C7	1.475(4)
C4−C5	1.534(4)	C10−C11	1.458(4)
C5−C10	1.559(4)	C11−C12	1.453(4)

[a] C−C bonds as part of the four-membered ring; [b] C−C bonds of the allylic part of the five-membered ring.

2.3. Comparison of cobalt complexes

The ^{31}P chemical shift for complexes [**28**] – [**31**] was found in a wide range between -22.4 and 105.6 ppm, as summarized in Table 17. Since the phosphorus atom in complex [**29**] is non-coordinating, it is significantly low-frequency shifted compared to all other complexes. Complex [**30**], bearing four CO ligands, shows resonances at lower ppm compared to complexes [**28**] and [**31**], which are only coordinated to sp^2 hybridized carbon atoms (alkenes, Cp, allyl, cyclobutene) apart from the P atom. In [**30**], the P−Co distance is also the longest, indicating the weakest P−Co bond within this series of cobalt complexes. This could also be due to the fact, that this complex embeds two Co[0] centers, while all other complexes contain one or two Co[I] atoms. The Co−Co distances are 2.58 and 2.63 Å in [**30**] and [**31**] respectively, both attributed to a single bond.

Table 17. Comparison of selected NMR chemical shifts [ppm] and bond lengths [Å] of cobalt complexes of this Chapter.

	^{31}P	P–Co	Co–Co
[28]	103.4	2.098(11)	-
[29]	-22.4	-	-
[30]	69.7	2.2039(5)	2.5768(4)
[31]	105.6 58.4	2.1600(8) 2.1790(9)	2.6288(6)

3. Copper complexes with ligands 1 and 27

3.1. Synthesis of monometallic copper complexes

Moving away from d^8 group 9 transition metals to group 11 transition metal complexes with d^{10} configuration, investigations on coordination of copper(I) to alkyne substituted tropPPh$_2$ ligands were carried out. Therefore, ligands **1** or **27** were reacted with one equivalent of CuCl in THF and heated to reflux overnight, until all CuCl dissolved and a clear yellow to orange solution had formed. The reaction schemes are shown in Figure 49a and b. Upon cooling down the reaction mixture to room temperature, large crystals of [**32**] or [**33**] could be obtained in almost quantitative yield. With the same method, single crystals suitable for X-ray diffraction analysis were obtained. The solid state structure of complex [**32**] is shown in Figure 49c. The structure show coordination of Cu to the phosphorus atom with the copper being in proximity to the trop olefinic bond, although, no Cu−C bond is formed.
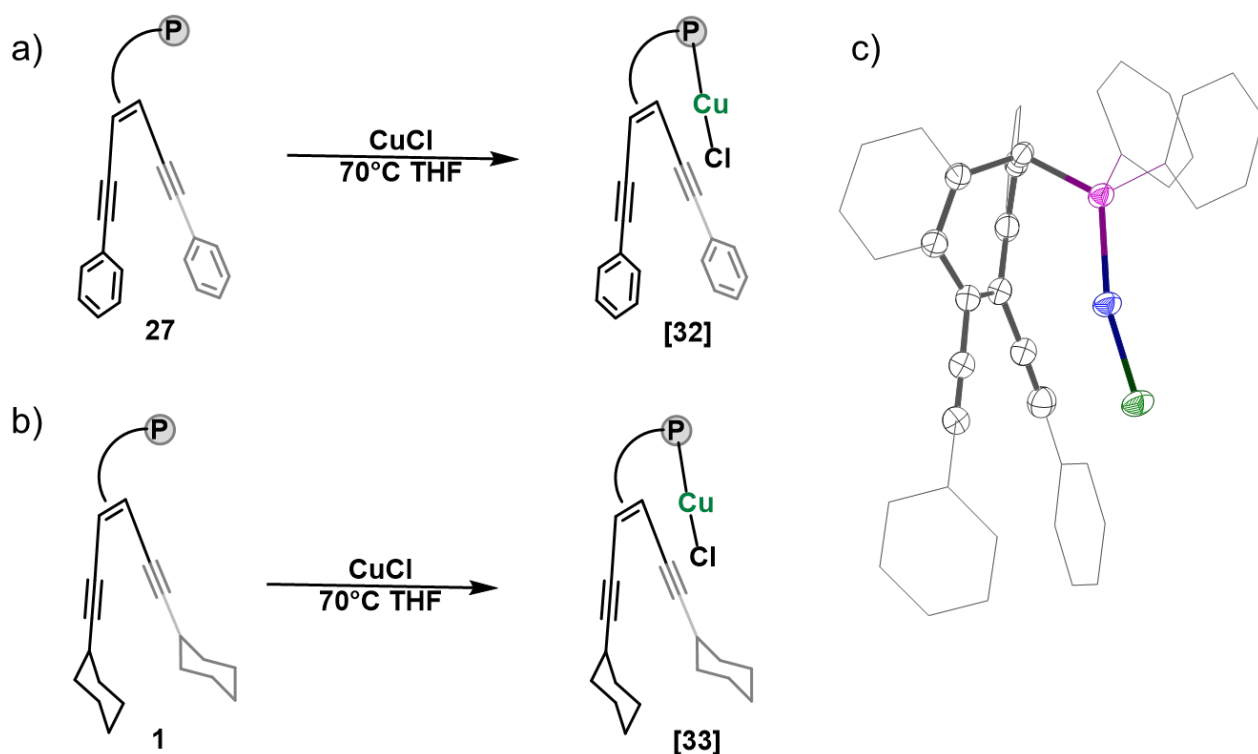
Figure 49. a) Synthesis of complex [**32**]; b) synthesis of complex [**33**]; c) solid state structure of [**32**]. Hydrogen atoms and solvent molecules omitted for clarity.

3.2. Synthesis of bimetallic and multi-metallic copper complexes

In order to obtain bimetallic copper(I) complexes, the same strategy of subchapter 3.1 was applied: ligands **1** or **27** were refluxed in THF with two equivalents of CuCl overnight, the crystalline complexes [**34**] and [**36**] were collected after cooling to -20°C. The synthetic routes are shown in Scheme 43a and b.

102
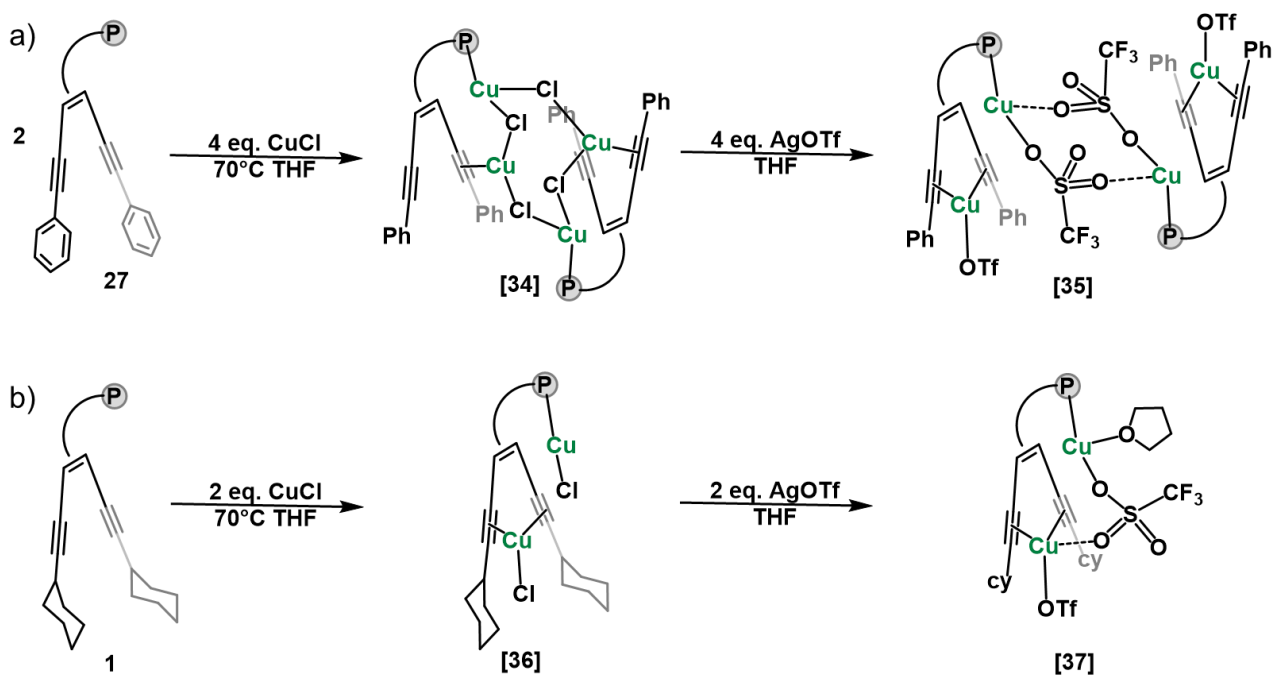
Scheme 43. a) Synthesis of dicopper complexes [**34**] and [**35**], b) synthesis of complexes [**36**] and [**37**].

In Chapter III, the coordination mode of Cu^I to the alkyne fragments was discussed, where the metal atom resides in a trigonal planar coordination sphere, which makes the formation of a metal-metal bond sterically impossible under these conditions. Single crystal analysis using XRD methods revealed the solid state structures of chloride containing complexes [**34**] and [**36**], depicted in Figure 50a and c. Both complexes coordinate two copper(I) metal atoms per ligand molecule but show a different structure overall. While complex [**36**], bearing cyclohexyl substituents at the alkynes, shows the expected structure with one CuCl fragment coordinated at the phosphorus atom and one fragment between the alkynes, a dimeric structure was observed for phenyl substituted complex [**34**]. Here, the additional CuCl fragment is not bound to both alkynes, but only to one of them, facing away from the trop-ligand. This coordination mode is probably favoured because the phenyl substituted alkynes are less electron rich than the cyclohexyl substituted alkynes in [**36**]. Therefore, a bridging mode is adopted by the chloride atoms: upon dimerization of two species an eight-membered ring with alternating Cu and Cl atoms is formed, that adopts a zig-zag structure.

Chloride abstraction of dimeric [**34**] with four equivalents AgOTf resulted in complex [**35**], which retained the dimeric structure, as seen in Scheme 43a and Figure 50b. Here, the Cu2 atom coordinates to both alkyne fragments in plane, while the two Cu1 atoms are bridged by the oxygen atoms of two triflate anions. This again forms an eight-membered ring, but under exclusion of the Cu2 atoms. Monomeric dicopper complex [**36**], bearing cyclohexyl substituents, was subjected to two equivalents of AgOTf to abstract both chloride atoms. The resulting complex [**37**] is depicted in

Scheme 43b and Figure 50d. The monomeric structure is retained, where both Cu atoms reside in a distorted trigonal planar coordination sphere (the third ligand on Cu1 is a molecule of THF). Additionally, a triflate anion is bridging the two copper metals via its oxygen atoms. For a detailed discussion of bond lengths and angles see Chapter 3.3 below.

The different structures obtained with ligands **1** and **27** must be a result from the electronic properties of the alkyne groups: while phenyl is an electron withdrawing group, cyclohexyl substituents are considered electron donating. Therefore, C≡C is more electron rich in **1** than in **27**. Presumably, the electron deficiency is balanced by the formation if Cu−Cl and Cu−O bridges, which seem to be more favourable than coordination of both alkyne groups in **[34]**. Overall, four unique structures containing two copper atoms per ligand were obtained.
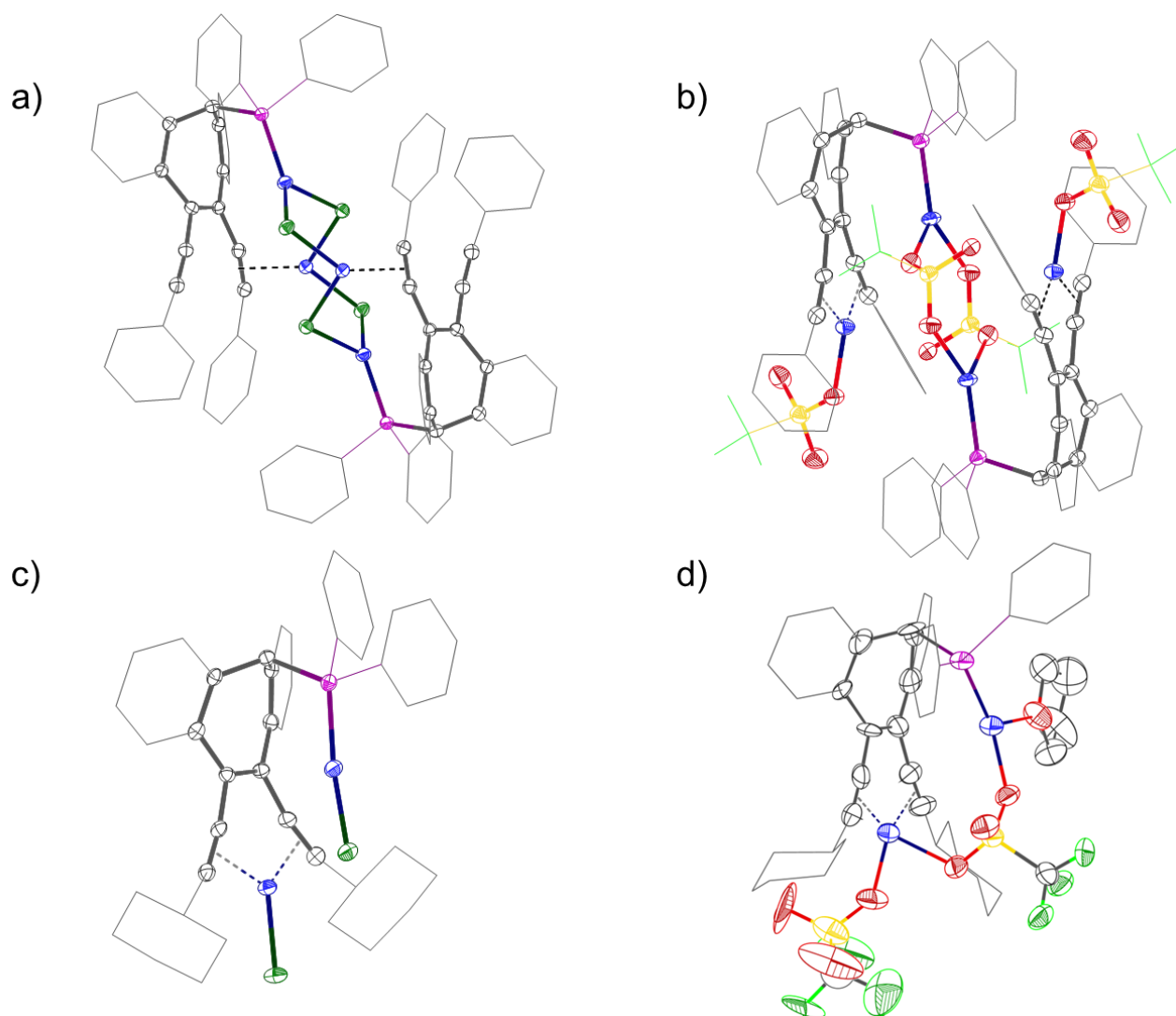
Figure 50. Solid state structure of copper complexes a) **[34]**, b) **[35]**, c) **[36]**, d) [**37**]. Hydrogen atoms and solvent molecules omitted for clarity.

3.3. Discussion of NMR data and bond lengths of complexes [32] - [37]

A comparison of selected NMR data and XRD data of presented copper complexes is listed in Table 18. Upon coordination of a copper atom to the P atom of ligand **1** or **27**, the signals in ^{31}P NMR were shifted from around -14 ppm to higher frequencies of 0.7 - 7.3 ppm. This is a significant change, although very much less pronounced as with similar Co, Rh and Ir complexes described with the same ligands, which showed resonances around 100 ppm in ^{31}P NMR. The reason could be the change from d^8 to d^{10} metals. Complexes [**32**] – [**37**] showed broad singlets in phosphorus NMR (chemical shifts are listen in Table 18), but sharp signals were observed in ^{1}H NMR spectra. Both naturally occurring copper isotopes are quadrupoles with S = 3/2. Since copper is directly coordinated to phosphorus, the nuclear spin leads to signal broadening. NMR spectra were recorded in CD_2Cl_2 or $CDCl_3$, other solvents were not able to fully dissolve the copper complexes investigated in this Chapter. When comparing ^{31}P chemical shifts between dinuclear and mononuclear copper complexes, no significant trend could be observed.

The P−Cu1 bond length is the shortest for monometallic [**32**] (2.16 Å) while it is roughly the same for all bimetallic complexes with around 2.17 Å. Interatomic distances for Cu1−Cu2 and Cu1−ct$_{(C1−C2)}$ are given in Table 18, although no chemical bonds are attributed to those values as the interatomic distances are too large for orbital overlap. Cu1−ct$_{(C1−C2)}$ distances are between 2.93 and 3.09 Å, which is larger than the sum of the Van Der Waals radii of Cu and C. Additionally, the C1−C2 bond does not elongate significantly, as expected when a coordination bond is formed. However, the Cu2 atom forms Cu−C bonds in bimetallic complexes, with Cu2−ct of 1.98 – 2.03 Å in length. The bond formation leads to elongation of 0.03 Å of alkyne C3−C4 bonds to 1.23 Å from uncoordinated 1.20 Å. Note that in [**34**], only one alkyne C≡C bond coordinates to Cu2. While in triflate complex [**35**] all Cu−O distances are in the same range, complex [**37**] shows larger differences. The interaction between Cu2 and O is rather long (2.38 Å) when compared to the two Cu−O$_{OTf}$ single bonds within this molecule (1.97 and 1.95 Å). The Cu−O$_{THF}$ bond length is intermediate with 2.10 Å. In summary, all copper compounds presented show a trigonal planar coordination environment together with similar bond distances and chemical shifts, even though the structural motifs and coordination modes differ substantially.

Table 18. Comparison of selected NMR chemical shifts [ppm] and bond lengths [Å] of copper complexes [32] - [37].

	[32]	[34]	[35]	[36]	[37]
^{31}P	3.1	-3.4	7.3	0.7	8.9
P−Cu1	2.1592(10)	2.1714(5)	2.1722(6)	2.1682(6)	2.160(5)
Cu1−Cu2[a]	-	3.5589(4)	4.1140(5)	3.8379(5)	4.179(3)
Cu1−ct(C1−C2)[a]	2.9315(5)	3.0109(3)	2.9273(3)	2.9856(4)	3.089(2)
C1−C2	1.385(5)	1.379(2)	1.380(3)	1.368(3)	1.34(3)
Cu1−L	2.1079(10)	2.2440(5)	2.0140(17)	2.1149(6)	1.968(11)[c] 2.096(13)[d]
Cu2−ct(C3−C4)	-	1.9336(3)	1.9993(3)	1.9976(3)	1.991(3)
Cu2−ct(C6−C7)	-	-	1.9985(3)	1.9815(3)	2.027(3)
C3−C4	1.201(5)	1.233(3) 1.202(3) [b]	1.230(3)	1.227(3)	1.21(3)
Cu2−L	-	2.3049(4)	1.9822(16)	2.1786(6)	1.946(13) 2.381(12)[c]

[a] Not attributed to a chemical bond, [b] uncoordinated C≡C, [c] Cu-O(OTf1), [d] Cu-O(THF).

4. Conclusion and Outlook

A series of Co^I and Co^0 complexes was prepared and characterized, where different coordination modes were observed. Although, no Co^I complex could be obtained which is in similar to Rh^I complexes described in Chapters II and III of this thesis. This is mainly attributed to the lack of similar Co^I precursors. Several different cobalt complexes with ligand **27** were obtained, and one (complex [**31**]) showed a cyclized dimer which probably was formed in a Pauson-Khand type reaction. Dicobalt complex [**30**] should be further investigated towards catalytic and electrochemical properties.

The synthesis of the presented copper(I) complexes was achieved by heating ligands **1** or **27** in THF with CuCl, which, depending on the stoichiometry, yielded mono- or bimetallic complexes. The chloride atoms could easily be abstracted with AgOTf. The coordination modes of presented complexes vary strongly in the way the copper atom coordinates to the alkynes.

In future research, the redox and spectrophotometric properties of the described complexes could be evaluated and leveraged for catalytic reactions. Especially the bimetallic copper complexes may be suitable catalysts for NO_x decomposition, as the nitrous gases could perfectly fit in the formed bimetallic pocket, where they could coordinate to both copper atoms at the same time. DFT calculations and molecular models (Cu_4S clusters) suggest bridging coordination of N_2O in nitrous oxide reductase between two copper atoms.[172]

CHAPTER V - Iridium Complexes as Catalysts for Alcohol Oxidation

1. Introduction

Alcohol oxidation is a key reaction in organic synthesis and is also relevant to hydrogen storage.[60] Previously, our group has found an [Ir(trop$_2$dach)]OTf ([38]OTf) complex to be a very active catalyst in oxidative alcohol dehydrogenation.[64,65] This catalyst is very selective towards primary alcohols, even unactivated ones, such as 1-octanol. Furthermore, the reaction usually proceeds within minutes and only needs 0.01 mol% catalyst loading if *p*-benzoquinone (BQ) is used as oxidant. Three equivalents of base (NaO*t*Bu) with respect to the catalyst were used to deprotonate the NH groups of the ligand (see Scheme 44).
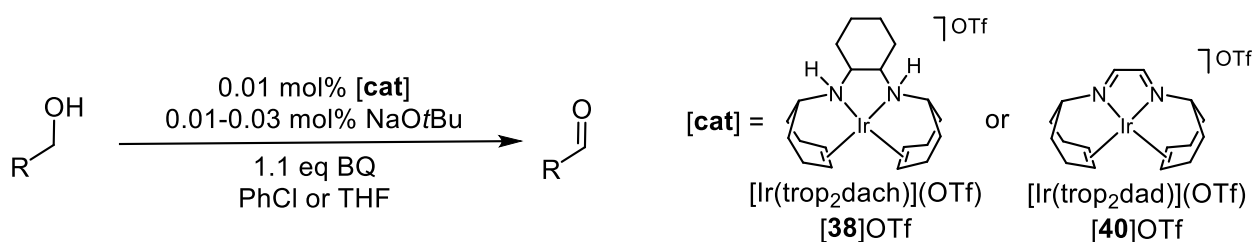
Scheme 44. Catalytic alcohol oxidation with iridium catalysts [38]OTf or [40]OTf.

Preliminary results indicated that the active catalyst would not be the amide complex with a saturated backbone, instead, dehydrogenation of the ligand to a diazadiene was proposed. This assumption was found to be true for a similar complex, lacking the cyclohexyl group: [Ir(trop$_2$dae)](OTf) [39]OTf is dehydrogenated to [Ir(trop$_2$dad)](OTf) [40]OTf under catalytic conditions (4 eq. of base and 4 eq. of BQ) as depicted in Scheme 45. Therefore, [40]OTf was synthesized by a former group member[173] and catalytic investigations were performed with this iridium complex with an unsaturated diazadiene (dad) unit in the ligand backbone.[130,174] This complex is very active and selective in the oxidative dehydrogenation of primary alcohols to aldehydes. The catalytic system is described in Scheme 44 and could proceed with only 0.01 mol% of base and THF as solvent.
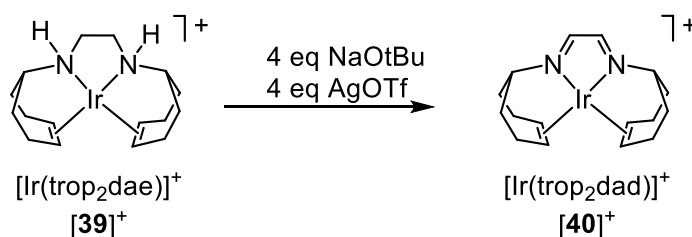
Scheme 45. Oxidative dehydrogenation of [Ir(trop$_2$dae)](OTf) [39]OTf to [Ir(trop$_2$dad)](OTf) [40]OTf.

The drawback is the use of stoichiometric amounts of BQ which produce substantial amounts of *p*-hydroquinone (HQ) waste. All attempts to replace this oxidant by different types of quinones, inorganic oxidants, as well as air, oxygen or N$_2$O gas have failed.[130,174,175] Electrochemical investigations on [38]OTf were performed in order to replace the chemical oxidant by electricity.[68] It was found that this approach led to a very active electrocatalytic system for alcohol dehydrogenation.

2. Reduction of [Ir(trop₂dad)]OTf ([40]OTf)
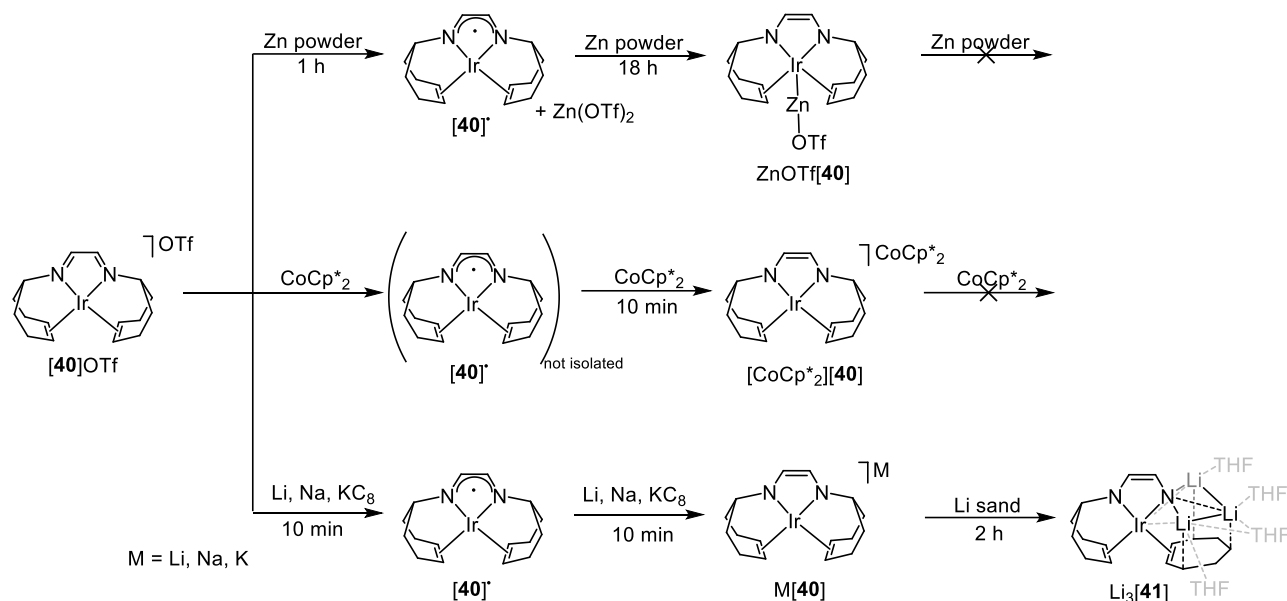
Scheme 46. Overview of reduction processes of [**40**]OTf described in this Chapter.

2.1. Previous results by our group

Mechanistic studies on complex [**40**]OTf involved the investigation of its redox chemistry. The dad unit in [**40**]OTf does not only act as redox non-innocent moiety but also behaves in a chemically non-innocent way (*vide infra*). The CV of complex [**40**]OTf shows two reversible reduction events at -0.66 and -1.35 V vs Fc/Fc⁺ (shown in Figure 51), a schematic representation of the redox processes is shown in Scheme 47. Chemical reduction with Zn leads to the neutral Ir-radical ([**40**]˙), which was characterized by EPR spectroscopy and is best described as a [Ir⁺(trop₂dad)˙⁻] with a [16+1] electron configuration with the unpaired electron located predominately on the diazadiene unit.[173] No solid state structure of [**40**]˙ was reported so far. The double reduced [Ir(trop₂dad)]⁻ ([**40**]⁻) was synthesized and characterized with [CoCp*₂]⁺ as counter ion (forming an almost insoluble salt).[174,176] When sodium metal was employed as reductant, a symmetric and soluble species was obtained (assumed to be Na[**40**]), and a follow-up reaction transformed the symmetrical anionic compound into an unknown asymmetric complex. None of those sodium derived species were previously structurally analyzed.
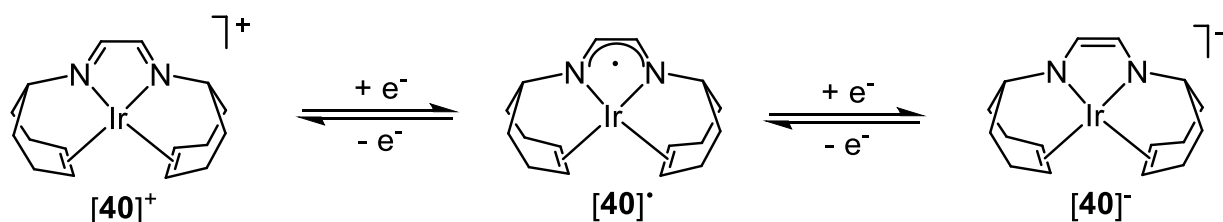
Scheme 47. Redox events of [**40**]OTf to neutral radical [**40**]˙ and double reduced anionic [**40**]⁻.
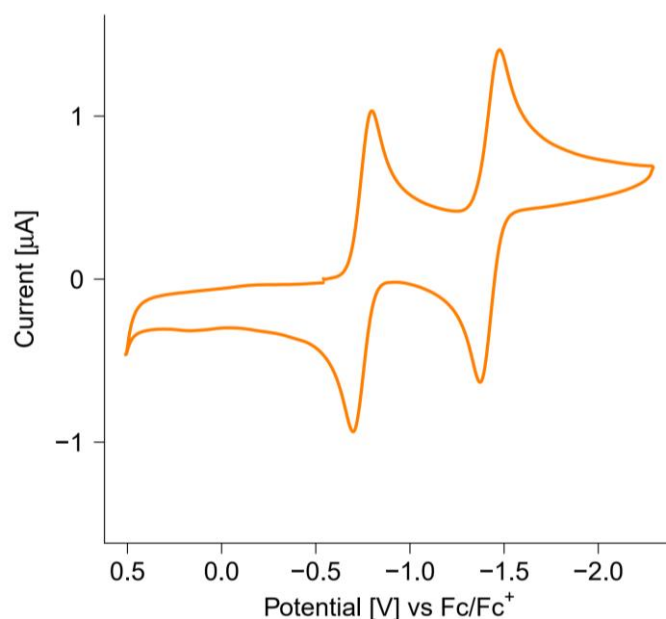
Figure 51. CV of 1 mM [**40**]OTf in THF with Pt WE, Pt on TiOx CE and Ag/Ag$^+$ RE and 100 mM nBu$_4$NPF$_6$ electrolyte.

2.2. Elemental Reductants

Previous investigations showed that [**40**]OTf can easily be reduced to the corresponding neutral radical complex [**40**]$^•$. The chemical one-electron reduction was repeated in this work, since no structure determination of [**40**]$^•$ using XRD techniques was reported so far. Stirring the complex with 10 eq. of activated zinc powder in THF for one hour leads to a grass green, highly soluble paramagnetic compound, as previously reported.[173] Single crystals were obtained and the solid state structure was determined via X-ray crystallography (shown in Figure 52), which shows the expected change in bond lengths (see Table 21 and discussion in Chapter 2.4 below).
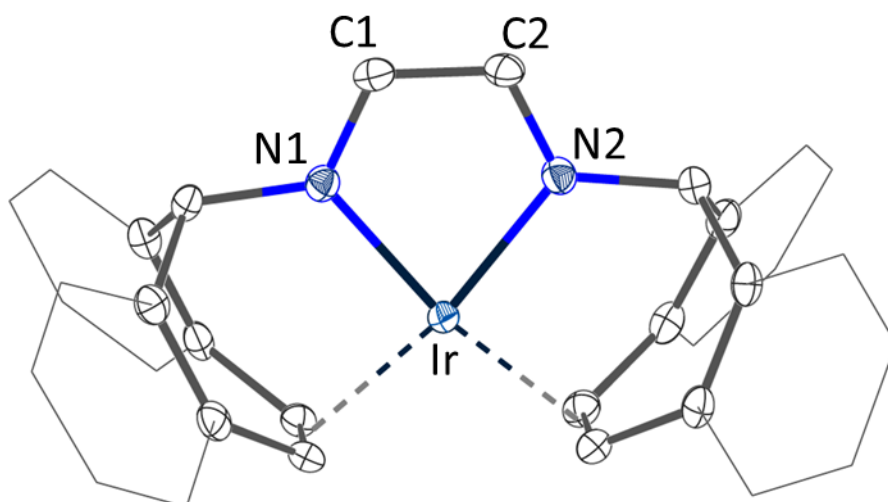
Figure 52. Solid state structure of [**40**]$^•$. Hydrogen atoms and solvent molecules omitted for clarity.

If [**40**]OTf is stirred with a large excess (> 10 eq.) of activated zinc powder in THF overnight, a pink solution is obtained indicating further reduction of the initially formed green radical [**40**]˙. This reaction cleanly yields the diamagnetic complex ZnOTf[**40**], as determined by ^{1}H NMR spectroscopy. Single crystals were investigated by X-ray crystallography, which showed coordination of a ZnOTf$^+$ fragment to the Ir center (see Figure 53a). Thereby, a metal-metal bond (Ir−Zn) is formed. This means that zinc, which has a rather positive reduction potential, is still able to successively transfer two electrons under these conditions, which is probably facilitated by the coordination of Zn to Ir. DFT calculations revealed the presence of a MO with an overlap of Ir and Zn based orbitals, as depicted in Figure 53b. This bimetallic core contains a Lewis-acidic ZnOTf$^+$ fragment bound to a Lewis-basic [Ir(trop$_2$dad)]$^-$ fragment. The donor-acceptor interaction of MOs is depicted in Figure 53b and is assumed to be the reason for the very intense pink-purple colour observed for ZnOTf[**40**].
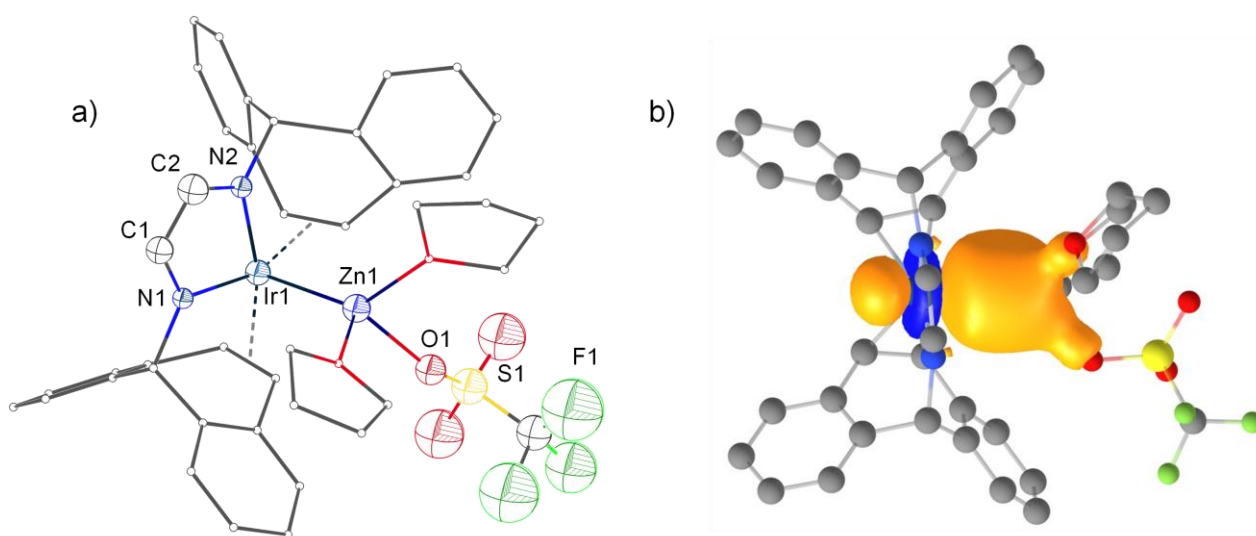
Figure 53. a) Solid state structure of ZnOTf[**40**]. Hydrogen atoms, counter ions and solvent molecules omitted for clarity, b) orbital plot of the relevant MO showing an overlap between Ir and Zn.

Former members of the Grützmacher group (Tewes and Häbe) have employed sodium as a reductant and analyzed the reactions by NMR spectroscopy,[174,176] but did not obtain any crystallographic data or any indications about the molecular structure of the assumed product. Starting from the previous experimental procedures, a modified protocol was developed in this work which allowed for the crystallization of the reduced iridium complexes.

It was possible to obtain a solid state structure which showed close contact of a sodium cation to the dad backbone in complex Na[**40**], as depicted in Figure 54. The overall structure is typical for a (hetero)cyclopentadienide ion interacting with an alkali metal cation. Three molecules of THF are additionally coordinated to the Na atom. The dad fragment likely carries most of the negative charge of the complex and forms a close ion pair with the sodium ion – that is the interaction between the IrN$_2$C$_2$$^-$ cycle and Na$^+$ which is electrostatic in nature. In contrast, NMR spectroscopy in solution

showed the formation of a symmetrical species, which indicates that the solvated sodium ion is likely not bound in solution (alternatively it may dissociate and be re-coordinated from the opposite side to the Ir-N_2C_2 cycle).
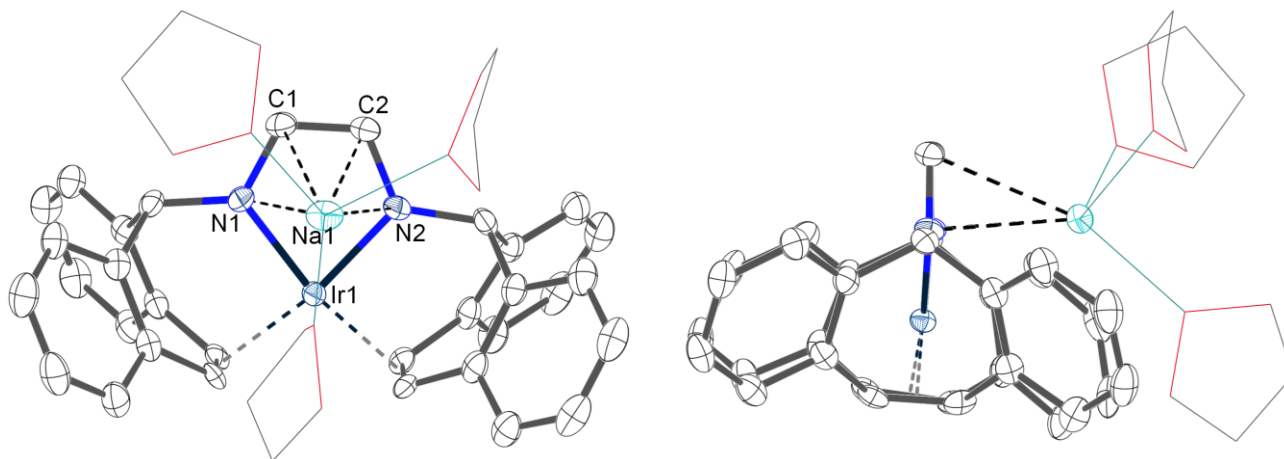
Figure 54. Solid state structure of Na[**40**] from different perspectives. Hydrogen atoms omitted for clarity.

If an excess of elemental lithium sand is used as a reducing agent, the poorly soluble green [**40**]OTf is reduced to the highly soluble grass green [**40**]ˑ which is then quickly further converted to the symmetrical, red Li[**40**] complex after stirring for 30 min. NMR spectroscopic data of the solution are in agreement with previously reported spectra with Na as reductant.[174] When reacted for a longer period of time, an unsymmetrical compound is obtained, as determined by ¹H NMR. Single crystals showed that it is a four times reduced species Li$_3$[**41**], the solid state structure is depicted in Figure 55. Three Li⁺ ions are coordinated and a striking structural change within the tetradentate ligand is observed: the trop moiety is cleaved off at the nitrogen atom of the dad backbone, but still remains in contact via Li-ion interactions. In this structure, the trop itself was reduced to the trop-anion, leading to a negatively charged, planar seven membered ring with conjugated phenyl rings. Formally, the structure of Li$_3$[**41**] is the result of a reductive insertion of a [Li(THF)$_2$] fragment into the N-trop bond. Note, that the both C=C_{trop} units – the one of the remaining intact N-trop unit and the one of the [trop]⁻ anion – remain coordinated to the iridium center. The trop-anion shows π-metal interactions with all three lithium ions, which are surrounded by three terminal THF molecules and one bridging one. The ¹H NMR spectrum matches the previously described asymmetric complex with Na metal as reductant.[174] This shows that upon prolonged reaction times, the trop moiety in [**40**]OTf can be reduced and in this case a stable complex compound was obtained and could be isolated.
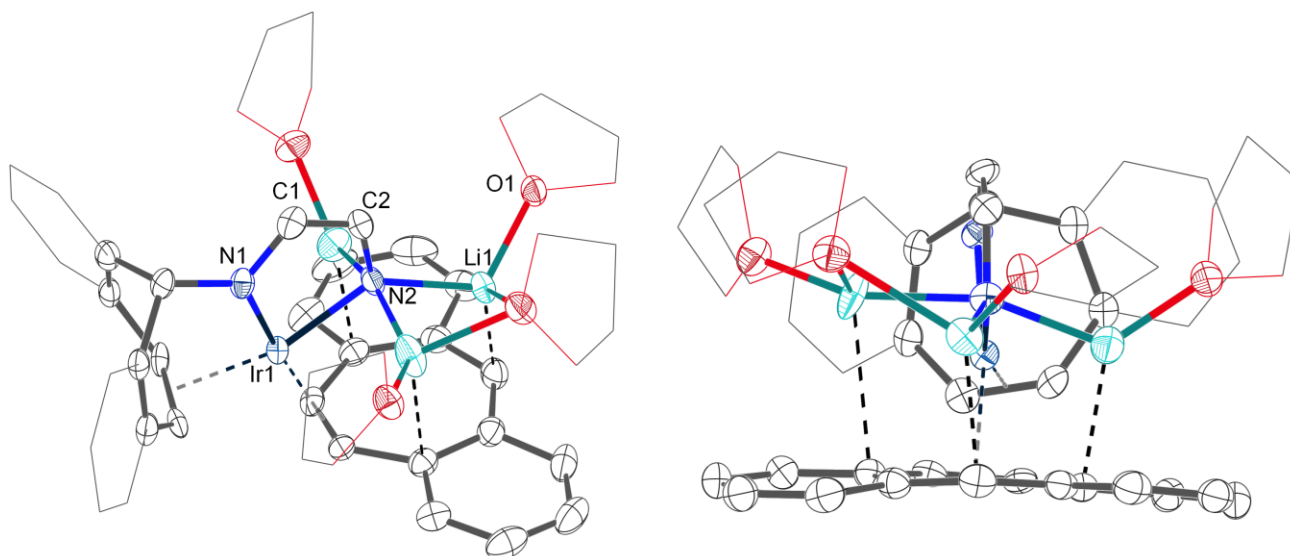
Figure 55. Solid state structure of fully reduced iridium complex Li$_3$[**41**] from different perspectives. Hydrogen atoms and solvent molecules omitted for clarity.

2.3. Organometallic reductants

As previously observed by Tewes, the use of two eq. of CoCp*$_2$ leads to an almost insoluble complex, single crystals were obtained by layering a solution of [**40**]OTf in THF with a solution of CoCp*$_2$.[174] The solid state structure and its NMR data have previously been reported and are listed for comparison in Table 19 and Table 20. If only one equivalent of CoCp$_2$ is used, the mono reduced species can not be isolated. Instead, ^{1}H NMR spectra show a mixture of several species, at least part of them being diamagnetic. If the reaction mixture is stirred over several days, the products start to converge towards one product. In order to find out what this species might be, further investigations were performed. As a result, an unusual dinuclear complex was isolated, which is formed by intermolecular C−C bond formation between two carbon centers within the dad units of two [Ir(trop$_2$dad)] moieties. These investigations are described in detail in subchapter 3.

2.4. Discussion of crystallographic data

An overview on the newly synthesized compounds is given in Scheme 48, crystallographic and NMR data are listed in Table 19 and Table 20, respectively. Visualization of trends in bond lengths is shown in Figure 56. An overlay of ^{1}H NMR spectra is depicted in Figure 57.
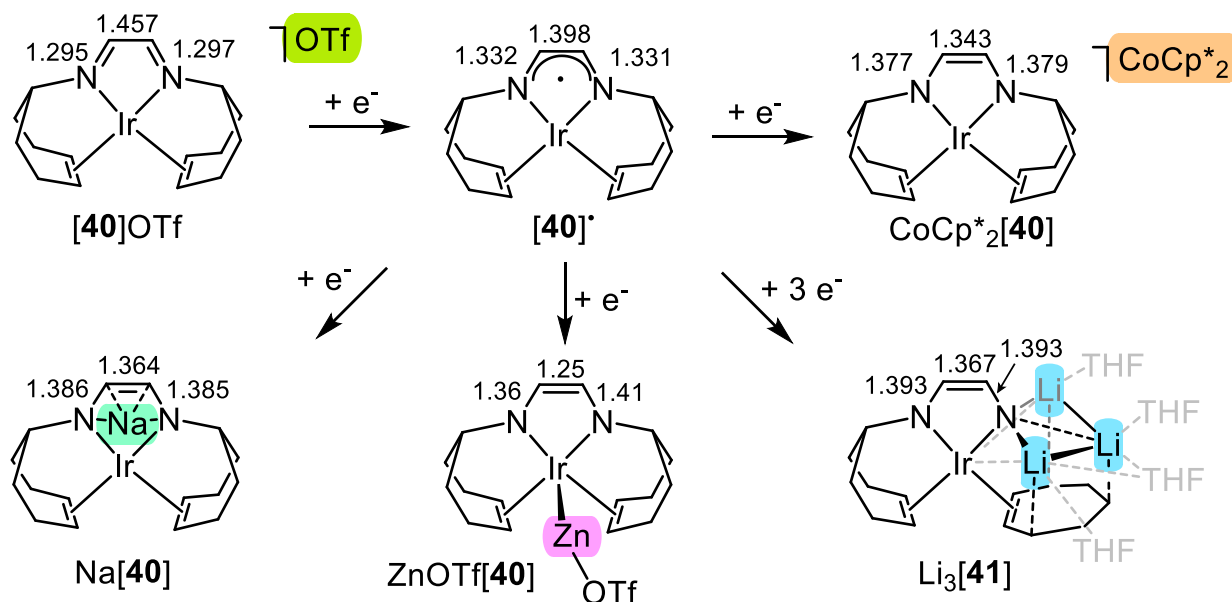
Scheme 48. Structures and bond lengths of all compounds from Chapter V.2.

The iridium center adopts a square planar coordination mode in all complexes (except for ZnOTf[**40**]). The radical complex [**40**]$^\bullet$ shows the expected change in bond lengths in the solid state structure, which are in agreement with DFT calculations from previous protocols.[173] Compared to the parent compound [**40**]OTf, the distances in the dad backbone of [**40**]$^\bullet$ show elongation of the N$-$C$_{dad}$ bonds (from 1.296 Å to 1.332 Å), while the C$-$C$_{dad}$ bond is significantly shortened (from 1.457 Å to 1.398 Å). At the same time, the Ir$-$N distances decrease from 2.012 Å to 1.992 Å (see also Table 19). As reported before, the bond lengths indicate that the unpaired electron is located on the dad backbone, while the metal center remains as d^8 Ir^I.[173]

The same trend is true for the doubly reduced [CoCp*$_2$][**40**], where the N$-$C$_{dad}$ bonds are further elongated (average 1.378 Å), while the C$-$C$_{dad}$ bond shortens to 1.343 Å. This structural change in the ligand framework indicates that the reduction takes place within the diazadiene unit, moving towards a bisamido olefin species. The changes in relevant bond lengths along the redox series is visualized in Figure 56.

Na[**40**], and [CoCp*$_2$][**40**] show very similar structural properties, although the dad and Ir$-$N bond lengths are slightly elongated due to the interaction of the Na cation with the ligand. The distance from Na to the centroid of the dad ligand is found at 2.53 Å, while there is little interaction between Ir and Na, as they are 3.11 Å apart.

114
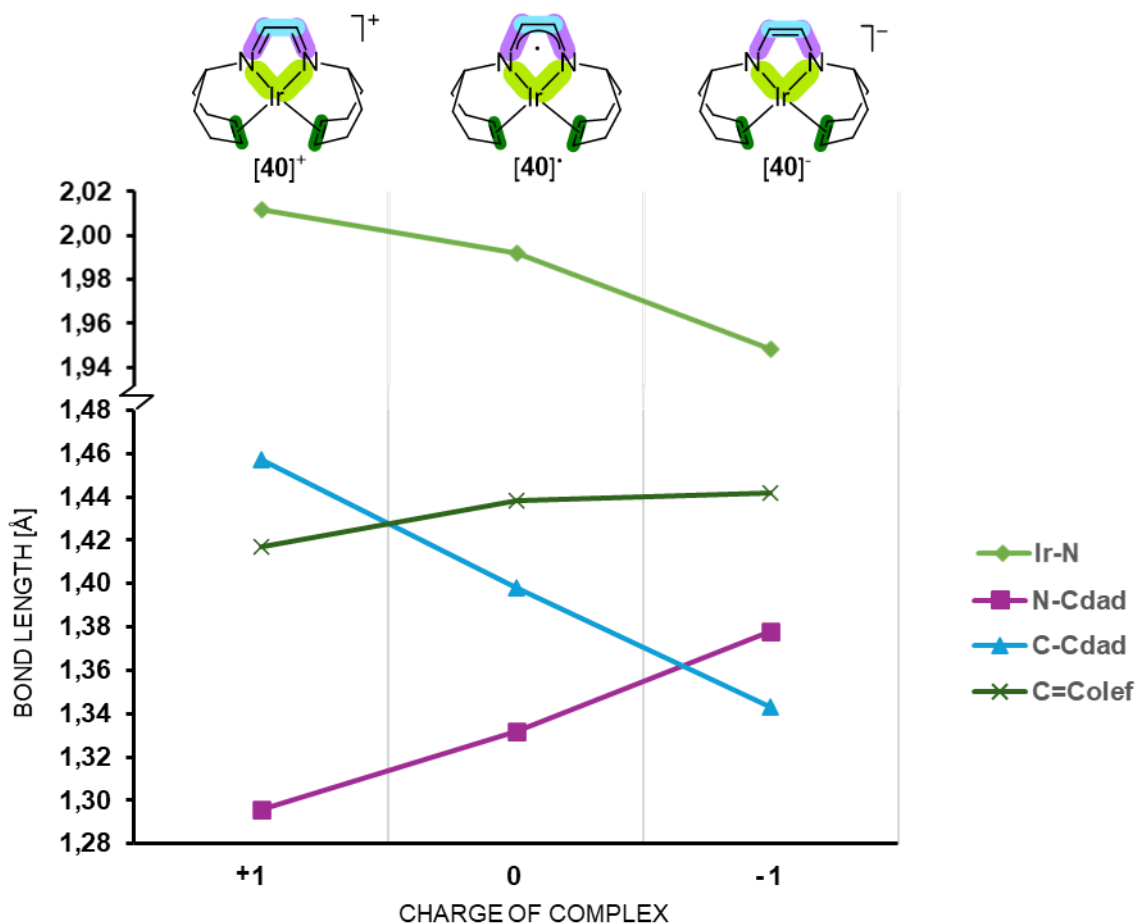
Figure 56. Summary of significant ligand bond distances across the redox series of [Ir(trop₂dad)] complexes.

Bond lengths of the dad fragment in Li3[**41**] are indistinguishable from the ones found in Na[**40**] within the accuracy of the measurement. After the dad backbone is reduced twice, further reduction leads to C−N bond cleavage since it can not take up more electrons. One trop fragment is reduced by one electron to become a planar trop-anion, which is still coordinated to Ir via the olefinic carbon atoms. The fourth electron in the reduction process leading to Li3[**41**] is stored at the nitrogen atom, which is not bound to trop anymore. Instead, three lithium cations connect the two ligand fragments with N−Li distances between 2.02 and 1.98 Å. The interaction of Li to the plane of the trop-anion is between 2.19 and 2.79 Å in distance.

In ZnOTf[**40**], the iridium center resides in a square pyramidal coordination sphere with −ZnOTf⁺ coordinated as a fifth ligand. This bimetallic interaction shows a Ir1 to Zn1 distance of 2.48 Å which is similar to previously reported unsupported Ir−Zn bonds.[177] The quality of the obtained single crystals was too low to allow for a detailed discussion of structural parameters. Although, it seems like the C−C bond is shortened even more and C−N is probably elongated, when compared to [CoCp*₂][**40**] or Na[**40**].

Table 19. Selected bond lengths [Å] of reduced species obtained from [**40**]OTf.

Charge	Compound	Ir−N	N−C$_{dad}$	C−C$_{dad}$	C=C$_{olef}$
+1	[**40**]OTf	2.013(1) 2.011(1)	1.295(2) 1.297(2)	1.457(3)	1.415(4) 1.418(3)
0	[**40**]•	1.990(2) 1.993(2)	1.332(3) 1.331(4)	1.398(4)	1.442(4) 1.430(4)
-1	[CoCp*$_2$][**40**]	1.952(5) 1.943(5)	1.379(8) 1.377(8)	1.343(8)	1.441(7) 1.443(8)
-1	Na[**40**]	1.971(3) 1.969(2)	1.386(4) 1.385(5)	1.364(5)	1.457(7) 1.449(4)
-1	ZnOTf[**40**]	1.94(4) 1.96(4)	1.36(6) 1.41(7)	1.25(7)	1.40(4) 1.43(5)
-3	Li$_3$[**41**]	1.970(3)[a] 2.034(3)[b]	1.393(5) 1.393(6)	1.367(5)	1.446(5)[a] 1.422(5)[c]

[a] Trop, [b] −N^{2-}, [c] trop-anion.

2.5. Discussion of NMR data

Another indication of the change of the electronic structure of the ligand upon reduction is the trends seen in the significant chemical shifts in the ^{1}H NMR spectra, where signals for C*H*$_{benz}$, *H*C=N and C*H*$_{olef}$ shift to lower frequencies (see also Table 20). A comparison of ^{1}H NMR spectra of complexes [**40**]OTf, [**40**]• and Na[**40**] is depicted in Figure 57. [**40**]OTf shows a symmetrical species with indicative resonances at 9.4 ppm corresponding to the dad protons *H*C=N. ^{1}H NMR of the radical species [**40**]• shows very broad signals around 12.7, 10.2 and 7.1 ppm, although no assignment could be done due to the paramagnetic properties of the compound. The double reduced complex [**40**]⁻ is diamagnetic and shows lower frequency shifts of all resonances in ^{1}H NMR with respect to [**40**]OTf (compare Table 20). While benzylic protons (C*H*$_{benz}$) are shifted by around 1.5 ppm, the variation for dad (*H*C=N) and olefinic (C*H*$_{olef}$) protons is more pronounced: 9.4 to 6.0 – 7.5 ppm ($\Delta\delta^1H_{HC=N} \approx 2.5$ ppm) and 5.6 to 2.7 ppm ($\Delta\delta^1H_{olef} \approx 3$ ppm), respectively.
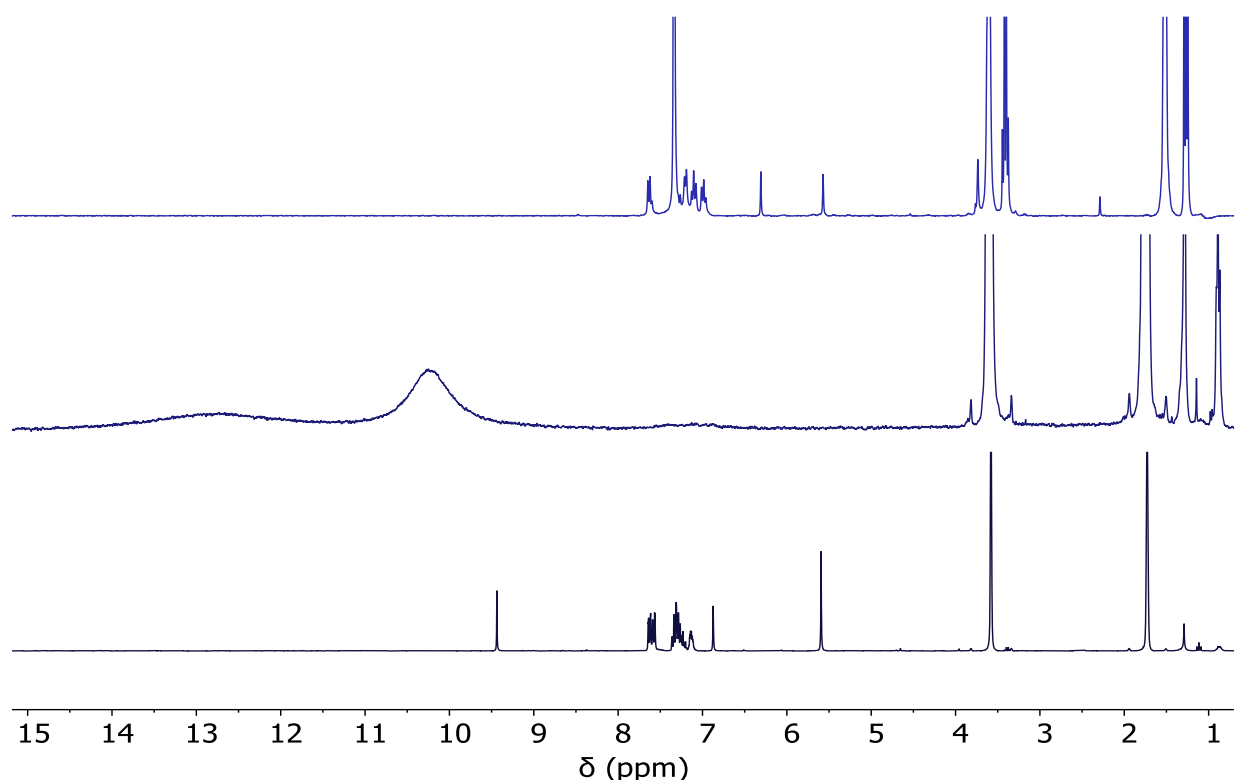
Figure 57. Comparison of ^{1}H NMR spectra of complexes Na[**40**], [**40**]• and [**40**]OTf (top to bottom).

The ^{1}H NMR spectrum of complex ZnOTf[**40**] shows an asymmetric species with $\delta^1H_{HC=N} = 7.15$ ppm, which is an intermediate shift compared to the doubly reduced species [CoCp*$_2$][**40**] where these protons resonance at 6.13 ppm and in cationic [**40**]OTf at 9.44 ppm. Furthermore, benzylic and olefinic protons in ZnOTf[**40**] show an intermediate chemical shift between [**40**]OTf and [CoCp*$_2$][**40**] (see Table 20).

Table 20. Selected ^{1}H and ^{13}C NMR chemical shifts [ppm] of reduced species derived from [**40**]OTf.

Charge	Compound	^{1}H NMR			^{13}C NMR		
		CH_{benz}	HC=N	CH_{olef}	CH_{benz}	C$_{dad}$	CH_{olef}
+1	[**40**]OTf	6.87	9.44	5.59	75.8	171.1	74.5
0	[**40**]•	12.73, 10.24, 7.40, 7.13, 6.87 (very broad)			-	-	-
-1	Na[**40**]	5.26	7.57	2.59	77.5	129.4	45.2
-1	[CoCp*$_2$][**40**]	5.11	5.97	2.80	-	120.1	49.1
-1	ZnOTf[**40**]	5.97	7.15	3.70, 4.11	-	-	-

3. Reaction of [40]OTf with reductive bases

3.1. Synthesis of dimerized species [42]

The addition of 1 eq. of base was found to have a large influence on the alcohol oxidation with catalyst [40]OTf. While for the investigated amine complex [38]OTf, the effect of the base is clear - deprotonation of the NH bonds in order to obtain the active amido species - it was not clear for [40]OTf lacking such acidic protons. It was reported that the addition of NaO*t*Bu to the reaction mixture allows lowering the catalyst loading from 0.1 mol% to as low as 0.01 mol%.[174] It was assumed that the base was necessary to activate the alcohol by deprotonation to form the alcoholate. But since the green parent compound [40]OTf immediately changes its colour to bright red upon addition of base, there must be some interaction with the iridium complex.

NaO*t*Bu and KO*t*Bu are known to not only act as bases but can also act as reductants. The role of KO*t*Bu as electron transfer reagent has been broadly investigated and often includes a radical mechanism.[178] This shows that this compound, generally classified as "strong base", is able to react in many more ways than simple deprotonation reactions. If [40]OTf was subjected to such a base, coordination of an −O*t*Bu fragment to the Ir center under formation of a penta-coordinated species does not take place, although previously observed before for S, Se and Te containing fragments.[176] By reaction of [40]OTf with 1 eq. of NaO*t*Bu in THF and crystallization from Et_2O at -20 °C, red single crystals were obtained which were subjected to XRD methods. Data analysis revealed a bimetallic complex which dimerized via C−C bond formation, the solid state structure of [42] is shown in Figure 58. If this reaction is monitored by ^{1}H NMR, no clean product can be observed, but a mixture of several compounds is present. Since this reaction is slow to converge to the final product, and the use of NaO*t*Bu leads to many side-products, the synthesis of dimeric [42] was optimized by using KH as reactant, which – again – can act as both: base and reductant. The synthetic pathway to obtain [42] is shown in Scheme 49.
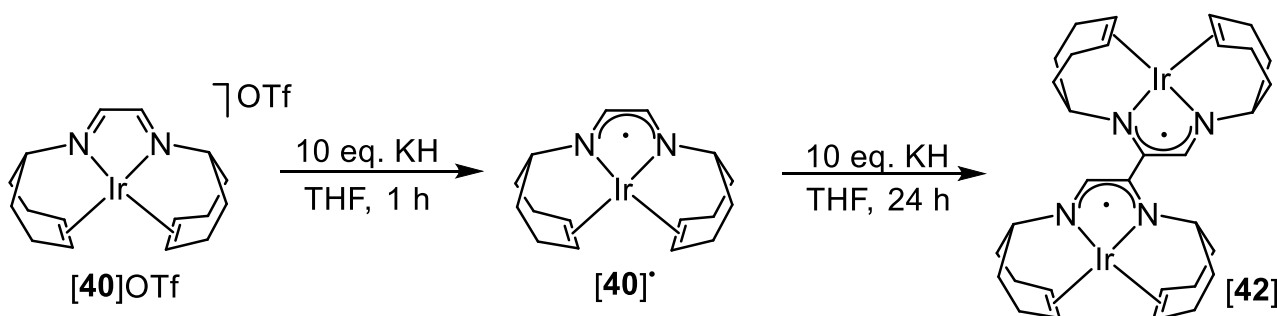
Scheme 49. Synthesis of dimeric species [42] from [40]OTf via [40]· with excess KH in THF.

Dimerization was also observed when only one equivalent of $CoCp_2$ was used (see also Section V.2.3). Since this reaction proceeds rather slowly, the use of two equivalents of $CoCp_2$ still leads to the monomeric anion [40]⁻ as it immediately crystallizes from the solution and thus does not leave a the [Ir(trop₂dad)]· radical formed as intermediate to dimerize upon C−C bond formation. In

order to obtain the dinuclear complex [**42**], rather precisely one equivalent of reducing agent has to be applied (except for solid KH), as various other reactions take place if used in excess (compare previous subchapter 2).
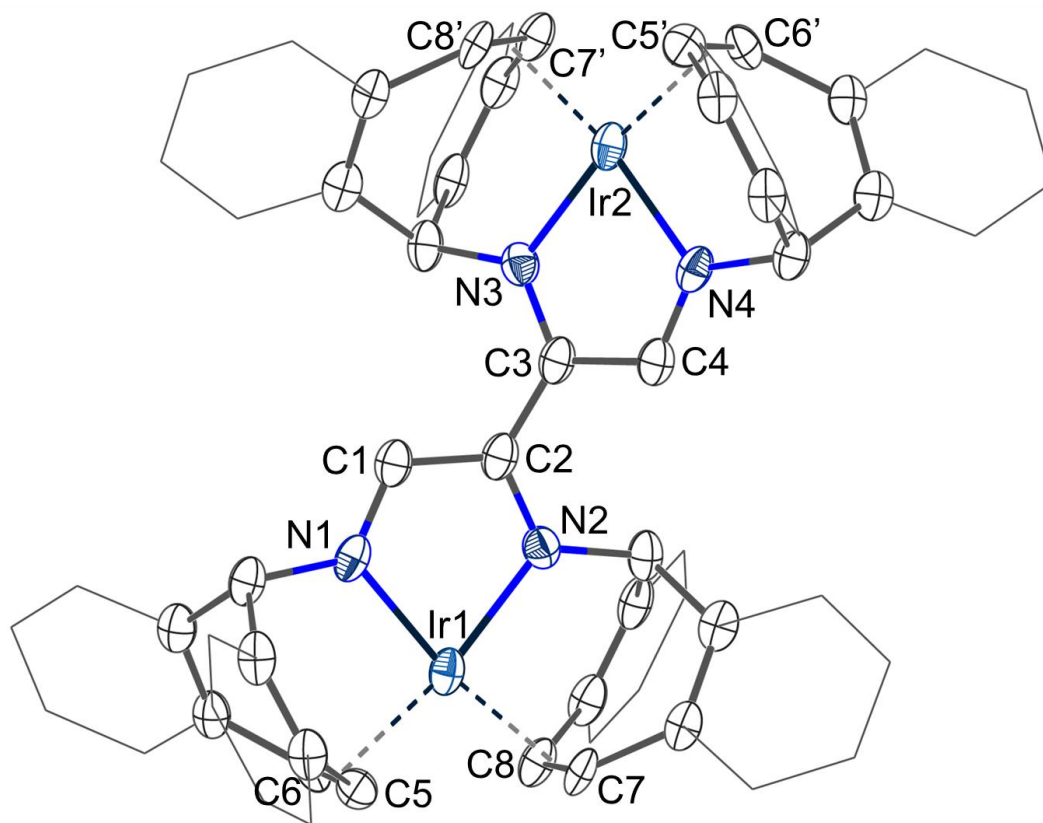
Figure 58. Solid state structure of [**42**]. Solvent molecules and hydrogen atoms omitted for clarity.

3.2. Structural characterization of [42]

Upon reduction and deprotonation of [**40**]OTf, again, reactivity at the ligand was observed. The solid state structure of [**42**] is shown in Figure 58, selected bond lengths and angles are listed in Table 21. The new C−C bond bridging the two dad units is in the range of a rather long double bond with 1.39 Å (C2−C3). Note that the two fragments do not form a planar $N_2C_4N_2$ π-system, but instead exhibit an angle of 133.3(3)° (twist angle between the N−C−C−N planes). The dimeric structure is asymmetric, where Ir−N and N−C bonds directly connected to the new C2−C3 bond (Ir1−N2, N2−C2, Ir2−N3, N3−C3,) are elongated compared to the ones further away from C2−C3 (N1, C1, N4, C4): the N−C$_{dad}$ bond lengths are elongated from 1.30 Å in [**40**]OTf to an averaged 1.36 Å (N2−C2, N3−C3) and 1.31 Å (N1−C1, N4−C4) in [**42**]. On the other hand, the C−C$_{dad}$ bonds are shortened from 1.46 Å to an averaged 1.43 Å. This change in bond distances indicates that delocalization of electrons along the backbone occurs. Bond distances from iridium to the nitrogen donor atoms are at 2.03 Å (Ir1−N2, Ir2−N3) and 2.00 Å (Ir1−N1, Ir2−N4) in average. Interestingly, for [**40**]OTf, the respective value is in the middle at around 2.01 Å, which means the dimerization leads to elongation

of one side while shortening the other. The C=C distances of the olefinic protons remain unchanged within the error of the measurement (all around 1.42 Å).

There is no clear trend observable when compared to the cationic or neutral monomeric species, some bond lengths are more similar to [**40**]OTf and some are closer [**40**]· (see Table 21). Significant are only the C−C$_{dad}$ distances, which decrease from [**40**]OTf to [**42**] to [**40**]·. A visualization of trends of bond distances is shown in Figure 59. Comparison needs to be done carefully, as the new C−C bond (replacing a C−H bond) has to be taken into account.
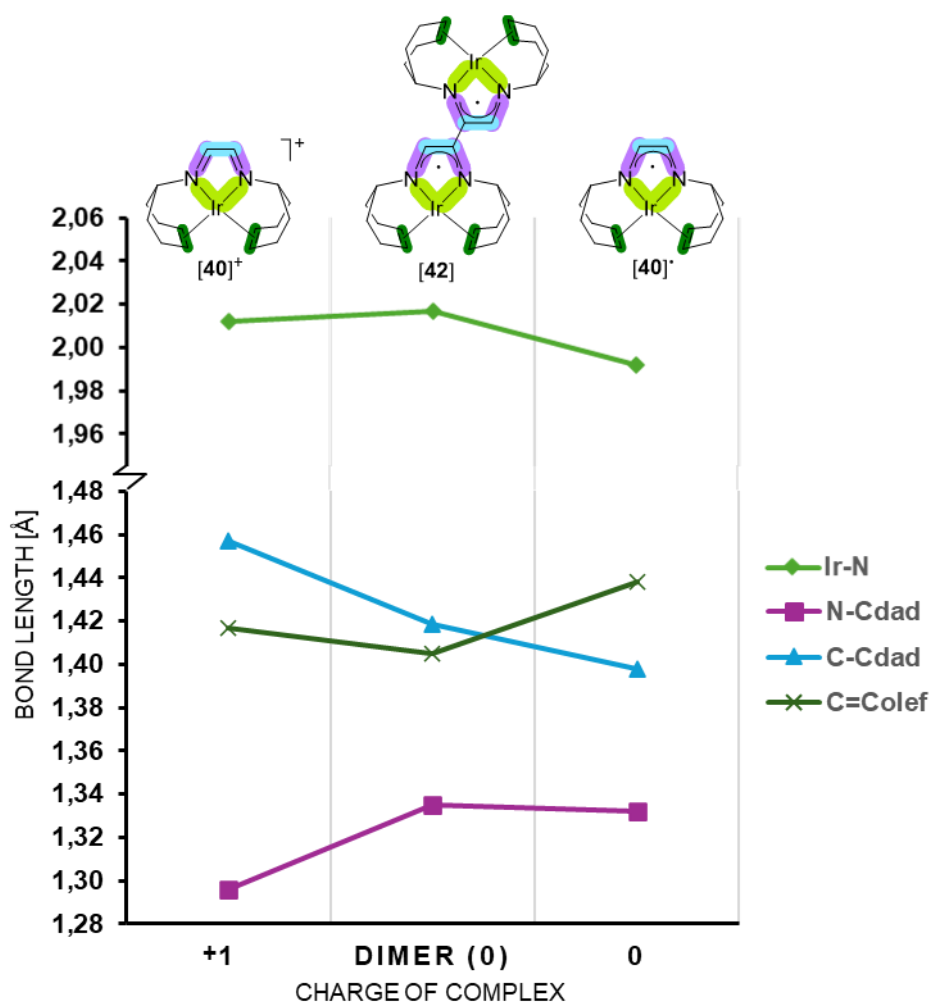
Figure 59. Summary of bond lengths of iridium dimer [**42**] with cationic [**40**]OTf and the neutral species [**40**]·.

Table 21. Selected bond lengths [Å] of dimeric species [**42**] compared to respective monomeric species.

Compound	Ir−N	N−C$_{dad}$	C−C$_{dad}$	C=C$_{olef}$
[**40**]OTf	2.013(1) 2.011(1)	1.295(2) 1.297(2)	1.457(3)	1.415(4) 1.418(3)
[**42**]	2.044(10)[a] 2.005(12) 2.021(10)[a] 1.997(14)	1.347(18)[a] 1.304(17) 1.378(17)[a] 1.310(16)	1.411(20) 1.451(19) 1.393(16)[b]	1.41(2) 1.42(2) 1.38(2) 1.41(3)
[**40**]•	1.990(2) 1.993(2)	1.332(3) 1.331(4)	1.398(4)	1.442(4) 1.430(4)

[a] Part of the N2−C2−C3−N3 chain, [b] new C−C bond (C2−C3).

3.3. NMR spectroscopic characterization of [42]

NMR spectroscopic analysis revealed that the dimerization leads to a loss in symmetry in [**42**] and the compound is indeed diamagnetic. Individual sets of signals are observed, in the ^{1}H NMR spectrum four doublets appear for the olefinic protons of the trop-fragment, as they couple with each other if they are not equivalent as in [**40**]OTf, where the coupling cannot be observed and only one singlet appears (a comparison of spectra is depicted in Figure 60). Furthermore, these signals appear at lower chemical shift of up to 2 ppm for [**42**] when compared to [**40**]OTf (CH_{olef} for [**40**]OTf δ[1]H = 5.59 ppm; and for [**42**] δ[1]H = 3.64, 3.96, 4.07, 4.29 ppm). The same trend to lower ppm is observed for CH_{benz} (from 6.87 ppm to 5.47 and 5.77 ppm) and the protons at the dad backbone (HC=N) (from 9.44 ppm to 7.89 ppm). Note that the integral for HC=N is half of the parent compound due to the removal of hydrogen atoms during dimerization. The same trends are observed for ^{13}C NMR data, as seen in Table 22.

A clear trend of indicative signals in ^{1}H NMR is observed when dimeric [**42**] is compared to the less or more reduced counterparts ([**40**]OTf and [CoCp*$_2$][**40**], respectively), as shown in Figure 61. The resonances for HC=N, CH_{olef} and CH_{benz} in [**42**] lay right in between the cationic and anionic species and show an almost linear trend.
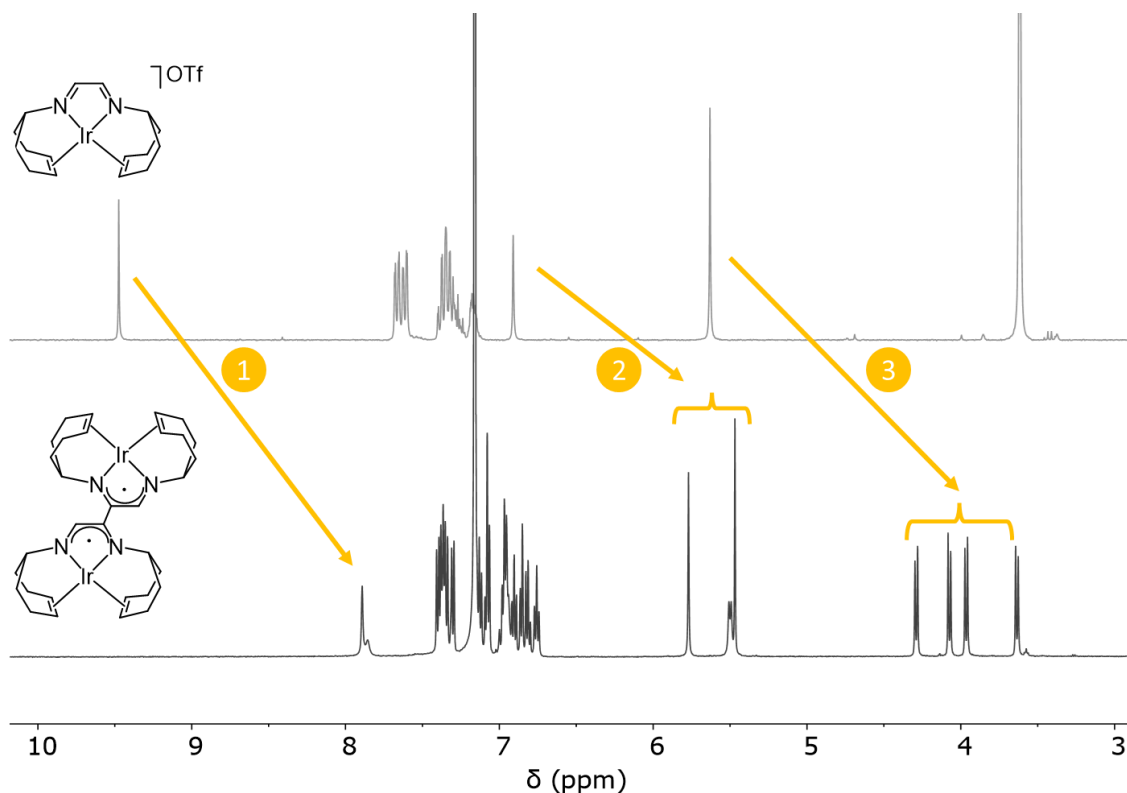
Figure 60. Overlay of ^{1}H NMR of [**40**]OTf (top) vs. [**42**] (bottom). The following numbering scheme is used: (1) *H*C=N, (2) C*H*benz, (3) C*H*olef. The loss of symmetry is seen by the inequivalent signals for each proton.
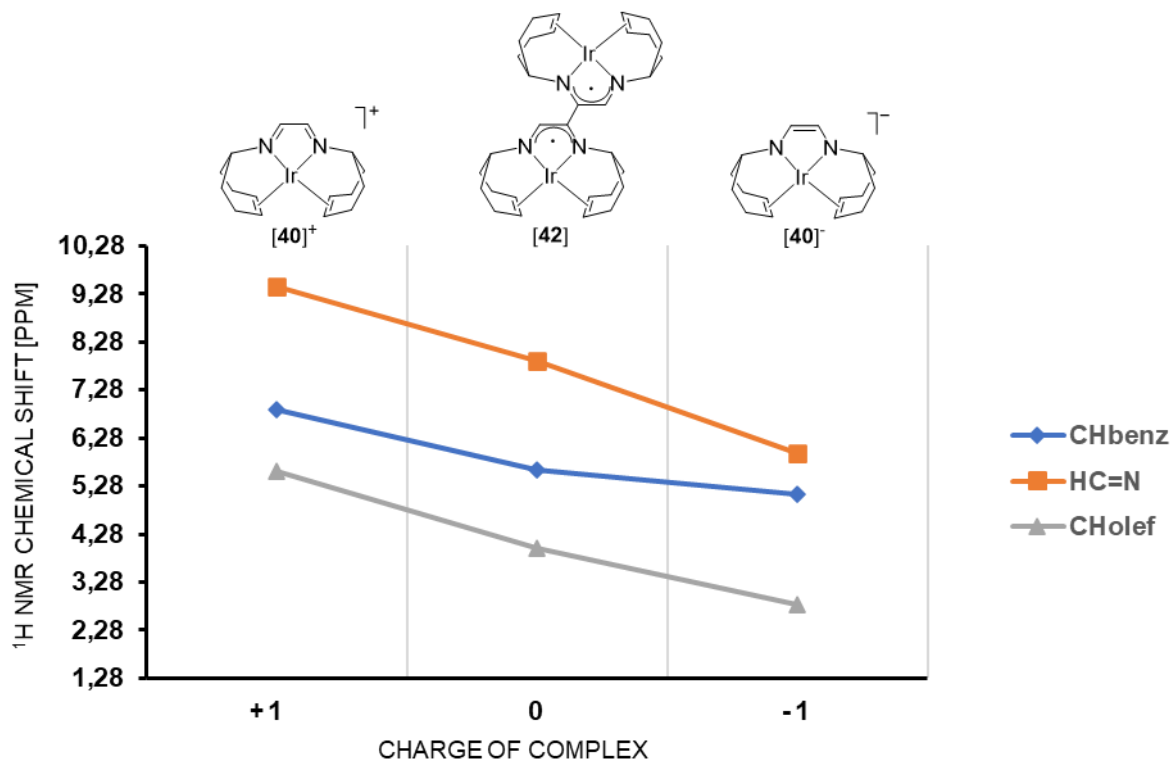
Figure 61. Summary of ^{1}H NMR chemical shifts, comparison of [**42**] with cationic [**40**]OTf and anionic [CoCp*$_2$][**40**].

Table 22. Selected ^{1}H and ^{13}C NMR chemical shifts [ppm] of [**40**]OTf, dimeric [**42**] and [CoCp*$_2$][**40**].

Compound	^{1}H NMR			^{13}C NMR		
	C*H*$_{benz}$	*H*C=N	C*H*$_{olef}$	*CH*$_{benz}$	*C*$_{dad}$	*CH*$_{olef}$
[**40**]OTf	6.87	9.44	5.59	75.8	171.1	74.5
[**42**]	5.77 5.47	7.89	3.64 3.96 4.07 4.29	70.44 75.76	155.00	64.82 64.61 58.22 57.67
[CoCp*$_2$][**40**]	5.11	5.97	2.80	-	-	-

3.4. UV-Vis

UV-Vis spectra of [**40**]OTf, [**40**]$^\bullet$ and [**42**] were measured in THF and are shown in Figure 63. In agreement with its reduced cationic charge (0 vs +1), [**40**]$^\bullet$ shows red-shifted maxima compared to the starting material [**40**]OTf, although the shift is rather modest (413 and 560 nm vs. 440 and 587 nm). As a consequence, both compounds appear green in solution. The spectrum of dimeric [**42**] shows a strong absorption maximum at 965 nm and a second peak at 331 nm, therefore the complex appears red in solution. These wavelengths are in strong contrast to the monomeric species and might result from conjugation of the dimerized dad backbone. TDDFT calculations for diiridium complex [**42**] are seen as overlay in Figure 63c. The calculations were performed with THF solvent model and broken symmetry option. In comparison to the experimental spectrum, the peak at highest wavenumbers differs around 200 nm (965 nm measured vs. 762 nm calculated), which is a rather large deviation. Given the overall shape of the spectrum together with the particularity of this very intense, sharp peak at high wavenumbers, the calculations are in acceptable agreement with the experimental data. Further theoretical investigations found that the TDDFT spectrum of the free ligand (trop$_2$dad)$_2$ exhibits similar features (Figure 63d) as with iridium atoms bound, therefore it is assumed that the sharp peak at high wavenumbers is a result of the conjugation of the ligand, rather than the interaction with the metal centers.
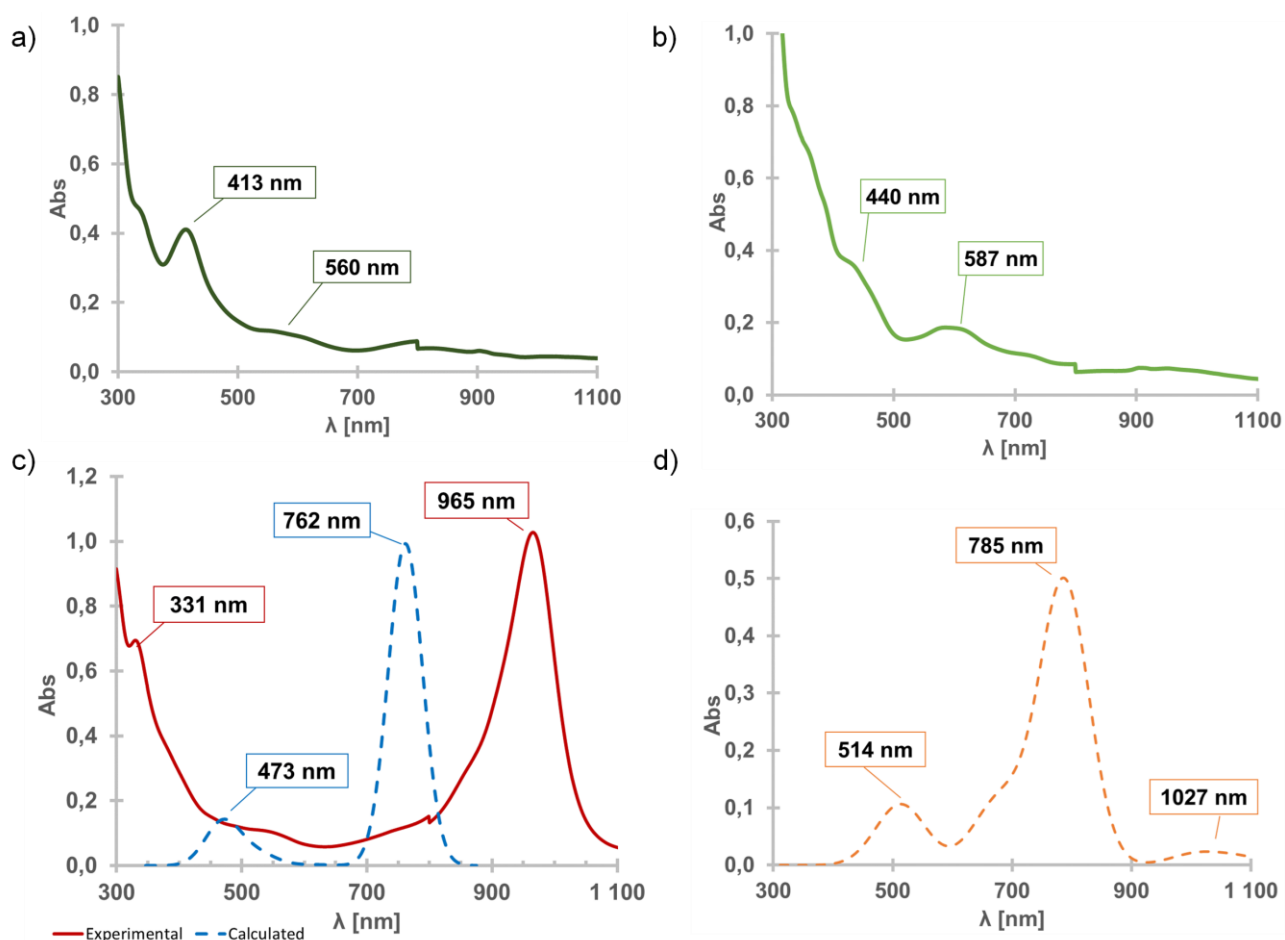
Figure 62. UV-Vis spectra of solutions in THF a) [**40**]OTf, b) [**40**]$^{\bullet}$ c) [**42**], overlay of experimental (red) and TDDFT calculated spectra (blue) and d) TDDFT calculated spectrum of the free ligand (trop$_2$dad)$_2$ as a neutral singlet.

3.5. Theoretical investigations

The electronic properties of neutral diiridium species [**42**] were analyzed with DFT calculations. The compound is neutral and diamagnetic, but the electronic structure may not be easily interpreted in a straightforward manner. For example, in order to allow for diamagnetism, the metal centers can be assumed to be iridium(+I) with an electron configuration of d^8. In that case, the ligand framework must be double negatively charged in an overall neutral species. The dad fragments are not arranged in a co-planar fashion but enclose a twist-angle of 133.3°, as seen in the solid

state structure (see section 3.2), which means that the electronic structure is more complicated than just a conjugated π-system with paired electrons. It can be assumed that each of the single electrons is delocalized over one dad unit, which leads to a diradical where both radicals are connected via a covalent C−C bond. This diradical can in principle have a triplet or singlet structure. Broken symmetry DFT calculations indicate that the singlet state is more stable than the triplet state by 8.48 kcal·mol^{-1}. A spin density plot is shown in Figure 63 where it is apparent that the two electrons are of opposite

spin and located exclusively on the dad units, which form a twisted N_4C_4 core. CASSCF(2,2) calculations revealed a 26 % diradical character, which was determined via the beta index.[179]
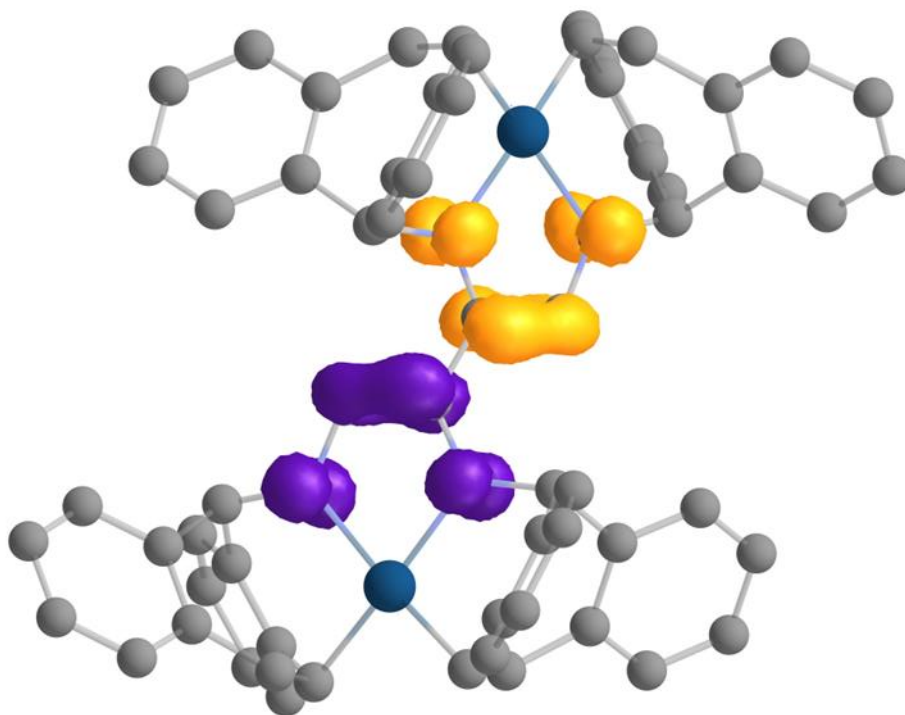
Figure 63. Spin density plot of [**42**] calculated with broken symmetry DFT methods.

DFT calculations of molecular orbitals (MO) with CASSCF(2,2) showed that one of the unpaired electrons is described by SOMO 1 mainly located along the C_4N_4 chain of the dad$_2$ backbone (C1−C2−C3−C4) with an occupancy of 1.19 (Figure 64a). The second electron with opposite spin occupies SOMO 2, which is delocalized over the same atoms (Figure 64b).
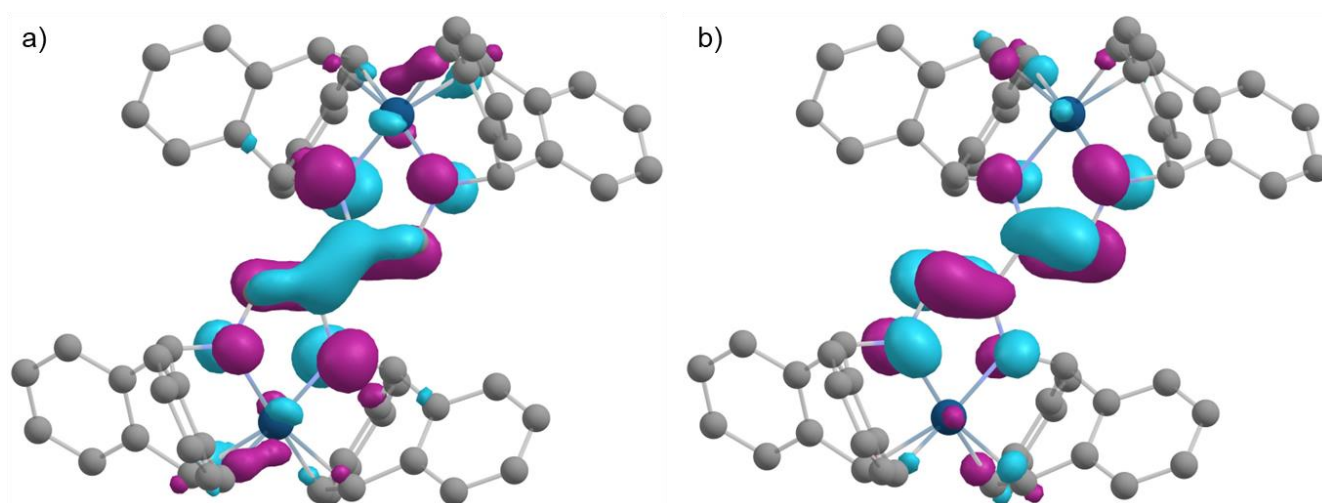
Figure 64. Calculated MOs of [**42**]: a) SOMO 1, occupancy 1.19; b) SOMO 2, occupancy 0.81.

3.6. Mechanistic investigations on the dimerization reaction

After reduction of [**40**]OTf, deprotonation of *H*C=N needs to occur for dimerization and formation of the new C−C bond in [**42**]. Therefore, the most effective reactants for dimerization seemed to be those, that can act as a reductant as well as a base, such as MO*t*Bu or MH (M = Na, K). The best results were obtained with KH added in excess to [**40**]OTf in THF. Thereby, the paramagnetic, green [**40**]˙ was observed as an intermediate via NMR, which then reacts to the [**42**] dimer.

The mechanism is still not clear but is assumed to proceed via a radical mechanism. MO*t*Bu are known to undergo radical reactions, as mentioned in Chapter V.1. The dimerization can be followed by NMR spectroscopy, but no clean reaction mixture is obtained. If TEMPO is added as radical scavenger to a solution of [**40**]OTf, no colour change from green to red appears after addition of KO*t*Bu. In contrast to the absence of TEMPO, a grass green homogeneous solution is obtained, that contains paramagnetic species. The ^{1}H NMR chemical shifts and the colour indicate that the addition of KO*t*Bu with TEMPO present did not lead to a dimerization reaction as in previously described reactions without TEMPO. Instead, complex [**40**]OTf is reduced to the [**40**]˙ radical. This supports the assumption that the dimerization reaction described earlier proceeds via a radical mechanism, which is suppressed with TEMPO present and the base only acts as reducing agent under these conditions. A possible reaction mechanism is depicted in Scheme 50.
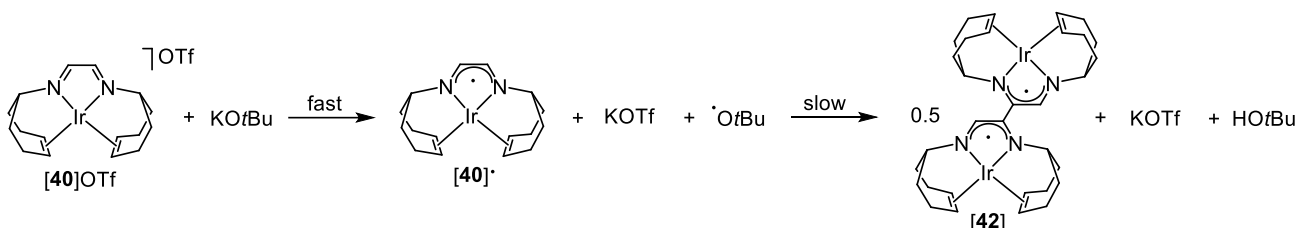
Scheme 50. Possible mechanism for the dimerization of [**40**]OTf with KO*t*Bu as reductant to form [**42**].

4. Other reactivities

4.1. Nucleophilic addition at [40]OTf
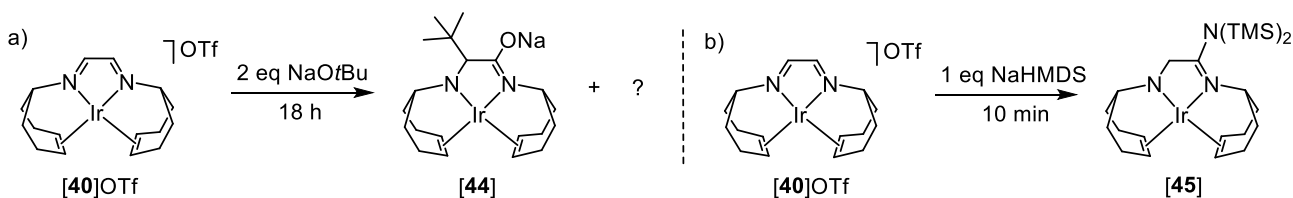
Scheme 51. a) Reaction of [**40**]OTf with 2 eq. of NaO*t*Bu; b) reaction of [**40**]OTf with 1 eq. of NaHMDS.

As described in the previous section, the addition of one equivalent of NaO*t*Bu base slowly leads to the formation of dimeric diiridium complex [**42**]. Although, if 2 eq. of NaO*t*Bu are added to [**40**]OTf, no dimerization is observed (similar to the use of two eq. of reductant). Instead, a mixture of at least two distinct compounds was seen in NMR spectra. One of them could be structurally analyzed by measuring XRD on a single crystal obtained from the reaction solution. This compound [**44**] formally

is the result of the addition of NaO*t*Bu to the dad backbone of the ligand. The solid state structure is shown in Figure 65. The *tert*-butyl group is attached to one dad carbon. This leads to a saturated C−N bond within the C_4N_4 backbone. On the other side, the −ONa fragment has replaced the hydrogen atom at *H*C=N. Most likely, the backbone was deprotonated by the second equivalent of base present. In the solid state, a dimer containing a central Na_2O_2 ring is formed as shown in Figure 65. Selected bond lengths are listed in Table 23 and show single bond character for N1−C1 (1.452 Å) and C1−C2 (1.542 Å) while C2−N2 remains unsaturated (1.325 Å). Due to this nucleophilic addition reaction, the conjugation of the former diazadiene is broken and the fragment coordinates as a mixed amido imino ligand. This is also reflected by the difference in Ir−N bond lengths: 1.959 Å for N1−Ir1 and 2.024 Å for N2−Ir1. Unfortunately, insufficient amounts of a pure sample could not be obtained and no NMR data can be given.
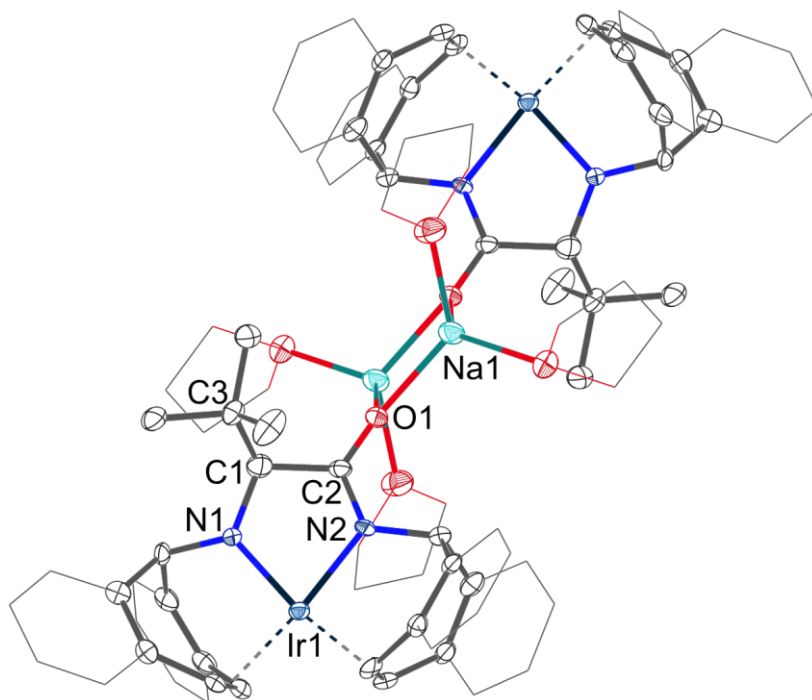
Figure 65. Solid state structure of [**44**]. Solvent molecules and hydrogen atoms omitted for clarity.

Table 23. Selected bond lengths [Å] of [**44**] and [**45**] compared to parent compound [**40**]OTf.

Compound	Ir−N	N−C$_{dad}$	C−C$_{dad}$	C=C$_{olef}$
[**40**]OTf	2.013(1) 2.011(1)	1.295(2) 1.297(2)	1.457(3)	1.415(4) 1.418(3)
[**44**]	1.959(3) 2.024(3)	1.452(5) 1.325(5)	1.542(6)	1.439(6) 1.449(6)
[**45**]	1.932(2) 2.045(2)	1.445(4) 1.302(4)	1.500(4)	1.439(4) 1.450(4)

In the course of screening the reactivity of different types of bases, a clean reaction of [**40**]OTf with NaHMDS was obtained. Surprisingly, in this case, [**42**] was not obtained, as with NaO*t*Bu, but a nucleophilic addition of the −N(TMS)$_2$ fragment at one carbon atom of the dad backbone took place to form compound [**45**]. This reaction is assumed to be accompanied by a proton shift to the adjacent C-atom. This leads to a structural change from the former dad −N=C−C=N− backbone to a −N$^-$−CH$_2$−C(N(TMS)$_2$)=N− fragment, which is coordinated in a mixed amido imino fashion. This is also reflected by the Ir−N bond lengths which strongly diverge: 2.045 Å for Ir−N and 1.932 Å for Ir=N. The saturated fragment shows a N−C bond distance of 1.445 Å while the unsaturated side, bearing the HMDS substituent, is found at 1.302 Å which does not differ significantly from the 1.296 Å of [**40**]OTf. The C−C bond is elongated from 1.457 to 1.500 Å, which shows that the delocalization is cancelled by partial saturation of the backbone. ^{1}H NMR spectroscopy also reflects the asymmetry of the complex, as the benzylic and olefinic protons are not chemically equivalent anymore. See Table 24 for a comparison of [**45**] with [**40**]OTf. δ^{1}H(C*H*$_{olef}$) = 4.11 and 3.37 ppm for [**45**], which is shifted to lower frequencies compared to 5.59 ppm in [**40**]OTf. The outstanding chemical shift of the *H*C=N in [**40**]OTf of 9.44 ppm has disappeared and is replaced with a resonance at 3.37 ppm for [**45**], which corresponds to a typical aliphatic shift.
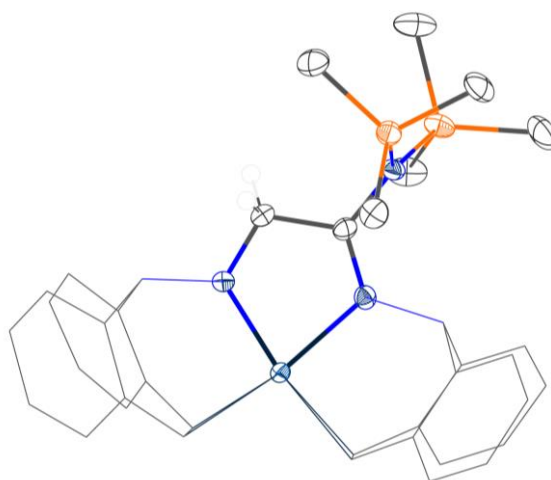
Figure 66. Solid state structure of [**45**]. Solvent molecules and most hydrogen atoms omitted for clarity.

Table 24. Selected ^{1}H NMR data of [**45**] compared to [**40**]OTf.

Compound	^{1}H NMR		
	C*H*$_{benz}$	*H*C=N	C*H*$_{olef}$
[**40**]OTf	6.87	9.44	5.59
[**45**]	6.37 5.26	4.49	4.11 3.37

4.2. Dimerization of methyl-substituted iridium complex [46]OTf

The methyl-substituted analogue to the [**40**]OTf complex, [Ir(^{Me}trop$_2$dad)]OTf, [**46**]OTf, was previously investigated by our group, but has been found to be less active in alcohol oxidation than the unsubstituted compound. Mechanistic investigations showed that upon addition of NaO*t*Bu to [**46**]OTf a dimerized species is again obtained in similar reaction to previously described [**42**]. Addition of base to [**46**]OTf leads to an anionic dimer, Na[**47**], which contains a central bicyclic unit, of which one is six-membered ring connecting the two iridium centers fused with a five-membered carbon cycle (see Scheme 52).
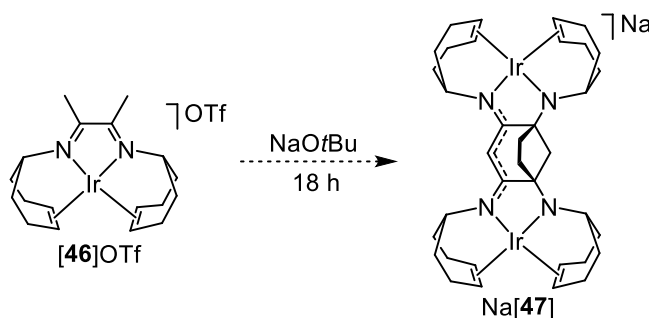
Scheme 52. Reaction of [**46**]OTf with NaO*t*Bu to obtain Na[**47**].

Figure 67 shows the solid state structure (a) and the structure obtained from DFT calculations (b). Since the quality of XRD data is rather low, experimental bond parameters are not discussed in detail here. But in combination with DFT calculations it can be shown that the part consisting of the C$_5$ cycle exclusively contains sp^3 hybridized carbon atoms (C2−C5−C4−C8−C7−C2), while the six-membered cycle contains a delocalized allylic unit (C3−C6−C1). This means that the Ir^I-Ir^I dimer is built up by a three times negatively charged ligand in complex Na[**47**] with a sodium cation as counterion. One negative charge is delocalized over the C3−C6−C1 allylic part, while the remaining two must be located on the nitrogen atoms.
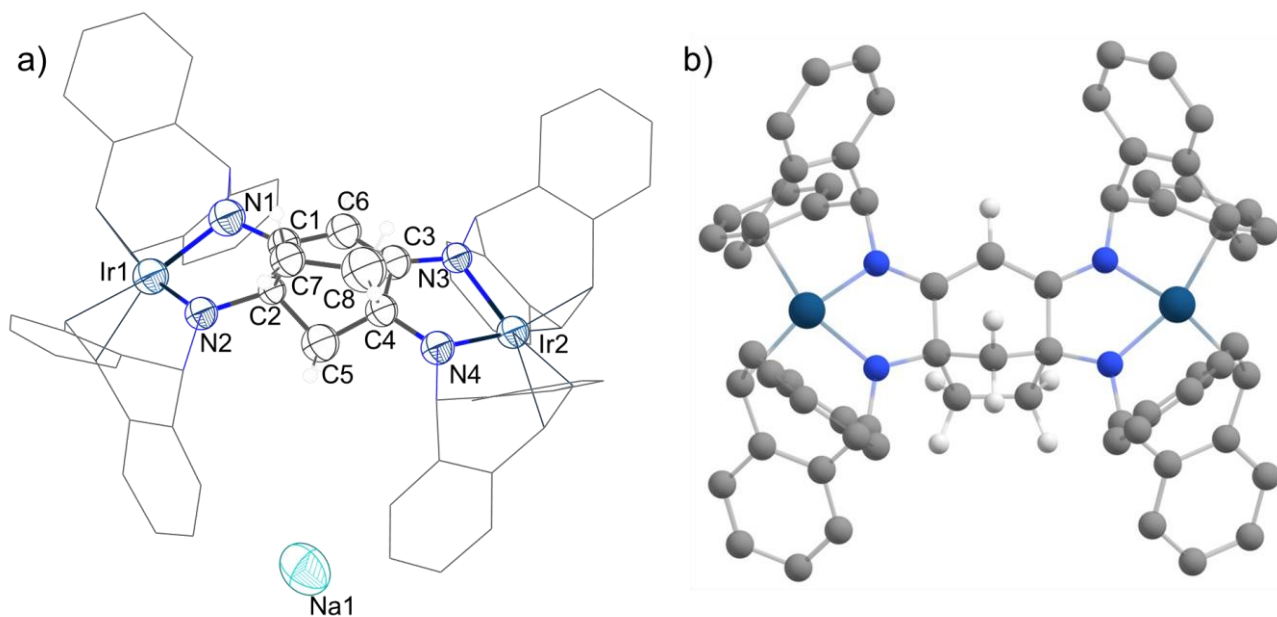
Figure 67. a) Solid state structure of Na[**47**].; b) DFT optimized structure of Na[**47**]. Hydrogen atoms at the trop fragments and solvent molecules omitted for clarity.

In this reaction, five protons were abstracted, while the charge of the complex is changed from 2·(+1) to -1, which is a reduction by three electrons in total. The alternative reaction mode is the removal of 5 H$^+$ and then oxidation by two electrons. The mechanism is certainly not straightforward but rather complex. The reaction mixtures contain a variety of species, which could not be identified and hence a detailed investigation leading to a better understanding of how this dimeric species has formed is presently not possible. Possibly, the formation of species like Na[**47**] explain why the alcohol oxidation is significantly slower with methyl substituted [**46**]OTf in comparison to unsubstituted [**40**]OTf.

5. Oxidative dehydrogenation of the ligand in [38]OTf

As elaborated in the introduction, it was assumed that the true active species of the catalytic cycle in the alcohol oxidation with [**38**]OTf is a diazadiene species. Therefore, attempts were made to isolate this complex. When [**38**]OTf was reacted with 4 eq. of oxidant (AgOTf or FcPF$_6$) and 4 eq. of base (NaOtBu) and the mixture was monitored by ^{1}H NMR spectroscopy, no clean product could be obtained. When trying to crystallize some product, only unwanted decomposition products were observed. Although, if *p*-benzoquinone (BQ) is used as oxidant, dehydrogenation of the C−H bonds in the dach backbone leads to formation of complex [**50**]$^\cdot$, as depicted in Scheme 53. The solid state structure of [**50**]$^\cdot$ is shown in Figure 68. This species very likely forms under the catalytic conditions of the alcohol oxidation reaction previously published.[65] Such metal-ion promoted oxidative dehydrogenation of amines is well established by numerous reports.[180] Although, here, not only the *H*C−N protons are removed, but also the saturated dach backbone is dehydrogenated to form a conjugated C$_6$ ring with unequally long C−C and C=C bonds (vide infra). The central N$_2$C$_6$ motif is therefore considered as a diiminoquinone (diq) fragment. The reaction cannot selectively be conducted by partially dehydrogenating the complex. Instead, the dehydrogenation steps appear to happen simultaneously to give the fully dehydrogenated compound as only and final isolated product. Furthermore, a reactant capable of taking up protons, such as BQ, is needed, as all other oxidants were not able to selectively convert [**38**]OTf to [**50**]$^\cdot$. The oxidation can also be performed starting directly from the isolated doubly deprotonated species K[**49**]. Only the radical [**50**]$^\cdot$ is obtained under these reaction conditions, even if an excess BQ is used in the presence of KOTf or NaBArF. This indicates that the oxidative strength of BQ (E° = -0.82 V vs Fc/Fc$^+$) is not sufficient to remove one electron from the radical [**50**]$^\cdot$ to obtain [**50**]OTf. Note that BQ can act as a two electron oxidant and two proton acceptor – which is formally equivalent to the addition of two hydrogen atoms to BQ.
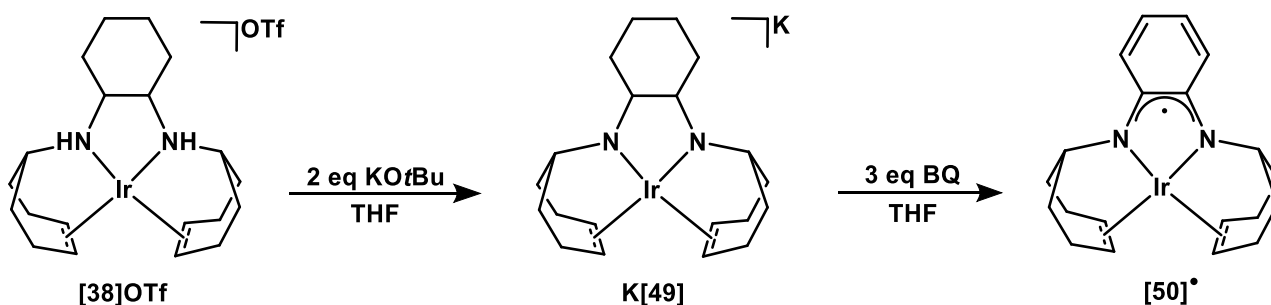
Scheme 53. Oxidative dehydrogenation of [**38**]OTf via K[**49**] with KOtBu and subsequent addition of BQ to obtain radical complex [**50**]$^\cdot$.
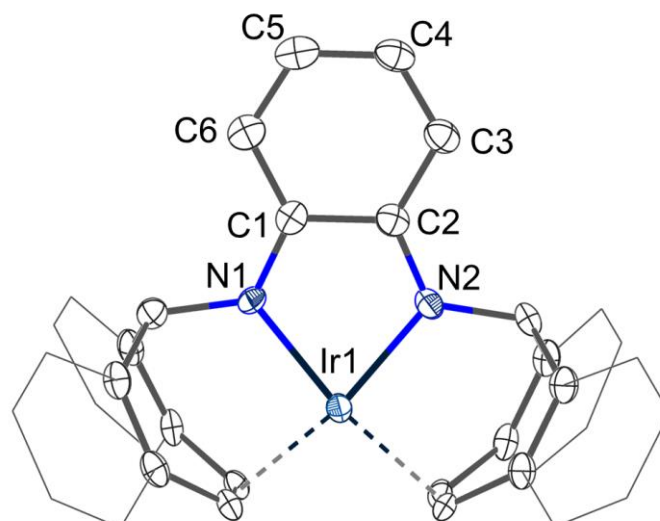
Figure 68. Solid state structure of [**50**]·. Hydrogen atoms and solvent molecules omitted for clarity.

The reaction of substoichiometric amounts of BQ with K[**49**] in MeCN leads to the formation of the anionic dehydrogenated species K[**50**] which is depicted in Figure 69. In the solid state, this compound forms a one-dimensional coordination polymer in which the potassium ion of the K(18-c-6) units bridge two [Ir(trop$_2$diq)] units via contacts to the phenyl rings of the trop ligands. The K to C distance was found at 3.199(6) Å.
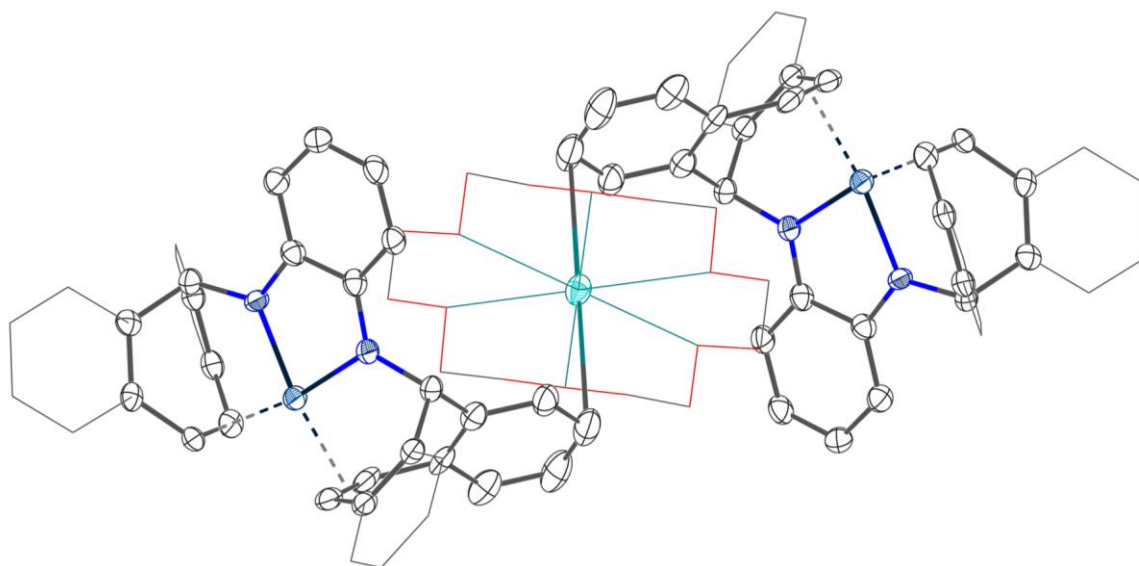
Figure 69. Solid state structure of K[**50**]. Only part of the polymeric structure is shown. Hydrogen atoms and solvent molecules omitted for clarity.

The structural data of the series of diq complexes is shown in Scheme 54 and listed in Table 25. Since [**50**]OTf could not be isolated so far, the structural data from DFT calculations for the cation are given. For [**50**]OTf and [**50**]·, the C$_6$ ring of the backbone shows alternating C−C bond lengths: two shorter bonds are observed for C3−C4 and C5−C6 (1.360 – 1.380 Å) and three longer ones for C2−C3, C4−C5 and C6−C1 (1.401 – 1.425 Å). In contrast, C1−C2 is found at 1.465 Å and 1.463 Å

for [**50**]OTf and [**50**]˙, respectively, being the longest bond in the C$_6$ ring. These data are in accord with the quinoidal structure assigned to the diiminoquinone (diq) form of the ligand shown below in Scheme 57. The C−N bonds in [**50**]˙ (av. of C1−N1 and C2−N2 = 1.343 Å) are longer by ~0.2 Å compared to [**50**]OTf (1.327 Å) and indicate the reduced state of the ligand. In contrast, the fully reduced anionic K[**50**] shows more evenly distributed bond distances over the N$_2$C$_6$ unit in the range of ~1.400 Å in average, except for C1−C2, which has again a longer bond distance of 1.441 Å. If this is compared to complexes [**50**]OTf and [**50**]˙, the former double bonds are elongated, while the single bonds were shortened. Additionally, C1−N1 and C2−N2 bonds were further elongated along the series from the cationic to neutral to anionic species. These findings indicate that the N$_2$C$_6$ unit of the ligand is highly redox-non innocent and takes up the negative charges transferred in a reduction process to finally give a delocalized conjugated π-system where the negative charge is distributed over the diq backbone.
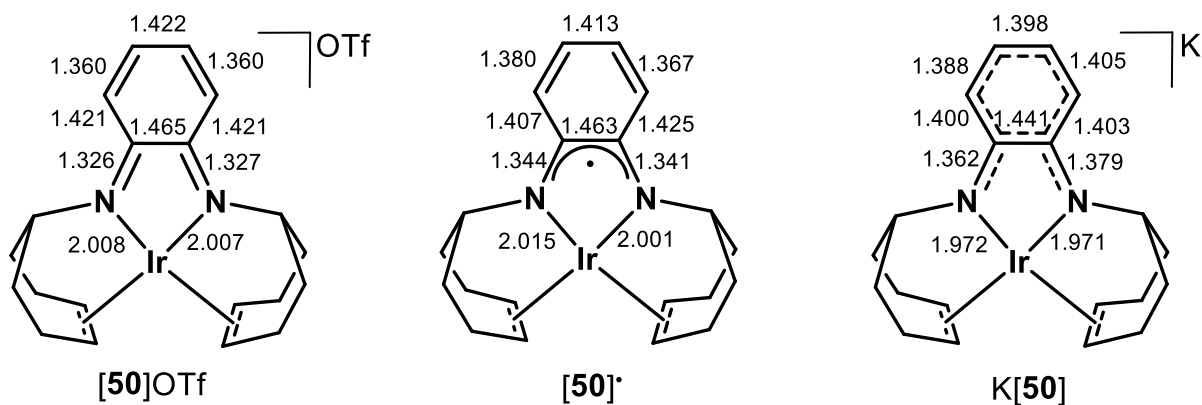
Scheme 54. Schematic representation of [**50**]OTf with calculated bond lengths, complexes [**50**]˙ and K[**50**] with experimental bond lengths [Å] obtained from single crystal XRD measurements.

Another trend can be observed in the Ir−N bond lengths across the redox series: while cationic [**50**]OTf shows the longest Ir−N1 and Ir2−N2 distances (av. 2.008 Å), they decrease slightly to neutral [**50**]˙ (av 2.007 Å) and significantly for K[**50**] (av. 1.972 Å). This strong decrease in bond lengths is attributed to the change of an amine to an amido donor ligand. Table 25 shows the same trend in Ir−N bonds for the saturated complex [Ir(trop$_2$dach)]OTf [**38**]OTf with NH groups compared to deprotonated K[**49**] exhibiting amido groups. Further structural parameters for these complexes are listed, which clearly show single bond character for all relevant C−C and C−N bonds.

Table 25. Selected bond lengths [Å] of iridium complexes with a N_2C_6 backbone derived from [**38**]OTf.

	Compound	Ir−N1 Ir−N2	N1−C1 N2−C2	C1−C2	C2−C3 C1−C6	C3−C4 C5−C6	C4−C5	C=C$_{olef}$
diiminoquinone	[**50**]OTf[a]	2.007 2.008	1.326 1.327	1.465	1.421 1.421	1.360 1.360	1.422	1.411 1.411
	[**50**]˙	2.001(4) 2.015(4)	1.341(6) 1.344(6)	1.462(6)	1.410(7) 1.425(7)	1.380(7) 1.367(7)	1.413(7)	1.424(6) 1.433(6)
	K[**50**]	1.971(4) 1.972(4)	1.379(6) 1.362(6)	1.441(6)	1.400(6) 1.403(7)	1.388(7) 1.405(7)	1.398(7)	1.453(7) 1.437(8)
diamino-cyclohexane	[**38**]OTf	2.095(3) 2.090(3)	1.503(4) 1.491(5)	1.546(5)	1.534(5) 1.529(5)	1.522(7) 1.506(6)	1.527(7)	1.421(6) 1.401(6)
	K[**49**]	1.988(3) 1.961(3)	1.455(5) 1.465(5)	1.529(5)	1.518(6) 1.533(5)	1.530(6) 1.521(6)	1.536(5)	1.445(6) 1.444(6)

[a] Calculated bond lengths.

6. Catalytic alcohol oxidation and the influence of bases

6.1. Oxidation of 1-octanol as model substrate

The highly successful catalytic system for alcohol oxidation with [**40**]OTf was further investigated with the new findings presented in the first part of this Chapter. The goal was to find out if the diiridium complex [**42**] is also an active species (or even the true catalyst) in the catalytic cycle and whether, with this catalyst, it would be possible to proceed under base-free conditions. This would allow for the selective dehydrogenation of more challenging base-sensitive substrates. All catalytic experiments were performed in 10 mL crip vials with septa and 1 mL of THF under air-free conditions. Conversions were monitored by taking aliquot samples which were diluted with CDCl$_3$ and analyzed with ^{1}H NMR spectroscopy. Conversions are determined via the integral of the aldehyde peak. No side products were observed unless otherwise stated. BQ was used as terminal oxidant and mesitylene served as internal standard.

6.1.1. *Influence of base on the oxidation of 1-octanol for catalysts [40]OTf, [40]˙ and [42]*

At first, the concentration of catalyst was kept at 0.01 mol% of iridium – corresponding to 0.005 mol% of diiridium compound [**42**]. The catalysis was performed in the presence or absence of base. In this series, the neutral mono iridium complex [**40**]˙ was also investigated in order to determine the dependence on starting from a catalyst in a reduced state. The results are depicted in a time versus conversion plots given in Figure 70. From this graph, the influence of the base on the catalytic conversion with mononuclear iridium complexes is apparent, as full conversion is obtained after ~3 min in the presence of base. In contrast, little conversion is obtained in the absence of base, even after several hours (see also Table 26). This statement is true for [**40**]OTf and [**40**]˙, where almost no difference in catalytic activity was observed. Thus, it can be assumed that both species are equally active in alcohol dehydrogenation. If bimetallic [**42**] is used as catalyst, base-dependence is again observed, but to a much lesser extent: in the absence of base a linear conversion rate is observed, which reaches 50% after 6 h. Although this catalytic system is much less active, it still shows that no base is required for [**42**], while no reactivity is observed with the mono iridium catalysts. Note, that if base is added to the catalytic mixture involving [**42**], the conversion reaches 50% after 3 min but never 100%. Instead, a plateau is reached at about 80% conversion. It is important to take into account that - as previously reported - the catalytic reactions using NaO*t*Bu as co-additive are highly exothermic and the solutions heat up to reflux for a few seconds during which the catalysis proceeds. Therefore, it might be beneficial to heat all samples to the same temperature in order to determine the influence of temperature on the catalysis.

Table 26. Catalytic dehydrogenation of 1-octanol with BQ as the hydrogen acceptor in THF. The conversion (yield of aldehyde) was determined by ^{1}H NMR.

entry	catalyst	cat [mol%]	NaOtBu [mol%]	conversion [%]				
				10 min	60 min	2 h	6 h	24 h
1	[42]	0.005	0.01	5	17	25	52	62
2	[42]	0.005	-	53	74	78	83	91
3	[40]OTf	0.01	0.01	100	100	100	100	100
4	[40]OTf	0.01	-	1	3	3	4	8
5	[40]˙	0.01	0.01	100	100	100	100	100
6	[40]˙	0.01	-	1	2	3	5	10
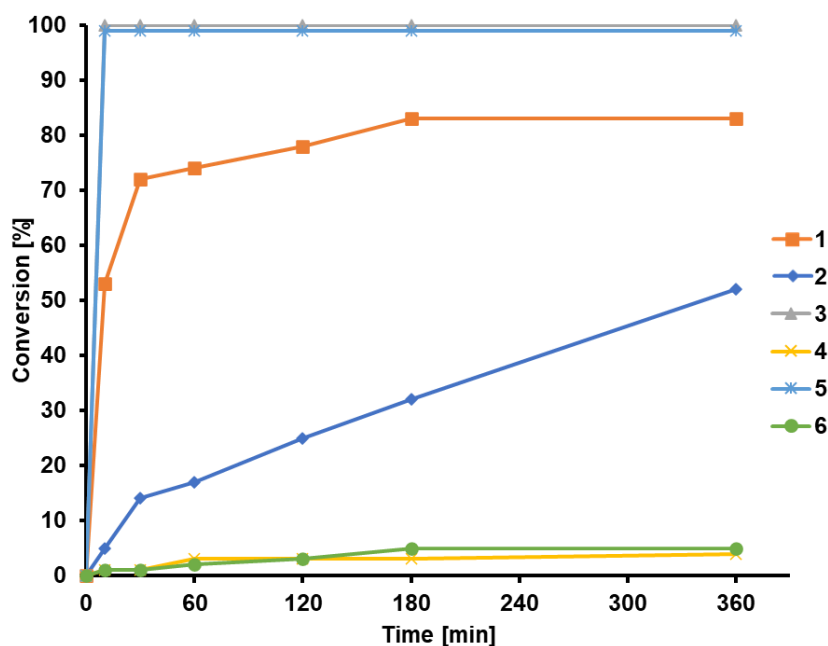
Figure 70. Plot showing the influence of the absence or presence of base on the oxidation of 1-octanol for catalysts [40]OTf, [40]˙ and [42] with data according to entries 1–6 in Table 26. The reactions were started at room temperature but in case of efficient catalysis (especially, 3 and 5) the temperature raised to the boiling point of THF (64°C).

6.1.2. Influence of catalyst loading on the base-free oxidation of 1-octanol

In the following experiments, [40]OTf and [42] were compared under base-free conditions for the alcohol oxidation of 1-octanol at different catalyst loadings. Again, the amount of Ir aliquots was kept the same between the mononuclear and dinuclear iridium catalyst. The results are depicted in a time versus conversion plot in Figure 71. The lowest catalyst loading of 0.005 mol% [42] gives 85% conversion of 1-octanol after 24 h. Although, if the loading is increased by a factor of 10 (0.05 mol%), full conversion is obtained in less than 5 min. This again is in contrast to the mono iridium complex [40]OTf which achieved at most 64% conversion with 0.1 mol% catalyst loading after 24 h and only

30% with 0.01 mol% catalyst loading. This shows that raising the catalyst loading allows for working under base-free conditions, which accounts for both catalysts, but the conversion rate is significantly higher with the dinuclear complex [**42**].

Table 27. Base-free catalytic dehydrogenation of 1-octanol with BQ as the hydrogen acceptor in THF. The conversion (yield of aldehyde) was determined by ^{1}H NMR.

entry	catalyst	cat [mol%]	NaOtBu [mol%]	conversion [%]			
				10 min	60 min	18 h	24 h
1	[**42**]	0.005	-	1	5	76	85
2	[**40**]OTf	0.01	-	1	8	33	30
3	[**42**]	0.05	-	96	95	95	95
4	[**40**]OTf	0.1	-	2	3	53	64
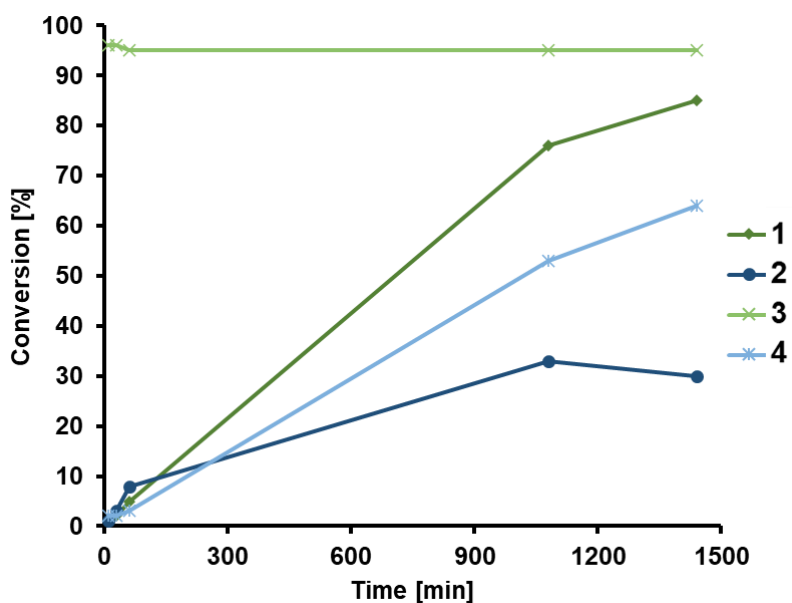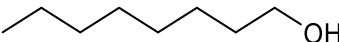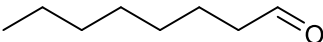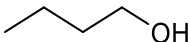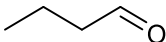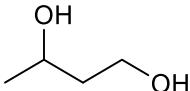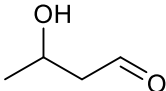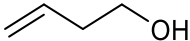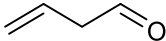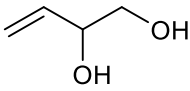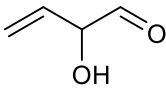
Figure 71. Time plot of catalytic conversions in the base-free oxidation of 1-octanol with complexes [**40**]OTf and [**42**] at different catalyst loadings. Entries 1–4 are according to Table 27.

6.2. Base-free oxidation of "challenging substrates" with [42] as catalyst

To extend the substrate scope, a study of different alcohols was conducted. More challenging molecules were chosen, which contain secondary alcohol groups next to the primary −OH group or unsaturated C=C bonds, or both additional functionalities. For oxidation reactions under base-free conditions, 0.01 mol% of catalyst [**42**] were added to the reaction mixture (the previously applied conditions using 0.005 mol% of the dinuclear iridium complex proved to be too low for effective alcohol oxidation). The substrate scope and NMR yields are given in Table 28, which are plotted in a time dependence plot shown in Figure 72.

Conversion of alcohol and yield of aldehyde are not equivalent here because of side reactions. It is likely that cyclization or polymerization takes place upon longer reaction times. The formation of esters from condensation of an aldehyde with an alcohol would also be possible. These products can not be monitored easily with ^{1}H NMR spectroscopy, therefore only the yields of aldehydes are given in this section.

Table 28. Base-free catalytic dehydrogenation of primary alcohols with BQ as the hydrogen acceptor. The yield of aldehyde was determined by ^{1}H NMR. Reactions were performed with 0.01 mol% of [**42**] in THF.

Entry	Substrate	Product	Time	NMR yield [%]
1	~~~~OH	~~~~O	60 min / 24 h	30 / 66
2	~~OH	~~O	60 min / 24 h	60 / 94
3	OH / OH (butane-1,3-diol)	OH / O	60 min / 24 h	38 / 10
4	=~OH	=~O	60 min / 24 h	30 / 22
5	=\OH, OH	=\O, OH	60 min / 24 h	5 / 9

The simple primary alcohols 1-octanol and 1-butanol (entries 1 and 2) show rather high yields of aldehyde (66% and 94% after 24 h, respectively) and continuing formation of aldehyde is observed over the course of the reaction. Other alcohols containing an additional functional group (butane-1,3-diol and but-3-en-1-ol; entries 3 and 4, respectively) show conversions of 30 – 38% after one hour, but quickly reach a plateau and aldehyde yields decrease. This is attributed to follow-up reactions taking place upon prolonged reaction times. The nature of these products has not been analyzed yet. The oxidation of but-3-ene-1,2-diol (entry 5) shows little conversion (9% after 24 h),

which keeps increasing over time slightly. In this set of experiments, the quite low catalyst loading of 0.01 mol% was used in order to better see differences in reactivity at slower conversion rates but was too low to reach full conversion within 24 h. Increasing the catalyst loading will lead to faster conversion, which might suppress formation of side products. Even though the yields presented in Table 28 and Figure 72 were not satisfying, the results still show that with [**42**] as catalyst, the addition of base is not necessarily required for the alcohol oxidation.
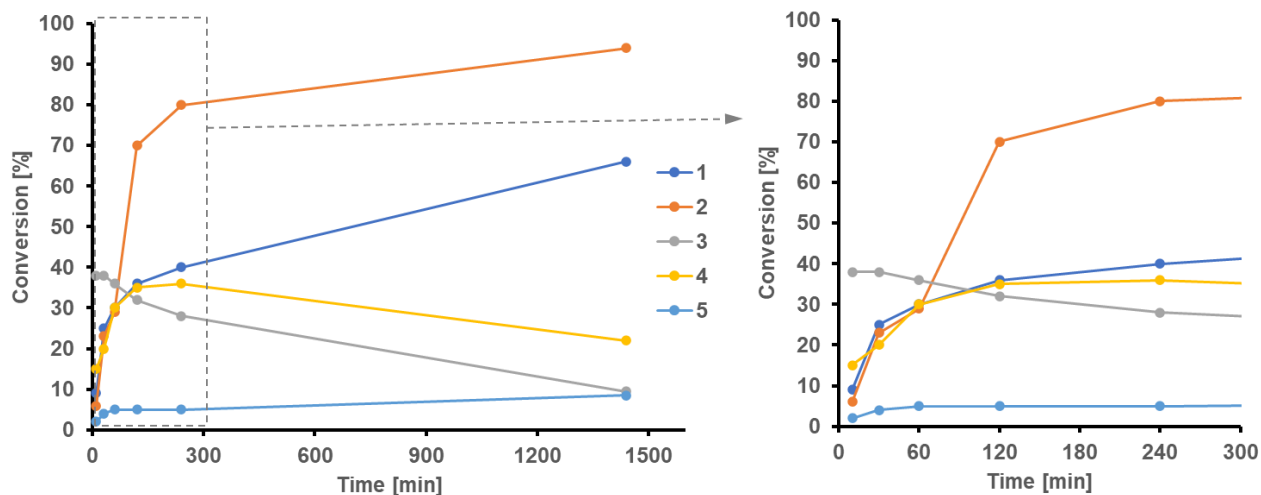
Figure 72. Conversion plot for the oxidation of different alcohols without addition of base according to entries 1–5 in Table 28 with 0.01 mol% of catalyst [**42**], and on the right side a zoom-in on the first 300 min.

6.3. Mechanistic investigations

The mechanism of alcohol oxidation with [**40**]OTf has long been under investigation, and the role of the base was unclear. The dinuclear iridium complex [**42**] gives further insight into possible catalytic cycles. Previous reports showed that if [**40**]OTf is pressurized with hydrogen gas, the dad backbone is hydrogenated to complex [**43**]OTf (Scheme 55a) and acting as cooperative ligand. The same result is obtained if [**40**]OTf is refluxed in EtOH. The finding of this hydrogenated [**43**]OTf complex under such conditions suggests that this species may play a role during catalysis.

Although, if the same two experiments are performed with dimeric compound [**42**], no reaction with hydrogen gas or ethanol were observed, even under harsh conditions. This is in strong contrast to [**40**]OTf, therefore the corresponding catalytic cycle for the alcohol oxidation with [**42**] depicted in Scheme 55b can not be the true reaction mechanism. Even though [**42**] does not add hydrogen to its backbone, it is highly active in the catalytic alcohol oxidation. Therefore, the role of compound [**43**]OTf in the catalytic cycle is to be questioned.

Another possibility is the catalysis to proceed via a radical mechanism or a simple redox reaction. If BQ is treated with NaOtBu, reduction to the dark blue SQ radical takes place. This can visually be observed during the setup of the catalysis. Since addition of base to the catalytic system is crucial, a radical mechanism seems rather likely.

Furthermore, it was shown that [**42**] is rather active in alcohol oxidation even without base – although the addition of base enhances the catalytic rate (see section 6.1.1). This could be due to the difference in redox potentials (compare section 7.3).
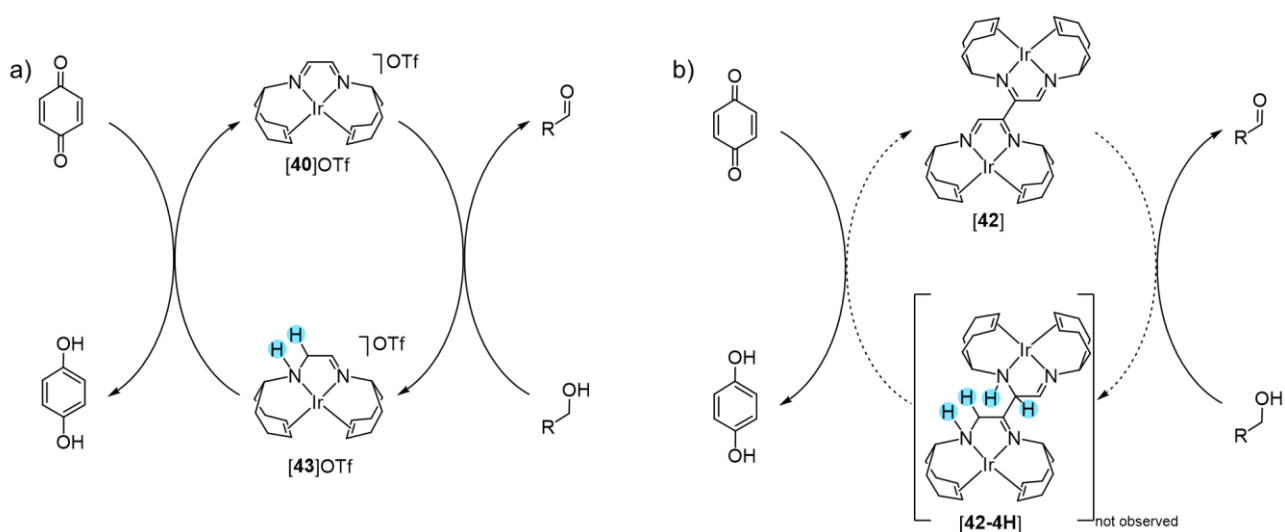
Scheme 55. a) Catalytic cycle proposed for [**40**]OTf via complex [**43**]OTf;[174] b) imagined related catalytic cycle for [**42**] where the hydrogenated intermediate [**29-4H**] is not observed.

7. Electrochemical investigations of iridium complexes

7.1. CV of bimetallic [Ir(trop₂dad)]₂ [42]

The CV of diiridium complex [42] in THF shows two reversible reduction events at -1.48 and -1.82 V and two reversible oxidation events at -0.09 and -0.40 V, as seen in Figure 73a. All four redox events are fully reversible, as determined by scan rate dependent CV measurements, depicted in Figure 73c and d.
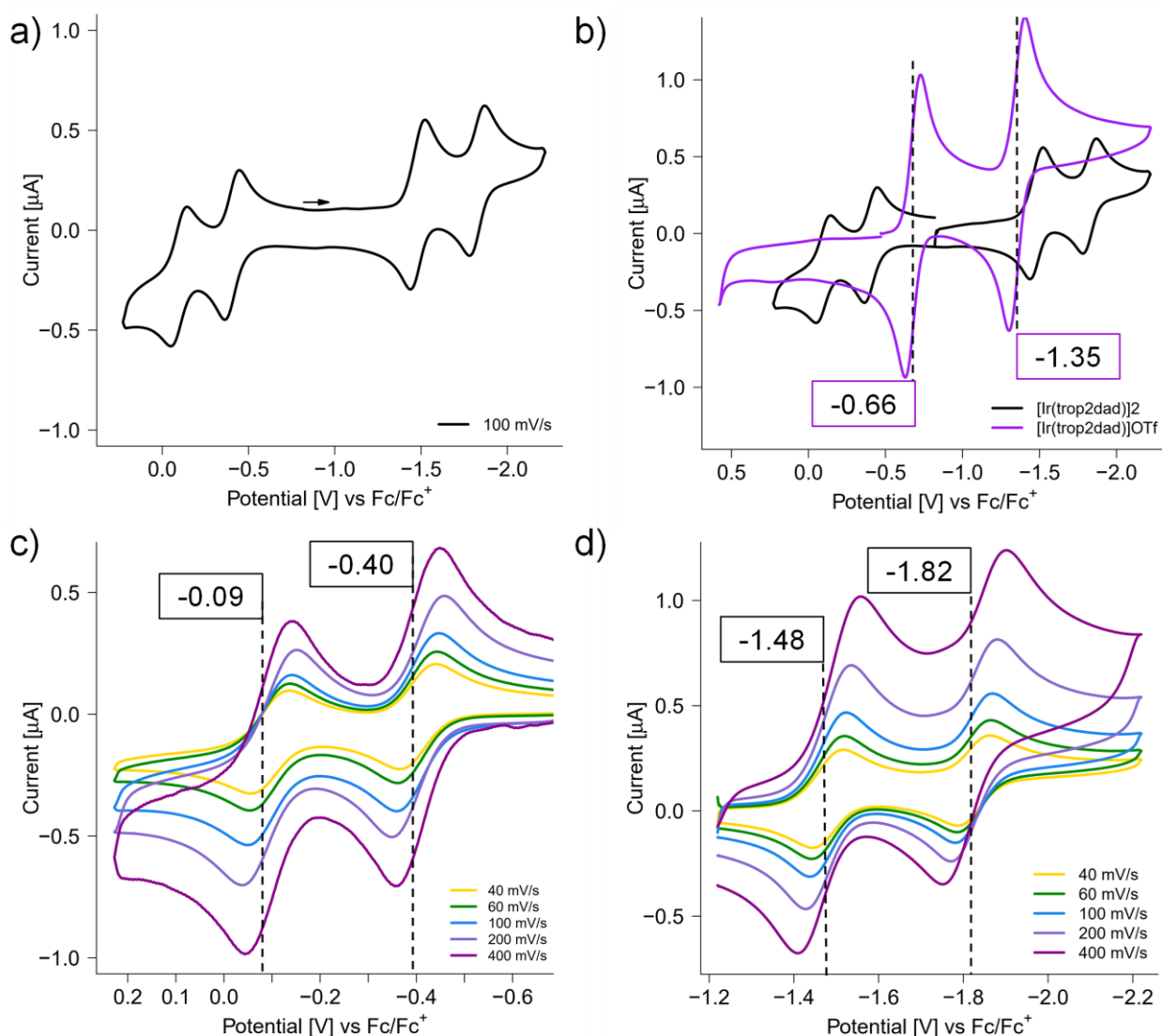
Figure 73. a) CV of [42], scan direction and OCP shown by an arrow; b) CV of [42] (black) with overlay of [40]OTf (purple); c) scan rate dependent CV of [42] (oxidative side); d) scan rate dependent CV of [42] (reductive side). Conditions: 1 mM analyte, 100 mM nBu₄NPF₆, THF, GC WE, Pt on TiO$_x$ CE, Ag/Ag⁺ RE, scan rate 100 mV/s.

When compared to the two reversible reduction events of the related monomeric cationic [40]OTf, the reduction events are shifted significantly to more negative potentials in the dinuclear neutral complex (Figure 73b). It has to be taken into account that the open circuit potentials (OCP) differ significantly: while [40]OTf has an OCP of -0.47 V, the dimerized species [42] already exhibits a

rather negative OCP of -0.82 V. This can be explained by the fact that [**42**] is obtained upon reduction of cationic [**40**]OTf and is thus a neutral compound. The same reasoning can be used to explain the two oxidation events of complex [**42**]. The OCP of [**42**] was found at around the same potential than that of [**40**]˙ (see Figure 73b), but here the even the first oxidation and reduction events are both shifted to more positive and negative potentials, respectively. Two consecutive electron transfer steps are observed at reductive potentials as well as oxidative potentials, which can be attributed to the dimeric nature of the complex. This means that the addition or removal of an electron to or from the second iridium fragment is less favorable than the first electron.

7.2. CV of [Ir(trop$_2$dach)]OTf ([38]OTf) and dehydrogenated [Ir(trop$_2$diq)] ([50]˙)

The CV of [**38**]OTf in THF shows an irreversible oxidation event at 0.63 V peak potential at 100 mV/s (black trace in Figure 74). The addition of 2 eq. of base leads to fully deprotonated amide species K[**49**] which shows an additional oxidation event at -0.18 V (blue trace in Figure 74).
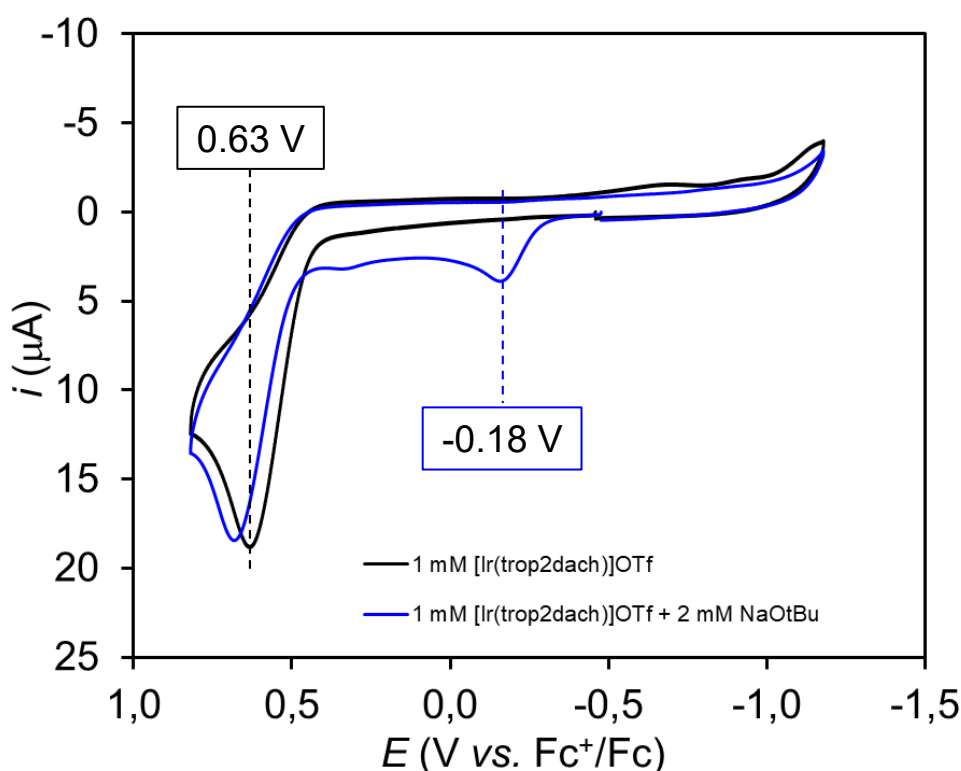
Figure 74. Overlay of CV of [**38**]OTf (black trace) and CV of *in-situ* double deprotonated species K[**49**] (blue trace). Conditions: 1 mM analyte, 100 mM *n*Bu$_4$NPF$_6$, THF, Pt disc WE, Pt wire CE, Ag/Ag$^+$ RE, scan rate 100 mV/s.

The appearance of an irreversible oxidation peak upon deprotonation at less positive potentials is in line with the findings presented in section 5 of this chapter, where it was shown that the deprotonated species K[Ir(trop$_2$dach)] K[**49**] can be fully dehydrogenated at the cyclohexyl backbone [Ir(trop$_2$diq)]. This structural modification in the ligand is assumed to cause the irreversible oxidation event at -0.18 V. On the contrary the diamine compound [**38**]OTf does not react with relatively mild oxidants

such as BQ, which is also reflected by the absence of an additional oxidation peak in CV. If the isolated [Ir(trop$_2$diq)] ([**50**]$^\bullet$) is measured in DMSO, cyclic voltammograms show a fully reversible oxidation at -0.84 V, as shown in Figure 75. Note that the OCP was found at a rather negative potential of around -1 V.
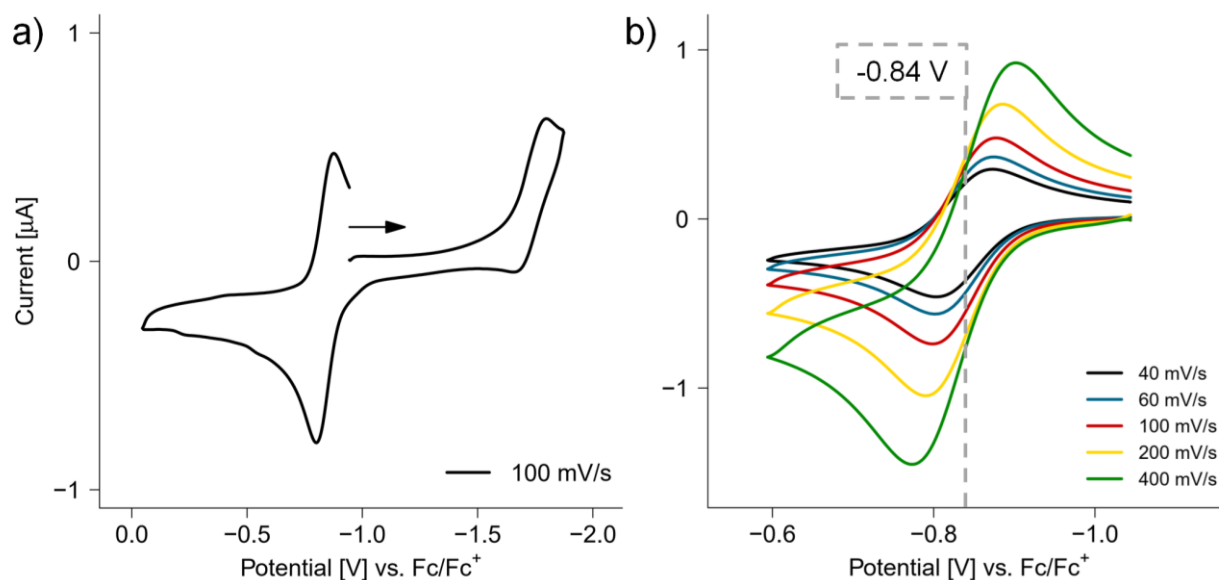
Figure 75. CV of [**50**]$^\bullet$ in DMSO. a) Full window; b) scan rate dependent measurement of isolated redox event at -0.84 V. Conditions: 1 mM analyte, 100 mM *n*Bu$_4$NPF$_6$, DMSO, Pt WE, Pt on TiO$_x$ CE, Ag/Ag$^+$ RE.

7.3. Comparison of redox potentials of iridium complexes

The redox potentials and cyclic voltammograms of [**40**]OTf and [**46**]OTf were previously reported and compared to dimeric [**42**] and BQ in Table 29. While [**40**]OTf is rather easy to reduce ($E^{1/2}$ = -0.66 and -1.35 V), more negative potentials have to be applied to reduce dinuclear [**42**] and methyl substituted [**46**]OTf. Relevant to catalytic applications is the redox potential of BQ, which was found with -0.88 V to be right between the reduction potentials of [**40**]OTf. This indicates that BQ is able to oxidize [**40**]$^\bullet$ to [**40**]OTf under these conditions. On the contrary, the oxidation potentials of [**42**] and [**46**]$^\bullet$ are more negative than of BQ, which means BQ is unable to oxidize those (quantitatively). The position of redox potentials will have an influence on the catalytic system and mechanistic investigations, as discussed later in this chapter.

Table 29. Redox potentials [V] of iridium complexes in THF investigated in this chapter.

	charge	compound	OCP	$E^{1/2}_{reduction}$	$E^{1/2}_{oxidation}$
dad	+1	[40]OTf	-0.5	-0.66 -1.35	-
	0	[40]•	-1.0	-1.35	-0.66
	0	[42]	-0.8	-1.48 -1.82	-0.40 -0.09
	+1	[46]OTf	-0.4	-0.90 -1.56	-
	0	[46]•	-1.2	-1.56	-0.90
dach	+1	[38]OTf	-0.7	-1.5*	0.63*
	-1	K[49]	-	-1.5*	-0.12* 0.63*
	0	[50]OTf•	-0.9	-1.7	-0.84
-	0	BQ	-	-0.8 -1.5	-

*Irreversible redox event, given is the peak potential E^P at 100 mV/s.

8. Electrochemical oxidation of alcohols

8.1. Cyclic voltametric experiments for catalytic investigations

8.1.1. Blank experiments

For the following electrocatalytic investigations THF or DME were chosen as solvent, because it was shown that MeCN reacts with the reduced iridium catalysts. A CV of the substrate benzyl alcohol (BnOH) in THF shows that it is not redox active within the applied potential window (Figure 76a). The base NaOtBu shows an irreversible electrochemical oxidation at 0.5 V peak potential (Figure 76b). If base is added to BnOH, the CV shows an increase of current at ~0.1 V peak potential. The current increases upon increasing the amount base (Figure 76a, blue and purple traces). Presumably the observed current is not due to alcohol oxidation but is attributed to background oxidation from the employed NaOtBu base.
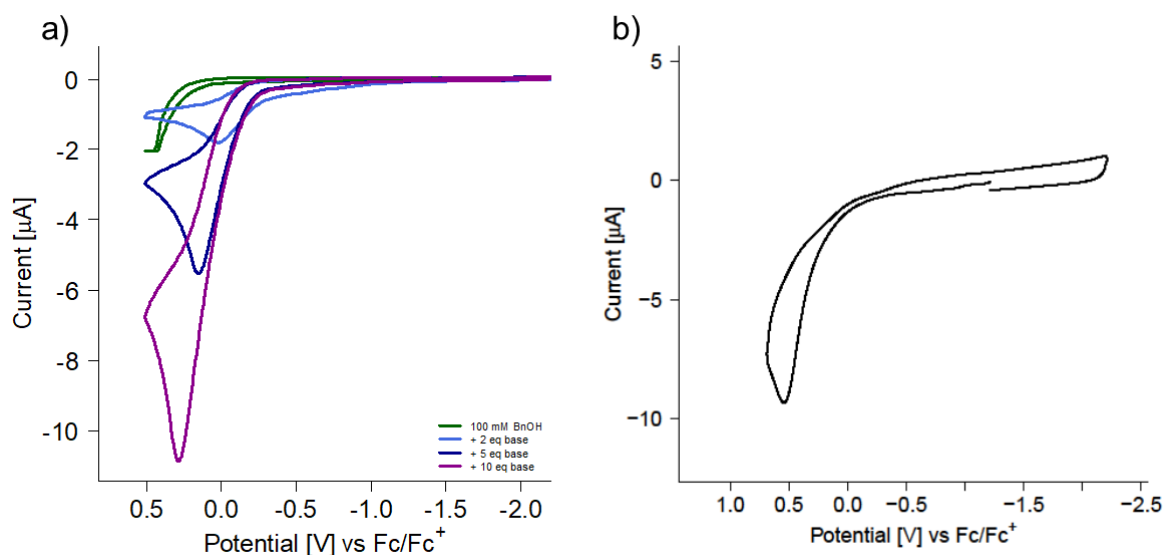
Figure 76. a) CV of BnOH (green trace) with varying amounts of NaOtBu base (blue, dark blue and purple trace); b) CV of NaOtBu. Conditions: 100 mM nBu$_4$NPF$_6$, THF, GC WE, Pt on TiO$_x$ CE, Ag/Ag$^+$ RE, scan rate 100 mV/s.

8.1.2. Mechanistic investigations on iridium complex [40]OTf

As previously reported, complex [**40**]OTf exhibits two fully reversible reduction events at -0.66 and -1.35 V (Figure 77a). If 100 mM BnOH is added as substrate to [**40**]OTf, no change in the CV was observed, which means no catalysis takes place without addition of base (Figure 77b).
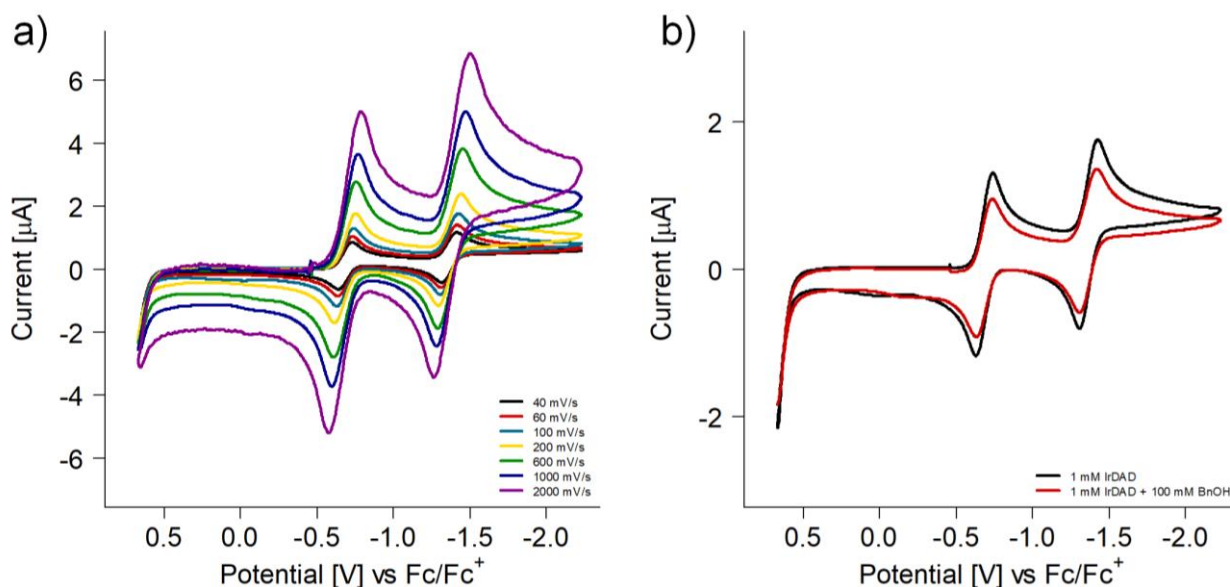
Figure 77. a) Scan rate dependent CV of [**40**]OTf; b) CV of [**40**]OTf (black trace) and [**40**]OTf BnOH added (red trace). Conditions: 1 mM [**40**]OTf, 100 mM BnOH, 100 mM nBu₄NPF₆, THF, GC_d WE; Pt on TiOx CE; RE: Ag/Ag⁺.

In order to determine the influence of base on [**40**]OTf electrochemically, varying amounts of base were added and CVs recorded, the voltammograms are plotted in Figure 78. The addition of 1–2 eq. of NaO*t*Bu to a solution of [**40**]OTf does not lead to any change in the CV, but the OCP shifts from -0.47 V to around -1.0 V. This is in line with previous results presented in this chapter, where reduction of [**40**]OTf by the NaO*t*Bu base was observed. Therefore, this CV shows the redox event of the [**40**]$^{\cdot}$ radical. The redox event that occurs at -0.66 V is now attributed to an oxidation. If an excess of base is added, this oxidation event becomes clearly irreversible due to a completely disappearance of the reverse peak. This could be due to the fact that new irreversible oxidation peaks appear between -0.3 and 0.2 V. It is not clear whether those events are appearing due to the oxidation of NaO*t*Bu (see also section 8.1.1) or due to interaction of the iridium complex with the base, e.g. formation of a different species.
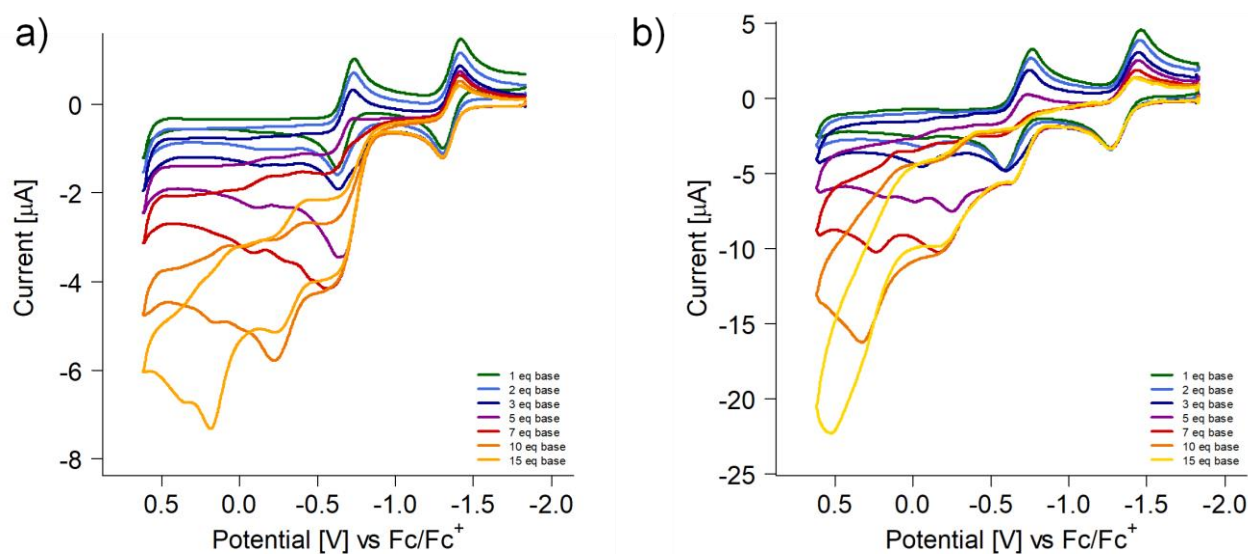
Figure 78. Overlaid CVs of [**40**]OTf with varying amounts of NaO*t*Bu added at 100 mV/s (a) and 1 V/s (b). Conditions: 100 mM *n*Bu$_4$NPF$_6$, THF, GC WE, Pt on TiO$_x$ CE, Ag/Ag$^+$ RE, scan rate 100 mV/s. Measurements were started from -1.9 V for comparative reasons.

When adding 100 mM BnOH substrate to a 1 mM solution of [**40**]OTf in THF and varying amounts of NaO*t*Bu, an increase of the peak current of the oxidation at -0.66 V is observed (light and dark blue traces in Figure 79a). This increase is attributed to a catalytic current resulting from alcohol oxidation. Although, the observed raise in current is rather low and drops at higher potentials, which may be a result of a slow reaction at the electrode surface.

Scan rate dependent measurements of the catalytic mixture indicate the same result, as depicted in Figure 79b. At low scan rates (100 and 200 mV/s, green and blue traces), the catalytic current is rather low. If the scan rate is raised to 1 or 2 V/s (dark blue and purple traces), the current does not only increase linearly as expected for higher scan rates, but also large oxidation currents between -0.5 and 0.5 V are observed. This finding can be attributed to kinetically hindered catalysis or deposition / adsorption of molecules on the electrode surface.

The orange traces in Figure 80 show blank experiments, where CV of base and alcohol were recorded in the absence of catalyst. The observed current is much higher than in the presence of [**40**]OTf (blue traces in Figure 80). Although, the catalytic onset potential is reduced by around 1 V upon addition of iridium catalyst, which is favorable for oxidation reactions because it means catalysis is facilitated and less positive potentials are required.
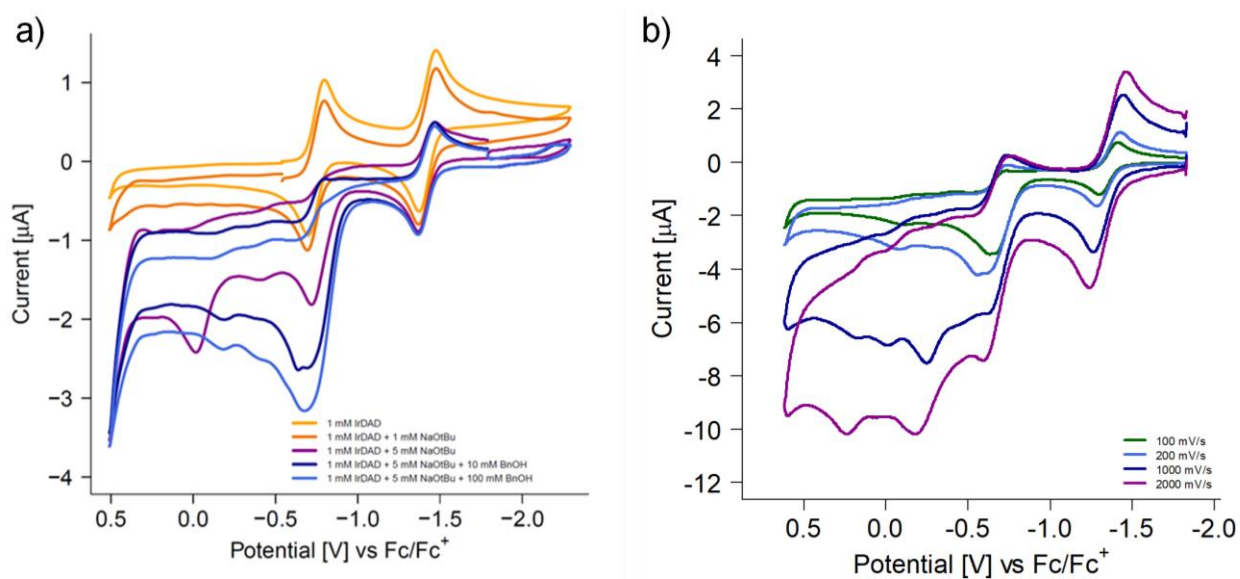
Figure 79. a) Overlaid CVs of [**40**]OTf with varying amounts of NaO*t*Bu and BnOH added at 100 mV/s; b) scan rate dependence of a mixture of 1 mM [**40**]OTf, 5 mM NaO*t*Bu and 100 mM BnOH. See colour coded insets for detailed description. Conditions: 100 mM *n*Bu₄NPF₆, THF, GC WE, Pt on TiOₓ CE, Ag/Ag⁺ RE, scan rate 100 mV/s.
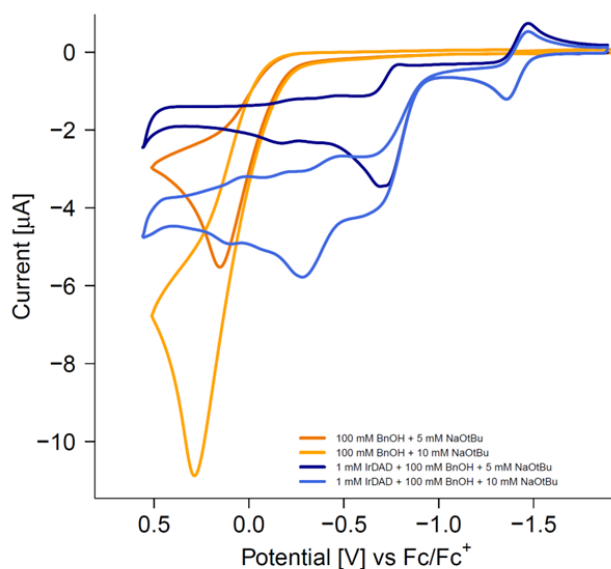
Figure 80. CV showing the influence of cat. [**40**]OTf on a mixture of NaO*t*Bu and BnOH. See colour coded insets for detailed description. Conditions: 100 mM *n*Bu₄NPF₆, THF, GC WE, Pt on TiOₓ CE, Ag/Ag⁺ RE, scan rate 100 mV/s.

8.1.3. Mechanistic investigations on diiridium complex [42]

When comparing the CVs of dinuclear [42] to in situ combined NaOtBu and [40]OTf, we can see a clear difference in redox events. Thus, different species are formed under these conditions (compare Figure 73b). Therefore, the dinuclear iridium complex [42] was separately investigated for electrocatalytic alcohol oxidation. The addition of one equivalent of NaOtBu to a solution of [42] leads to irreversible oxidation events. On the other hand, the reductions remain reversible (see Figure 81a). This reactivity was also observed for [40]OTf, where addition of base does not influence the reduction but only the oxidation event (compare Figure 78 of the previous section).

If 10 mM BnOH is added to a solution of [42], no catalytic current is observed (black trace in Figure 81b). The addition of NaOtBu base leads to the appearance of a shoulder at the first oxidation wave which is enhanced by the increase of the amount of base used (red and blue traces in Figure 81b). Note that the current does not increase further if 100 mM BnOH are added to the solution (not shown). This leads to the assumption that the current increase does not stem from catalytic alcohol oxidation, but some background oxidation. To be certain about this statement, bulk electrolysis needs to be performed, because the reaction at the electrode surface might be slow and reach saturation in the CV experiment.
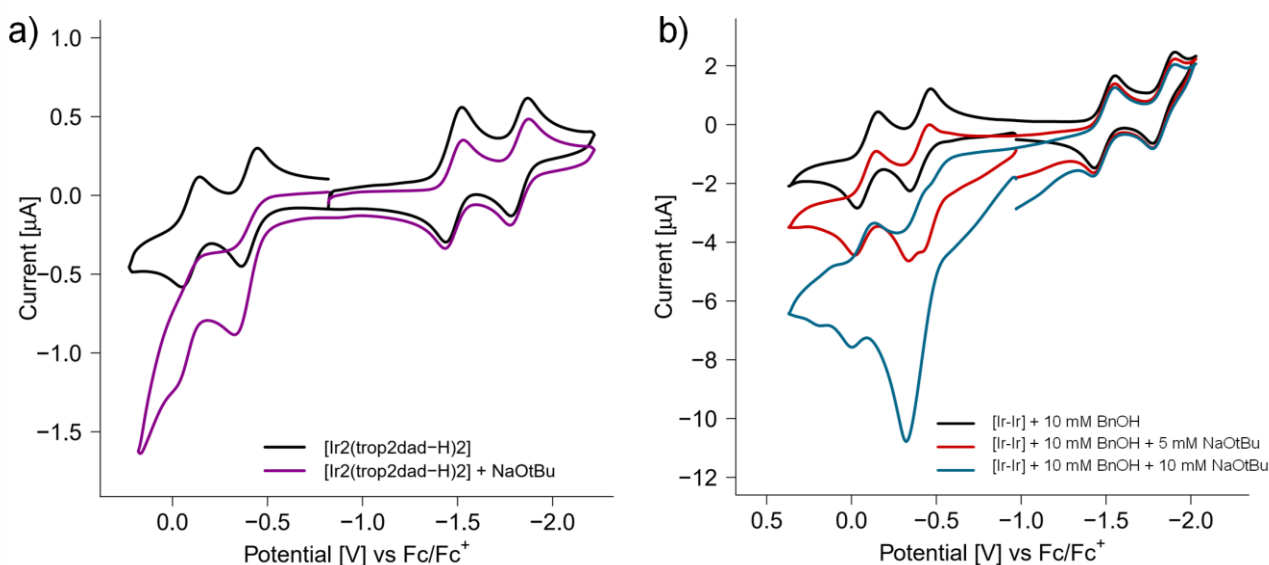
Figure 81. a) Overlaid CV of [42] (black trace) and with 1 eq. of NaOtBu added (purple trace) at 100 mV/s; b) CV of 1 mM [42] with BnOH and NaOtBu added. See colour coded insets for detailed description. Conditions: 100 mM nBu$_4$NPF$_6$, THF, GC WE, Pt on TiO$_x$ CE, Ag/Ag$^+$ RE, scan rate 100 mV/s.

8.1.4. Mechanistic investigations on methylated iridium complex [*46*]OTf

The CV of methyl substituted [**46**]OTf is similar to complex [**40**]OTf, although the redox events appear at slightly lower potentials (see Table 29). The addition of NaO*t*Bu to [**46**]OTf leads to the appearance of an irreversible oxidation peak around 0 V and shifts the OCP to more negative potentials (see blue trace in Figure 82). The appearance of the new oxidation peak could result from deprotonation of the methyl groups and formation of an enamine species, which has been previously reported.[176] While this oxidation peak appears, the current of the reduction events decreases, indicating a decrease of the concentration of the initial [**46**]OTf species. If BnOH is added, a substantial increase in current around 0 V is observed, which is at the same E^P as the peak resulting from deprotonation of [**46**]OTf. This could result from a catalytic current of alcohol oxidation or might be background oxidation of other molecules. To find out this assumption, bulk electrolysis experiments are performed to determine the amount of aldehyde formed (see section 8.3).
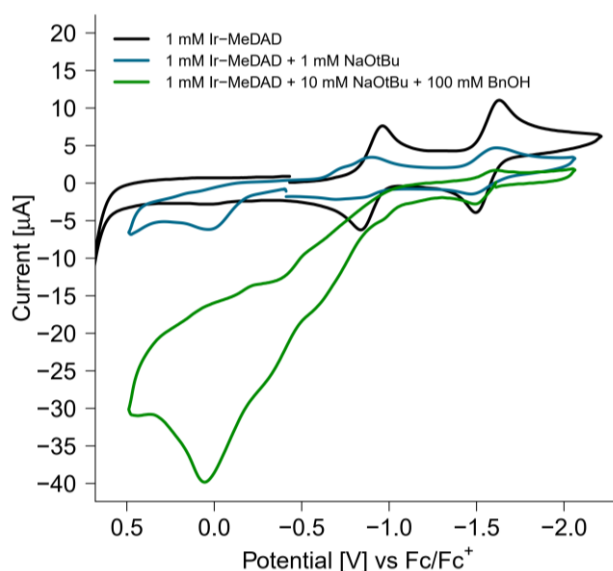
Figure 82. Overlaid CVs of complex [**46**]OTf (black trace), with 1 eq. of NaO*t*Bu (blue trace) and 10 eq. of NaO*t*Bu with 100 mM BnOH. Conditions: 100 mM *n*Bu$_4$NPF$_6$, THF, GC WE, Pt on TiO$_x$ CE, Ag/Ag$^+$ RE, scan rate 100 mV/s.

8.1.5. Mechanistic investigations on [Ir(trop$_2$dach)]OTf complex [*38*]OTf

Complex [**38**]OTf, with its saturated backbone and two NH groups, was previously found an active electrocatalyst in *o*-DCB.[68] Due to the impracticability of this solvent, other solvents for electrochemical applications were investigated. DCM gave similar CV results to *o*-DCB but is not the best solvent for electrochemistry either. It was found that MeCN reacts with the reduced complex and could therefore not be used. Therefore, THF was chosen for further investigation. Previous reports used NaOPh as a base, but it leads to background oxidation. Therefore, NaO*t*Bu was chosen as base for deprotonation of the catalyst. The deprotonation of [**38**]OTf leads to the appearance of an irreversible oxidation peak at -0.25 V, which is increased upon addition of BnOH substrate (shown in Figure 83).
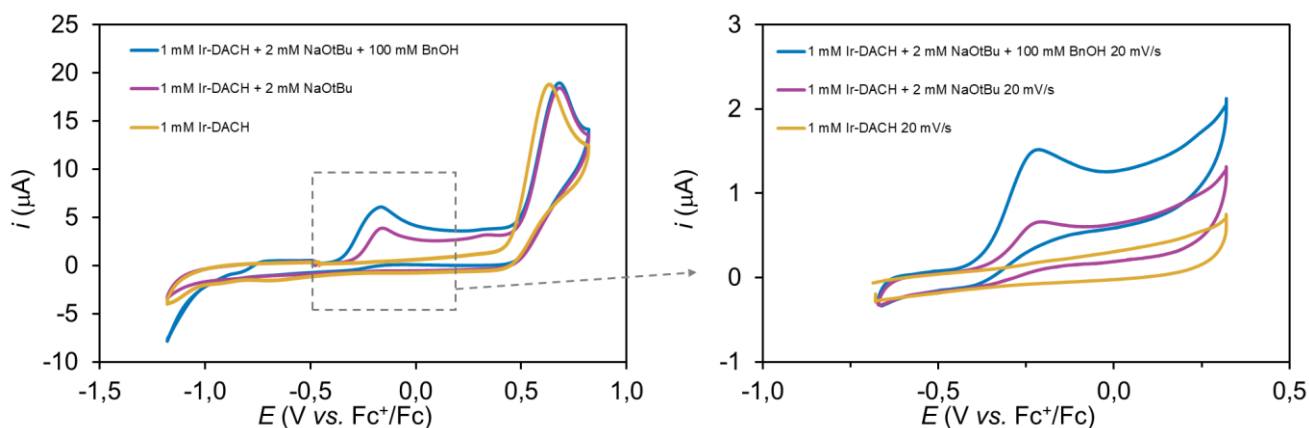
Figure 83. CV of [**38**]OTf (orange trace), [**38**]OTf + 2 eq. NaOtBu (pink trace), [**38**]OTf + 2 eq. NaOtBu + 100 eq. BnOH (blue trace) at 100 mV/s (left side) and respective isolated peaks at 20 mV/s (right side). Conditions: 100 mM nBu$_4$NPF$_6$, THF, GC WE, Pt CE, Ag/Ag$^+$ RE, scan rate 100 mV/s.

8.2. Overpotential measurement of [**38**]OTf

The overpotential of the alcohol oxidation with [**38**]OTf was determined to be 1.2 V, the respective plot and experimental conditions are depicted in Figure 84. The experiment was performed according to literature procedures.[56] The lower the overpotential, the more efficient is the catalysis. The value of 1.2 V is rather high compared to other catalysts.[67,181]
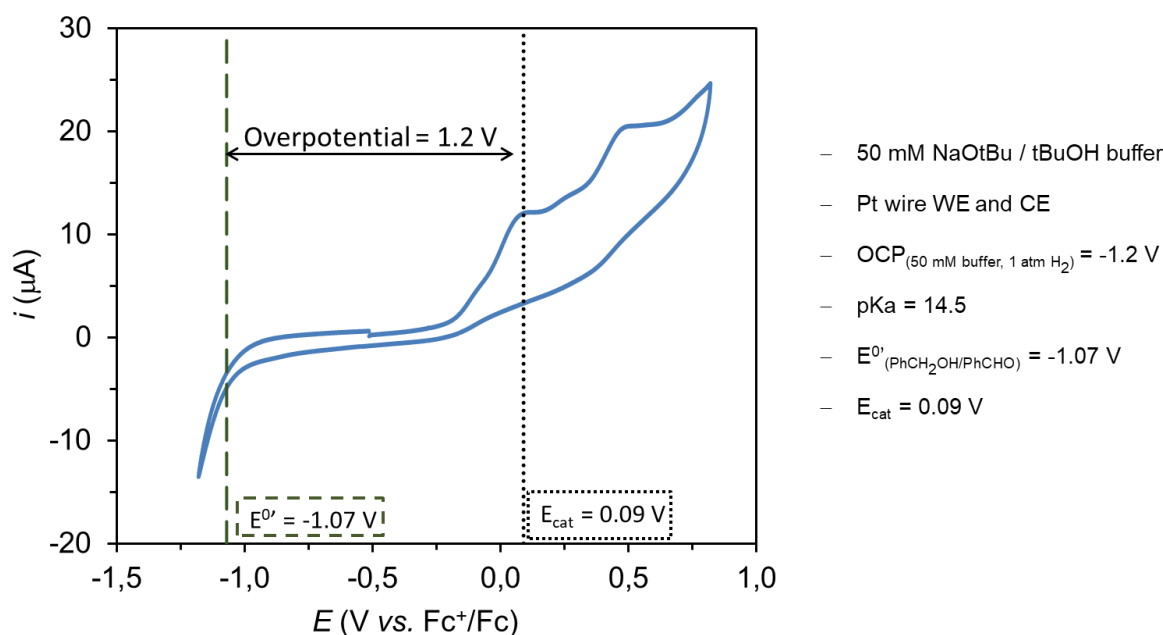
- 50 mM NaOtBu / tBuOH buffer
- Pt wire WE and CE
- OCP$_{(50\ mM\ buffer,\ 1\ atm\ H_2)}$ = -1.2 V
- pKa = 14.5
- E$^{0'}$$_{(PhCH_2OH/PhCHO)}$ = -1.07 V
- E$_{cat}$ = 0.09 V

Figure 84. CV for determination of overpotential for the oxidation of BnOH with [**38**]OTf; conditions and experimental values are given on the right.

8.3. Bulk electrolysis for the electrochemical alcohol oxidation

A previous report showed that complex [**38**]OTf is an active electrocatalyst for the electrochemical alcohol oxidation in o-DCB.[68] Since chlorinated solvents are not sustainable, their replacement by halogen-free solvents (such as THF or MeCN) is desirable. Those would also have a higher dielectric constant and are thus more practical for electrochemical applications. Furthermore, an alkyl

substituted phenolate base was employed in the previously reported reaction, which was envisioned to be replaced by a simpler and redox-inactive base such as NaO*t*Bu.

The investigations by cyclic voltammetry described in sections 8.1 showed an increase of current upon addition of alcohol to the reaction. To find out if this is due to a catalytic current with product formation, bulk electrolysis was performed. Therefore, different setups were tested with large surface electrodes and a vessel that allowed for stirring of the solutions. RVC (reticulated vitreous carbon / carbon foam) or Pt-mesh electrodes were used as working and counter electrodes, which were connected via gold wire or copper wires. Divided cells were used as reaction vessels, where the working and the counter compartment are separated by a microporous glass frit to inhibit unwanted crossover between the compartments. The problem with this setup is the high resistance, which is a problem for the used solvents THF and DME, which both have a rather low dielectric constant. In order to circumvent this problem, higher electrolyte concentrations were employed: 150-200 mM nBu$_4$NPF$_6$ instead of the standard 100 mM concentration.

Platinum wire counter electrodes were used, since they promote hydrogen evolution as side reaction, which is the ideal case. As for the chemical alcohol oxidation with [**40**]OTf, electrochemically it seems like the addition of base is necessary for obtaining catalytical current (see previous subchapter). Therefore, different amounts of base (NaO*t*Bu) were added, in order to investigate its influence. If hydrogen evolution is hindered at the counter electrode, the addition of base is crucial to take up the protons from the alcohol oxidation reaction happening at the WE.

The divided cell was held at a fixed potential performing a chronoamperometry (CA). This method is often preferred over chronopotentiometry (CP) because controlling the applied potential leads to less unwanted side reactions in case the current is dropping (which would lead to a change to more extreme potentials with these settings). The drawback here is that the amount of charge passed is different for each experiment. But the most important value here is the faradaic efficiency, which shows how much of the electricity used has actually gone into product formation and is thereby a measure of the selectivity of the process to the formation of aldehyde. This value is obtained by dividing the obtained yield of aldehyde (which was determined by ^{1}H NMR spectroscopy) by its theoretical yield, which is calculated from the passed charge. The yield of the reaction is also important but differs strongly on reaction times and the practical setup. The theoretical yield is calculated by equation 1.

$$FE = \frac{n*z*F}{Q} = \frac{yield_{(measured)}}{yield_{(theoretical)}} * 100\ \% \qquad (1)$$

z = number of electrons required for the product formation
n = number of moles of product
F = faraday constant
Q = charge passed

An undivided setup was tested with [**38**]OTf, but only 11% yield and a faradaic efficiency of 44% could be obtained after 18 h (see Table 30, entries 2 and 3). Blank experiments showed no conversion of alcohol (entry 1). When [**40**]OTf is compared to [**38**]OTf, which was used in all other catalyses, a rather low yield (6%) was obtained together with some side products (Table 30, entry 4). Even though the yields were very low, acceptable faradaic efficiency was obtained. Probably the yields could be increased by optimization of the reaction setup.

Table 31 and Table 32 show the results of the performed CA and CP experiments with a divided cell setup. Blank experiments showed no conversion of alcohol. The addition of base seems to be crucial, although high amounts of NaO*t*Bu (50 mol%) seem to have a negative influence on the catalytic conversion when compared to 10 mol% of base. The best result was obtained with entry 2 in Table 31, where a FE of 34% was achieved, although the absolute yield of 19% after 20 h is rather low. CA with divided cells also showed moderate yields (10 – 18%, see Table 32), but the data collection did not allow for a reasonable determination of FE.

The data presented in this section is rather preliminary and should be repeated in order to get reliable values. In addition, all bulk electrolyses were performed under air, which could lead to side products and decomposition of the complex catalyst over time.

8.3.1. Results with an undivided cell setup

Table 30. Chronoamperometry in THF with an undivided cell and RVC WE and Pt wire CE, 1 mol% catalyst and 0.34 mmol BnOH substrate. CA was run at a constant potential of 0.6 V for 18 h.

entry	catalyst	NaOtBu [mol%]	Yield [%]	Charge passed [C]	FE [%]
1	-	50	0	1.4	0
2	[**38**]OTf	5	11	16.5	44
3	[**38**]OTf	50	4	6.2	42
4	[**40**]OTf	50	6	10	40

8.3.2. Results with a divided cell setup

Table 31. Chronopotentiometry in THF with a divided cell and Pt wire WE and CE, 1 mol% catalyst and 0.67 mmol 4-MeOBnOH substrate. CP was run at a constant current of 1 mA for 20 h.

entry	catalyst	NaOtBu [mol%]	Yield [%]	Charge passed [C]	FE [%]
1	[**38**]OTf	5	14	72	25
2	[**38**]OTf	10	19	72	34
3	[**38**]OTf	50	12	72	21

Table 32. Chronoamperometry in THF with a divided cell and RVC WE and Pt wire CE, 1 mol% catalyst and 0.67 mmol 4-MeOBnOH substrate. CA was run at a constant potential of 0.2 V for 18 h.

entry	catalyst	NaOtBu [mol%]	Yield [%]	Charge passed [C]	FE [%]
1	-	50	0	0.4	0
2	[**38**]OTf	10	10	7.2	167
3	[**38**]OTf	50	18	11.6	200

9. Conclusion and outlook

In the first part of this chapter, the variety of products resulting from reduction reactions of [**40**]OTf was described. Not only the neutral radical [**40**]•, but also doubly reduced species with different (partially coordinated) counter ions could be structurally and spectroscopically investigated. Interestingly, a four times reduced species Li$_3$[**41**] was obtained, where for the first time, the cleavage of the N$_{dad}$−C$_{trop}$ bond was observed.

Furthermore, the combination of basic and reductive conditions led to the dimerized bimetallic species [**42**] including a coupled biradical motif. This compound could be fully characterized and DFT calculations gave insight into its electronic properties. Furthermore, it was found that the C−H bond at the dad backbone in [**40**]OTf is very reactive towards nucleophilic attack in general. This was not only demonstrated with the ligand dimerization but also addition of NaHMDS or NaOtBu to the dad upon C−C, C−N and C−O bond formation.

Further reactivity studies on iridium dach complex [**38**]OTf showed another modification of the ligand, under basic and oxidative conditions. Oxidative dehydrogenation of the cyclohexyl backbone led to fully dehydrogenated [**50**] with a planar C$_6$ ring including conjugated double bonds. This species is likely formed under catalytic conditions of alcohol oxidation, the role of [**50**] as catalyst is still under investigation. BQ was used as oxidant and hydrogen acceptor, which seems to have a redox potential too low to form the fully oxidized cationic [**50**]OTf. Therefore, the use of substituted BQ derivatives might help with obtaining the desired cationic compound structurally related to [**40**]OTf.

In the next section, chemical alcohol dehydrogenation with bimetallic [**42**] and BQ as oxidant was performed. Since [**42**] is already a reduced species, the need for additional base was investigated. It was found that under certain conditions no base is needed to obtain satisfying catalytic activity. Although, optimization of reaction conditions is still needed.

Mechanistic investigations showed that the imagined catalytic cycle (hydrogenation of the dad backbone) can not be true for the dinuclear iridium catalyst [**42**]. Therefore, it has to be questioned for cationic [**40**]OTf likewise, since it is assumed that both catalysts proceed with the same mechanism. More experimental data will be needed to get better understanding of the reaction mode.

Electrochemical investigations were performed on all iridium complexes presented, which were subsequently extended for electrochemical alcohol oxidation. Therefore, CVs were measured to determine the influence of base and alcohol on the current response. Significant, although not very large, catalytic currents were observed. It has to be kept in mind that background oxidation from bases such as NaOtBu and NaOPh can occur and interfere with catalysis.

The catalytic currents from the CVs were confirmed with bulk electrolysis, which showed that complexes [**40**]OTf and [**38**]OTf are able to electrocatalytically oxidize alcohols to aldehydes. The experiments were performed in THF with NaO*t*Bu as base. Blank experiments showed no conversion of alcohol. Different setups were tested for bulk electrolysis, each of them giving different aldehyde yields and faradaic efficiencies. Further studies on bulk electrolysis are needed in order to get more reliable values. In addition, all electrolyses should be performed under inert atmosphere to eliminate the possibility of interference with oxygen or water.

Further electrochemical experiments could include the addition of catalytic amounts of BQ under inert atmosphere to the catalytic system. With this, BQ would act as mediator which is regenerated at the electrode surface after reoxidation of the catalyst. Additionally, the concentration of the catalytic system in electrochemical experiments was rather low compared to the chemical alcohol oxidation conditions. Preliminary results showed that a high concentration of alcohol is required for the catalysis to proceed efficiently. Therefore, the same reaction concentrations should be employed in electrochemical alcohol oxidation. It has to be kept in mind that the conductivity of the solution has to be sufficiently high, which might have to be adapted by addition of larger amounts of electrolyte.

CHAPTER VI – General Conclusion and Outlook

Chapter VI – General Conclusion and Outlook

This work has shown that the presence of a second metal center can be beneficial and alters the reactivity of the ligand sphere. Several ligand reactivities of the carbon based fragments of the ligands were observed. The non-innocent behaviour of the ligands in the presented transition metal complexes plays an important role – chemically and for redox reactions.

A dirhodium complex featuring an alkyne substituted trop ligand was subjected to reductive and basic conditions, which led to different rearrangement reactions within the carbon sphere of the ligand (Chapter II). Detailed electrochemical investigations were performed and DFT calculations complemented the experimental characterization. The strong difference in reactivity of the mono rhodium equivalent proved the importance of the second metal atom for the formation of stable products.

The same ligand was used to generate further hetero bimetallic complexes with $Rh^I Pt^{II}$ or $Rh^I Cu^I$ metal centers for N_2O or NO reduction (Chapter III). Although none of the conducted experiments showed relevant catalytic activity, further experiments could be conducted to find the right reaction conditions. The platinum containing complexes decompose under H_2 atmosphere, but Rh-Cu complexes have not yet been tested under catalytic conditions and seem promising candidates. Future work could focus on the described amine based complexes and their catalytic application. Therefore, the complexation reaction needs to be optimized to introduce a second metal atom.

To move away from precious metals towards first-row transition metals, cobalt and copper complexes were synthesized (Chapter IV). Remarkable coordination properties of the alkyne ligands were observed, depending on the precise chemical environment. With those bimetallic complexes in hand, further investigations could focus on electrochemical or catalytic applications.

The final part of this thesis showed mechanistic investigations on the reactivity of iridium complexes under the conditions of alcohol oxidation (Chapter V). Therefore, the catalysts were subjected to a reductive or oxidative environment. The presence of base (NaO*t*Bu or KO*t*Bu) was found to play a significant role in reactivity and led to dimerization or dehydrogenation of the ligands on the iridium center. Catalytic alcohol oxidation was performed with the obtained diiridium complex to possibly eliminate the need for the addition of base. The reaction conditions for some challenging substrates still leave room for further optimization. After detailed cyclic voltammetry measurements of the complexes, electrochemical alcohol oxidation was attempted. Although catalytic currents were observed in CV, the formation of aldehyde could only be confirmed in preliminary experiments. These should be repeated and reaction conditions (including the electrochemical setup) improved to get the best possible results for alcohol oxidation without the need for a chemical oxidant.

CHAPTER VII - Experimental

1. General remarks

All reactions and manipulations were conducted under an argon atmosphere using standard Schlenk and glovebox techniques unless stated otherwise. Solvents were either obtained from an MBraun Solvent Purification System or dried and stored according to common procedures. $Br_2tropOH$ (**S1**),[69,182] $[Rh_2(COE)_4OTf_2]$,[183] $[Ir(trop_2dad)]OTf$ ([**40**]OTf)[173] and $[Ir(trop_2dach)]OTf$ ([**38**]OTf)[65] were synthesized according to literature procedures. All other compounds were commercially available. NMR spectra were recorded with a Bruker 200, 300, 400 or 500 MHz NMR spectrometer at room temperature unless otherwise stated. NMR spectra were referenced to TMS (^{1}H and ^{13}C), $BF_3 \cdot OEt_2$ ([11]B), $CFCl_3$ (^{19}F), H_3PO_4 (^{31}P), $Rh(acac)_3$ ([103]Rh). Chemical shifts [δ] are given as dimensionless numbers in ppm and the absolute values of the coupling constants are given in Hertz [Hz]. Multiplicities are abbreviated as singlet (s), doublet (d), triplet (t), quartet (q) and broad (br). The chemical shift ([103]Rh) values are in ppm and were calculated by determining the absolute frequency of the cross peak and relating it to the arbitrary reference frequency (Ξ([103]Rh) = 3.16 MHz at 100.00 MHz).

Alkyne carbons are indicated as $C_{C\equiv C}$, aromatic carbon and hydrogens as C_{ar} and CH_{ar}, quaternary carbons as C_q, benzylic as C_{benz} and CH_{benz}, propargylic on the cyclohexyl group as CH_{cy}, rest of the cyclohexyl group as CH_{ali} and olefinic as C_{olef}. Single crystals suitable for X-ray diffraction were coated with polyisobutylene oil in a glovebox, transferred to a nylon loop and then transferred to the goniometer of an Oxford SynergyS, Oxford Excalibur or D8-Venture diffractometer equipped with a copper X-ray tube (λ = 1.5406 Å).

2. Compounds of Chapter II

(CyC≡C)₂tropOH (S2)
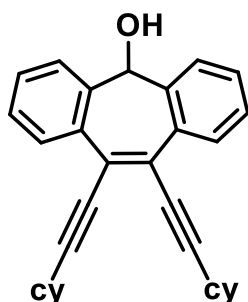
Br$_2$tropOH (**S1**) (5.0 g, 13.7 mmol, 1 eq.) was dissolved in a 1:1 mixture of toluene and triethylamine (150 mL). Tetrakis(triphenylphosphine) palladium (0) (0.79 g, 0.05 eq.) and copper(I) iodide (0.13 g, 0.05 eq.) and degassed cyclohexylacetylene (5.5 mL, 4.5 g, 3 eq.) were added and the resulting mixture was heated to 60°C for 3 days. The resulting dark mixture was filtered over a pad of celite. The filtrate was then concentrated in vacuo and the resulting dark brown residue triturated with n-hexane until a red-brown solid was obtained. The product was purified by column chromatography (silica, *n*-hexane / DCM / ethylacetate 14 / 3 / 1, Rf = 0.3) and recrystallized from the eluent solvent. **S2** was obtained as off-white powder (1.8 g, 31.3 %).

^{1}H NMR (300 MHz, CDCl$_3$) δ 7.72 (d, *J* = 7.7 Hz, 2H, C*H*$_{ar}$), 7.62 (d, *J* = 7.7 Hz, 2H, C*H*$_{ar}$), 7.32 (t, *J* = 7.6 Hz, 2H, C*H*$_{ar}$), 7.18 (t, *J* = 7.6 Hz, 2H, C*H*$_{ar}$), 5.22 (s, 1H, C*H*$_{benz}$), 2.74 (tt, *J* = 8.7, 4.0 Hz, 2H, C*H*$_{cy}$), 2.45 (d, *J* = 3.5 Hz, 1H, O*H*), 2.00 – 1.72 (m, 8H, C*H*$_{ali}$), 1.68 – 1.47 (m, 3H, C*H*$_{ali}$), 1.43 – 1.29 (m, 6H, C*H*$_{ali}$).

^{13}C NMR (75 MHz, CDCl$_3$) δ 142.57 (C$_{ar}$), 132.65 (C$_{ar}$), 129.00 (C$_{ar}$), 128.41 (C$_{ar}$), 128.29 (C$_{ar}$), 126.19 (C$_{ar}$), 120.58 (C$_{ar}$), 102.70 (C$_{ar}$), 82.48 (C$_{C≡C}$), 70.01 (C$_{C≡C}$), 32.78 (C$_{ali}$), 32.75 (C$_{ali}$), 30.41 (C$_{cy}$), 26.15 (C$_{ali}$), 24.98 (C$_{ali}$).

(CyC≡C)2tropCl (S3)
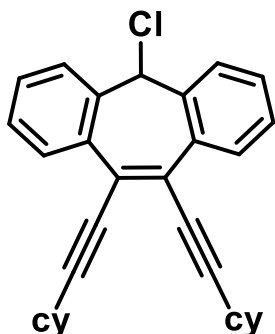
(CyCC)$_2$tropOH (**S2**) (1.7 g, 4.2 mmol, 1 equiv.) was dissolved in dry DCM (80 mL) and cooled to 0°C. Next, a solution of distilled SOCl$_2$ (0.34 mL, 4.6 mmol, 1.1 equiv.) and pyridine (0.38 mL, 4.6 mmol, 1.1 equiv.) in dry DCM (20 mL) was added dropwise and stirred for 30 minutes at 0°C and another 30 minutes at room temperature. The solvent was then removed using an external cooling trap. The residue was suspended in little amounts of toluene, filtered over celite to remove pyridinium chloride and the filtrate was concentrated in vacuo. The toluene was evaporated, and the resulting sticky solid was triturated with hexane until a yellowish solid of **S3** (1.5 g, 80 %) was obtained. NMR spectra showed a mixture of endo and exo conformers present in solution.

^{1}H NMR (300 MHz, CDCl$_3$) δ 1.0-2.0 (m, 20H, C*H*$_{ali}$), 2.69 (m, 2H, C*H*$_{cy}$), 5.57 (s, 0.42H, C*H*Cl, major conformer), 5.96 (s, 0.58 H, C*H*Cl, minor conformer), 7.40 – 7.02 (m, 6H, C*H*$_{ar}$), 7.76 – 7.59 (m, 2H, C*H*$_{ar}$), 7.91 (dd, *J* = 8.0, 1.9 Hz, 1H, C*H*$_{ar}$).

^{13}C NMR (75 MHz, CDCl$_3$) δ 139.40 (C$_{ar}$), 138.83 (C$_{ar}$), 134.94 (C$_{ar}$), 133.21 (C$_{ar}$), 130.96 (C$_{ar}$), 129.10 (C$_{ar}$), 128.73 (C$_{ar}$), 128.69 (C$_{ar}$), 128.40 (C$_{ar}$), 128.30 (C$_{ar}$), 128.27 (C$_{ar}$), 126.96 (C$_{ar}$), 126.75 (C$_{ar}$), 125.36 (C$_{ar}$), 122.70 (C$_{ar}$), 103.16 (C$_{C≡C}$, conformer 1), 102.94 (C$_{C≡C}$, conformer 2), 82.66 (C$_{C≡C}$, conformer 1), 82.07 (C$_{C≡C}$, conformer 2), 65.60 (CH$_{benz}$, conformer 1), 60.27 (CH$_{benz}$, conformer 2), 32.74 (C$_{ali}$), 32.69 (C$_{ali}$), 32.65 (C$_{ali}$), 30.43 (C$_{cy}$), 30.29 (C$_{cy}$), 26.10 (C$_{ali}$), 26.07 (C$_{ali}$), 25.02 (C$_{ali}$), 24.90 (C$_{ali}$).

(CyC≡C)₂tropPPh₂ (1)
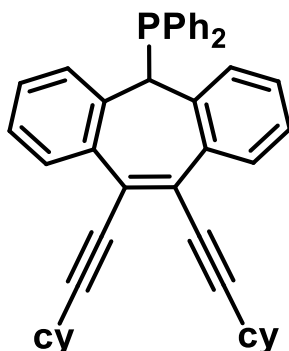
(CyCC)₂tropCl (**S3**) (1.40 g, 3.2 mmol, 1 equiv.) was suspended in a mixture of dry toluene (16 mL) and dry *n*-hexane (8 mL). Then, diphenylphosphine (0.63 mL, 3.5 mmol, 1.1 equiv.) was added. The reaction mixture was stirred at 50°C over the weekend, while yellow precipitate was formed. The solution mixture was heated to reflux (80°C) for 30 minutes and after it was cooled down degassed sodium carbonate (7 mL, 10% in H_2O) was added. The solution was heated to 50°C for 3 hours before it was heated to reflux (80°C) for 30 minutes. After cooling down, the toluene phase was separated from the aqueous phase and extracted twice with toluene. The solvent was evaporated, and the red oil was washed and triturated with *n*-hexane until a powder was obtained. The bright red solid was stirred vigorously in acetonitrile (4 mL) and a pinkish powder was precipitated out of the solution. The product was filtrated, dried, washed with *n*-hexane and dried under vacuum. The off-white powder can be recrystallized from hot toluene. Yield 1.0 g, 53 %. Colourless crystals suitable for X-ray diffraction were obtained from slow diffusion of *n*-hexane in a solution of benzene. Elemental analysis for $C_{43}H_{41}P \cdot (Na_2CO_3)_{0.1}$ calculated (%): C 86.37, H 6.90; found (%): C 86.69, H 7.18.

^{1}H NMR (300 MHz, C_6D_6) δ 8.11 (dd, *J* = 7.8, 1.4 Hz, 2H, C*H*ar), 7.45 (ddd, *J* = 8.2, 6.8, 1.8 Hz, 4H, C*H*ar), 7.06 – 6.57 (m, 12H, C*H*ar), 4.82 (d, $^2J_{PH}$ = 5.6 Hz, 1H, C*H*benz), 2.86 – 2.57 (m, 2H, C*H*cy), 1.93 – 1.55 (m, 12H, C*H*ali), 1.44 – 1.06 (m, 8H, C*H*ali).

^{13}C NMR (75 MHz, C_6D_6) δ 141.49 (d, *J* = 8.9 Hz, *C*Har), 138.97 (*C*Har), 138.68 (*C*Har), 136.22 (d, *J* = 4.4 Hz, *C*Har), 133.92 (d, $^2J_{CP}$ = 20.1 Hz, 4 C, CHar), 130.54 (*C*Har), 130.40 (d, $^4J_{CP}$ = 6.3 Hz, 2 C, Colef), 129.21, 129.17, 128.70, 128.37, 128.07, 127.98, 126.29, 101.97 (s, 2 C, *C*≡C), 84.40 (s, 2 C, Cc≡c), 56.83 (d, $^1J_{CP}$ = 21.9 Hz, 1 C, CHbenz), 32.94 (s, 1 C, CH₂), 32.89 (s, 1 C, Cali), 30.56 (s, 2 C, *C*Hcy), 26.29 (s, 1 C, Cali), 24.90 (s, 4 C, Cali).

^{31}P{^{1}H} NMR (121.5 MHz, C_6D_6): *δ* -14.0 (s, 1 P, tropP).

[(((CyC≡C)₂tropPPh₂)Rh₂(μ-Cl)₂]₂ ([2])
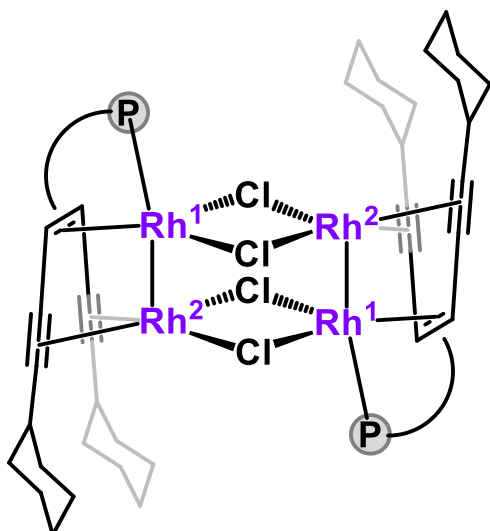
[Rh₂(μ-Cl)₂(COE)₄] (244 mg, 0.340 mmol, 1 equiv.) and (CyC≡C)₂tropPPh₂ (**1**) (200 mg, 0.340 mmol, 1 equiv.) were stirred in 2 mL of benzene. After 15 minutes a precipitate started to appear. The reaction mixture was stirred overnight and then filtrated. The solid was washed with *n*-hexane until all cyclooctene was removed. The orange-red solid was then dried under reduced pressure. Yield: 240 mg (82 %). Bright red crystals were obtained by slow diffusion of hexane into a solution of DCM. Elemental analysis for $C_{86}H_{82}Cl_4P_2Rh_4 \cdot (CH_2Cl_2)$ calculated (%): C 57.54, H 4.66; found (%): C 57.83, H 4.85.

^{1}H NMR (300 MHz, CD₂Cl₂) δ 7.93 (d, *J* = 7.6 Hz, 2H, C*H*ar), 7.61 (t, *J* = 9.0 Hz, 4H, C*H*ar), 7.45 – 6.84 (m, 16H, C*H*ar), 4.86 (dd, *J* = 14.2 Hz, 2.6 Hz, 1H, C*H*benz), 2.60 – 2.47 (m, 2H, C*H*cy), 2.65 – 2.02 (m, 6H, C*H*ali), 1.95 – 1.51 (m, 8H, C*H*ali), 1.50 – 1.08 (m, 6H, C*H*ali).

^{13}C NMR (75 MHz, CD₂Cl₂) δ 135.83 (d, *J* = 7.5 Hz, 2C, C$_{ar}$), 134.47 (dd, *J* = 4.3, 1.7 Hz, 2C, C$_{ar}$), 132.92 (d, *J* = 9.4 Hz, 2C, C$_{ar}$), 130.63 (CH$_{ar}$), 130.07 (CH$_{ar}$), 129.04 (d, *J* = 2.4 Hz, 2C, C$_{ar}$), 127.92, 127.84, 127.39, 126.79, 126.66, 126.34, 125.36, 83.49 (d, *J* = 14.4 Hz, 2C, C$_{C≡C}$), 69.85 (d, *J* = 7.4 Hz, 2C, C$_{C≡C}$), 49.26 (d, $^1J_{CP}$ = 26.1 Hz, 1C, CH$_{benz}$), 38.89 (d, *J* = 15.1 Hz, 2C, C$_{olef}$), 34.78 (C$_{ali}$), 33.13 (d, *J* = 26.4 Hz) (C$_{ali}$), 25.29 (C$_{ali}$), 25.11 (d, *J* = 4.6 Hz, C$_{ali}$).

^{31}P NMR (121 MHz, CD₂Cl₂) δ 101.23 (dd, $^1J_{PRh}$ = 212.4 Hz, $^2J_{PRh}$ = 4.5 Hz, tropP).

[103]Rh NMR (15.8 MHz, CD₂Cl₂): *δ* -6724 (d, $^1J_{RhP}$ = 212.8 Hz, Rh[1]), -4736 (d, $^2J_{PRh}$ = 108.5 Hz, Rh[2]).

[((CyC≡C)₂tropPPh₂)Rh₂OTf₂] ([3])
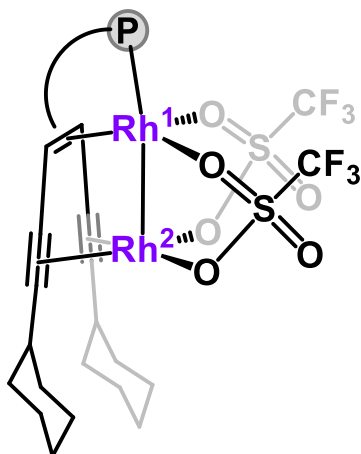
(CyC≡C)₂tropPPh₂ (**1**) (100 mg, 0.170 mmol, 1 eq.) was stirred with [Rh₂(COE)₄OTf₂] (160 mg, 0.170 mmol, 1 eq.) for 1 h in 5 mL THF. The solvent was removed in vacuo and the dark brown solid washed with hexane until all COE was removed. The product can be recrystallized from THF/hexane. Yield: 160 mg (87 %). Crystals suitable for X-ray diffraction were grown from slow diffusion of *n*-hexane into a solution of [**3**] in DCM. Elemental analysis for $C_{45}H_{41}F_6O_6PRh_2S_2$ calculated (%): C 49.46, H 3.78; found (%): C 49.30, H 4.29.

^{1}H NMR (500 MHz, Acetonitrile-*d₃*) δ 8.03 (dd, *J* = 7.7, 1.3 Hz, 2H, C*H*ar), 7.65 (tt, *J* = 7.1, 1.7 Hz, 2H, C*H*ar), 7.57 (ddt, *J* = 9.9, 6.8, 1.5 Hz, 4H, C*H*ar), 7.54 – 7.46 (m, 7H, C*H*ar), 7.44 – 7.32 (m, 4H, C*H*ar), 5.50 (dd, *J* = 15.3, 2.7 Hz, 1H, C*H*benz), 2.88 (td, *J* = 10.7, 5.3 Hz, 2H, C*H*cy), 2.54 (d, *J* = 12.2 Hz, 2H, C*H*ali), 2.47 (dd, *J* = 12.6, 4.1 Hz, 2H, C*H*ali), 2.05 – 1.77 (m, 9H, C*H*ali), 1.67 (dddd, *J* = 15.1, 13.0, 9.9, 3.5 Hz, 5H, C*H*ali), 1.58 – 1.46 (m, 2H, C*H*ali).

^{13}C NMR (126 MHz, Acetonitrile-*d₃*) δ 135.48 (Car), 134.36 (Car), 133.05 (d, J = 9.2 Hz, Car), 131.63 (Car), 129.24 (d, J = 6.8 Hz, Car), 128.77 (Car), 128.52 – 128.18 (m, Car), 127.74 (Car), 126.86 (Car), 83.48 (d, J = 12.2 Hz, Cc≡c), 68.58 (d, J = 6.7 Hz, Cc≡c), 47.54 (d, J = 27.2 Hz, CHbenz), 37.51 (d, J = 15.9 Hz, Colef) 35.19 (Cali), 33.79 (Cali), 33.53 (Cali), 25.59 (Cali), 25.35 (Cali).

^{19}F NMR (471 MHz, Acetonitrile-*d₃*) δ -79.30 (s, OTf).

^{31}P NMR (162 MHz, Acetonitrile-*d₃*) δ 106.03 (dd, $^1J_{PRh}$ = 191.7 Hz, $^2J_{PRh}$ = 5.7 Hz, tropP); (121 MHz, CD₂Cl₂) δ 97.24 (dd, $^1J_{PRh}$ = 217.8 Hz, $^2J_{PRh}$ = 3.8 Hz, tropP).

[103]Rh NMR (15.8 MHz, Acetonitrile-*d₃*): *δ* -6973 (d, $^1J_{RhP}$ = 197.2 Hz, Rh¹), -688 (d, $^2J_{RhP}$ = 194.1 Hz, Rh²).

[((CyC≡C)₂tropPPh₂)Rh₂bipy₂](OTf)₂ ([4](OTf)₂)
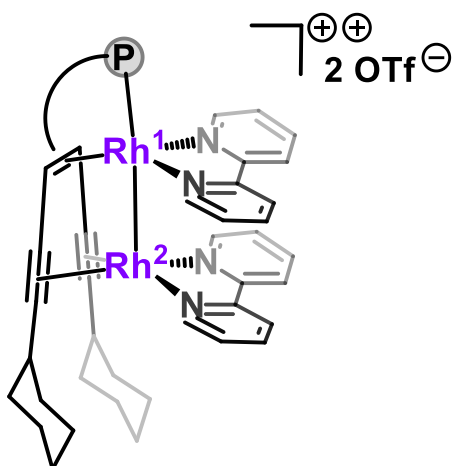
Method 1: Rh₂OTf₂ ([**3**]) (100 mg, 0.092 mmol, 1 eq.) and bipy (29 mg, 0.183 mmol, 2 eq.) were stirred in 5 mL THF for 10 min. After a few minutes a solid started to appear (the product is only moderately soluble in THF). The solvent was removed and washed with hexane to obtain a dark red powder. Yield: 122 mg (95 %).

Method 2: [((CyC≡C)₂tropPPh₂)Rh₂(μ-Cl)₂]₂ ([**2**]) (100 mg, 0.058 mmol, 1 eq.) and bipy (36 mg, 0.231 mmol, 4 eq.) were stirred for 5 min in 5 mL THF, then KOTf (43 mg, 0.231 mmol, 4 eq.) was added and the mixture was stirred overnight. The solid KCl was filtered off, washed with 5mL MeCN and the solution dried in vacuo. The dark red powder was washed with hexane and Et₂O. Yield: 130 mg (80 %). Crystals were grown from slow diffusion of hexane into a solution of THF.

UV-Vis (THF): λ_{max} = 535, 390 nm. Elemental analysis for $C_{65}H_{57}F_6N_4O_6PRh_2S_2 \cdot (K_1C_1F_3O_3S_1)_{0.2}$ calculated (%): C 54.28, H 3.89, N 3.88; found (%): C 54.29, H 4.12, N 4.01.

^{1}H NMR (500 MHz, CD₃CN) δ 8.42 (d, J = 5.3 Hz, 2H, CH_{ar}), 8.35 (d, J = 7.8 Hz, 2H, CH_{ar}), 8.11 (d, J = 5.7 Hz, 2H, CH_{ar}), 7.90 (td, J = 7.8, 1.6 Hz, 2H, CH_{ar}), 7.83 (d, J = 8.0 Hz, 2H, CH_{ar}), 7.56 (p, J = 7.4, 6.4 Hz, 6H, CH_{ar}), 7.35 (t, J = 7.5 Hz, 2H, CH_{ar}), 7.29 (dd, J = 7.4, 5.8 Hz, 2H, CH_{ar}), 7.26 (d, J = 7.5 Hz, 2H, CH_{ar}), 7.20 (t, J = 7.7 Hz, 2H, CH_{ar}), 6.96 (td, J = 7.9, 2.4 Hz, 4H, CH_{ar}), 6.81 – 6.73 (m, 7H, CH_{ar}), 5.27 (dd, J = 15.2, 2.8 Hz, 1H, CH_{benz}), 2.59 (ddd, J = 11.4, 7.8, 3.6 Hz, 2H, CH_{cy}), 2.51 (d, J = 13.1 Hz, 2H, CH_{ali}), 2.19 (d, J = 12.7 Hz, 2H, CH_{ali}), 1.91 – 1.63 (m, 10H, CH_{ali}), 1.45 – 1.23 (m, 5H, CH_{ali}).

^{13}C NMR (126 MHz, CD₃CN) δ 156.28 (C$_{ar}$), 154.87 (C$_{ar}$), 153.31 (C$_{ar}$), 152.12 (C$_{ar}$), 151.50 (C$_{ar}$), 144.40 (C$_{ar}$), 141.64 (C$_{ar}$), 139.77 (C$_{ar}$), 136.85 (d, J = 7.9 Hz, C$_{ar}$), 136.49 (C$_{ar}$), 133.09 (d, J = 9.0 Hz, C$_{ar}$), 131.94 (d, J = 2.7 Hz, C$_{ar}$), 131.65 (C$_{ar}$), 130.25 (d, J = 6.9 Hz, C$_{ar}$), 129.40 (C$_{ar}$), 129.12 (d, J = 10.1 Hz, C$_{ar}$), 128.67 (C$_{ar}$), 128.33 (C$_{ar}$), 128.03 (C$_{ar}$), 127.50 (C$_{ar}$), 123.95 (C$_{ar}$), 123.43 (C$_{ar}$), 88.18 (d, J = 11.7 Hz, C$_{C≡C}$), 79.42 (d, J = 6.4 Hz, C$_{C≡C}$), 49.26 (d, J = 26.9 Hz, C$_{benz}$), 38.58 (d, J =

14.0 Hz, C_{olefin}), 37.28 (C_{cy}), 34.84 (C_{ali}), 34.78 (C_{ali}), 32.32 (C_{ali}), 26.94 (C_{ali}), 26.53 (C_{ali}), 26.19 (C_{ali}), 23.36 (C_{ali}).

^{19}F NMR (471 MHz, CD$_3$CN) δ -79.29 (s, OTf). ^{31}P NMR (202 MHz, CD$_3$CN) δ 96.32 (dd, J = 192.6, 9.4 Hz, tropP).

^{103}Rh NMR (16 MHz, CD$_3$CN) δ -7045 (d, $^{1}J_{RhP}$ = 194.2 Hz, Rh^1), -744 (d, $^{2}J_{RhP}$ = 189.3 Hz, Rh^2).

[((CyC≡C)₂tropPPh₂)Rh₂bipy₂](OTf) ([4](OTf))
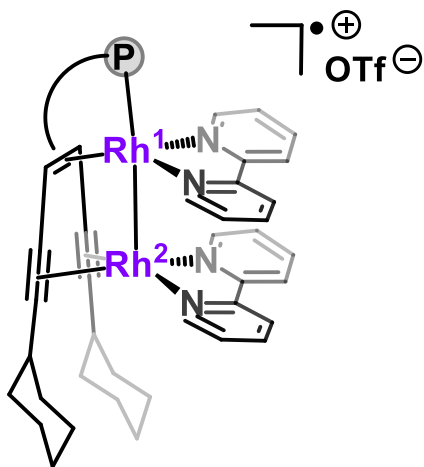
[((CyC≡C)₂tropPPh₂)Rh₂bipy₂]OTf₂ ([**4**](OTf)₂) (22 mg, 0.016 mmol, 1 eq.) was stirred with sodium naphthalenide solution (0.1 M in THF, 157 µL, 0.016 mmol, 1 eq.) and 15-crown-5 (3.5 mg, 0.016 mmol, 1 eq.) for 1 h. The solution was filtrated and placed in a freezer at -20°C to obtain a crystalline, dark red, paramagnetic product, which was washed with hexane and Et₂O. Yield: 10 mg (60 %). Crystals suitable for X-ray diffraction were grown from a saturated THF solution at -20 °C.

UV-Vis (MeCN): λ$_{max}$ = 579, 390 nm.

Elemental analysis for C$_{64}$H$_{57}$F$_3$N$_4$O$_3$PRh$_2$S calculated (%): C 61.20, H 4.57, N 4.46; found (%): C 61.40, H 4.81, N 4.74.

[((CyC≡C)₂tropPPh₂)Rh(μ-Cl)]₂ ([5])
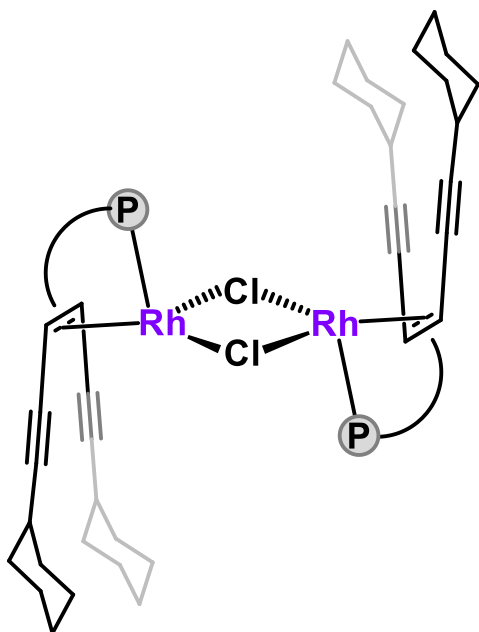
[Rh₂(μ-Cl)₂(H₂C=CH₂)₄] (66 mg, 0.170 mmol, 0.5 equiv.) and (CyC≡C)₂tropPPh₂ (**1**) (200 mg, 0.340 mmol, 1 equiv.) were stirred in 2 mL of benzene. After 15 minutes a precipitate started to appear. The reaction mixture was stirred for 3 h and then filtrated. The orange solid was washed with *n*-hexane twice and dried under reduced pressure. Yield: 190 mg (77 %). Bright red crystals were obtained from a toluene solution at -20 °C. Elemental analysis for $C_{86}H_{82}Cl_4P_2Rh_2$ calculated (%): C 71.03, H 5.68; found (%): C 69.83, H 6.26.

¹H NMR (300 MHz, CDCl₃) δ 8.11 (dd, *J* = 7.6, 1.5 Hz, 1H, C*H*ar), 7.89 – 7.64 (m, 2H, C*H*ar), 7.38 – 7.09 (m, 5H, C*H*ar), 7.01 (d, *J* = 7.6 Hz, 1H, C*H*ar), 4.90 (dd, *J* = 13.4, 3.3 Hz, 1H, C*H*benz), 2.74 (td, *J* = 9.6, 8.4, 4.3 Hz, 1H, C*H*cy), 2.16 – 2.01 (m, 2H, C*H*ali), 1.91 (td, *J* = 9.3, 4.5 Hz, 2H, C*H*ali), 1.85 – 1.74 (m, 1H, C*H*ali), 1.66 (d, *J* = 6.9 Hz, 1H, C*H*ali), 1.50 (d, *J* = 12.6 Hz, 4H, C*H*ali).

¹³C NMR (75 MHz, CDCl₃) δ 137.10 (Car), 137.06 (Car), 135.18 (Car), 135.09 (Car), 133.79 (Car), 133.66 (Car), 131.52 (Car), 130.89 (Car), 130.70 (Car), 130.66 (Car), 128.86 (Car), 128.39 (Car), 128.20 (Car), 128.16 (Car), 128.06 (Car), 127.50 (Car), 127.20 (Car), 112.41 (CC≡C), 112.35 (CC≡C), 57.96 (d, *J* = 12.1 Hz, CHolefin), 50.03 (d, *J* = 30.3 Hz, CHbenz), 32.17 (Cali), 32.15 (Cali), 31.27 (Cali), 26.01 (Cali), 25.01 (Cali), 24.98 (Cali).

³¹P NMR (202 MHz, CDCl₃) δ 113.45 (d, ¹*J*RhP = 267.8 Hz, tropP).

¹⁰³Rh NMR (16 MHz, CD₂Cl₂) δ -7405.6 (d, ¹*J*RhP = 269.8 Hz, Rh).

[((CyC≡C)₂tropPPh₂)Rhbipy](OTf) ([6](OTf))
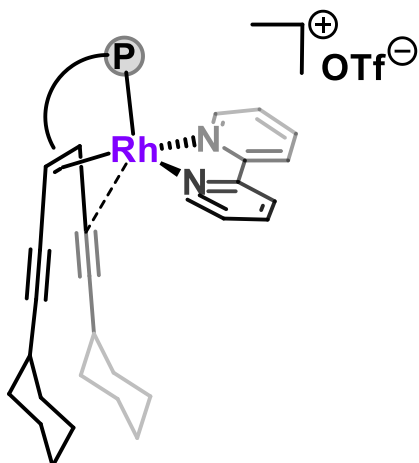
[((CyC≡C)₂tropPPh₂)Rh(μ-Cl)]₂ ([5]) (100 mg, 0.058 mmol, 1 eq.) and bipy (18 mg, 0.156 mmol, 2 eq.) were stirred for 5 min in 5 mL THF, then KOTf (22 mg, 0.156 mmol, 2 eq.) was added and the mixture was stirred for 3 h. The solid KCl was filtered off, and the solvent removed in vacuo. The dark red powder was washed with hexane and Et₂O. Yield: 125 mg (91 %). Single crystals were grown from a chloroform solution layered with *n*-hexane. Elemental analysis for $C_{54}H_{49}F_3N_2O_3PRhS$ calculated (%): C 65.06, H 4.95, N 2.81; found (%): C 65.24, H 5.14, N 4.15.

^{1}H NMR (200 MHz, THF-d_8) δ 8.81 (d, *J* = 7.9 Hz, 4H, C*H*$_{ar}$), 8.25 (d, *J* = 7.8 Hz, 2H, C*H*$_{ar}$), 8.12 (t, *J* = 8.4 Hz, 2H, C*H*$_{ar}$), 7.46 – 7.13 (m, 10H, C*H*$_{ar}$), 7.09 – 6.86 (m, 8H, C*H*$_{ar}$), 5.25 (dd, *J* = 13.8, 3.2 Hz, 1H, C*H*$_{benz}$), 2.60 – 2.35 (m, 2H, C*H*$_{cy}$), 1.73 – 1.12 (m, 20H, C*H*$_{ali}$).

^{13}C NMR (126 MHz, CDCl₃) δ 153.91 (C$_{ar}$), 152.04 (C$_{ar}$), 140.19 (C$_{ar}$), 137.02 (C$_{ar}$), 135.83 (C$_{ar}$), 131.91 (C$_{ar}$), 131.84 (C$_{ar}$), 131.23 (C$_{ar}$), 129.94 (C$_{ar}$), 129.56 (C$_{ar}$), 129.35 (C$_{ar}$), 128.37 (C$_{ar}$), 128.29 (C$_{ar}$), 128.14 (C$_{ar}$), 127.83 (C$_{ar}$), 127.78 (C$_{ar}$), 127.09 (C$_{ar}$), 126.17 (C$_{ar}$), 123.83 (C$_{ar}$), 107.85 (d, *J* = 5.9 Hz, C$_{C≡C}$), 78.54 (C$_{C≡C}$), 50.93 (d, *J* = 29.1 Hz, CH$_{benz}$), 47.11 (d, *J* = 12.7 Hz, C$_{olefin}$), 32.33 (C$_{ali}$), 31.15 (C$_{cy}$), 24.88 (C$_{ali}$), 24.86 (C$_{ali}$).

^{19}F NMR (188 MHz, THF-d_8) δ -79.00 (s, OTf).

^{31}P NMR (81 MHz, THF-d_8) δ 111.61 (d, $^1J_{RhP}$ = 225.4 Hz, tropP); (202 MHz, CDCl₃) δ 111.07 (d, $^1J_{RhP}$ = 226.4 Hz, tropP).

^{103}Rh NMR (16 MHz, THF-d_8) δ -7086.43 (d, $^1J_{RhP}$ = 229.0 Hz, Rh).

[((CyC≡C)(CyC=C)tropPPh₂)Rhbipy]₂ ([6]₂)
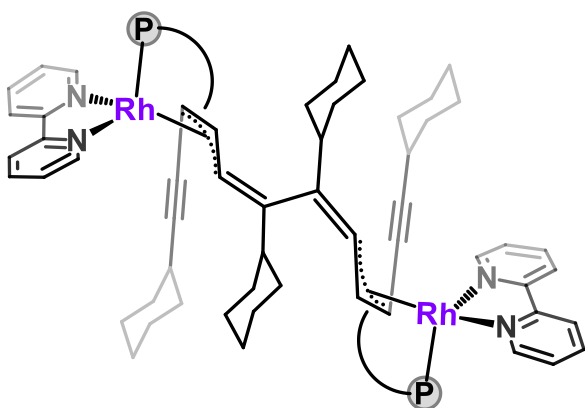
[((CyC≡C)₂tropPPh₂)Rhbipy](OTf) ([**6**](OTf)) (14 mg, 0.014 mmol, 1 eq.) was dissolved in 0.5 mL DFB and CoCp*₂ (5 mg, 0.014 mmol, 1 eq.) was added as a solution in 0.5 mL DFB. The mixture was stirred overnight while a green solid started to appear. The solid was filtrated off and the remaining dark green solid washed with hexane and Et₂O. Yield: 12 mg, 77 %. Crystals suitable for X-ray diffraction were grown from slow diffusion of *n*-hexane into a solution of THF.

^{1}H NMR (300 MHz, THF-d_8) δ 9.87 (d, *J* = 5.2 Hz, 2H), 8.57 – 8.47 (m, 4H), 8.32 – 8.21 (m, 4H), 8.08 (d, *J* = 8.1 Hz, 2H), 7.91 – 7.76 (m, 4H), 7.65 (tt, *J* = 7.6, 1.9 Hz, 2H), 7.45 (dd, *J* = 7.4, 5.2 Hz, 2H), 7.37 – 7.11 (m, 6H), 7.05 – 6.63 (m, 24H), 6.55 – 6.23 (m, 8H), 4.95 (d, *J* = 11.4 Hz, 2H, CH$_{benz}$), 2.48 – 2.31 (m, 2H), 2.06 – 1.87 (m, 4H), 1.59 (dq, *J* = 22.7, 10.8 Hz, 10H), 1.41 – 1.26 (m, 12H), 1.12 (d, *J* = 13.5 Hz, 4H), 1.00 (d, *J* = 10.7 Hz, 4H), 0.94 – 0.78 (m, 2H), 0.65 – 0.51 (m, 4H), 0.30 – 0.08 (m, 4H).

^{31}P NMR (121 MHz, THF-d_8) δ 64.37 (d, *J* = 173.7 Hz, tropP).

[((6,7-dicyclohexyl-2,10-dibenzyl-cycloundeca-4,5,7,8-tetraene)PPh₂)Rh₂bipy₂] ([7])
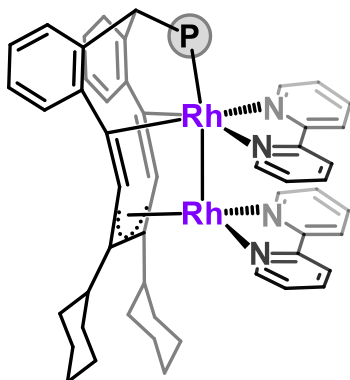
[((CyC≡C)₂tropPPh₂)Rh₂bipy₂]OTf₂ ([**4**](OTf)₂) (30 mg, 0.02 mmol, 1 eq.) was dissolved in 1 mL DFB and CoCp*₂ (16 mg, 0.05 mmol, 2.2 eq.) was added as a solution in 1 mL DFB. The mixture was stirred overnight while a green solid started to appear. The solid was filtrated off and suspended in THF. The mixture was dried and the remaining dark green solid washed with hexane and Et₂O. Yield: 20 mg, 83 %. Crystals suitable for X-ray diffraction were grown from slow diffusion of *n*-hexane into a solution of pyridine.

UV-Vis (THF): λ_{max} = 860, 700 nm. Elemental analysis for $C_{63}H_{57}N_4PRh_2 \cdot (CoC_{20}H_{30}F_3O_3S)_{0.4}$ calculated (%): C 66.05, H 5.36, N 4.32; found (%): C 65.80, H 5.59, N 5.52.

¹H NMR (500 MHz, THF-d_8) δ 7.89 (d, *J* = 5.8 Hz, 2H, C*H*ₐᵣ), 7.74 (d, *J* = 6.1 Hz, 2H, C*H*ₐᵣ), 7.51 (d, *J* = 6.7 Hz, 2H, C*H*ₐᵣ), 7.19 (d, *J* = 8.1 Hz, 2H, C*H*ₐᵣ), 7.11 (d, *J* = 7.3 Hz, 2H, C*H*ₐᵣ), 7.07 − 6.92 (m, 8H, C*H*ₐᵣ), 6.82 (dt, *J* = 6.4, 3.4 Hz, 10H, C*H*ₐᵣ), 6.64 (t, *J* = 7.5 Hz, 2H) , C*H*ₐᵣ, 6.45 (t, *J* = 6.3 Hz, 2H, C*H*ₐᵣ), 5.98 (t, *J* = 6.4 Hz, 2H, C*H*ₐᵣ), 5.09 (dd, *J* = 16.2, 2.6 Hz, 1H, C*H*benz), 2.56 (tt, *J* = 11.4, 3.4 Hz, 2H, C*H*cy), 2.15 (d, *J* = 12.5 Hz, 2H, C*H*ali), 1.98 (d, *J* = 13.4 Hz, 2H, C*H*ali), 1.83 − 1.68 (m, 6H, C*H*ali), 1.60 (q, *J* = 10.7 Hz, 4H, C*H*ali), 1.41 − 1.24 (m, 6H, C*H*ali).

¹H NMR (300 MHz, Pyridine- d_5) δ 8.18 (d, J = 4.5 Hz, 2H, C*H*ₐᵣ), 7.99 (d, J = 5.6 Hz, 2H, C*H*ₐᵣ), 7.94 (dd, J = 7.6, 1.5 Hz, 2H, C*H*ₐᵣ), 7.42 (d, J = 6.3 Hz, 1H, C*H*ₐᵣ), 7.32 (t, J = 6.8 Hz, 1H, C*H*ₐᵣ), 7.18 − 6.91 (m, 10H, C*H*ₐᵣ), 6.74 (t, J = 7.5 Hz, 2H, C*H*ₐᵣ), 6.58 (t, J = 6.6 Hz, 2H, C*H*ₐᵣ), 6.15 (t, J = 6.3 Hz, 2H, C*H*ₐᵣ), 5.50 (dd, J = 16.3, 1.9 Hz, 1H, C*H*benz), 2.74 (d, J = 11.0 Hz, 2H, C*H*cy), 2.38 (d, J = 12.2 Hz, 2H, C*H*ali), 1.98 (d, J = 11.7 Hz, 2H, C*H*ali), 1.85 − 1.69 (m, 14H, C*H*ali), 1.68 − 1.61 (m, 3H, C*H*ali), 1.35 − 1.24 (m, 12H, C*H*ali).

¹³C NMR (126 MHz, Pyridine-d_5) δ 152.83 (CHₐᵣ), 151.65 (CHₐᵣ), 143.00 (d, *J* = 18.6 Hz, C-Rh), 141.57 (Cq), 133.26 (d, *J* = 10.0 Hz, CHₐᵣ), 132.16 (d, *J* = 6.8 Hz, CHₐᵣ), 129.38 (CHₐᵣ), 128.94 (CHₐᵣ), 128.20 (d, *J* = 8.6 Hz, CHₐᵣ), 127.72 (CHₐᵣ), 127.24 (CHₐᵣ), 121.98 − 121.18 (m, CHₐᵣ), 121.66 (d, *J* = 6.4 Hz, CHₐᵣ), 121.58 (CHₐᵣ), 120.67 (CHₐᵣ), 118.08 (dd, *J* = 11.8, 5.4 Hz, Callyl2), 114.49 (CHₐᵣ),

72.19 (d, J = 6.1 Hz , C_{allyl1}), 47.80 (d, J = 31.3 Hz, CH_{benz}), 39.60 (C_{cy}), 37.92 (C_{ali}), 36.05 (C_{ali}), 27.77 (C_{ali}), 27.65 (C_{ali}), 27.08 (C_{ali}).

^{31}P NMR (203 MHz, THF-d_8) δ 18.85 (dd, J = 180.6, 21.0 Hz, tropP). (Pyridine-d_5) δ 18.64 (dd, J = 180.7, 21.8 Hz, tropP).

^{103}Rh NMR (16 MHz, THF-d_8) δ -7167.6 (d, $^1J_{RhP}$ = 180.8 Hz, Rh^1); (16 MHz, Pyridine-d_5) δ -7163.3 (d, $^1J_{RhP}$ = 179.2 Hz, Rh^1).No signal for Rh^2 could be detected due to low solubility.

[((Cy=C=C)(CyC≡C)tropPPh₂)Rh₂bipy₂](OTf) ([8](OTf))
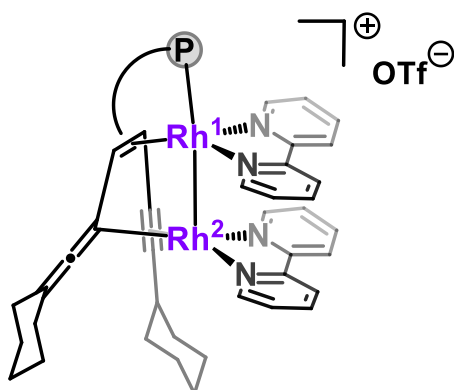
[((CyC≡C)₂tropPPh₂)Rh₂bipy₂]OTf₂ ([**4**](OTf)₂) (20 mg, 14.2 mmol, 1 eq.) was dissolved in 1 mL THF and KO*t*Bu (1.6 mg, 14.2 mmol, 1 eq.) was added dropwise as 5 M solution in THF, while the dark red solution immediately turned dark green. After stirring for 15 min, the solvent was removed in vacuo and the dark green solid was washed with Et₂O and hexane. Yield: expected 17.9 mg (%). Crystals suitable for X-ray diffraction were grown from slow evaporation of Et₂O into a solution of THF. UV-Vis (THF): λ_{max} = 630, 370 nm. Elemental analysis for $C_{64}H_{56}F_3N_4O_3PRh_2S\cdot(KCF_3O_3S)_{0.3}$ calculated (%): C 58.89, H 4.30, N 4.27; found (%): C 58.48, H 4.70, N 4.04.

^{1}H NMR (500 MHz, THF-d_8) δ 9.33 (d, J = 7.8 Hz, 1H, CH_{ar}), 9.07 (d, J = 5.8 Hz, 1H, CH_{ar}), 8.35 (dd, J = 10.1, 6.3 Hz, 3H, CH_{ar}), 8.22 (dd, J = 23.2, 8.1 Hz, 2H, CH_{ar}), 8.01 – 7.75 (m, 4H, CH_{ar}), 7.54 (q, J = 9.2, 8.7 Hz, 2H, CH_{ar}), 7.38 – 7.14 (m, 3H, CH_{ar}), 7.14 – 7.01 (m, 8H, CH_{ar}), 6.85 (q, J = 6.3, 5.5 Hz, 4H, CH_{ar}), 6.82 – 6.71 (m, 4H, CH_{ar}), 6.68 – 6.57 (m, 1H, CH_{ar}), 4.92 (d, J = 12.5 Hz, 1H, CH_{benz}), 2.69 (d, J = 10.4 Hz, 3H, CH_{ali}), 2.57 (s, 1H, CH_{ali}), 2.36 – 2.24 (m, 1H, CH_{ali}), 2.14 (d, J = 14.2 Hz, 4H, CH_{ali}), 2.02-1.55 (m, 11H, CH_{ali}), 1.54 – 1.21 (m, 1H, CH_{ali}).

^{13}C NMR (126 MHz, THF-d_8) δ 184.01 (C=C=C), 157.27 (C_{ar}), 154.69 (C_{ar}), 154.31 (C_{ar}), 153.89 (C_{ar}), 153.48 (C_{ar}), 152.21 (C_{ar}), 149.86 (C_{ar}), 144.20 (d, J = 9.1 Hz, C_{ar})), 140.73 (d, J = 8.1 Hz, C_{ar})), 138.48 (d, J = 4.5 Hz, C_{ar}), 137.71 (C_{ar}), 133.08 (d, J = 9.1 Hz, C_{ar}), 132.96 (d, J = 9.1 Hz, C_{ar}), 130.13 (CH_{ar}), 128.44 (dd, J = 9.1, 2.7 Hz, C_{ar}), 127.87 (d, J = 17.7 Hz, C_{ar}), 126.19 (d, J = 3.6 Hz, C_{ar}), 125.94 (C_{ar}), 125.42 (C_{ar}), 109.55 (d, J = 22.7 Hz, C=C=C-Rh), 94.62 ($C_{cy, q}$), 87.09 (d, J = 5.4 Hz, C≡C), 85.25 (d, J = 5.4 Hz, C≡C), 52.40 (d, J = 22.7 Hz, CH$_{benz}$), 37.90 (d, J = 25.4 Hz, C_{olefin}), 36.59 (C_{ali}), 35.63 (C_{ali}), 34.77 (CH$_{cy}$), 28.09 (C_{ali}), 27.71 (C_{ali}), 27.04 (C_{ali}).

^{31}P NMR (203 MHz, THF-d_8) δ 78.46 (dd, J = 193.9, 29.7 Hz, tropP).

^{19}F NMR (471 MHz, THF-d_8) δ -79.21 (s, OTf).

^{103}Rh NMR (16 MHz, THF-d_8) δ -7342.5 (d, $^1J_{RhP}$ = 195 Hz, Rh^1), -5372.4 (d, $^2J_{RhP}$ = 227 Hz, Rh^2).

[((Cy=C=C)₂tropPPh₂)Rh₂bipy₂] ([9])
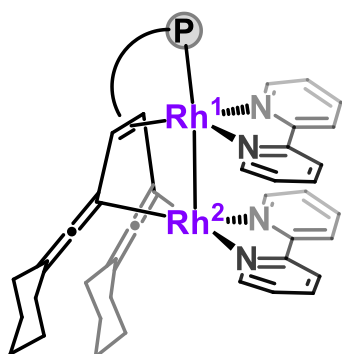
Because of the instability of the product, the complex was generated *in-situ* in an NMR tube. [((CyC≡C)₂tropPPh₂)Rh₂bipy₂]OTf₂ ([**4**](OTf)₂) (10 mg, 7.1 mmol, 1 eq.) was dissolved in 0.4 mL THF-d_8 and KOtBu-d_9 (1.72 mg, 14.2 mmol, 2 eq.) was added in two portions and shaken. The solution turned green immediately, NMR spectra were recorded when ^{31}P NMR showed full conversion or at several time points were recorded after shaking for 10 min.

^{1}H NMR (400 MHz, THF-d_8) δ 9.45 (d, J = 7.9 Hz, 1H, CH_{ar}), 9.27 (t, J = 7.2 Hz, 2H, CH_{ar}), 8.61 (d, J = 4.9 Hz, 2H, CH_{ar}), 8.48 (d, J = 7.9 Hz, 1H, CH_{ar}), 8.31 (d, J = 7.7 Hz, 1H, CH_{ar}), 7.81 (td, J = 7.7, 2.0 Hz, 1H, CH_{ar}), 7.51 (d, J = 8.1 Hz, 1H, CH_{ar}), 7.43 (t, J = 7.3 Hz, 1H, CH_{ar}), 7.37 (d, J = 8.1 Hz, 1H, CH_{ar}), 7.35 – 7.15 (m, 4H, CH_{ar}), 7.09 – 6.97 (m, 6H, CH_{ar}), 6.86 – 6.78 (m, 5H, CH_{ar}), 6.73 (dd, J = 7.2, 3.0 Hz, 6H, CH_{ar}), 6.56 (dd, J = 7.8, 4.9 Hz, 1H, CH_{benz}), 4.57 (d, J = 13.0 Hz, 1H, CH_{ali}), 2.73 (dt, J = 13.0, 4.9 Hz, 1H, CH_{ali}), 2.39 (ddd, J = 12.8, 9.4, 4.4 Hz, 1H, CH_{ali}), 2.27 (dt, J = 13.0, 4.4 Hz, 2H, CH_{ali}), 1.97 (ddd, J = 13.2, 9.3, 4.2 Hz, 1H, CH_{ali}), 1.91 – 1.76 (m, 1H, CH_{ali}), 1.68 – 1.31 (m, 3H, CH_{ali}).

^{13}C NMR (126 MHz, THF-d_8) δ 184.40 (s, C=C=C), 154.93 (s, CH$_{ar}$), 154.81 (s, CH$_{ar}$), 153.25 (s, CH$_{ar}$), 152.35 (s, CH$_{ar}$), 150.08 (s, C$_q$), 147.06 (d, J_{CP} = 12.5 Hz, C$_q$), 138.61 (s, CH$_{ar}$), 134.82 (s, CH$_{ar}$), 132.93 (d, J = 10.2 Hz, CH$_{ar}$), 131.77 (s, CH$_{ar}$), 128.41 (s, CH$_{ar}$), 127.86 (s, CH$_{ar}$), 127.79 (s, CH$_{ar}$), 124.18 (d, J = 6.4 Hz, CH$_{ar}$), 121.09 (d, J = 13.5 Hz, CH$_{ar}$), 114.64 (d, J_{CRh} = 25.9 Hz, C=C=C-Rh), 89.56 (s, C$_{cy, q}$), 53.98 (d, J_{CP} = 19.4 Hz, CH$_{benz}$), 37.05 (s, C$_{olef}$), 35.69 (s, CH$_{2, ali}$), 28.55 (s, CH$_{2, ali}$), 28.40 (s, CH$_{2, ali}$), 26.55 (s, CH$_{2, ali}$), 25.98 (s, CH$_{2, ali}$).

^{31}P NMR (202 MHz, THF-d_8) δ 60.95 (dd, J = 193.2, 54.3 Hz, tropP).

^{103}Rh NMR (16 MHz, THF-d_8) δ -7606.0 (d, $^1J_{RhP}$ = 192 Hz, Rh^1), -6183 (d, $^2J_{RhP}$ = 54 Hz, Rh^2).

[((CyC≡C)₂tropPPh₂)Rh₂(Ph^Fdad)(OTf)](OTf) ([11(OTf))
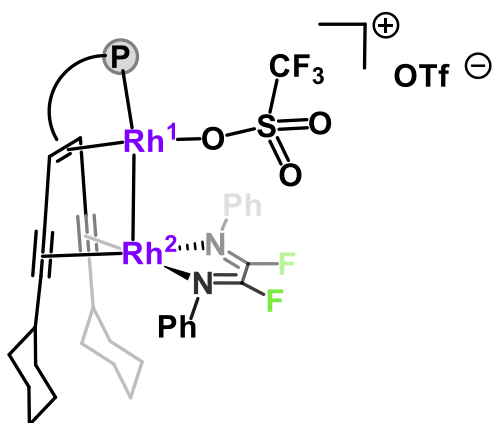
Rh₂OTf₂ ([**3**]) (53 mg, 0.049 mmol, 1 eq.) and Ph^Fdad (12 mg, 0.049 mmol, 1 eq.) were stirred in 3 mL THF for 10 min. The solvent was removed and washed with hexane to obtain a dark red powder. Yield: 60 mg (93 %).

^{1}H NMR (500 MHz, THF-d_8) δ 7.92 (d, J = 6.3 Hz, 5H), 7.81 – 7.67 (m, 4H), 7.53 (t, J = 7.9 Hz, 3H), 7.60 – 7.30 (m, 8H), 7.26 (dd, J = 5.8, 3.4 Hz, 4H), 7.21 – 7.12 (m, 2H), 5.34 (dd, J = 15.0, 2.7 Hz, 1H), 2.24 (d, J = 12.4 Hz, 2H), 1.99 (t, J = 11.5 Hz, 1H), 1.60 – 1.51 (m, 3H), 1.50 – 1.34 (m, 2H), 1.20 (qd, J = 12.1, 3.4 Hz, 2H), 1.12 – 0.90 (m, 4H), 0.48 (d, J = 11.9 Hz, 2H).

^{13}C NMR (126 MHz, THF-d_8) δ 151.81 (dd, J = 333.8, 49.5 Hz, C$_{dad}$-F), 137.72, 137.23, 134.81 (d, J = 10.9 Hz), 134.56 (d, J = 8.2 Hz), 132.05 (d, J = 2.7 Hz), 131.47 (d, J = 5.9 Hz), 130.16, 129.73, 129.26, 129.02 (d, J = 10.0 Hz), 128.89, 127.50, 126.52, 87.84 (d, J = 11.8 Hz, C≡C), 71.38, 69.01 (d, J = 7.3 Hz, C≡C), 50.55 (d, J = 27.2 Hz, CH$_{benz}$), 47.27 (d, J = 15.0 Hz, C$_{olef}$), 36.12, 34.68, 33.51, 32.58, 27.48, 26.39 (d, J = 16.8 Hz), 25.86, 23.57.

^{19}F NMR (471 MHz, THF-d_8) δ -41.48 (s, Fdad), -78.75 (bs, OTf), -79.33 (bs,OTf).

^{31}P NMR (203 MHz, THF-d_8) δ 85.42 (dd, J = 216.4, 3.7 Hz).

^{103}Rh NMR (16 MHz, THF-d_8) δ -7104.56 (d, J = 218.0 Hz).

3. Compounds of Chapter III

[(CyC≡C)₂tropPPh₂RhClPtMe₂] ([14])
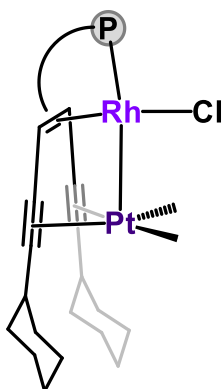
268 mg (1 eq., 0.184 mmol) of [**5**] and 100.8 mg (0.95 eq., 0.175 mmol) of [Pt₂(SMe₂)₂Me₂] were combined in a flask and dissolved in 10 mL of dry DCM. The mixture was stirred for one hour and concentrated to 2-3 mL and left at room temperature overnight. The solvent was decanted off and the solid was washed with hexane. The bright red solid dried under vacuum. 198 mg (0.208 mmol, yield: 56 %) of the product was obtained.

^{1}H NMR (300 MHz, CD₂Cl₂) δ 8.03 (dd, J = 7.8, 1.4 Hz, 2H$_{ar}$), 7.67 (ddt, J = 11.1, 7.1, 1.4 Hz, 4H$_{ar}$), 7.39 – 7.11 (m, 10H$_{ar}$, PPh₂), 6.97 (dt, J = 7.5, 1.4 Hz, 2H$_{ar}$), 4.81 (dd, $^2J_{PH}$ = 14.4 Hz, $^3J_{RhH}$ = 2.6 Hz, 1H$_{benz}$), 2.82 (tt, J = 10.1, 3.6 Hz, 2H, CHCH₂), 2.41 – 2.17 (m, 4H, CH₂), 1.94 – 1.64 (m, 12H, CH₂), 1.46 (s, $^2J_{PtH}$ = 91.7 Hz, 6 H, Pt(CH₃)₂), 1.42 – 1.26 (m, 4H, CH₂).

^{13}C NMR (75 MHz, CD₂Cl₂) δ 134.93 – 134.66 (m, 2C$_{quat}$), 134.27 (d, $^4J_{CP}$ = 9.9 Hz, 4C, CH$_{ar}$), 131.42 (s, 2C$_{quat}$), 131.15 (d, $^4J_{CP}$ = 2.5 Hz, 4C, CH$_{ar}$), 130.79 (s, 2C$_{quat}$), 129.73 (d, $^4J_{CP}$ = 6.5 Hz, 2C, CH$_{ar}$), 128.48 (d, $^3J_{CP}$ = 10.3 Hz, 4C, CH$_{ar}$), 128.06 (s, 2C$_{quat}$, C=C$_{trop}$), 127.97 (s, 2C, CH$_{ar}$), 127.90 (s, 2C, CH$_{ar}$), 97.96 (s, 2C, C≡CCy), 85.01 (s, 2C$_{quat}$, C≡CCy), 51.15 (d, $^1J_{CP}$ = 26.9 Hz, CH$_{benz}$), 34.58 (s, 2C, CH₂), 34.18 (s, 2C, CH₂), 34.01 (, 2C, CHCH₂), 26.28 (s, 4C, CH₂), 25.99 (s, 2C, CH₂), 9.44 (s, 2C, Pt(CH₃)₂)

^{31}P NMR (121 MHz, CD₂Cl₂) δ 88.35 (dd, $^1J_{PRh}$ = 217.9 Hz, $^2J_{PPt}$ = 517.5 Hz)

^{103}Rh NMR (15.8 MHz, CD₂Cl₂) δ -7086.75 (dd, $^1J_{RhP}$= 217.62 Hz, $^1J_{Rh-Pt}$ = 208.47 Hz).

[(CyC≡C)₂tropPPh₂RhOTfPtMe₂] ([15])
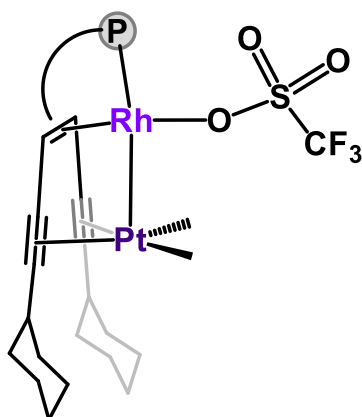
41 mg (1 eq., 43.05 μmol) of [**14**] and 11.1 mg (1 eq., 43.05 μmol) of AgOTf were dissolved in 2 mL dry THF. The solution was stirred for 3.5 hours and then filtered over celite. The solvent was removed, resulting in 41 mg (38.47 μmol, yield: 89 %) of orange product.

^{1}H NMR (300 MHz, CD₂Cl₂) δ 8.08 (dd, J = 7.8, 1.5 Hz, 2H$_{ar}$), 7.62 – 7.50 (m, 4H$_{ar}$), 7.45 – 7.14 (m, 10H, PPh₂), 6.92 (d, $^3J_{HH}$ = 7.4 Hz, 2H$_{ar}$), 4.64 (dd, $^2J_{PH}$ = 14.6, $^3J_{RhH}$ = 2.8 Hz, 1H$_{benz}$), 3.73 – 3.63 (m, 2H, CHCH₂), 2.90 – 2.77 (m, 4H, CH₂), 2.45 – 1.44 (m, 16H, CH₂), 1.42 (s, $^2J_{PtH}$ = 89.8 Hz, 6H, Pt(CH₃)₂)

^{13}C NMR (126 MHz, CD₂Cl₂) δ 135.86 (s, 2C$_{quat}$) , 134.88 (d, $^1J_{CP}$ = 7.4 Hz, 2C$_{quat}$), 134.21 (d, $^4J_{CP}$ = 10.4 Hz, 4C, CH$_{ar}$), 131.73 (d, $^4J_{CP}$ = 2.7 Hz, 2C, CH$_{ar}$), 129.96 (d, $^4J_{CP}$ = 6.5 Hz, 2C, CH$_{ar}$), 129.03 (s, 2C$_{quat}$), 128.67 (d, $^3J_{CP}$ = 4.6 Hz, 4C, CH$_{ar}$), 128.57 (s, 4C, CH$_{ar}$), 128.42 (s, 2C$_{quat,}$ C=C$_{trop}$), 99.93 (s, 2C$_{quat,}$ C≡CCy), 83.91 (s, 2C$_{quat}$, C≡CCy), 50.91 (d, $^1J_{CP}$ = 28.3 Hz, CH$_{benz}$), 34.44 (s, 2C, CH₂), 34.01(s, 2C, CH₂) 33.98(s, 2C, CHCH₂), 27.16 (s, 2C, CH₂), 26.19 (s, 2C, CH₂), 25.91(s, 2CH₂), 7.54, (s, 2C, Pt(CH₃)₂)

^{19}F NMR (471 MHz, CD₂Cl₂) δ -78.08 (s, 3F, OTf)

^{31}P NMR (121 MHz, CD₂Cl₂) δ 88.47 (d, $^1J_{PRh}$ = 213.7 Hz), 87.59 (d, $^2J_{PPt}$ = 528.0 Hz)

^{103}Rh NMR (16 MHz, CD₂Cl₂) δ -6851.35 (d, $^1J_{RhP}$ = 213.7 Hz)

^{195}Pt NMR (107 MHz, CD₂Cl₂) δ -3292.07 (d, $^2J_{PtP}$ = 540.4 Hz)

[(CyC≡C)₂tropPPh₂Rh(MeCN)₂PtMe₂]BArF ([16])
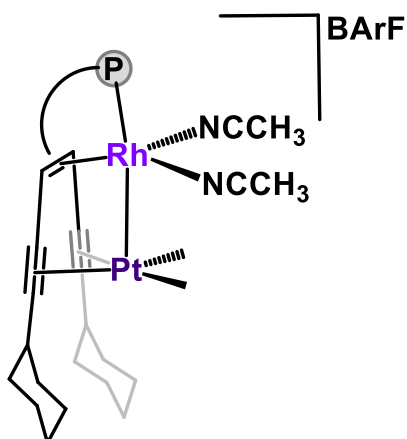
[**14**] (20 mg. 1 eq., 21 µmol) and NaBArF (18.6 mg, 1 eq., 21 µmol) were combined in 1 mL of MeCN and stirred for 2 hours at room temperature. The solution was filtered over celite, and the residue dried under vacuum.

^{1}H NMR (500 MHz, CD$_2$Cl$_2$) δ 8.02 (dd, J = 7.9, 1.4 Hz, 2H$_{ar}$), 7.72 (dt, J = 5.0, 2.3 Hz, 8H, BAr^F), 7.57 (s, 4H, BAr^F), 7.50 – 7.22 (m, 10H$_{ar}$, PPh$_2$), 7.02 (dd, J = 7.5, 1.5 Hz, 6H$_{ar}$), 4.81 (dd, $^2J_{PH}$ = 15.2 Hz, $^3J_{RhH}$ = 2.4 Hz, 1H$_{benz}$), 2.87 (ddt, J = 10.5, 6.8, 3.8 Hz, 2H, CHCH$_2$), 2.41 – 1.62 (m, 16H, CH$_2$), 1.47 (dddd, J = 29.6, 26.4, 13.8, 6.4 Hz, 4H, CH$_2$), 1.36 (s, 3H, NCCH$_3$), 1.16 (t, $^2J_{PtH}$ = 14.0 Hz, 6H, Pt(CH$_3$)$_2$)

^{11}B NMR (96 MHz, CD$_2$Cl$_2$) δ -6.60 (d, J = 5.4 Hz, BArF).

^{13}C NMR (126 MHz, CD$_2$Cl$_2$) δ 162.32 (dd, $^1J_{BC}$ = 99.6, 49.8 Hz, 4C, BAr^F), 134.40 (d, $^4J_{CP}$ = 10.1 Hz, 4C, CH$_{ar}$), 132.35 (d, $^2J_{CP}$ = 2.8 Hz, 2C$_{quat}$), 130.06 (d, $^4J_{CP}$ = 6.7 Hz, 2C, CH$_{ar}$), 129.80 (s, 2C$_{quat}$), 129.41 (d, $^3J_{CP}$ = 10.5 Hz, 2C, CH$_{ar}$), 129.31 (dd, J = 5.8, 2.9 Hz, 8C$_{quat}$, BAr^F), 128.82 (d, $^1J_{CP}$ = 10.5 Hz, 2C$_{quat}$), 129.31 (dd, J = 5.8, 2.9 Hz, 8CH, BAr^F), 129.06 (dd, J = 5.6, 3.0 Hz, 2C, CH$_{ar}$), 128.43 (s, 2C$_{quat}$, C=C$_{trop}$), 128.91 – 121.86 (m, 8C, CF$_3$), 117.74 – 116.62 (m, 4C, BAr^F), 101.37 (s, 2C, C≡CCy), 34.43 (s, 2C, CH$_2$), 34.09 (s, 1C, CHCH$_2$), 33.99 (s, 2C, CH$_2$), 26.12 (s, 2C, CH$_2$), 26.03 (s, 2C, CH$_2$), 25.85 (s, 2C, CH$_2$), 23.23 (s, C$_{quat}$, NCCH$_3$), 15.41 (s, 2C, Pt(CH$_3$)$_2$), 8.79 (s, 1C, NCCH$_3$)

^{19}F NMR (282 MHz, CD$_2$Cl$_2$) δ -62.85 (s, 24F, BArF).

^{31}P NMR (202 MHz, CD$_2$Cl$_2$) δ 89.91 (dd, $^1J_{PRh}$ = 198.1 Hz, $^2J_{PPt}$ = 529.3 Hz).

^{103}Rh NMR (16 MHz, CD$_2$Cl$_2$) δ -7329.23 (d, $^1J_{RhP}$ = 197.26 Hz)

^{195}Pt NMR (107 MHz, CD$_2$Cl$_2$) δ -3234.08 (d, $^2J_{PtP}$ = 545.7 Hz).

178

[(CyC≡C)₂tropPPh₂Rh(Cl)CuCl]₂ [18]
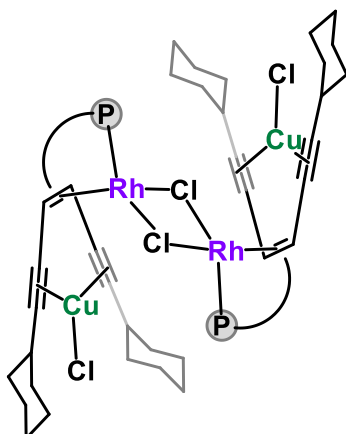
[**5**] (20 mg, mmol, 1 eq.) and CuCl (20 mg, mmol, 1 eq.) were suspended in 1 mL THF. The mixture heated to 50°C overnight. The solvent was removed under vacuo and the residue redissolved in chloroform. The product purified by crystallization from a solution of chloroform at -20 °C.

^{1}H NMR (200 MHz, CDCl₃) δ 8.18 – 8.00 (m, 4H), 7.71 – 7.53 (m, 6H), 7.31 – 6.81 (m, 9H), 4.84 (d, J = 14.9 Hz, 1H, CH$_{benz}$), 3.38 – 3.00 (m, 2H), 2.78 – 2.53 (m, 2H), 2.31 – 2.11 (m, 5H), 1.64 (dd, J = 103.6, 36.2 Hz, 33H).

^{31}P NMR (81 MHz, CDCl₃) δ 100.49 (d, J = 214.5 Hz, tropP).

[(CyC≡C)₂tropPPh₂Rh(Cl)(MeCN)CuCl] [19]
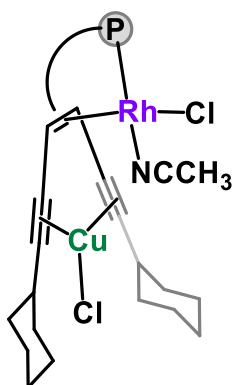
[**5**] (20 mg, mmol, 1 eq.) and [Cu(MeCN)₄]BF₄ (20 mg, mmol, 1 eq.) were combined in 1 mL MeCN and a few drops of DCM added. The product purified by crystallization from slow diffusion of THF into a solution of MeCN at -20 °C.

^{1}H NMR (300 MHz, CD₃CN) δ 8.37 (d, J = 8.0 Hz, 2H), 7.67 – 7.54 (m, 4H), 7.42 – 7.28 (m, 2H), 7.26 – 7.14 (m, 7H), 7.07 (t, J = 7.4 Hz, 2H), 6.96 (d, J = 7.5 Hz, 2H), 5.00 (d, J = 14.7 Hz, 1H, CH$_{benz}$), 2.69 (dt, J = 9.6, 5.4 Hz, 2H), 1.98 (s, 0H), 1.85 – 1.78 (m, 4H), 1.73 – 1.52 (m, 2H), 1.52 – 1.37 (m, 7H).

^{31}P NMR (121 MHz, CD₃CN) δ 97.97 (d, J = 201.3 Hz, tropP).

[(CyC≡C)₂tropPPh₂Rh(OTf)(MeCN)Cu(MeCN)] [20]
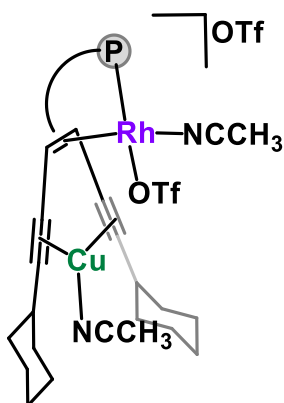
[**5**] (20 mg, mmol, 1 eq.) was combined with AgOTf (1 eq.) in THF to form [$^{(CyC≡C)2}$tropPPh₂Rh(OTf)]. Then, [Cu(MeCN)₄]OTf (20 mg, mmol, 1 eq.) was added. The product purified by crystallization from slow diffusion of iPr₂O into a solution of THF at -20 °C.

^{31}P NMR (121 MHz, THF) δ 105.61 (d, J = 182.5 Hz, tropP).

^{19}F NMR (282 MHz, THF) δ -78.12 (OTf).

(PhC≡C)₂tropNHtrop (22a)
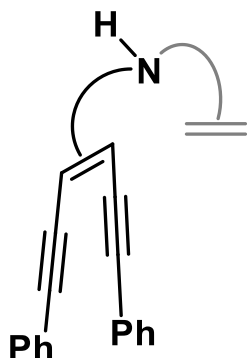
(PhC≡C)₂tropCl (3.16 g, 7.4 mmol) and tropNH₂ (1.58 g, 7.6 mmol) were dissolved in a mixture of dry toluene (30 mL) and dry triethylamine (10 mL). A catalytic amount of CuI (16 mg, 0.08 mmol) was added, and the reaction mixture was stirred at 80°C for 24 h. The temperature was increased to 100°C and it was stirred for another hour. A saturated aq. solution of Na_2CO_3 (40 mL) was added, which changed its color to light blue after stirring for 10 min. The organic phase was separated, washed with deionised water (2 x 40 mL) and dried over $MgSO_4$. The solvent was evaporated in vacuo and the product was recrystallized from ethyl acetate. The resulting off-white crystals from were washed with hexane to obtain 2.65 g (60 %) of white powder.

^1H NMR (300 MHz, C_6D_6) δ 8.02 – 7.12 (CH_{arom}), 5.04 (d, J = 10.7 Hz, 1H, CH_{benz}), 4.03 (s, 1H, CH_{benz}), 3.07 (d, J = 11.3 Hz, 1H, NH).

^{13}C NMR (75 MHz, C_6D_6) δ 142.52 – 122.27 (C_{arom}), 98.19 (C_{alkyne}), 91.85 (C_{alkyne}), 66.47 (C_{benz}), 57.13 (C_{benz}).

(CyC≡C)₂tropNHtrop (22b)
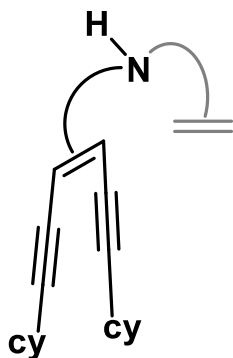
(CyC≡C)₂tropCl (**S3**) (1.28 g, 2.9 mmol) and tropNH₂ (0.62 g, 3.0 mmol) were dissolved in a mixture of toluene (14 mL) and triethylamine (4.5 mL). Then CuI (12 mg, 0.06 mmol) was added, and the mixture was stirred at 70°C for 48 h. The temperature was increased to 80°C and stirred for another 24 h. An aqueous, saturated solution of Na_2CO_3 (15 mL) was added to the orange-red solution with the white precipitate. It was stirred for 1 h, the phases were separated, and the organic phase washed with deionized water and dried over $MgSO_4$. The solvent was removed in vacuo and the brownish residue was recrystallize from ethyl acetate and pentane. The residue was washed with hexane (3 x 4 mL) and dried in vacuo, obtaining an off-white powder as the desired product. Yield: 0.56 g (32 %).

^{1}H NMR (300 MHz, CDCl₃) δ 7.73 –6.83 (H$_{arom}$), 4.85 (s, 1H, H$_{benz}$), 3.78 (s, 1H, H$_{benz}$), 2.84 (s, 1H, R₂NH), 2.66 –1.19 (H$_{alkyl}$).

[((PhC≡C)₂tropNHtrop)Rh(ACN)₂]BF₄ ([23a]BF₄)
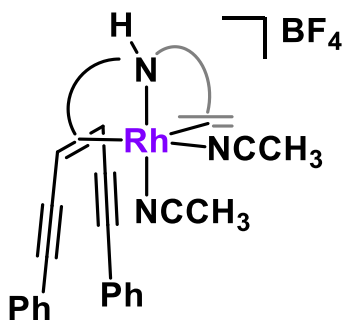
(PhC≡C)₂tropNHTrop (300 mg, 1.05 eq.) and [Rh(COD)₂]BF₄ (194 mg, 1 eq.) were combined in a flask with 6 mL dry acetonitrile and heated to 60 °C overnight. The solvent was evaporated, and the residue washed with hexane until all COD was removed. The intense-yellow solid was dried under vacuum yielding 403 mg (97 %). Crystals suitable for X-ray diffraction were grown by slow diffusion of *n*-hexane into a solution of DCM.

^{1}H NMR (500 MHz, CD₂Cl₂) δ 8.42 (d, *J* = 7.9 Hz, 1H), 7.94 (d, *J* = 7.9 Hz, 1H), 7.69 – 7.19 (m, 17H), 7.19 – 7.04 (m, 2H), 6.97 (ddd, *J* = 14.1, 8.4, 3.2 Hz, 4H), 6.10 (d, *J* = 9.5 Hz, 1H), 5.73 (d, *J* = 9.5 Hz, 1H), 5.01 (s, 2H), 3.91 (s, 1H), 1.87 (s, NCC*H*₃, 3H), 1.78 (s, NCC*H*₃, 3H).

^{13}C NMR (126 MHz, CD₂Cl₂) δ 136.67, 135.82, 135.75, 134.81, 133.86, 132.11, 131.28, 130.92, 130.06, 129.24, 129.04, 128.99, 128.97, 128.90, 128.85, 128.77, 128.64, 128.52, 128.48, 128.32, 128.10 (d, *J* = 4.5 Hz), 127.87, 127.71, 127.35, 127.05, 126.92, 123.82 (d, *J* = 28.5 Hz), 120.81 (d, *J* = 6.4 Hz), 93.58 (d, *J* = 73.1 Hz, NC*C*H₃, 1C), 92.58 (d, *J* = 69.9 Hz, NC*C*H₃, 1C), 75.33 (d, *J* = 12.9 Hz, C_olef), 73.64 (d, *J* = 9.8 Hz, C_benz), 72.36 (C_benz), 71.69 (d, *J* = 23.1 Hz, C_olef), 3.13 (s, NCC*H*₃, 1C), 2.28 (s, NCC*H*₃, 1C).

^{103}Rh NMR (16 MHz, CD₂Cl₂) δ -5645 ppm (s).

[((PhC≡C)₂tropNHtrop)Rh(ACN)₂]OTf ([23a]OTf)
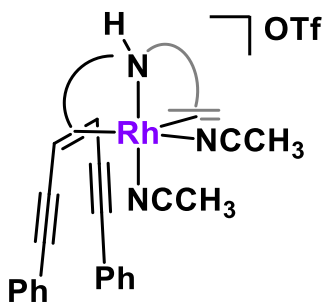
(PhC≡C)₂tropNHtrop (**22a**) (10 mg, 17 µmol) and [Rh(COD)₂]OTf (16 mg, 34 µmol) were dissolved in MeCN (0.5 mL). It was stirred and heated to 70°C for 30 min. DCM (0.1 mL) was added, and it was heated to 70°C for 24 h. The reaction mixture was filtered, and the product purified by crystallization at -20°C.

^{1}H NMR (300 MHz, CD$_2$Cl$_2$) δ 8.34 (d, J = 7.9 Hz, 1H, H$_{arom}$), 7.83 (d, J = 7.9 Hz, 1H, H$_{arom}$), 7.70 – 6.65 (m, 24H, H$_{arom}$), 6.06 (dd, J = 9.4, 2.8 Hz, 1H, H$_{olef}$), 5.71 (d, J = 9.5 Hz, 1H, H$_{olef}$), 4.70 (s, 2H, H$_{benz}$), 4.63 (s, 1H, R$_2$NH), 1.86 (s, 3H, NCCH$_3$), 1.55 (s, 3H, NCCH$_3$).

^{13}C NMR (75 MHz, CD$_2$Cl$_2$) δ 131.78 – 127.14 (C$_{arom}$), 74.73 (C$_{olef}$), 73.04 (C$_{benz}$), 72.80 (C$_{benz}$).

[((PhC≡C)₂tropNHtrop)Rh(COD)]OTf ([24a]OTf)
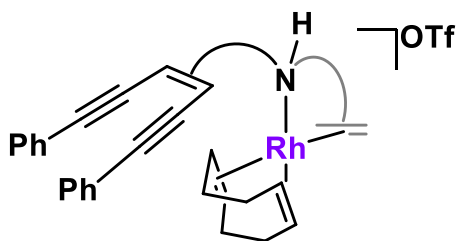
(PhC≡C)₂tropNHtrop (**22a**) (50 mg, 84 µmol) and [Rh(COD)₂]OTf (39 mg, 84 µmol) were dissolved in toluene (1 mL) resulting in an orange solution with a dark-red precipitate. The reaction mixture was stirred for 2.5 h, which turned it into a clear yellowish-orange solution. It was filtered and the solvent was evaporated in vacuo. The resulting solid was triturated with hexane twice, obtaining an orange powder as the desired product. Yield: 50 mg (62 %).

^{1}H NMR (300 MHz, toluene-d_8) δ 8.58 (d, J = 7.7 Hz, 1H, H$_{arom}$), 8.42 (d, J = 7.7 Hz, 1H, H$_{arom}$), 8.17 – 6.59 (m, 32H, H$_{arom}$), 5.98 (d, J = 10.8 Hz, 1H, H$_{benz}$), 5.77 (d, J = 11.3 Hz, 1H, H$_{benz}$), 4.66 (s, 1H, H$_{olef}$ (COD)), 4.51 (s, 1H, H$_{olef}$ (COD)), 4.10 (t, J = 11.1 Hz, 1H, R$_2$NH), 3.12 (s, 1H, H$_{alkyl}$ (COD)), 2.32 (d, J = 8.4 Hz, 1H, H$_{alkyl}$ (COD)), 2.21 – 0.92 (m, H$_{alkyl}$).

^{13}C NMR (75 MHz, THF) δ 136.65, 136.04, 135.05, 134.05, 132.07, 131.80, 131.24, 130.07, 129.63, 129.52, 128.99, 128.65, 128.51, 128.07, 127.93, 127.52, 127.40, 127.19, 127.11, 126.85, 126.77, 126.64, 126.46, 126.43, 126.36, 126.25, 125.01, 124.80, 121.33, 121.09, 96.56 (d, J = 14.2 Hz, 2C, C$_{olefin}$(CCPh)), 89.49 (CCPh), 88.50 (CCPh), 80.91 (d, J = 13.7 Hz, CH$_{benz}$), 79.68 (d, J = 11.7 Hz, CH$_{benz}$), 68.07 (C$_{olefin}$), 67.68 (C$_{olefin}$), 51.82 (q, J = 27.4 Hz, 1C, CF$_3$), 28.62 (COD), 27.74 (COD), 25.78 (COD).

^{19}F NMR (282 MHz, toluene-d_8) δ -77.66 (OTf).

[((PhC≡C)₂tropNHtrop)Rh(COD)]BArF ([24a]BArF)
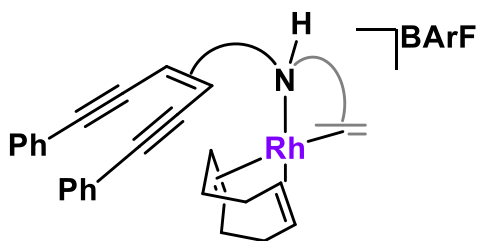
(PhC≡C)₂tropNHtrop (**22a**) (50 mg, 84 µmol) and [Rh(COD)₂]BArF (111 mg, 84 µmol) were dissolved in toluene (1 mL) resulting in a red solution with red precipitate. The reaction mixture was stirred for 2.5 h, which turned it into a clear yellowish-red solution. It was filtered and put into the fridge. The resulting solid was washed with hexane and dried, Obtaining the desired product as red crystals. Yield: 107 mg (70 %).

^{1}H NMR (500 MHz, C₆D₆) δ 8.39 (dt, *J* = 5.0, 2.3 Hz, 8H, BArF), 7.96 (dd, *J* = 7.9, 1.3 Hz, 1H, H$_{arom}$), 7.74 (dd, *J* = 7.8, 1.4 Hz, 1H, H$_{arom}$), 7.66 (s, 4H, BArF), 7.62 (m, 2H, H$_{arom}$), 7.39 (m, 2H, H$_{arom}$), 7.20 – 6.75 (m, 16H, H$_{arom}$), 6.34 (dd, *J* = 9.1, 2.4 Hz, 1H, H$_{olef}$), 6.21 (dd, *J* = 7.9, 1.2 Hz, 1H, H$_{arom}$), 6.01 (dd, *J* = 7.7, 1.2 Hz, 1H, H$_{arom}$), 4.75 (d, J = 7.3 Hz, 1H, H$_{olef}$ (COD)), 4.72 (t, J = 7.6 Hz, 1H, H$_{olef}$ (COD)), 4.43 (d, *J* = 3.1 Hz, 1H, H$_{benz}$), 4.25 (d, *J* = 9.2 Hz, 1H, H$_{olef}$), 4.18 (d, *J* = 11.1 Hz, 1H, H$_{benz}$), 3.91 (dd, *J* = 11.2, 3.1 Hz, 1H, R₂NH), 2.61 (q, *J* = 7.8 Hz, 1H, H$_{olef}$ (COD)), 2.53 (q, *J* = 7.9 Hz, 1H, H$_{olef}$ (COD)), 1.66 – 0.64 (m, H$_{alkyl}$).

^{11}B NMR (161 MHz, C₆D₆) δ -5.91 (BArF).

^{13}C NMR (126 MHz, C₆D₆) δ 136.35 – 117.76 (C$_{arom}$), 97.50 (C$_{olef}$), 75.03 (C$_{olef}$), 69.61 (C$_{benz}$), 66.76 (C$_{benz}$), 33.85 – 24.13 (C$_{alkyl}$).

^{19}F NMR (471 MHz, C₆D₆) δ -62.05 (BArF).

[((CyC≡C)₂tropNHtrop)Rh(COD)]BArF ([24b]BArF)
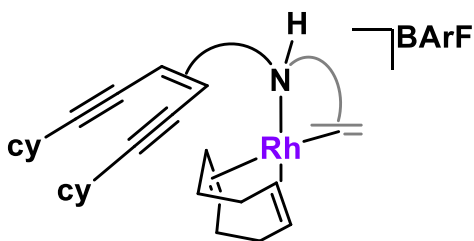
(CyCC)₂tropNHtrop (**22b**) (50 mg, 82 μmol) and [Rh(COD)₂]BArF (97 mg, 82 μmol) were dissolved in toluene (2 mL). The solution turned red. It was stirred for 19 h, the solvent was evaporated in vacuo. It was triturated and washed with hexane to obtain a red powder as the desired product.

^{1}H NMR (300 MHz, CD₂Cl₂) δ 7.87 (d, J = 7.9 Hz, 1H, H$_{arom}$), 7.76 (d, J = 6.0 Hz, 1H, H$_{arom}$), 7.64 (dt, J = 5.2, 2.3 Hz, 16H, BArF), 7.51 – 7.04 (m, 20H, H$_{arom}$), 6.51 – 6.09 (m, 3H, H$_{arom}$), 5.49 (d, J = 11.0 Hz, 1H, H$_{olef}$ (COD)), 5.38 (t, J = 7.2 Hz, 1H, H$_{olef}$ (COD)), 5.11 (d, J = 16.9 Hz, 2H, H$_{olef}$ (COD)), 4.85 (d, J = 9.3 Hz, 1H, H$_{benz}$), 4.37 (d, J = 11.1 Hz, 1H, H$_{benz}$), 4.00 (d, J = 11.3 Hz, 1H, R₂NH), 3.32 (q, J = 8.0 Hz, 1H, H$_{olef}$ (COD)), 2.81 – 0.72 (m, H$_{alkyl}$).

^{13}C NMR (75 MHz, CD₂Cl₂) δ 135.20 (C$_{arom}$), 31.96 (C$_{alkyl}$), 23.03 (C$_{alkyl}$), 14.24 (C$_{alkyl}$).

^{19}F NMR (282 MHz, CD₂Cl₂) δ -62.85 (d, J = 7.8 Hz, BArF).

[(PhC≡C)₂tropNHCu]₂(BF₄)₂ [25](BF4)₂
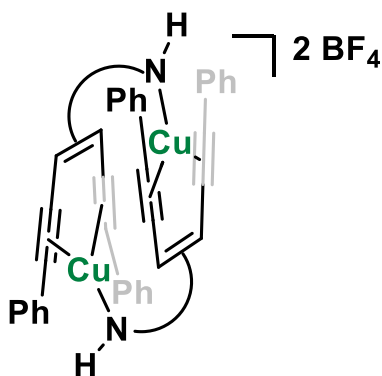
(PhC≡C)₂tropNHtrop (**22a**) (100 mg, 167 μmol) and [Cu(ACN)₄]BF₄ (53 mg, 167 μmol) were dissolved in THF (2.5 mL) and stirred for 3 h. The mixture was evaporated under vacuum to obtain a yellow powder in 80 mg (93 %) yield.

^{1}H NMR (300 MHz, CD₂Cl₂) δ 7.85 – 6.96 (m, 14H, H$_{arom}$), 3.67 (m, 2H, NH), 1.82 (m, 2H, H$_{benz}$).

[(PhC≡C)₂tropNHtropCu(MeCN)₂]BF₄ [26]BF4
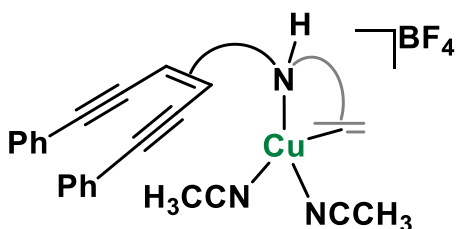
(PhC≡C)₂tropNHtrop (**22a**) (10 mg, 16.7 μmol) and [Cu(ACN)₄]BF₄ (5.3 mg, 16.7 μmol) were combined in 1 mL DCM and placed in the sonicator until fully dissolved. The solution was layered with toluene to obtain [**26**]BF4 as a yellow powder.

^{1}H NMR (300 MHz, CD₂Cl₂) δ 7.80 (d, *J* = 7.7 Hz, 2H), 7.53 – 7.44 (m, 6H), 7.40 (s, 2H), 7.37 – 7.21 (m, 22H), 6.42 (d, *J* = 15.9 Hz, 2H), 5.50 (s, 1H, CH$_{benz}$), 5.23 (s, 1H, CH$_{benz}$), 3.91 (d, *J* = 12.7 Hz, 1H, CH$_{olef}$), 3.65 (d, *J* = 12.4 Hz, 1H, CH$_{olef}$), 1.90 (s, 12H, NCCH₃).

4. Compounds of Chapter IV

[(PhC≡C)₂tropPPh₂CoCp] ([28])
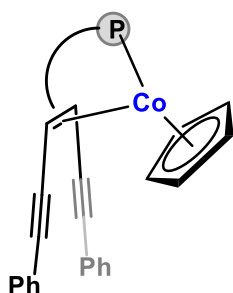
(PhC≡C)$_2$tropPPh$_2$ (**27**) (154 mg, 0.267 mmol, 1 eq.) and CoCp(CO)$_2$ (48 mg, 0.267 mmol, 1 eq.) were dissolved in 5 mL THF and irradiated with UV light for 4 hours. The resulting orange crystalline needles were collected by filtration and did not require further purification. Yield: 100 mg (65 %).

^{1}H NMR (300 MHz, C$_6$D$_6$) δ 8.98 (d, J = 8.0 Hz, 2H, CH$_{ar}$), 7.71 (d, J = 6.1 Hz, 4H, CH$_{ar}$), 7.43 (t, J = 8.5 Hz, 4H, CH$_{ar}$), 7.12 – 6.87 (m, 16H, CH$_{ar}$), 6.82 (t, J = 7.4 Hz, 2H, CH$_{ar}$), 6.59 (d, J = 7.4 Hz, 2H, CH$_{ar}$), 4.78 (s, 5H CH$_{cp}$), 4.41 (d, J = 15.6 Hz, 1H, CH$_{benz}$).

^{13}C NMR (75 MHz, C$_6$D$_6$) δ 141.10, 135.07, 133.21, 133.08, 131.46, 130.17, 129.98, 129.95, 128.73, 128.59, 126.99, 126.44, 125.00, 100.73 (C≡C), 90.55 (Cp), 90.00 (C≡C), 52.57 (CH$_{benz}$).

^{31}P NMR (121 MHz, C$_6$D$_6$) δ 103.36 (s, tropP).

^{59}Co NMR (118 MHz, C$_6$D$_6$) δ -2600 (very broad).

[(PhC≡C)₂tropPPh₂Co(HMDS)₂] [29]
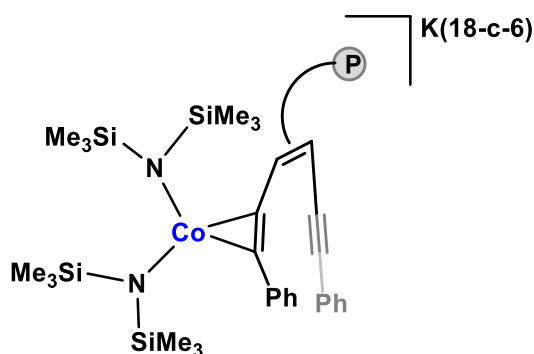
(PhC≡C)$_2$tropPPh$_2$ (**27**) (30 mg, 0.052 mmol, 1 eq.) and K(18-c-6)[Co(HMDS)$_2$] (20 mg, 0.052 mmol, 1 eq.) were combined in 1 mL THF. The solution turned bordeaux red immediately. Single crystals were grown from layering with hexane.

^{31}P NMR (81 MHz, THF) δ -22.36.

[(PhC≡C)₂tropPPh₂Co₂(CO)₄] [30]
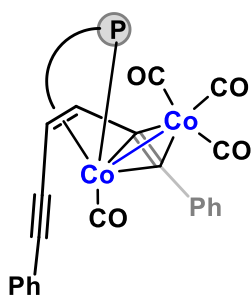
(PhC≡C)₂tropPPh₂ (**27**) (50 mg, 0.0 mmol, 1 eq.) and [Co₂(CO)₈] (30 mg, 0.0 mmol, 1 eq.) were combined in 3 mL of toluene. Gas evolution was observed while the solution turned dark green immediately. Th mixture was stirred for 24 h before the solvent was removed under vacuo. Single crystals of [**30**] were obtained from slow diffusion of hexane into a solution of toluene at -20°C.

^1H NMR (500 MHz, C₆D₆) δ 8.54 (d, J = 8.1 Hz, 1H), 8.15 (d, J = 7.7 Hz, 2H), 7.94 (d, J = 7.4 Hz, 1H), 7.53 (t, J = 8.9 Hz, 2H), 7.04 – 6.58 (m, 27H), 6.65 (s, 1H), 6.33 (d, J = 7.7 Hz, 1H), 4.68 (d, J = 13.8 Hz, 1H, CH_benz).

^{13}C NMR (126 MHz, C₆D₆) δ 212.79 (CO), 201.05 (CO), 140.89, 140.85, 140.57, 137.44, 137.39, 136.87, 136.81, 136.60, 136.57, 134.21, 134.12, 133.22, 133.14, 132.42, 131.39, 131.37, 131.32, 130.57, 130.30, 129.02, 127.05, 126.32, 124.91, 123.31, 119.50, 94.95 (d, J = 4.7 Hz), 89.64, 51.81 (d, J = 16.1 Hz, CH_benz), 41.48.

^{31}P NMR (202 MHz, C₆D₆) δ 69.65 (bs).

[(cyclized-(PhC≡C)₂tropPPh₂)₂Co₂] [31]
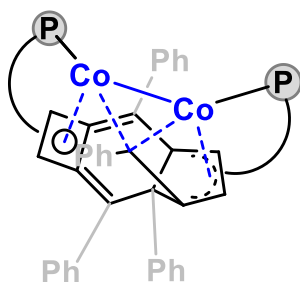
(PhC≡C)₂tropPPh₂ (**27**) (20 mg, 1 eq.), [Co(HMDS)₂] (12.5 mg, 1 eq.), PPh₃ (9.1 mg, 1.05 eq.) and Zn powder (32 mg, 15 eq.) were combined in 1 mL of DME. After stirring for 3 days, only 15 % conversion was observed by ^{31}P NMR. Crystals suitable for XRD were obtained by slow diffusion of hexane into a solution of [**31**] in DME.

^{31}P NMR (121 MHz, None) δ 105.64, 58.44.

[(PhC≡C)₂tropPPh₂CuCl] [32]
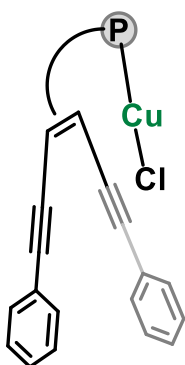
CuCl (17 mg, 0.17 mmol, 1 eq.) and (PhC≡C)$_2$tropPPh$_2$ (**27**) (100 mg, 0.17 mmol, 1 eq.) were suspended in a dry THF (5 mL) and heated to 70°C overnight. Large orange crystals formed upon slowly cooling down the reaction mixture. The supernatant was decanted off and the collected crystals washed with hexane and dried under vacuum.

^{1}H NMR (300 MHz, CD$_2$Cl$_2$) δ 8.01 (d, J = 7.7 Hz, 1H), 7.81 – 7.71 (m, 3H), 7.55 (dd, J = 11.3, 7.5 Hz, 3H), 7.43 – 7.29 (m, 7H), 7.34 – 7.24 (m, 3H), 7.23 (d, J = 7.4 Hz, 1H), 7.09 (d, J = 7.5 Hz, 2H), 5.10 (d, J = 14.5 Hz, 1H), .

^{13}C NMR (75 MHz, THF) δ 135.41, 135.19, 133.10, 131.51, 130.93, 130.55, 129.58, 129.38, 129.07, 124.88, 101.03, 92.74, 68.39, 55.61, 26.56, 26.03.

^{31}P NMR (121 MHz, CD$_2$Cl$_2$) δ 3.12.

[(CyC≡C)₂tropPPh₂CuCl] [33]
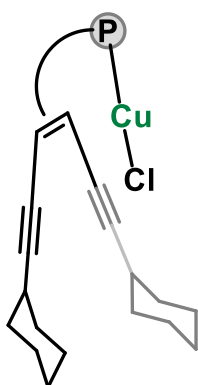
CuCl (1.7 mg, 0.017 mmol) and (CyCC)$_2$tropPPh$_2$ (10 mg, 0.017 mmol) were heated to 70°C in 0.5 mL THF overnight.

^{31}P NMR (121 MHz, THF) δ -1.07.

[(PhC≡C)₂tropPPh₂Cu₂(μ-Cl)₂]₂ [34]
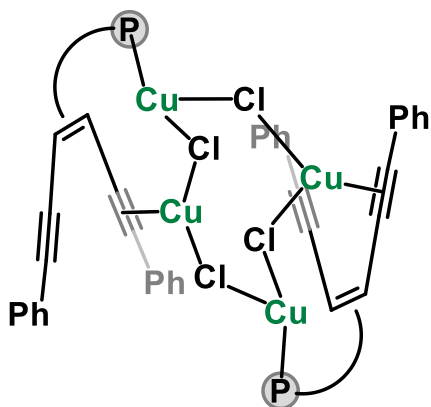
CuCl (34 mg, 0.34 mmol, 2 eq.) and (PhC≡C)₂tropPPh₂ (**27**) (99 mg, 0.17 mmol, 2 eq.) were suspended in a dry THF (5 mL) and heated to 70°C overnight. Large orange crystals formed upon slowly cooling down the reaction mixture. The supernatant was decanted off and the collected crystals were washed with hexane and dried under vacuum.

^{1}H NMR (200 MHz, CD₂Cl₂) δ 7.92 – 7.77 (m, 12H), 7.61 – 7.45 (m, 8H), 7.40 – 7.16 (m, 32H), 7.15 – 7.07 (m, 4H), 5.09 (d, J = 13.7 Hz, 2H), .

^{13}C NMR (50 MHz, CD₂Cl₂) δ 138.12, 134.61, 134.31, 134.19, 134.10, 132.86, 130.97, 130.69, 130.55, 129.76, 129.04, 128.84, 128.78, 128.06, 123.08, 102.03, 94.09, 68.16.

^{31}P NMR (81 MHz, CD₂Cl₂) δ -0.54.

[(PhC≡C)₂tropPPh₂Cu₂OTf₂] [35]
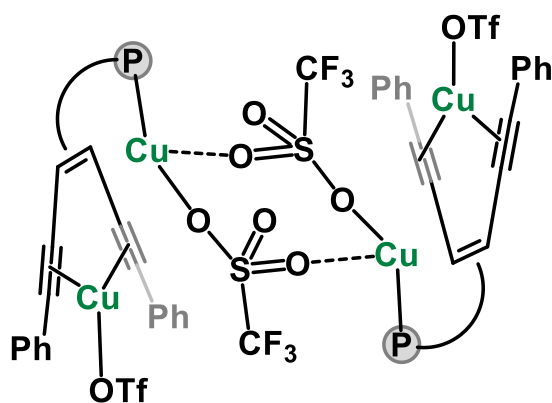
[(PhC≡C₂)tropPPh₂Cu₂(μ-Cl)₂]₂ [**34**] (15 mg, 1 eq.) and AgOTf (10 mg, 4 eq.) were combined in 1 mL THF which immediately led to AgCl precipitating from the solution. After filtration of the mixture, the solvent was removed in vacuo to obtain an orange powder. Single crystals suitable for X-ray measurement were grown from slow diffusion of Et₂O into a solution of [**35**] in DFB.

^{31}P NMR (81 MHz, THF) δ 7.33.

^{19}F NMR (188 MHz, THF) δ -69.65.

[(CyC≡C)₂tropPPh₂Cu₂Cl₂] [36]
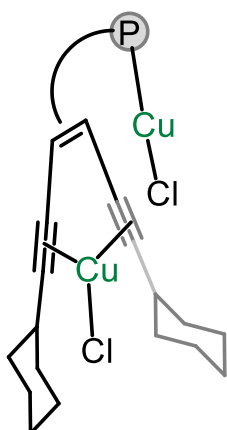
CuCl (34 mg, 0.34 mmol) and (CyCC)₂tropPPh₂ (99 mg, 0.17 mmol) were dissolved in a dry THF (7 mL). The yellow solution was stirred at 70°C overnight. The product was filtrated, washed with hexane and dried in vacuo to obtain the product as a yellow powder. Yield: 60 mg (61.3 %).

^{1}H NMR (200 MHz, CD₂Cl₂) δ 7.77 (dd, *J* = 7.3, 1.9 Hz, 2H), 7.62 – 7.15 (m, 14H), 7.13 – 6.99 (m, 2H), 5.12 (d, *J* = 14.8 Hz, 1H), 3.26 (dt, *J* = 9.8, 5.6 Hz, 2H), 2.33 – 2.17 (m, 4H), 1.90 – 1.61 (m, 2H), 1.56 – 1.22 (m, 6H).

^{13}C NMR (50 MHz, CD₂Cl₂) δ 134.50, 134.21, 131.52, 130.86, 130.55, 129.29, 129.08, 128.29, 109.34, 88.43, 68.16, 34.64, 33.01, 32.87, 26.25, 25.99, 25.69.

^{31}P NMR (81 MHz, CD₂Cl₂) δ -0.03.

[(CyC≡C)₂tropPPh₂Cu₂OTf₂] [37]
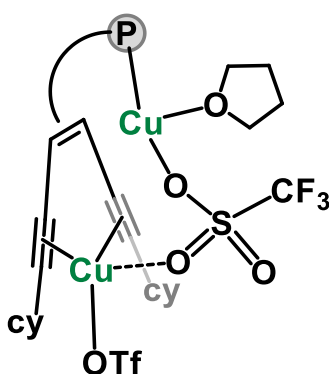
To a solution of [**36**] (14 mg, 1 eq.) in 1 mL THF, AgOTf (9 mg, 2 eq.) was added, which immediately lead to AgCl precipitating from the solution. After filtration of the mixture, the solvent was removed in vacuo to obtain an orange powder. Single crystals suitable for X-ray measurement were grown from slow diffusion of hexane into a solution of THF.

^{31}P NMR (121 MHz, THF) δ 8.88.

5. Compounds of Chapter V

[Ir(trop₂dad)] [40]˙
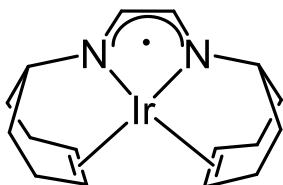
[Ir(trop₂dad)]OTf ([**40**]OTf) (50 mg, 0.064 mmol, 1 eq.) was suspended in 3 mL THF and an excess Zn powder (40 mg, 0.642 mmol, 10 eq.) was added. The suspension was stirred for one hour and filtered. The solvent was removed in vacuo and the green powder used without further purification. Single crystals suitable for X-ray diffraction measurement were obtained by slow diffusion of hexane into a solution of toluene at -20°C.

Paramagnetic compound.

¹H NMR (300 MHz, THF-*d₈*) δ 12.73 (vbr), 10.24 (br), 7.40 - 6.87 (br, weak).

Na[Ir(trop₂dad)] Na[40]
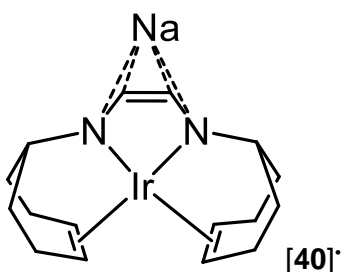
[Ir(trop₂dad)] ([**40**]˙) (30 mg, 0.048 mmol, 1 eq.) was dissolved in 1 mL THF and NaO*t*Bu powder (5 mg, 0.048 mmol, 1 eq.) was added. The suspension was stirred for one hour and filtered. The solvent was removed in vacuo and the green powder used without further purification. Single crystals suitable for X-ray diffraction measurement were obtained by slow diffusion of hexane into a solution of toluene at -20°C.

Paramagnetic compound.

[(ZnOTf)Ir(trop₂dad)] ZnOTf[40]
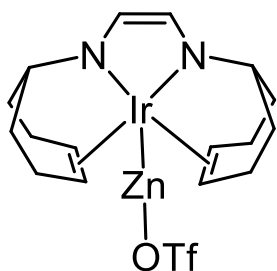
[Ir(trop₂dad)]OTf ([**40**]OTf) (50 mg, 0.064 mmol, 1 eq.) was suspended in THF and an excess Zn powder (80 mg, 1.284 mmol, 20 eq.) was added. The suspension was stirred overnight, while it changed colour from green to pink. After filtration, the solvent was removed in vacuo and the pink powder was recrystallized from a solution of toluene layered with hexane at -20°C.

^{1}H NMR (300 MHz, THF-d_8) δ 7.80 (d, J = 7.5 Hz, 2H, CH$_{ar}$), 7.34 (d, J = 7.4 Hz, 2H, CH$_{ar}$), 7.15 (s, 2H, HC=N), 7.14 – 6.99 (m, 8H, CH$_{ar}$), 6.92 (t, J = 7.4 Hz, 2H, CH$_{ar}$), 6.85 (t, J = 7.3 Hz, 2H, CH$_{ar}$), 6.76 (t, J = 7.3 Hz, 2H, CH$_{ar}$), 5.97 (s, 2H, CH$_{benz}$), 4.11 (d, J = 9.0 Hz, 2H, CH$_{olef}$), 3.70 (d, J = 9.1 Hz, 2H, CH$_{olef}$).

^{19}F NMR (282 MHz, THF-d_8) δ -80.26, -81.01.

[Li₃Ir(tropdad)(trop)] Li3[41]
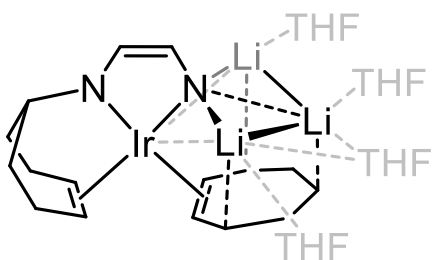
[Ir(trop₂dad)]OTf ([**40**]OTf) (39 mg, 0.050 mmol, 1 eq.) was suspended in THF and an excess Li sand (20 mg, 0.771 mmol, 20 eq.) was added. The suspension was stirred for one hour, while it changed color from green to red to pinkish red. After filtration, the solvent was removed in vacuo and the bordeaux red powder was recrystallized from a solution of THF layered with hexane.

^{1}H NMR (300 MHz, C₆D₆) δ 7.45 (t, J = 7.3 Hz, 2H, CH$_{ar}$), 7.14 – 6.98 (m, 2H, CH$_{ar}$), 6.93 (t, J = 7.6 Hz, 2H, CH$_{ar}$), 6.81 (t, J = 7.6 Hz, 2H, CH$_{ar}$), 6.13 (s, 1H, CH$_{dad}$), 5.39 (s, 1H, CH$_{dad}$), 3.56 (s, 2H, CH$_{olef}$), 3.42 (d, J = 6.3 Hz, 16H), THF, 1.42 – 1.28 (m, 16H, THF).

[Ir(trop₂dad)]₂ [42]
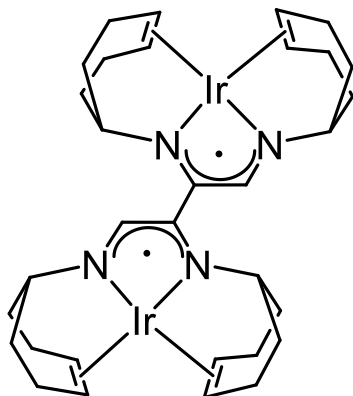
[Ir(trop₂dad)]OTf ([**40**]OTf) (40 mg, 0.051 mmol, 1 eq.) was suspended in 3 mL THF and an excess KH (20 mg, 0.51 mmol, 10 eq.) was added. After stirring the mixture for 24 h, the solvent was removed in vacuo. The dark red residue was extracted with toluene and filtrated over a pad of celite. Removing the solvent in vacuo yielded the product as a red powder, which could be recrystallized from toluene. Crystals suitable for X-ray diffraction were grown from a solution of [**42**] in toluene layered with hexane at -20°C. Yield: 26 mg (80%). Elemental analysis for $C_{64}H_{46}Ir_2N_4$ calculated (%): C 61.23, H 3.69, N 4.46; found (%): C 61.18, H 4.35, N 4.11.

^{1}H NMR (500 MHz, C_6D_6) δ 7.89 (s, 2H, HC=N), 7.42 – 7.32 (m, 8H, CH_{ar}), 7.30 (dd, J = 7.6, 1.3 Hz, 2H, CH_{ar}), 7.14 – 7.04 (m, 6H, CH_{ar}), 7.01 – 6.93 (m, 6H, CH_{ar}), 6.90 (td, J = 7.4, 1.6 Hz, 2H, CH_{ar}), 6.86 (dd, J = 7.6, 1.6 Hz, 2H, CH_{ar}), 6.81 (td, J = 7.3, 1.3 Hz, 2H, CH_{ar}), 6.76 (t, J = 7.4 Hz, 2H, CH_{ar}), 5.77 (s, 2H, CH_{olef}), 5.50 (d, J = 7.5 Hz, 2H, CH_{ar}), 5.47 (s, 2H, CH_{benz}), 4.29 (d, J = 8.4 Hz, 2H, CH_{olef}), 4.07 (d, J = 8.4 Hz, 2H, CH_{olef}), 3.96 (d, J = 8.4 Hz, 2H, CH_{olef}), 3.64 (d, J = 8.4 Hz, 2H, CH_{olef}).

^{13}C NMR (126 MHz, C_6D_6) δ 155.00 (s, HC=N), 149.84 (s, C_{ar}), 146.58 (s, C_{ar}), 143.39 (s, C_{ar}), 142.12 (s, C_{ar}), 141.94 (s, C_{ar}), 140.09 (s, C_{ar}), 139.02 (s, C_{ar}), 138.21 (s, C_{ar}), 129.87 (s, C_{ar}), 129.35 (s, C_{ar}), 127.47 (s, C_{ar}), 127.37 (s, C_{ar}), 126.23 (s, C_{ar}), 126.15 (s, C_{ar}), 126.00 (s, C_{ar}), 125.80 (s, C_{ar}), 125.41 (s, C_{ar}), 75.76 (s, CH_{benz}), 70.44 (s, CH_{benz}), 64.82 (s, CH_{olef}), 64.61 (s, CH_{olef}), 58.22 (s, CH_{olef}), 57.67 (s, CH_{olef}).

[Ir(trop₂dad-HMDS)] [45]
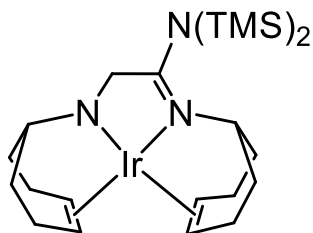
[Ir(trop₂dad)]OTf (40 mg, 0.051 mmol, 1 eq.) was suspended in THF and NaHMDS (18 mg, 0.051 mmol, 1 eq.) was added. A color change from green to red was observed. The suspension was stirred for one hour and filtered. The solvent was removed in vacuo and the orange powder recrystallized from a solution of Et₂O at -20°C.

^{1}H NMR (300 MHz, C₆D₆) δ 7.57 – 7.49 (m, 4H, CH$_{ar}$), 7.10 – 6.82 (m, 12H, CH$_{ar}$), 6.37 (s, 1H, CH$_{benz}$), 5.26 (s, 1H, CH$_{benz}$), 4.49 (s, 2H, CH$_{olef}$), 4.11 (s, 2H, CH$_{olef}$), 3.37 (s, 2H, N-CH₂), -0.23 (s, 17H, Si-CH₃).

[Ir(trop₂diq)]˙ [50]˙
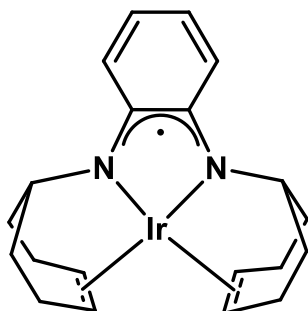
[Ir(trop₂dach)]OTf ([**38**]OTf) (30 mg, 0.036 mmol, 1 eq.) was dissolved in THF and a KO*t*Bu added (8.3 mg, 0.074 mmol, 2 eq.). After stirring for 10 min, BQ (11.6 mg, 0.108 mmol, 3 eq.) was added to the solution and stirred overnight. The formed solid was filtrated off and the solution dried in vacuo. The red complex was crystallized from MeCN or THF.

Paramagnetic radical.

APPENDIX

Crystallographic data

Chapter II

*Crystal data and structure refinement for **1**, [**2**] and [**3**].*

	1	[**2**]	[**3**]
Identification code	2313840	2313435	2313858
Empirical formula	$C_{172}H_{164}P_4$	$C_{100}H_{98}Cl_4P_2Rh_4$	$C_{45}H_{41}F_6O_6PRh_2S_2$
Formula weight	2354.90	1915.16	1092.69
Temperature/K	100.01(10)	100.00(10)	100.00(10)
Crystal system	monoclinic	triclinic	triclinic
Space group	$P2_1/c$	P-1	P-1
a/Å	34.4780(2)	11.9627(2)	10.3184(3)
b/Å	10.96194(4)	13.1950(2)	10.6661(3)
c/Å	38.1963(3)	14.07830(10)	20.2792(6)
α/°	90	96.1990(10)	100.752(3)
β/°	116.6055(9)	101.4310(10)	99.799(3)
γ/°	90	104.3630(10)	100.050(3)
Volume/Å^3	12907.50(17)	2080.97(5)	2111.09(11)
Z	4	1	2
ρ_{calc}g/cm^3	1.212	1.528	1.719
μ/mm^{-1}	0.963	8.216	8.271
F(000)	5024.0	976.0	1100.0
Crystal size/mm^3	0.25 × 0.21 × 0.17	0.15 × 0.04 × 0.035	0.079 × 0.049 × 0.044
Radiation	Cu Kα (λ = 1.54184)	Cu Kα (λ = 1.54184)	Cu Kα (λ = 1.54184)
2Θ range for data collection/°	4.66 to 160.554	6.494 to 160.568	8.636 to 103.856
Index ranges	-44 ≤ h ≤ 43, -13 ≤ k ≤ 13, -48 ≤ l ≤ 48	-15 ≤ h ≤ 15, -16 ≤ k ≤ 15, -17 ≤ l ≤ 17	-10 ≤ h ≤ 10, -10 ≤ k ≤ 10, -16 ≤ l ≤ 20
Reflections collected	514049	32201	14157
Independent reflections	27919 [R_{int} = 0.0953, R_{sigma} = 0.0330]	8866 [R_{int} = 0.0517, R_{sigma} = 0.0465]	4623 [R_{int} = 0.0395, R_{sigma} = 0.0435]
Data/restraints/parameters	27919/0/1585	8866/136/590	4623/0/560
Goodness-of-fit on F^2	1.050	1.166	1.033
Final R indexes [I>=2σ (I)]	R_1 = 0.0450, wR_2 = 0.1155	R_1 = 0.0435, wR_2 = 0.1256	R_1 = 0.0276, wR_2 = 0.0642
Final R indexes [all data]	R_1 = 0.0551, wR_2 = 0.1214	R_1 = 0.0465, wR_2 = 0.1282	R_1 = 0.0312, wR_2 = 0.0668
Largest diff. peak/hole / e Å^{-3}	0.32/-0.41	1.11/-1.98	0.38/-0.50

Appendix

Crystal data and structure refinement for [4](OTf)₂, [4](OTf) and [5].

	[4](OTf)$_2$	[4](OTf)	[5]
Identification code	2313437	2313436	2313428
Empirical formula	$C_{73}H_{73}F_6N_4O_8PRh_2S_2$	$C_{66.58}H_{59.67}F_3N_{4.5}O_3PRh_2S$	$C_{128}H_{130}Cl_2P_2Rh_2$
Formula weight	1549.26	1296.69	2006.97
Temperature/K	100.00(12)	100.15	100.01(10)
Crystal system	triclinic	monoclinic	triclinic
Space group	P-1	P2$_1$/n	P-1
a/Å	13.8174(4)	9.93520(10)	13.1434(3)
b/Å	16.2833(5)	43.1896(5)	15.1938(4)
c/Å	17.0904(5)	13.45180(10)	15.2523(3)
α/°	110.982(3)	90	79.262(2)
β/°	105.836(3)	98.4280(10)	65.253(2)
γ/°	96.016(2)	90	67.904(2)
Volume/Å^3	3365.06(19)	5709.80(10)	2561.48(12)
Z	2	4	1
ρ_{calc}g/cm^3	1.529	1.508	1.301
μ/mm^{-1}	0.653	5.791	0.457
F(000)	1588.0	2651.0	1052.0
Crystal size/mm^3	0.14 × 0.07 × 0.025	0.091 × 0.04 × 0.038	0.234 × 0.155 × 0.125
Radiation	Mo Kα (λ = 0.71073)	Cu Kα (λ = 1.54184)	MoKα (λ = 0.71073)
2Θ range for data collection/°	3.682 to 52.744	4.092 to 160.818	3.62 to 56.976
Index ranges	-17 ≤ h ≤ 17, -20 ≤ k ≤ 20, -21 ≤ l ≤ 21	-12 ≤ h ≤ 12, -54 ≤ k ≤ 52, -10 ≤ l ≤ 16	-17 ≤ h ≤ 16, -19 ≤ k ≤ 20, -20 ≤ l ≤ 20
Reflections collected	78472	53414	59764
Independent reflections	13728 [R_{int} = 0.0750, R_{sigma} = 0.0658]	12189 [R_{int} = 0.0439, R_{sigma} = 0.0372]	11623 [R_{int} = 0.0467, R_{sigma} = 0.0403]
Data/restraints/parameters	13728/186/943	12189/215/745	11623/90/737
Goodness-of-fit on F^2	1.060	1.076	1.049
Final R indexes [I>=2σ (I)]	R$_1$ = 0.0562, wR$_2$ = 0.1212	R$_1$ = 0.0642, wR$_2$ = 0.1794	R$_1$ = 0.0344, wR$_2$ = 0.0751
Final R indexes [all data]	R$_1$ = 0.0796, wR$_2$ = 0.1346	R$_1$ = 0.0690, wR$_2$ = 0.1835	R$_1$ = 0.0412, wR$_2$ = 0.0790
Largest diff. peak/hole / e Å^{-3}	1.47/-0.87	1.40/-1.16	0.61/-0.54

Appendix

Crystal data and structure refinement for [6](OTf), [6]₂. and [7].

	[6](OTf)	[6]₂	[7]
Identification code	2313426	2313427	2313511
Empirical formula	$C_{55}H_{50}Cl_3F_3N_2O_3PRhS$	$C_{118}H_{122}N_4O_3P_2Rh_2$	$C_{68}H_{62}N_5PRh_2$
Formula weight	1116.26	1911.95	1186.01
Temperature/K	100.00(10)	100.00(10)	100.01(11)
Crystal system	triclinic	monoclinic	triclinic
Space group	P-1	P2₁/c	P-1
a/Å	9.65720(10)	19.23010(10)	9.8012(4)
b/Å	12.00310(10)	25.78890(10)	13.3777(4)
c/Å	22.2473(2)	21.44500(10)	21.7694(6)
α/°	100.3980(10)	90	102.651(2)
β/°	96.5460(10)	112.2980(10)	96.454(3)
γ/°	99.7380(10)	90	96.355(3)
Volume/Å³	2471.99(4)	9839.81(10)	2740.32(16)
Z	2	4	2
ρ_{calc}g/cm³	1.500	1.291	1.437
μ/mm⁻¹	5.469	3.441	5.510
F(000)	1144.0	4008.0	1220.0
Crystal size/mm³	? × ? × ?	0.168 × 0.021 × 0.018	0.11 × 0.008 × 0.007
Radiation	Cu Kα (λ = 1.54184)	Cu Kα (λ = 1.54184)	Cu Kα (λ = 1.54184)
2Θ range for data collection/°	7.634 to 161.9	4.966 to 160.574	4.202 to 136.498
Index ranges	-12 ≤ h ≤ 12, -15 ≤ k ≤ 13, -28 ≤ l ≤ 28	-24 ≤ h ≤ 24, -32 ≤ k ≤ 30, -27 ≤ l ≤ 27	-11 ≤ h ≤ 11, -12 ≤ k ≤ 16, -26 ≤ l ≤ 25
Reflections collected	93869	234983	37113
Independent reflections	10595 [R_{int} = 0.0658, R_{sigma} = 0.0309]	21411 [R_{int} = 0.0569, R_{sigma} = 0.0266]	10005 [R_{int} = 0.1018, R_{sigma} = 0.0918]
Data/restraints/parameters	10595/0/631	21411/73/1196	10005/0/685
Goodness-of-fit on F²	1.056	1.083	1.008
Final R indexes [I>=2σ (I)]	R₁ = 0.0459, wR₂ = 0.1252	R₁ = 0.0458, wR₂ = 0.1176	R₁ = 0.0625, wR₂ = 0.1545
Final R indexes [all data]	R₁ = 0.0505, wR₂ = 0.1284	R₁ = 0.0483, wR₂ = 0.1191	R₁ = 0.0865, wR₂ = 0.1704
Largest diff. peak/hole / e Å⁻³	1.58/-0.85	1.49/-0.94	2.26/-1.72

Crystal data and structure refinement for [8](OTf) and [11].

	[8](OTf)	[11]
Identification code	2313512	CS3_058_auto
Empirical formula	$C_{68}H_{67}F_3N_4O_4PRh_2S$	$C_{59}H_{51}F_8N_2O_6PRh_2S_2$
Formula weight	1326.85	1350.93
Temperature/K	100.00(10)	100.01(10)
Crystal system	monoclinic	orthorhombic
Space group	$P2_1/c$	Pnma
a/Å	21.5586(6)	24.8149(3)
b/Å	9.9941(3)	15.6555(2)
c/Å	26.8646(10)	17.0275(2)
α/°	90	90
β/°	90.466(3)	90
γ/°	90	90
Volume/Å^3	5788.0(3)	6615.01(14)
Z	4	4
ρ_{calc}g/cm^3	1.523	1.356
μ/mm^{-1}	5.733	5.449
F(000)	2725.0	2732.0
Crystal size/mm^3	0.17 × 0.05 × 0.04	0.1 × 0.1 × 0.1
Radiation	Cu Kα (λ = 1.54184)	Cu Kα (λ = 1.54184)
2Θ range for data collection/°	6.58 to 161.874	6.296 to 149
Index ranges	-27 ≤ h ≤ 27, -8 ≤ k ≤ 12, -34 ≤ l ≤ 31	-29 ≤ h ≤ 30, -19 ≤ k ≤ 17, -20 ≤ l ≤ 21
Reflections collected	50039	48249
Independent reflections	12345 [R_{int} = 0.0349, R_{sigma} = 0.0320]	7020 [R_{int} = 0.0772, R_{sigma} = 0.0400]
Data/restraints/parameters	12345/164/958	7020/0/403
Goodness-of-fit on F^2	1.114	1.139
Final R indexes [I>=2σ (I)]	R_1 = 0.0623, wR_2 = 0.1366	R_1 = 0.0742, wR_2 = 0.1822
Final R indexes [all data]	R_1 = 0.0671, wR_2 = 0.1390	R_1 = 0.0769, wR_2 = 0.1836
Largest diff. peak/hole / e Å^{-3}	1.07/-1.19	1.62/-2.46

Chapter III

Crystal data and structure refinement for [14] and [15].

	[14]	[15]
Identification code	CS161	RhOTfPtMe2
Empirical formula	C46H49Cl3PPtRh	C92H94F6O6P2Pt2Rh2S2
Formula weight	1037.17	2131.73
Temperature/K	100.00(10)	100.00(10)
Crystal system	monoclinic	monoclinic
Space group	P21/n	P21/c
a/Å	15.6016(3)	17.9427(3)
b/Å	18.4145(2)	16.5105(2)
c/Å	16.1659(3)	32.3767(5)
α/°	90	90
β/°	117.621(2)	98.6010(10)
γ/°	90	90
Volume/Å3	4115.09(14)	9483.5(2)
Z	4	4
ρcalcg/cm3	1.674	1.493
μ/mm-1	4.062	3.420
F(000)	2056.0	4224.0
Crystal size/mm3	0.75 × 0.52 × 0.1	0.7 × 0.2 × 0.2
Radiation	Mo Kα (λ = 0.71073)	Mo Kα (λ = 0.71073)
2Θ range for data collection/°	4.424 to 57.46	3.37 to 57.094
Index ranges	-20 ≤ h ≤ 20, -24 ≤ k ≤ 24, -21 ≤ l ≤ 21	-23 ≤ h ≤ 23, -21 ≤ k ≤ 21, -39 ≤ l ≤ 41
Reflections collected	97984	223725
Independent reflections	10108 [Rint = 0.0800, Rsigma = 0.0590]	22432 [Rint = 0.0709, Rsigma = 0.0454]
Data/restraints/parameters	10108/0/471	22432/0/1029
Goodness-of-fit on F2	1.067	1.090
Final R indexes [I>=2σ (I)]	R1 = 0.0491, wR2 = 0.0954	R1 = 0.0447, wR2 = 0.0993
Final R indexes [all data]	R1 = 0.0729, wR2 = 0.1036	R1 = 0.0528, wR2 = 0.1057
Largest diff. peak/hole / e Å-3	1.96/-1.02	1.58/-1.31

Appendix

Crystal data and structure refinement for[16] and [17].

	[16]	[17]
Identification code	CS2_072	CS3_121_auto
Empirical formula	$C_{75}H_{60}BF_{18}N_2OPPtRh$	$C_{45}H_{47}NO_2PPtRh$
Formula weight	754.43	962.80
Temperature/K	100.00(10)	100.00(10)
Crystal system	triclinic	monoclinic
Space group	P-1	P2$_1$/n
a/Å	13.0055(2)	9.63280(10)
b/Å	23.0582(4)	31.5768(2)
c/Å	30.6944(5)	12.88320(10)
α/°	110.034(2)	90
β/°	98.828(2)	102.6120(10)
γ/°	92.327(2)	90
Volume/Å^3	8502.2(3)	3824.17(6)
Z	14	4
ρ_{calc}g/cm^3	2.063	1.672
μ/mm^{-1}	6.527	10.924
F(000)	5109.0	1912.0
Crystal size/mm^3	0.34 × 0.3 × 0.2	0.5 × 0.18 × 0.15
Radiation	Mo Kα (λ = 0.71073)	Cu Kα (λ = 1.54184)
2Θ range for data collection/°	3.536 to 58.802	5.598 to 160.942
Index ranges	-17 ≤ h ≤ 17, -31 ≤ k ≤ 31, -42 ≤ l ≤ 41	-11 ≤ h ≤ 8, -39 ≤ k ≤ 40, -16 ≤ l ≤ 16
Reflections collected	341907	64039
Independent reflections	43286 [Rint = 0.0744, Rsigma = 0.0660]	8275 [R_{int} = 0.0603, R_{sigma} = 0.0314]
Data/restraints/parameters	43286/284/2451	8275/0/450
Goodness-of-fit on F^2	1.029	1.102
Final R indexes [I>=2σ (I)]	R1 = 0.0961, wR2 = 0.2525	R_1 = 0.0425, wR$_2$ = 0.1126
Final R indexes [all data]	R1 = 0.1306, wR2 = 0.2851	R_1 = 0.0445, wR$_2$ = 0.1142
Largest diff. peak/hole / e Å^{-3}	11.36/-4.61	2.94/-1.40

Appendix

*Crystal data and structure refinement for [**18**], [**19**] and [**20**].*

	[**18**]	[**19**]	[**20**]
Identification code	CS3_080_auto	CS2_086	CS2_160_auto
Empirical formula	$C_{46}H_{44}Cl_{11}CuPRh$	$C_{52}H_{52}Cl_2CuNPRh$	$C_{49}H_{47}CuF_6N_2O_6PRhS_2$
Formula weight	1184.18	959.26	1135.42
Temperature/K	100.00(10)	102(3)	100.01(10)
Crystal system	triclinic	monoclinic	triclinic
Space group	P-1	I2/a	P-1
a/Å	13.44370(10)	26.5457(7)	16.9565(3)
b/Å	14.51030(10)	11.6454(2)	17.0162(2)
c/Å	14.69210(10)	32.8755(7)	17.9124(3)
α/°	65.5010(10)	90	71.5240(10)
β/°	68.6220(10)	112.343(3)	74.0490(10)
γ/°	84.4330(10)	90	87.9200(10)
Volume/Å3	2423.58(4)	9400.0(4)	4705.91(13)
Z	2	8	4
ρcalcg/cm3	1.623	1.356	1.603
μ/mm-1	9.445	0.986	5.201
F(000)	1192.0	3952.0	2312.0
Crystal size/mm3	0.5 × 0.2 × 0.2	0.423 × 0.318 × 0.211	0.4 × 0.2 × 0.15
Radiation	Cu Kα (λ = 1.54184)	Mo Kα (λ = 0.71073)	Cu Kα (λ = 1.54184)
2Θ range for data collection/°	6.708 to 160.64	3.318 to 51.362	5.414 to 160.996
Index ranges	-17 ≤ h ≤ 17, -18 ≤ k ≤ 18, -18 ≤ l ≤ 18	-32 ≤ h ≤ 32, -14 ≤ k ≤ 14, -40 ≤ l ≤ 40	-21 ≤ h ≤ 21, -19 ≤ k ≤ 21, -22 ≤ l ≤ 22
Reflections collected	94400	108252	67977
Independent reflections	10348 [Rint = 0.0713, Rsigma = 0.0307]	8929 [Rint = 0.0945, Rsigma = 0.0474]	19739 [R_{int} = 0.0594, R_{sigma} = 0.0546]
Data/restraints/parameters	10348/0/541	8929/0/525	19739/0/1229
Goodness-of-fit on F2	1.092	1.046	1.092
Final R indexes [I>=2σ (I)]	R1 = 0.0383, wR2 = 0.1013	R1 = 0.0387, wR2 = 0.0887	R_1 = 0.0375, wR2 = 0.0964
Final R indexes [all data]	R1 = 0.0396, wR2 = 0.1024	R1 = 0.0544, wR2 = 0.0962	R_1 = 0.0445, wR2 = 0.1003
Largest diff. peak/hole / e Å-3	1.26/-0.90	0.68/-0.51	0.76/-0.91

*Crystal data and structure refinement for **22a** and [**23a**]BF$_4$*

	22a	[23a]BF$_4$
Identification code	(PhCC)2tropNHtrop	CS2_014am
Empirical formula	C$_{50}$H$_{39}$NO$_2$	C$_{50}$H$_{37}$BF$_4$N$_3$Rh
Formula weight	685.82	869.54
Temperature/K	100.00(10)	273.15
Crystal system	triclinic	monoclinic
Space group	P-1	P2$_1$/n
a/Å	12.3960(5)	9.1182(10)
b/Å	13.1084(4)	15.6332(17)
c/Å	13.2768(4)	28.267(3)
α/°	90.051(3)	90
β/°	113.107(3)	93.763(2)
γ/°	108.171(3)	90
Volume/Å3	1866.48(12)	4020.7(8)
Z	2	4
ρcalcg/cm3	1.220	1.436
μ/mm-1	0.073	0.483
F(000)	724.0	1776.0
Crystal size/mm3	0.4 × 0.1 × 0.1	0.1 × 0.1 × 0.1
Radiation	Mo Kα (λ = 0.71073)	MoKα (λ = 0.71073)
2Θ range for data collection/°	3.798 to 58.67	2.888 to 46.204
Index ranges	-17 ≤ h ≤ 16, -17 ≤ k ≤ 18, -17 ≤ l ≤ 18	-10 ≤ h ≤ 10, -17 ≤ k ≤ 17, -30 ≤ l ≤ 31
Reflections collected	49711	25569
Independent reflections	9308 [R$_{int}$ = 0.0528, R$_{sigma}$ = 0.0470]	5598 [R$_{int}$ = 0.0674, R$_{sigma}$ = 0.0575]
Data/restraints/parameters	9308/0/483	5598/0/534
Goodness-of-fit on F2	1.031	0.942
Final R indexes [I>=2σ (I)]	R$_1$ = 0.0587, wR$_2$ = 0.1214	R$_1$ = 0.0338, wR$_2$ = 0.0750
Final R indexes [all data]	R$_1$ = 0.0848, wR$_2$ = 0.1346	R$_1$ = 0.0459, wR$_2$ = 0.0790
Largest diff. peak/hole / e Å-3	0.49/-0.24	0.89/-0.24

*Crystal data and structure refinement for [**24a**]BArF, [**25**](BF$_4$)$_2$ and [**26**]BF$_4$*

	[**24a**]BArF	[**25**](BF$_4$)$_2$	[**26**]BF$_4$
Identification code	TB_32_auto	TB_06_auto	CS2_040_0m
Empirical formula	C$_{86}$H$_{55}$BF$_{24}$NRh	C$_{31}$H$_{21}$BCuF$_4$N	C$_{51}$H$_{39}$BCl$_2$CuF$_4$N$_3$
Formula weight	1672.03	557.84	915.10
Temperature/K	100.01(10)	100.00(10)	100.0
Crystal system	triclinic	monoclinic	triclinic
Space group	P-1	P2$_1$/n	P-1
a/Å	10.42330(10)	17.0510(4)	12.1226(7)
b/Å	18.7646(2)	12.9822(3)	13.0327(7)
c/Å	20.0629(2)	23.1233(4)	16.4752(9)
α/°	105.7160(10)	90	101.730(2)
β/°	101.7620(10)	103.454(2)	98.952(2)
γ/°	99.1590(10)	90	117.077(2)
Volume/Å3	3601.10(7)	4978.09(19)	2175.4(2)
Z	2	8	2
ρcalcg/cm3	1.542	1.489	1.397
μ/mm-1	2.901	1.684	2.309
F(000)	1688.0	2272.0	940.0
Crystal size/mm3	0.4 × 0.1 × 0.1	? × ? × ?	? × ? × ?
Radiation	Cu Kα (λ = 1.54184)	Cu Kα (λ = 1.54184)	CuKα (λ = 1.54178)
2Θ range for data collection/°	5.724 to 160.616	7.322 to 126.85	5.714 to 146.032
Index ranges	-13 ≤ h ≤ 12, -23 ≤ k ≤ 23, -25 ≤ l ≤ 25	-19 ≤ h ≤ 18, -14 ≤ k ≤ 15, -26 ≤ l ≤ 24	-14 ≤ h ≤ 14, -16 ≤ k ≤ 16, -20 ≤ l ≤ 20
Reflections collected	59858	26291	66860
Independent reflections	15447 [R$_{int}$ = 0.0486, R$_{sigma}$ = 0.0432]	7824 [R$_{int}$ = 0.0519, R$_{sigma}$ = 0.0628]	8580 [R$_{int}$ = 0.0612, R$_{sigma}$ = 0.0327]
Data/restraints/parameters	15447/0/1049	7824/0/701	8580/0/561
Goodness-of-fit on F2	1.113	1.098	1.058
Final R indexes [I>=2σ (I)]	R$_1$ = 0.0415, wR$_2$ = 0.1087	R$_1$ = 0.0612, wR$_2$ = 0.1116	R$_1$ = 0.0397, wR$_2$ = 0.1068
Final R indexes [all data]	R$_1$ = 0.0437, wR$_2$ = 0.1102	R$_1$ = 0.0869, wR$_2$ = 0.1203	R$_1$ = 0.0434, wR$_2$ = 0.1132
Largest diff. peak/hole / e Å-3	1.02/-1.04	0.45/-0.47	0.59/-0.70

Chapter IV

Crystal data and structure refinement for [28], [29] and [30]

	[28]	[29]	[30]
Identification code	CS092r	CS3_008_2_auto	CS3_131_auto
Empirical formula	$C_{20}H_{30}PCo$	$C_{88}H_{120}CoKN_2O_{10}PSi_4$	$C_{47}H_{29}Co_2O_4P$
Formula weight	360.34	1607.21	806.53
Temperature/K	100.0	99.98(11)	99.99(10)
Crystal system	triclinic	triclinic	triclinic
Space group	P1	P-1	P-1
a/Å	13.0338(8)	15.8174(2)	10.1805(2)
b/Å	13.5257(9)	16.2366(3)	12.8865(3)
c/Å	22.4884(13)	20.7053(4)	15.1241(4)
α/°	98.001(4)	78.812(2)	88.219(2)
β/°	90.054(4)	70.438(2)	77.222(2)
γ/°	118.650(4)	65.540(2)	71.082(2)
Volume/Å3	3434.8(4)	4551.40(16)	1828.71(8)
Z	8	2	2
ρcalcg/cm3	1.394	1.173	1.465
μ/mm-1	8.640	2.985	7.890
F(000)	1536.0	1718.0	824.0
Crystal size/mm3	? × ? × ?	? × ? × ?	? × ? × ?
Radiation	CuKα (λ = 1.54178)	Cu Kα (λ = 1.54184)	Cu Kα (λ = 1.54184)
2Θ range for data collection/°	3.98 to 138.68	4.538 to 160.442	5.998 to 160.666
Index ranges	-15 ≤ h ≤ 15, -16 ≤ k ≤ 16, -27 ≤ l ≤ 27	-19 ≤ h ≤ 20, -18 ≤ k ≤ 20, -25 ≤ l ≤ 26	-13 ≤ h ≤ 13, -16 ≤ k ≤ 13, -18 ≤ l ≤ 19
Reflections collected	44477	64382	26588
Independent reflections	20816 [R_{int} = 0.2837, R_{sigma} = 0.3387]	19172 [R_{int} = 0.0497, R_{sigma} = 0.0471]	7698 [R_{int} = 0.0311, R_{sigma} = 0.0305]
Data/restraints/parameters	20816/3/1784	19172/0/979	7698/0/487
Goodness-of-fit on F2	1.361	1.048	1.063
Final R indexes [I>=2σ (I)]	R_1 = 0.2411, wR_2 = 0.3926	R_1 = 0.0814, wR_2 = 0.2361	R_1 = 0.0323, wR_2 = 0.0789
Final R indexes [all data]	R_1 = 0.3235, wR_2 = 0.4278	R_1 = 0.0964, wR_2 = 0.2513	R_1 = 0.0344, wR_2 = 0.0798
Largest diff. peak/hole / e Å-3	1.33/-2.01	1.69/-0.75	0.28/-0.41

Crystal data and structure refinement for [31], [32] and [34]

	[31]	[32]	[34]
Identification code	CS059	CS2_038	CS3_121_auto
Empirical formula	$C_{25}H_{35}P_2CoO_{0.14}$	$C_{45}H_{29}ClCuO_{0.5}P$	$C_{47}H_{37}Cl_2Cu_2OP$
Formula weight	458.68	707.64	846.71
Temperature/K	100.00(10)	100.01(11)	100.00(10)
Crystal system	triclinic	monoclinic	triclinic
Space group	P-1	$P2_1/c$	P-1
a/Å	13.3405(4)	12.2632(4)	11.4571(4)
b/Å	13.7770(6)	16.9135(3)	13.1259(6)
c/Å	19.6766(8)	16.7144(4)	13.6699(3)
α/°	82.523(4)	90	89.437(3)
β/°	82.465(3)	98.830(2)	88.945(2)
γ/°	88.955(3)	90	66.986(4)
Volume/Å3	3554.7(2)	3425.71(15)	1891.80(13)
Z	7	4	2
ρcalcg/cm3	1.500	1.372	1.486
μ/mm-1	1.013	0.796	3.368
F(000)	1702.0	1456.0	868.0
Crystal size/mm3	? × ? × ?	? × ? × ?	? × ? × ?
Radiation	Mo Kα (λ = 0.71073)	Mo Kα (λ = 0.71073)	Cu Kα (λ = 1.54184)
2Θ range for data collection/°	3.422 to 56.7	3.446 to 56.908	61.56 to 160.598
Index ranges	-17 ≤ h ≤ 16, -17 ≤ k ≤ 18, -23 ≤ l ≤ 15	-15 ≤ h ≤ 16, -22 ≤ k ≤ 22, -21 ≤ l ≤ 22	-10 ≤ h ≤ 14, -15 ≤ k ≤ 15, -17 ≤ l ≤ 3
Reflections collected	17201	80597	5436
Independent reflections	12624 [R_{int} = 0.0254, R_{sigma} = 0.0720]	8155 [R_{int} = 0.0780, R_{sigma} = 0.0561]	3474 [R_{int} = 0.0290, R_{sigma} = 0.0470]
Data/restraints/parameters	12624/0/923	8155/20/435	3474/0/213
Goodness-of-fit on F2	1.058	0.764	1.427
Final R indexes [I>=2σ (I)]	R_1 = 0.0519, wR_2 = 0.0974	R_1 = 0.0617, wR_2 = 0.1759	R_1 = 0.0615, wR_2 = 0.1774
Final R indexes [all data]	R_1 = 0.0741, wR_2 = 0.1070	R_1 = 0.1005, wR_2 = 0.2241	R_1 = 0.0692, wR_2 = 0.1850
Largest diff. peak/hole / e Å-3	0.60/-0.56	1.49/-0.43	0.77/-0.71

Crystal data and structure refinement for [35], [36] and [37]

	[35]	[36]	[37]
Identification code	CS4_098_cyCu2OTf2	CS3_123_auto	CS3_124_auto
Empirical formula	$C_{99}H_{100}Cu_4F_{12}O_{14}P_2S_4$	$C_{43}H_{41}Cl_2Cu_2P$	$C_{51}H_{33}Cu_2F_8O_6PS_2$
Formula weight	2186.12	786.71	615.65
Temperature/K	100.00(10)	100.00(10)	100.00(10)
Crystal system	orthorhombic	triclinic	triclinic
Space group	$Pna2_1$	P-1	P-1
a/Å	22.4849(4)	11.4306(3)	13.0554(3)
b/Å	10.7011(3)	12.5103(3)	14.3437(3)
c/Å	40.1773(9)	14.1875(4)	14.3584(4)
α/°	90	97.079(2)	62.839(3)
β/°	90	113.382(2)	73.215(2)
γ/°	90	95.842(2)	78.701(2)
Volume/Å3	9667.2(4)	1822.55(9)	2283.88(11)
Z	4	2	4
ρcalcg/cm3	1.502	1.434	1.790
μ/mm-1	2.843	3.423	4.082
F(000)	4496.0	812.0	1264.0
Crystal size/mm3	? × ? × ?	? × ? × ?	? × ? × ?
Radiation	Cu Kα (λ = 1.54184)	Cu Kα (λ = 1.54184)	Cu Kα (λ = 1.54184)
2Θ range for data collection/°	4.398 to 114.166	6.9 to 161.176	6.946 to 160.742
Index ranges	$-24 \leq h \leq 12$, $-11 \leq k \leq 9$, $-43 \leq l \leq 42$	$-14 \leq h \leq 14$, $-15 \leq k \leq 15$, $-18 \leq l \leq 15$	$-16 \leq h \leq 16$, $-18 \leq k \leq 18$, $-18 \leq l \leq 17$
Reflections collected	31124	27089	36593
Independent reflections	11383 [R_{int} = 0.0356, R_{sigma} = 0.0450]	7777 [R_{int} = 0.0391, R_{sigma} = 0.0348]	9744 [R_{int} = 0.0408, R_{sigma} = 0.0393]
Data/restraints/parameters	11383/13/1225	7777/0/434	9744/0/631
Goodness-of-fit on F2	1.075	1.066	1.189
Final R indexes [I>=2σ (I)]	R_1 = 0.0857, wR_2 = 0.2178	R_1 = 0.0400, wR_2 = 0.1125	R_1 = 0.0426, wR_2 = 0.1428
Final R indexes [all data]	R_1 = 0.0946, wR_2 = 0.2242	R_1 = 0.0430, wR_2 = 0.1147	R_1 = 0.0469, wR_2 = 0.1484
Largest diff. peak/hole / e Å-3	1.91/-0.47	0.75/-0.70	0.83/-0.88

Chapter V

*Crystal data and structure refinement for [**40**]· and Na[**40**]*

	[**40**]·	Na[**40**]
Identification code	CS_US_087_TolHex	CS_US_106_ZnNa
Empirical formula	$C_{39}H_{32}IrN_2$	$C_{92}H_{103}Ir_2N_4Na_2O_7$
Formula weight	720.86	1807.16
Temperature/K	99.99(10)	100.01(10)
Crystal system	orthorhombic	monoclinic
Space group	Pbca	P2$_1$/n
a/Å	16.5376(3)	19.69820(10)
b/Å	13.1925(3)	17.31670(10)
c/Å	25.9765(5)	23.53020(10)
α/°	90	90
β/°	90	100.5450(10)
γ/°	90	90
Volume/Å3	5667.4(2)	7890.78(7)
Z	8	4
ρcalcg/cm3	1.690	1.521
μ/mm-1	4.744	7.008
F(000)	2856.0	3660.0
Crystal size/mm3	0.11 × 0.04 × 0.04	0.15 × 0.12 × 0.08
Radiation	Mo Kα (λ = 0.71073)	Cu Kα (λ = 1.54184)
2Θ range for data collection/°	3.988 to 61.62	5.388 to 160.402
Index ranges	-23 ≤ h ≤ 22, -16 ≤ k ≤ 18, -36 ≤ l ≤ 32	-25 ≤ h ≤ 24, -19 ≤ k ≤ 22, -30 ≤ l ≤ 29
Reflections collected	43152	101020
Independent reflections	7392 [R_{int} = 0.0366, R_{sigma} = 0.0281]	17110 [R_{int} = 0.0389, R_{sigma} = 0.0287]
Data/restraints/parameters	7392/0/380	17110/0/966
Goodness-of-fit on F2	1.060	1.136
Final R indexes [I>=2σ (I)]	R_1 = 0.0228, wR_2 = 0.0562	R_1 = 0.0293, wR_2 = 0.0795
Final R indexes [all data]	R_1 = 0.0355, wR_2 = 0.0600	R_1 = 0.0322, wR_2 = 0.0812
Largest diff. peak/hole / e Å-3	0.94/-0.52	1.39/-1.07

*Crystal data and structure refinement for Li$_3$[**41**], [**42**] and [**44**].*

	Li$_3$[**41**]	[**42**]	[**44**]
Identification code	CS_US_107_Li_solid	CS_US_104_KH_TolHex	CS_US_090_2Na
Empirical formula	C$_{48}$H$_{56}$IrLi$_3$N$_2$O$_4$	C$_{92}$H$_{78}$Ir$_2$N$_4$	C$_{48}$H$_{55}$IrN$_2$NaO$_4$
Formula weight	937.96	1623.98	939.13
Temperature/K	100.01(12)	100.0(2)	100.01(13)
Crystal system	monoclinic	monoclinic	triclinic
Space group	P2$_1$/n	C2/c	P-1
a/Å	13.19410(10)	25.49560(10)	10.6674(2)
b/Å	15.15000(10)	21.04750(10)	11.5619(2)
c/Å	20.6091(2)	25.9713(2)	18.1417(3)
α/°	90	90	94.1650(10)
β/°	90.8430(10)	96.9670(10)	99.977(2)
γ/°	90	90	108.661(2)
Volume/Å3	4119.12(6)	13833.78(14)	2068.07(7)
Z	4	8	2
ρcalcg/cm3	1.512	1.559	1.508
μ/mm-1	6.636	7.738	6.717
F(000)	1904.0	6496.0	954.0
Crystal size/mm3	0.1 × 0.03 × 0.02	0.16 × 0.05 × 0.04	? × ? × ?
Radiation	Cu Kα (λ = 1.54184)	Cu Kα (λ = 1.54184)	Cu Kα (λ = 1.54184)
2Θ range for data collection/°	7.242 to 160.392	5.462 to 160.968	4.994 to 160.686
Index ranges	-16 ≤ h ≤ 16, -19 ≤ k ≤ 18, -26 ≤ l ≤ 25	-24 ≤ h ≤ 31, -26 ≤ k ≤ 26, -33 ≤ l ≤ 33	-13 ≤ h ≤ 13, -13 ≤ k ≤ 14, -23 ≤ l ≤ 23
Reflections collected	55035	76432	40206
Independent reflections	8933 [R$_{int}$ = 0.0551, R$_{sigma}$ = 0.0371]	14876 [R$_{int}$ = 0.0352, R$_{sigma}$ = 0.0259]	8896 [R$_{int}$ = 0.0593, R$_{sigma}$ = 0.0474]
Data/restraints/parameters	8933/0/527	14876/0/895	8896/75/508
Goodness-of-fit on F2	1.065	1.085	1.091
Final R indexes [I>=2σ (I)]	R$_1$ = 0.0392, wR$_2$ = 0.1045	R$_1$ = 0.0360, wR$_2$ = 0.0894	R$_1$ = 0.0409, wR$_2$ = 0.1045
Final R indexes [all data]	R$_1$ = 0.0447, wR$_2$ = 0.1093	R$_1$ = 0.0403, wR$_2$ = 0.0920	R$_1$ = 0.0444, wR$_2$ = 0.1062
Largest diff. peak/hole / e Å-3	3.02/-1.12	2.05/-1.45	2.12/-1.08

*Crystal data and structure refinement for [**45**], Na[**47**] and [**50**]*

	[**45**]	Na[**47**]	[**50**]
Identification code	CS_US_095_orange	CS_US_065	CS_US_134_6BQ_MeCN
Empirical formula	$C_{40}H_{42}IrN_3O_{0.5}Si_2$	$C_{88}H_{85}Ir_2N_4NaO_7$	$C_{36}H_{26}IrN_2$
Formula weight	821.14	1717.98	678.79
Temperature/K	100.00(10)	100.00(10)	100.00(10)
Crystal system	triclinic	monoclinic	monoclinic
Space group	P-1	$P2_1/n$	$P2_1/c$
a/Å	9.2143(2)	16.5518(3)	11.50830(10)
b/Å	12.3116(2)	21.8619(9)	12.98440(10)
c/Å	17.6440(3)	21.9003(5)	17.0358(2)
α/°	77.317(2)	90	90
β/°	86.064(2)	96.784(2)	90.2410(10)
γ/°	68.592(2)	90	90
Volume/Å3	1817.87(6)	7869.2(4)	2545.61(4)
Z	2	4	4
ρcalcg/cm3	1.500	1.450	1.771
μ/mm-1	3.772	6.950	10.371
F(000)	824.0	3448.0	1332.0
Crystal size/mm3	? × ? × ?	? × ? × ?	0.05 × 0.03 × 0.02
Radiation	Mo Kα (λ = 0.71073)	Cu Kα (λ = 1.54184)	Cu Kα (λ = 1.54184)
2Θ range for data collection/°	3.9 to 61.672	5.732 to 103.892	7.682 to 160.48
Index ranges	$-12 \leq h \leq 12, -17 \leq k \leq 15, -22 \leq l \leq 24$	$-16 \leq h \leq 16, -11 \leq k \leq 14, -22 \leq l \leq 22$	$-14 \leq h \leq 14, -13 \leq k \leq 16, -21 \leq l \leq 21$
Reflections collected	28227	14842	21960
Independent reflections	9210 [R_{int} = 0.0406, R_{sigma} = 0.0440]	6160 [R_{int} = 0.0511, R_{sigma} = 0.0662]	5468 [R_{int} = 0.0406, R_{sigma} = 0.0369]
Data/restraints/parameters	9210/0/430	6160/0/412	5468/0/352
Goodness-of-fit on F2	1.055	1.823	1.134
Final R indexes [I>=2σ (I)]	R_1 = 0.0273, wR_2 = 0.0687	R_1 = 0.1810, wR_2 = 0.4291	R_1 = 0.0324, wR_2 = 0.0849
Final R indexes [all data]	R_1 = 0.0322, wR_2 = 0.0701	R_1 = 0.2027, wR_2 = 0.4429	R_1 = 0.0356, wR_2 = 0.0871
Largest diff. peak/hole / e Å-3	1.33/-1.36	9.40/-7.59	1.45/-1.56

Bibliography

[1]   A. Wang, X. Y. Liu, C. Y. Mou, T. Zhang, J Catal 2013, 308, 258–271.

[2]   I. G. Powers, C. Uyeda, ACS Catal 2017, 7, 936–958.

[3]   N. P. Mankad, Chemistry - A European Journal 2016, 22, 5822–5829.

[4]   A. Volbeda, M. H. Charon, C. Piras, E. C. Hatchikian, M. Frey, J. C. Fontecilla-Camps, Nature 1995, 373, 580–587.

[5]   H. C. Böttcher, M. Graf, K. Mereiter, K. Kirchner, Organometallics 2004, 23, 1269–1273.

[6]   L. H. Gade, Angewandte Chemie International Edition 2000, 39, 2658–2678.

[7]   L. J. Clouston, R. B. Siedschlag, P. A. Rudd, N. Planas, S. Hu, A. D. Miller, L. Gagliardi, C. C. Lu, J Am Chem Soc 2013, 135, 13142–13148.

[8]   M. Caporali, L. Gonsalvi, V. Mirabello, A. Ienco, G. Manca, F. Zanobini, M. Peruzzini, Eur J Inorg Chem 2014, 1652–1659.

[9]   P. A. Rudd, S. Liu, N. Planas, E. Bill, L. Gagliardi, C. C. Lu, Angewandte Chemie - International Edition 2013, 52, 4449–4452.

[10] R. J. Eisenhart, L. J. Clouston, C. C. Lu, Acc Chem Res 2015, 48, 2885–2894.

[11] T. Nguyen, A. D. Sutton, M. Brynda, J. C. Fettinger, G. J. Long, P. P. Power, Science (1979) 2005, 310, 844–847.

[12] H. Schmidbaur, A. Schier, Chem Soc Rev 2012, 41, 370–412.

[13] J. Campos, Nat Rev Chem 2020, 4, 696–702.

[14] J. Adams, D. M. Spero, Tetrahedron 1991, 47, 1765–1808.

[15] H. M. L. Davies, D. Morton, Chem Soc Rev 2011, 40, 1857–1869.

[16] H. M. L. Davies, J. R. Manning, Nature 2008, 451, 417–424.

[17] J. Ye, R. C. Cammarota, J. Xie, M. V. Vollmer, D. G. Truhlar, C. J. Cramer, C. C. Lu, L. Gagliardi, ACS Catal 2018, 8, 4955–4968.

[18] M. K. Karunananda, N. P. Mankad, J Am Chem Soc 2015, 137, 14598–14601.

[19] D. R. Pye, N. P. Mankad, Chem Sci 2017, 8, 1705–1718.

[20] F. J. Lombard, M. J. Coster, Org Biomol Chem 2015, 13, 6419–6431.

[21] R. Uson, J. Fornies, P. Espinet, C. Fortuao, M. Tomas, A. J. Welch, 1988, 3005–3009.

[22] M. Melnik, O. Sprusansky, C. E. Holloway, Crystallographic and Structural Characterization of Heterometallic Platinum Compounds. Part II. Heterobinuclear Pt Compounds with Pt·· ·M (M = Transition or Lantanide Metal) > 3.0 Å, 2012.

[23] H. Chen, L. Chen, G. Chen, M. Robert, T. C. Lau, ChemPhysChem 2021, 22, 1835–1843.

[24] A. M. Borys, E. Hevia, Trends Chem 2021, 3, 803–806.

[25] F. Mongin, A. Harrison-Marchand, Chem Rev 2013, 113, 7563–7727.

[26] S. D. Robertson, M. Uzelac, R. E. Mulvey, Chem Rev 2019, 119, 8332–8405.

[27] R. Seki, N. Hara, T. Saito, Y. Nakao, J Am Chem Soc 2021, 143, 6388–6394.

[28] A. Logallo, E. Hevia, Chemical Communications 2023, 59, 5383–5386.

[29] R. Hrdina, Eur J Inorg Chem 2021, 2021, 501–528.

[30] H. D. Manamperi, C. E. Moore, C. Turro, Chemical Communications 2021, 57, 1635–1638.

[31] D. C. Powers, T. Ritter, Nat Chem 2009, 1, 302–309.

[32] Y. Y. Zhou, D. R. Hartline, T. J. Steiman, P. E. Fanwick, C. Uyeda, Inorg Chem 2014, 53, 11770–11777.

[33] C. Uyeda, C. M. Farley, Acc Chem Res 2021, 54, 3710–3719.

[34] M. Desage-El Murr, in Redox-Active Ligands, 2024, pp. 1–20.

[35] V. Lyaskovskyy, B. De Bruin, ACS Catal 2012, 2, 270–279.

[36] H. Grützmacher, Angewandte Chemie - International Edition 2008, 47, 1814–1818.

[37] J. R. Khusnutdinova, D. Milstein, Angewandte Chemie 2015, 127, 12406–12445.

[38] R. H. Crabtree, New Journal of Chemistry 2011, 35, 18–23.

[39] V. K. K. Praneeth, M. R. Ringenberg, T. R. Ward, Angewandte Chemie - International Edition 2012, 51, 10228–10234.

[40] B. De Bruin, P. Gualco, N. D. Paul, in Ligand Design in Metal Chemistry: Reactivity and Catalysis, Wiley, 2016, pp. 176–204.

[41] O. R. Luca, R. H. Crabtree, Chem Soc Rev 2013, 42, 1440–1459.

[42] R. Eisenberg, H. B. Gray, Inorg Chem 2011, 50, 9741–9751.

[43] E. N. Nikolaevskaya, N. O. Druzhkov, M. A. Syroeshkin, M. P. Egorov, Coord Chem Rev 2020, 417, DOI 10.1016/j.ccr.2020.213353.

[44] P. Maire, T. Büttner, F. Breher, P. Le Floch, H. Grützmacher, Angewandte Chemie - International Edition 2005, 44, 6318–6323.

[45] T. Zweifel, J. V. Naubron, T. Büttner, T. Ott, H. Grützmacher, Angewandte Chemie - International Edition 2008, 47, 3245–3249.

[46] R. H. Crabtree, The Organometallic Chemistry of the Transition Metals, Wiley, 2014.

[47] J. L. Templeton, in ADVANCES IN ORGANOMETALLIC CHEMISTRY, 1989, pp. 1–100.

[48] U. Belluco, R. Bertani, R. A. Michelin, M. Mozzon, Platinum-Alkynyl and-Alkyne Complexes: Old Systems with New Chemical and Physical Perspectives, 2000.

[49] N. J. Long, C. K. Williams, Angewandte Chemie - International Edition 2003, 42, 2586–2617.

[50] H. Katayama, F. Ozawa, Coord Chem Rev 2004, 248, 1703–1715.

[51] R. Wiedemann, P. Steinert, O. Gevert, H. Werner, J Am Chem Soc 1996, 118, 2495–2496.

[52] W. I. Dzik, B. De Bruin, Organometallic Chemistry 2011, 37, 46–78.

[53] N. Elgrishi, K. J. Rountree, B. D. McCarthy, E. S. Rountree, T. T. Eisenhart, J. L. Dempsey, J Chem Educ 2018, 95, 197–206.

[54] C. Kingston, M. D. Palkowitz, Y. Takahira, J. C. Vantourout, B. K. Peters, Y. Kawamata, P. S. Baran, Acc Chem Res 2020, 53, 72–83.

[55] J.-M. Savéant, C. Costentin, in Elements of Molecular and Biomolecular Electrochemistry, Wiley, 2019, pp. 1–80.

[56] A. L. Speelman, J. B. Gerken, S. P. Heins, E. S. Wiedner, S. S. Stahl, A. M. Appel, Energy Environ Sci 2022, 1–15.

[57] C. M. Galvin, R. M. Waymouth, J Am Chem Soc 2020, 142, 19368–19378.

[58] M. C. Leech, K. Lam, Nat Rev Chem 2022, 6, 275–286.

[59] T. Suzuki, Chem Rev 2011, 111, 1825–1845.

[60] M. Trincado, J. Bösken, H. Grützmacher, Coord Chem Rev 2021, 443, 213967.

[61] M. Trincado, D. Banerjee, H. Grützmacher, Energy Environ Sci 2014, 7, 2464–2503.

[62] C. Parmeggiani, F. Cardona, Green Chemistry 2012, 14, 547–564.

[63] A. E. Wendlandt, S. S. Stahl, Angewandte Chemie International Edition 2015, 54, 14638–14658.

[64] N. Donati, M. Königsmann, D. Stein, L. Udino, H. Grützmacher, Comptes Rendus Chimie 2007, 10, 721–730.

[65] M. Königsmann, N. Donati, D. Stein, H. Schönberg, J. Harmer, A. Sreekanth, H. Grützmacher, Angewandte Chemie - International Edition 2007, 46, 3567–3570.

[66] C. W. Anson, S. Ghosh, S. Hammes-Schiffer, S. S. Stahl, J Am Chem Soc 2016, 138, 4186–4193.

[67] F. Wang, S. S. Stahl, Acc Chem Res 2020, 53, 561–574.

[68] P. J. Bonitatibus, M. P. Rainka, A. J. Peters, D. L. Simone, M. D. Doherty, Chemical Communications 2013, 49, 10581–10583.

[69] P. Jurt, O. G. Salnikov, T. L. Gianetti, N. V. Chukanov, M. G. Baker, G. Le Corre, J. E. Borger, R. Verel, S. Gauthier, O. Fuhr, K. V. Kovtunov, A. Fedorov, D. Fenske, I. V. Koptyug, H. Grützmacher, Chem Sci 2019, 10, 7937–7945.

[70] P. Jurt, A. S. Abels, J. J. Gamboa-Carballo, I. Fernández, G. Le Corre, M. Aebli, M. G. Baker, F. Eiler, F. Müller, M. Wörle, R. Verel, S. Gauthier, M. Trincado, T. L. Gianetti, H. Grützmacher, Angewandte Chemie - International Edition 2021, 60, 25372–25380.

[71] L. Bettucci, C. Bianchini, W. Oberhauser, M. Vogt, H. Grützmacher, Dalton Transactions 2010, 39, 6509–6517.

[72] F. Breher, H. Rüegger, M. Mlakar, M. Rudolph, S. Deblon, H. Schönberg, S. Boulmaâz, J. Thomaier, H. Grützmacher, Chemistry - A European Journal 2004, 10, 641–653.

[73] C. Schweinzer, P. Coburger, H. Grützmacher, Advanced Science 2024, DOI 10.1002/advs.202400072.

[74] H.-P. Boehm, Angewandte Chemie 1966, 78, 617–628.

[75] S. Samad, K. S. Loh, W. Y. Wong, T. K. Lee, J. Sunarso, S. T. Chong, W. R. Wan Daud, Int J Hydrogen Energy 2018, 43, 7823–7854.

[76] H. Marsh, F. Rodríguez-Reinoso, in Activated Carbon (Eds.: H. Marsh, F. Rodríguez-Reinoso), Elsevier Science Ltd, Oxford, 2006, pp. 13–86.

[77] C. S. Allen, F. Ghamouss, O. Boujibar, P. J. F. Harris, Proceedings of the Royal Society A: Mathematical, Physical and Engineering Sciences 2022, 478, DOI 10.1098/rspa.2021.0580.

[78] A. Burian, J. C. Dore, K. Jurkiewicz, Reports on Progress in Physics 2019, 82, DOI 10.1088/1361-6633/aae882.

[79] T. J. Bandosz, M. J. Biggs, K. E. Gubbins, Y. Hattori, T. Liyama, K. Kaneko, J. Pikunic, K. T. Thomson, in Chemistry & Physics of Carbon, CRC Press, 2003, pp. 41–61.

[80] A. C. Tripathi, S. A. Saraf, S. K. Saraf, Materials 2015, 8, 3068–3100.

[81] N. Jung, D. Y. Chung, J. Ryu, S. J. Yoo, Y. E. Sung, Nano Today 2014, 9, 433–456.

[82] H. S. Kim, Y. Lee, J. G. Lee, H. J. Hwang, J. Jang, S. M. Juon, A. Dorjgotov, Y. G. Shul, Electrochim Acta 2016, 193, 191–198.

[83] Y. Zhou, K. Neyerlin, T. S. Olson, S. Pylypenko, J. Bult, H. N. Dinh, T. Gennett, Z. Shao, R. O'Hayre, Energy Environ Sci 2010, 3, 1437–1446.

[84] W. C. Trogler, Organometallic Radical Processes, De Gruyter, 1990.

[85] D. Astruc, Electron Transfer and Radical Processes in Transition-Metal Chemistry, John Wiley & Sons, 1995.

[86] W. E. Geiger, Organometallics 2007, 26, 5738–5765.

[87] N. G. Connelly, in Molecular Electrochemistry of Inorganic, Bioinorganic and Organometallic Compounds, Springer Netherlands, Dordrecht, 1993, pp. 317–329.

[88] D. A. Valyaev, O. V Semeikin, N. A. Ustynyuk, Coord Chem Rev 2004, 248, 1679–1692.

[89] N. A. Ustynyuk, O. V Gusev, L. N. Novikova, M. G. Peterleitner, L. I. Denisovich, T. A. Peganova, O. V Semeikin, D. A. Valyaev, Journal of Solid State Electrochemistry 2007, 11, 1621–1634.

[90] R. Lomoth, Antioxid Redox Signal 2013, 19, 1803–1814.

[91] W. J. Bowyer, W. E. Geiger, J Am Chem Soc 1985, 107, 5657–5663.

[92] C. A. Gamelas, E. Herdtweck, J. P. Lopes, C. C. Romão, Organometallics 1999, 18, 506–515.

[93] J. A. Reingold, K. L. Virkaitis, G. B. Carpenter, S. Sun, D. A. Sweigart, P. T. Czech, K. R. Overly, J Am Chem Soc 2005, 127, 11146–11158.

[94] R. L. Lord, C. K. Schauer, F. A. Schultz, M. H. Baik, J Am Chem Soc 2011, 133, 18234–18242.

[95] J. Edwin, W. E. Geiger, Structural Changes Coupled to Two-Electron-Transfer Reactions: Oxidation Mechanism of Pseudo-Triple-Decker Complexes of Co and Rh*, 1990.

[96] W. E. Geiger, A. Salzer, J. Edwin, W. von Philipsborn, -Umberto Piantini, A. L. Rheingold, Electrochemically Induced Insertion of Ruthenium Atoms into a C-C Bond: Reversible Slicing of a Cyclooctatetraene Ligand1 2", 1990.

[97] T. Takao, M. Moriya, H. Suzuki, Organometallics 2007, 26, 1349–1360.

[98] P. A. Schauer, P. J. Low, Eur J Inorg Chem 2012, 390–411.

[99] E. Furimsky, Carbons and Carbon-Supported Catalysts in Hydroprocessing, The Royal Society Of Chemistry, 2008.

[100] L. Li, Z. H. Zhu, Z. F. Yan, G. Q. Lu, L. Rintoul, Appl Catal A Gen 2007, 320, 166–172.

[101] C. H. Bartholomew, R. J. Farrauto, in Fundamentals of Industrial Catalytic Processes, John Wiley & Sons, Inc., 2010, pp. 487–559.

[102] P. Serna, B. C. Gates, Acc Chem Res 2014, 47, 2612–2620.

[103] Z. A. C. Ramli, S. K. Kamarudin, Nanoscale Res Lett 2018, 13, DOI 10.1186/s11671-018-2799-4.

[104] S. Sui, X. Wang, X. Zhou, Y. Su, S. Riffat, C. jun Liu, J Mater Chem A Mater 2017, 5, 1808–1825.

[105] C. R. Raj, A. Samanta, S. H. Noh, S. Mondal, T. Okajima, T. Ohsaka, J Mater Chem A Mater 2016, 4, 11156–11178.

[106] S. Jayabal, G. Saranya, D. Geng, L. Y. Lin, X. Meng, J Mater Chem A Mater 2020, 8, 9420–9446.

[107] A. Dutta, P. Mondal, Journal of Physical Chemistry C 2018, 122, 16925–16939.

[108] L. Dubicki, R. L. Martin, Inorg Chem 1970, 9, 673–675.

[109] A. M. Arif, R. A. Jones, M. H. Seeberger, B. R. Whittlesey, T. C. Wrirght, Inorg Chem 1986, 25, 3943–3949.

[110] S. Nakajima, D. Yokogawa, Y. Nakao, H. Sato, S. Sakaki, Organometallics 2004, 23, 4672–4681.

[111] D. Ostendorf, C. Landis, H. Grützmacher, Angewandte Chemie - International Edition 2006, 45, 5169–5173.

[112] C. J. Elsevier, B. Kowall, H. Kragten, Inorg Chem 1995, 34, 4836–4839.

[113] M. Buhl, M. Håkansson, A. H. Mahmoudkhani, L. Öhrström, Organometallics 2000, 19, 5589–5596.

[114] H. Schönberg, S. Boulmaâz, M. Wörle, L. Liesum, A. Schweiger, H. Grützmacher, Angewandte Chemie International Edition 1998, 37, 1423–1426.

[115] P. Maire, F. Breher, H. Schönberg, H. Grützmacher, Organometallics 2005, 24, 3207–3218.

[116] B. de Bruin, J. C. Russcher, H. Grützmacher, J Organomet Chem 2007, 692, 3167–3173.

[117] F. F. Puschmann, J. Harmer, D. Stein, H. Rüegger, B. De Bruin, H. Grützmacher, Angewandte Chemie - International Edition 2010, 49, 385–389.

[118] F. F. Puschmann, H. Grützmacher, B. De Bruin, J Am Chem Soc 2010, 132, 73–75.

[119] M. D. Carr, L. H. Gan, I. Reid, J. Chem. Soc., Perkin Trans. 2 1973, 668–672.

[120] R. J. Bushby, Quarterly Reviews, Chemical Society 1970, 24, 585.

[121] J. Y. Becker, Tetrahedron 1976, 32, 3041–3043.

[122] M. Feofanov, D. I. Sharapa, V. Akhmetov, Green Chemistry 2022, 24, 4761–4765.

[123] Z. Wang, Y. Wang, L. Zhang, J Am Chem Soc 2014, 136, 8887–8890.

[124] S. Aime, A. J. Deeming, M. B. Hursthouse, J. D. J. Backer-Dirks, J. Chem. Soc., Dalton Trans. 1982, 1625–1629.

[125] A. J. Amoroso, L. P. Clarke, J. E. Davies, J. Lewis, H. R. Powell, P. R. Raithby, G. P. Shields, J Organomet Chem 2001, 635, 119–131.

[126] C. Sze-Wai Lau, W.-T. Wong, Journal of the Chemical Society, Dalton Transactions 1999, 607–614.

[127] M. I. Bruce, A. C. Meier, N. N. Zaitseva, B. W. Skelton, A. H. White, Aust J Chem 2001, 54, 319–324.

[128] S. Attali, F. Dahan, R. Mathieu, Organometallics 1986, 5, 1376–1379.

[129] D. A. J. Harding, E. G. Hope, K. Singh, G. A. Solan, Polyhedron 2012, 33, 360–366.

[130] Bösken Jonas, Ruthenium Diazabutadiene Olefin Complexes for (Electro)Catalytic Dehydrogenations, Dissertation Nr. 28352, ETH Zürich, 2022.

[131] P. Jurt, Small Molecule Activation by Dirhodium and Rhodium-Platinum Complexes, Dissertation Nr. 27139, ETH Zürich, 2021.

[132] D. S. Lee, I. Köhler, E. Grobler, F. Rohrer, R. Sausen, L. Gallardo-Klenner, J. G. J. Olivier, F. J. Dentener, A. F. Bouwman, Atmos Environ 1997, 31, 1735–1749.

[133] A. R. Ravishankara, J. S. Daniel, R. W. Portmann, Science (1979) 2009, 326, 123–125.

[134] J. Hansen, M. Sato, Proc Natl Acad Sci U S A 2004, 101, 16109–16114.

[135] G. W. LaPier, Trans Am Nucl Soc 1984, 46, 9.

[136] R. J. Laumbach, H. M. Kipen, Journal of Allergy and Clinical Immunology 2012, 129, 3–11.

[137] M. W. Chase, J. Phys. Chem. Ref. Data Monogr. 1998, 9, 1.

[138] H. Fan, K. G. Caulton, Polyhedron 2007, 26, 4731–4736.

[139] L. B. Maia, J. J. G. Moura, Chem Rev 2014, 114, 5273–5357.

[140] K. Brown, M. Tegoni, M. Prudêncio, A. S. Pereira, S. Besson, J. J. Moura, I. Moura, C. Cambillau, Nat Struct Biol 2000, 7, 191–195.

[141] N. Russo, D. Fino, G. Saracco, V. Specchia, Catal Today 2007, 119, 228–232.

[142] H. Cassel, E. Glückauf, Zeitschrift für Physikalische Chemie 1932, 19B, DOI 10.1515/zpch-1932-1906.

[143] T. L. Gianetti, S. P. Annen, G. Santiso-Quinones, M. Reiher, M. Driess, H. Grützmacher, Angewandte Chemie - International Edition 2016, 55, 1854–1858.

[144] T. L. Gianetti, R. E. Rodríguez-Lugo, J. R. Harmer, M. Trincado, M. Vogt, G. Santiso-Quinones, H. Grützmacher, Angewandte Chemie - International Edition 2016, 55, 15323–15328.

[145] R. Zeng, M. Feller, Y. Ben-David, D. Milstein, J Am Chem Soc 2017, 139, 5720–5723.

[146] R. Zeng, M. Feller, Y. Diskin-Posner, L. J. W. Shimon, Y. Ben-David, D. Milstein, J Am Chem Soc 2018, 140, 7061–7064.

[147] G. B. Wijeratne, M. Bhadra, M. A. Siegler, K. D. Karlin, J Am Chem Soc 2019, 141, 17962–17967.

[148] W. P. Griffith, Advances in Organometallic Chemistry 1969, 7, 211–239.

[149] G. B. Richter-Addo, P. Legzdins, Chem Rev 1988, 88, 991–1010.

[150] S. G. Clarkson, F. Basolo, Inorg Chem 1973, 12, 1528–1534.

[151] A. G. Whittaker, D. M. Yost, J Am Chem Soc 1949, 71, 3135–3137.

[152] B. B. Wayland, A. R. Newman, Inorg Chem 1981, 20, 3093–3097.

[153] A. Czap, F. W. Heinemann, R. Van Eldik, Inorg Chem 2004, 43, 7832–7843.

[154] I. Ara, J. Forniés, M. A. García-Monforte, B. Menjón, R. M. Sanz-Carrillo, M. Tomas, A. C. Tsipis, C. A. Tsipis, Chemistry - A European Journal 2003, 9, 4094–4105.

[155] M. R. Gyton, B. Leforestier, A. B. Chaplin, Angewandte Chemie - International Edition 2019, 58, 15295–15298.

[156] C. Laporte, C. Böhler, H. Schönberg, H. Grützmacher, J Organomet Chem 2002, 641, 227–234.

[157] C. Lichtenberg, M. Adelhardt, M. Wörle, T. Büttner, K. Meyer, H. Grützmacher, Organometallics 2015, 34, 3079–3089.

[158] Martin. Karplus, J Am Chem Soc 1963, 85, 2870–2871.

[159] C. Hansch, A. Leo, R. W. Taft, Chem Rev 1991, 91, 165–195.

[160] P. Chirik, R. Morris, Acc Chem Res 2015, 48, 2495.

[161] D. L. Anderson, J Geophys Res 1983, 88 Suppl, 41–52.

[162] M. Trincado, A. J. Rosenthal, M. Vogt, H. Grützmacher, Eur J Inorg Chem 2014, 1599–1604.

[163] M. Vogt, B. de Bruin, H. Berke, M. Trincado, H. Grützmacher, Chem Sci 2011, 2, 723–727.

[164] R. E. Rodríguez-Lugo, B. de Bruin, M. Trincado, H. Grützmacher, Chemistry - A European Journal 2017, 23, 6795–6802.

[165] C. Lichtenberg, L. Viciu, M. Adelhardt, J. Sutter, K. Meyer, B. De Bruin, H. Grützmacher, Angewandte Chemie - International Edition 2015, 54, 5766–5771.

[166] T. L. Gianetti, R. E. Rodríguez-Lugo, J. R. Harmer, M. Trincado, M. Vogt, G. Santiso-Quinones, H. Grützmacher, Angewandte Chemie - International Edition 2016, 55, 15323–15328.

[167] P. L. Pauson, I. U. Khand, Ann N Y Acad Sci 1977, 295, 2–14.

[168] J. D. Ricker, L. M. Geary, Top Catal 2017, 60, 609–619.

[169] S. E. Gibson, A. Stevenazzi, Angewandte Chemie - International Edition 2003, 42, 1800–1810.

[170] C. Ferrer, J. Benet-Buchholz, A. Riera, X. Verdaguer, Chemistry - A European Journal 2010, 16, 8340–8346.

[171] J. Thomaier, S. Boulmaâz, H. Schönberg, H. Rüegger, A. Currao, H. Grützmacher, H. Hillebrecht, H. Pritzkow, New Journal of Chemistry 1998, 22, 947–958.

[172] S. C. Rathnayaka, N. P. Mankad, Coord Chem Rev 2021, 429, 213718.

[173] F. Breher, C. Böhler, G. Frison, J. Harmer, L. Liesum, A. Schweiger, H. Grützmacher, Chemistry - A European Journal 2003, 9, 3859–3866.

[174] F. Tewes, Iridium-Catalyzed Dehydrogenation of Alcohols, Dissertation Nr. 18705, ETH Zürich, 2009.

[175] V. Sacchetti, New Trop-Based Ligands and Their Application in Catalysis, Dissertation Nr. 23218, ETH Zürich, 2016.

[176] K. Häbe, Chemie von "Non-Innocent" Liganden: Rhodium in Stickstoff-Olefinkomplexen, Dissertation Nr. 16835, ETH Zürich, 2006.

[177] F. Taullaj, A. J. Lough, U. Fekl, Acta Crystallogr E Crystallogr Commun 2019, 75, 1824–1827.

[178] J. P. Barham, G. Coulthard, K. J. Emery, E. Doni, F. Cumine, G. Nocera, M. P. John, L. E. A. Berlouis, T. McGuire, T. Tuttle, J. A. Murphy, J Am Chem Soc 2016, 138, 7402–7410.

[179] B. Braïda, S. E. Galembeck, P. C. Hiberty, J Chem Theory Comput 2017, 1, DOI 10.1021/acs.jctc.7b00399ï.

[180] F. R. Keene, Metal-Ion Promotion of the Oxidative Dehydrogenation of Coordinated Amines and Alcohols, 1999.

[181] J. E. Nutting, J. B. Gerken, A. G. Stamoulis, D. L. Bruns, S. S. Stahl, Journal of Organic Chemistry 2021, 86, 15875–15885.

[182] B. Taljaard, J. H. Taljaard, C. Imrie, M. R. Caira, European J Org Chem 2005, 2607–2619.

[183] H. Werner, M. Bosch, M. E. Schneider, C. Hahn, F. Kukla, M. Manger, B. Windmüller, B. Weberndörfer, M. Laubender, Journal of the Chemical Society, Dalton Transactions 1998, 3549–3558.

List of compounds

$(CyC{\equiv}C)_2tropPPh_2$	**1**
$[((CyC{\equiv}C)_2tropPPh_2)Rh_2(\mu\text{-}Cl)_2]_2$	**[2]**
$[((CyC{\equiv}C)_2tropPPh_2)Rh_2OTf_2]$	**[3]**
$[((CyC{\equiv}C)_2tropPPh_2)Rh_2bipy_2](OTf)_2$	**[4](OTf)$_2$**
$[((CyC{\equiv}C)_2tropPPh_2)Rh_2bipy_2](OTf)$	**[4](OTf)**
$[((CyC{\equiv}C)_2tropPPh_2)Rh(\mu\text{-}Cl)]_2$	**[5]**
$[((CyC{\equiv}C)_2tropPPh_2)Rhbipy](OTf)$	**[6]**
$[((dicyclohexyldibenzyl\text{-}cycloundeca\text{-}tetraene)PPh_2)Rh_2bipy_2]$	**[7]**
$[((Cy{=}C{=}C)(CyC{\equiv}C)tropPPh_2)Rh_2bipy_2](OTf)$	**[8]**
$[((Cy{=}C{=}C)_2tropPPh_2)Rh_2bipy_2]$	**[9]**
Ph^Fdad	**10**
$[((CyC{\equiv}C)_2tropPPh_2)Rh_2(Ph^Fdad)(OTf)](OTf)$	**[11]**
$[((CyC{\equiv}C)_2tropPPh_2)Rh_2(Phdad)(OTf)](OTf)$	**[12]**
$[((CyC{\equiv}C)(CyCH_2C)tropPPh_2)Rh_2OTf_2]$	**[13]**
$[((CyCH{=}CH)(CyCH_2C)tropPPh_2)Rh_2OTf_2]$	**[13-H2]**
$[(CyC{\equiv}C)_2tropPPh_2RhClPtMe_2]$	**[14]**
$[(CyC{\equiv}C)_2tropPPh_2RhOTfPtMe_2]$	**[15]**
$[(CyC{\equiv}C)_2tropPPh_2Rh(MeCN)_2PtMe_2]BArF$	**[16]**
$[(CyC{\equiv}C)_2tropPPh_2Rh(NO_2)PtMe_2]$	**[17]**
$[(CyC{\equiv}C)_2tropPPh_2Rh(Cl)CuCl]_2$	**[18]**
$[(CyC{\equiv}C)_2tropPPh_2Rh(Cl)(MeCN)CuCl]$	**[19]**
$[(CyC{\equiv}C)_2tropPPh_2Rh(OTf)(MeCN)Cu(MeCN)]$	**[20]**
$Rh_2\text{-}Cu\text{-}(cyTropP)$	**[21]**
$(PhC{\equiv}C)_2tropNHtrop$	**22a**
$(CyC{\equiv}C)_2tropNHtrop$	**22b**
$[((PhC{\equiv}C)_2tropNHtrop)Rh(ACN)_2]^+$	**[23a]$^+$**

[((CyC≡C)$_2$tropNHtrop)Rh(ACN)$_2$]$^+$	**[23b]**$^+$
[((PhC≡C)$_2$tropNHtrop)Rh(ACN)$_2$]BF$_4$	**[23a]**BF$_4$
[((PhC≡C)$_2$tropNHtrop)Rh(ACN)$_2$]OTf	**[23a]**OTf
[((PhC≡C)$_2$tropNHtrop)Rh(COD)]$^+$	**[24a]**$^+$
[((PhC≡C)$_2$tropNHtrop)Rh(COD)]$^+$	**[24b]**$^+$
[((PhC≡C)$_2$tropNHtrop)Rh(COD)]OTf	**[24a]**OTf
[((PhC≡C)$_2$tropNHtrop)Rh(COD)]BArF	**[24a]**BArF
[((CyC≡C)$_2$tropNHtrop)Rh(COD)]BArF	**[24b]**BArF
[(PhC≡C)$_2$tropNHCu]$_2$(BF$_4$)$_2$	**[25]**(BF$_4$)$_2$
[(PhC≡C)$_2$tropNHtropCu(MeCN)$_2$]BF$_4$	**[26]**BF$_4$
(PhC≡C)$_2$tropPPh$_2$	**27**
[(PhC≡C)$_2$tropPPh$_2$CoCp]	**[28]**
[(PhC≡C)$_2$tropPPh$_2$Co(HMDS)$_2$]	**[29]**
[(PhC≡C)$_2$tropPPh$_2$Co$_2$CO$_4$]	**[30]**
[(cyclized-(PhC≡C)$_2$tropPPh$_2$)$_2$Co$_2$]	**[31]**
[(PhC≡C)$_2$tropPPh$_2$CuCl]	**[32]**
[(CyC≡C)$_2$tropPPh$_2$CuCl]	**[33]**
[(PhC≡C)$_2$tropPPh$_2$Cu$_2$(μ-Cl)$_2$]$_2$	**[34]**
[(PhC≡C)$_2$tropPPh$_2$Cu$_2$OTf$_2$]	**[35]**
[(CyC≡C)$_2$tropPPh$_2$Cu$_2$Cl$_2$]	**[36]**
[(CyC≡C)$_2$tropPPh$_2$Cu$_2$OTf$_2$]	**[37]**
[Ir(trop$_2$dach)]OTf	**[38]**OTf
[Ir(trop$_2$dae)]OTf	**[39]**OTf
[Ir(trop$_2$dad)]OTf	**[40]**OTf
[Ir(trop$_2$dad)]	**[40]**$^{\bullet}$
[Ir(trop$_2$dad)]$^-$	**[40]**$^-$
Na[Ir(trop$_2$dad)]	Na**[40]**

ZnOTf[Ir(trop$_2$dad)]	ZnOTf[**40**]
[Li$_3$Ir(tropdad)(trop)]	Li$_3$[**41**]
[Ir(trop$_2$dad)]$_2$	[**42**]
[Ir(trop$_2$mima)]OTf	[**43**]OTf
[Ir(trop$_2$dad(tBu)ONa)]	[**44**]
[Ir(trop$_2$dad(HMDS))]	[**45**]
[Ir(trop$_2$^{Me}dad)]OTf	[**46**]OTf
[Ir(trop$_2$^{Me}dad)]	[**46**]$^{\cdot}$
[Ir(trop$_2$^{Me}dad)]$_2$	Na[**47**]
[Ir(trop$_2$dach)]-H	[**48**]
K[Ir(trop$_2$dach)]-2H	K[**49**]
[Ir(trop$_2$diq)]OTf	[**50**]OTf
[Ir(trop$_2$diq)]	[**50**]
trop$_2$dad	**51**
trop$_2$Medad	**52**
trop$_2$DACH	**53**

List of abbreviations

Å	Angström (1 Å = 10^{-10} m)
°	Degree
°C	Degree Celsius
acac	Acetoacetate
ar	Aromatic
ATR	Attenuated Total Reflectance
av.	average
BArF	Tetrakis(3,5-bis(trifluoromethyl)phenyl)borate
br	Broad
benz	Benzylic
BQ	1,4-Benzoquinone
cat.	Catalyst / catalytic
COD	1,5-Cyclooctadiene
COE	Cyclooctene
COSY	Homo-Nuclear Shift Correlation Spectroscopy
ct	Centroid
CV	Cyclic Voltammetry
CW	Continuous Wave
Cy	Cyclohexyl
dach	Diaminocyclohexane
dad	1,4-Diazabuta-1,3-diene
dae	Diaminoethane
DCM	Dichloromethane
diq	1,2-Diiminoquinone
Dipp	Diisopropylphenyl
DMSO	Dimethyl sulfoxide
EPR	Electron Paramagnetic Resonance
eq.	Equivalent
Fc	Ferrocene
Fc^+	Ferrocenium Ion
h	Hour
HQ	1,4-Hydroquinone
Hz	Hertz
IBO	Intrinsic bond orbital
IR	Infra Red
J	Coupling Constant
K	Kelvin
L	Liter

M	Metal
Me	Methyl
mg	Milligram
mima	Mono(imine)mono(amine)
min	Minute
mL	Milliliter
mmol	Millimol
mol	Mol
MO	Molecular orbital
NMR	Nuclear Magnetic Resonance
NOESY	Nuclear Overhauser Effect Spectroscopy
olef	Olefin
OTf	Triflate
PA	Phenylacetylene
ppm	Parts per million
rt	Room temperature
s	Second
T	temperature
TEMPO	2,2,6,6-Tetramethylpiperidine-1-oxyl
t, *tert*	Tertiary
THF	Tetrahydrofuran
TMS	Trimethylsilane
TON	Turnover number
trop	Dibenzotropylidene
UV/Vis	Ultraviolet/visible
λ	Wavelength